

**THERMAL CONSTRAINTS ON GREAT THRUST  
EARTHQUAKE RUPTURE ZONES**

by


Daniel Alexander Oleskevich  
B.Sc., University of Waterloo, 1993


A Thesis Submitted in Partial Fulfillment of the  
Requirements for the Degree of


MASTERS OF SCIENCE


in the School of Earth and Ocean Sciences

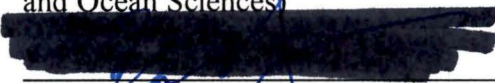
We accept this thesis as conforming  
to the required standard

  
\_\_\_\_\_  
Dr. Roy D. Hyndman, Supervisor (Pacific Geoscience Centre, Geological Survey of  
Canada and School of Earth and Ocean Sciences, University of Victoria)

  
\_\_\_\_\_  
Dr. George D. Spence, Co-Supervisor (School of Earth and Ocean Sciences)

  
\_\_\_\_\_  
Dr. Kathy Gillis, Departmental Member (School of Earth and Ocean Sciences)

  
\_\_\_\_\_  
Dr. Garry C. Rogers, Outside Member (Pacific Geoscience Centre and School of Earth  
and Ocean Sciences)

  
\_\_\_\_\_  
Dr. Kelvin Wang, Outside Member (Pacific Geoscience Centre)

  
\_\_\_\_\_  
Dr. John F. Cassidy, External Examiner (Pacific Geoscience Centre)

© Daniel Oleskevich, 1996  
University of Victoria

All rights reserved. This thesis may not be produced in whole or in part, by  
photocopy or other means, without the permission of the author.

deformation front and the downdip limit extends approximately beneath the coast. The width estimates for both profiles match the 1944-46 great thrust coseismic and interseismic geodetic data very well.

For the South Alaska Margin, a wide seismogenic zone of 200+30 km is proposed, mainly because of the greater plate age and shallow dip. The seaward limit is reached about 70 km landward of the deformation front, and the downdip thermal limit occurs around a depth of 80 km. Subduction thrust earthquakes generally occur to a maximum depth of 45 km. In this case, the serpentinized forearc mantle may limit the downdip extent of the seismogenic zone at a depth of about 40-45 km. This limit corresponds well with the width obtained from the dislocation model fit to the coseismic deformation associated with the 1964 great thrust earthquake. For the Chile Margin, variations in the seismogenic zone widths are proposed due to the variations in subducting Nazca Plate age, ranging from 5 to 50 Ma. The widths are 120+30 km for the South Chile profile, 70+30 km for the Valparaiso profile, 55+20 km for the Coquimbo profile, 60+30 km for the Taltal profile, and 60+30 km for the North Chile profile. These widths are compared with the dislocation model width estimates from great earthquake deformation data on the southern two profiles. There is good agreement with the South Chile profile and poorer agreement with the Valparaiso profile.

Examiners:



Dr. Roy D. Hyndman, Supervisor (Pacific Geoscience Centre and School of Earth and Ocean Sciences)



Dr. George D. Spence, Co-Supervisor (School of Earth and Ocean Sciences)



Dr. Kathy Gillis, Departmental Member (School of Earth and Ocean Sciences)



Dr. Garry C. Rogers, Outside Member (Pacific Geoscience Centre and School of Earth and Ocean Sciences)

Supervisor: Dr. Roy Hyndman

## ABSTRACT

This thesis examines the updip and downdip limits to great earthquake rupture on subduction thrust faults. It tests the hypothesis that the updip limit is thermally controlled with the onset of stick-slip behaviour associated with dehydration of marine clays around 100-150°C, and that the downdip limit is controlled either by, (a) stable sliding that starts at temperatures around 350°C where the thrust is still in contact with overlying continental crustal rocks or, (b) stable sliding that is induced by serpentinized forearc mantle if the mantle corner is reached along the thrust before 350°C. The thermal limit is generally the case for the subduction of young, hot oceanic plates, while the serpentinized control is for the subduction of old, cold oceanic plates. Detailed numerical thermal models have been generated to estimate the thrust plane downdip temperatures of four continental subduction zones: Cascadia, Nankai (southwest Japan), South central Alaska, and Chile. Temperatures along the thrust are dependent on several parameters: the convergence rate, the sediment thickness on the incoming oceanic plate, the oceanic plate age, the dip profile, the thermal conductivity, the radiogenic heat generation, and the thermal heat capacity. The thermal and forearc mantle limits from the numerical models have then been compared to the interseismic locked zone width as estimated from geodetic surface deformation patterns and to coseismic rupture estimates from seismic and tsunami data. With one exception, there is good agreement between the proposed updip and downdip limits to the seismogenic zone and the great earthquake rupture and interseismic geodetic modelling.

For Cascadia, the estimated seismogenic locked and transition zone widths are 45+45 km for the Vancouver Island profile, 85+85 km for the Olympic Peninsula profile, 55+55 km for the Columbia River profile, and 45+45 km for the mid-Oregon profile. The landward limit of the locked zone is 40-50 km seaward of the coast, except for off the Olympic Peninsula where it is only 20-30 km from the coast. The limit is in good agreement with modelling of interseismic geodetic data. For Nankai, the widths are 80+40 km for the Tonankai profile and 120+55 km for the Nankaido profile. The seaward limit is ~30 km landward of the



---

Dr. Kelin Wang, Outside Member (Pacific Geoscience Centre)



---

Dr. John F. Cassidy, External Examiner (Pacific Geoscience Centre)

## TABLE OF CONTENTS

|   |           |
|---|-----------|
| ABSTRACT .....  | ii        |
| TABLE OF CONTENTS .....                                 | v         |
| LIST OF TABLES .....                                    | x         |
| LIST OF FIGURES .....                                   | x         |
| ACKNOWLEDGMENTS .....                                   | xiv       |
| <br>  |           |
| <b>CHAPTER I INTRODUCTION .....</b>                     | <b>1</b>  |
| 1.1 SUBDUCTION THRUST EARTHQUAKES .....                 | 1         |
| 1.2 SLIP BEHAVIOUR OF THE SUBDUCTION THRUST .....       | 4         |
| 1.3 PURPOSE OF STUDY .....                              | 5         |
| 1.3.1 Regions of study .....                            | 6         |
| 1.4 OUTLINE OF THESIS .....                             | 7         |
| <br>  |           |
| <b>CHAPTER II GEOLOGIC &amp; TECTONIC SETTING .....</b> | <b>8</b>  |
| 2.1 INTRODUCTION .....                                  | 8         |
| 2.2 CASCADIA .....                                      | 8         |
| 2.2.1 Sediment sections .....                           | 10        |
| Deep sea & trench-fill sediments .....                  | 10        |
| Accretionary prism .....                                | 10        |
| 2.2.2 Continental Geology .....                         | 12        |
| 2.3 SOUTH ALASKA .....                                  | 14        |
| 2.3.1 Sediment sections .....                           | 15        |
| Deep sea & trench-fill sediments .....                  | 15        |
| Accretionary prism .....                                | 16        |
| 2.3.2 Continental Geology .....                         | 17        |
| 2.4 CHILE .....   | 19        |
| 2.4.1 Sediment sections .....                           | 21        |
| Deep sea & trench-fill sediments .....                  | 21        |
| Accretionary prism .....                                | 23        |
| 2.4.2 Continental Geology .....                         | 23        |
| 2.5 NANKAI .....  | 25        |
| 2.5.1 Sediment sections .....                           | 27        |
| Deep sea & trench-fill sediments .....                  | 27        |
| Accretionary prism .....                                | 28        |
| 2.5.2 Continental Geology .....                         | 28        |
| <br>  |           |
| <b>CHAPTER III THERMAL MODELLING APPROACH .....</b>     | <b>29</b> |

|  |    |
|--|----|
| 3.1 INTRODUCTION .....   | 29 |
| 3.2 LIMITS TO THE SEISMOGENIC ZONE .....                                       | 29 |
| 3.2.1 Sliding behaviour .....  | 29 |
| 3.2.2 The downdip temperature limit .....                                      | 30 |
| 3.2.3 The updip temperature limit .....  | 32 |
| 3.2.4 The serpentinization of mantle rocks: an alternative downdip limit ..... | 33 |
| 3.3 HEAT TRANSFER THEORY .....   | 35 |
| 3.3.1 The 1-D thermal model .....  | 35 |
| 3.3.2 The 2-D thermal model .....  | 36 |
| 3.4 APPLICATION OF THE 2-D MODEL PARAMETERS .....                              | 37 |
| 3.4.1 Non-thermal parameters .....   | 38 |
| Sediment accumulation rate & prism structure .....                             | 38 |
| Plate dip profile .....  | 39 |
| Convergence rate & plate age .....   | 40 |
| 3.4.2 Thermal parameters .....   | 41 |
| Thermal Conductivity .....   | 41 |
| Radiogenic heat generation .....   | 41 |
| 3.4.3 Frictional heating .....   | 42 |
| 3.4.4 The effect of volcanic arcs .....  | 43 |
| 3.4.5 Finite element grid .....  | 43 |
| 3.5 CASCADIA .....   | 45 |
| 3.5.1 Non-thermal parameters .....   | 45 |
| Sediment accumulation rate & prism structure .....                             | 45 |
| Low conductivity and low heat generation terranes .....                        | 46 |
| Plate dip profile .....  | 46 |
| Convergence rate & plate age .....   | 50 |
| 3.5.2 Thermal parameters .....   | 51 |
| Thermal conductivity .....   | 51 |
| Radiogenic heat generation .....   | 52 |
| 3.6 SOUTH ALASKA .....   | 53 |
| 3.6.1 Non-thermal parameters .....   | 53 |
| Sediment accumulation rate & prism structure .....                             | 53 |
| Plate dip profile .....  | 53 |
| Convergence rate & plate age .....   | 56 |
| 3.6.2 Thermal parameters .....   | 57 |
| Thermal conductivity .....   | 57 |
| Radiogenic heat production .....   | 57 |
| 3.7 CHILE .....  | 57 |
| 3.7.1 Non-thermal parameters .....   | 57 |
| Sediment accumulation rate & prism structure .....                             | 57 |
| Plate dip profile .....  | 58 |
| Convergence rate & plate age .....   | 61 |

|  |  |           |
|--|--|-----------|
| 3.7.2  | Thermal parameters                                   | 62        |
|  | Thermal conductivity                                 | 62        |
|  | Radiogenic heat production                           | 64        |
| 3.8  | NANKAI   | 65        |
| 3.8.1  | Non-thermal parameters                               | 65        |
|  | Sediment accumulation rate & prism structure         | 65        |
|  | Plate dip profile                                    | 66        |
|  | Convergence rate & plate age                         | 66        |
| 3.8.2  | Thermal parameters                                   | 67        |
|  | Thermal conductivity                                 | 67        |
|  | Radiogenic heat production                           | 68        |
| <b>CHAPTER IV THERMAL RESULTS</b>              |  | <b>69</b> |
| 4.1  | INTRODUCTION   | 69        |
| 4.2  | CASCADIA   | 69        |
| 4.2.1  | Thermal model results                                | 69        |
|  | Temperature-depth profiles                           | 69        |
|  | Surface heat flow data                               | 70        |
|  | Low conductivity/radiogenic heat generation terranes | 71        |
|  | The effects of a shallow dipping plate               | 73        |
| 4.2.2  | Temperature fields                                   | 73        |
| 4.2.3  | Uncertainty analysis                                 | 75        |
|  | Non-thermal parameters                               | 76        |
|  | Thermal parameters                                   | 78        |
|  | Frictional heating                                   | 81        |
| 4.3  | SOUTH ALASKA & CHILE                                 | 83        |
| 4.3.1  | Thermal model results                                | 83        |
|  | Temperature-depth profiles                           | 83        |
|  | Surface heat flow data                               | 84        |
|  | Low conductivity/radiogenic heat generation terranes | 85        |
|  | The effect of volcanic arcs                          | 86        |
| 4.3.2  | Temperature fields                                   | 86        |
| 4.3.3  | Uncertainty analysis                                 | 89        |
| 4.4  | NANKAI MARGIN  | 91        |
| 4.4.1  | Thermal model results                                | 91        |
|  | Temperature-depth profiles                           | 91        |
|  | Surface heat flow data                               | 91        |
| 4.4.2  | Temperature fields                                   | 93        |
| 4.4.3  | Uncertainty Analysis                                 | 93        |
| <b>CHAPTER V SEISMOGENIC WIDTH CONSTRAINTS</b> |  | <b>96</b> |

|       |   |     |
|-------|---|-----|
| 5.1   | INTRODUCTION                              | 96  |
| 5.2   | SEISMOGENIC WIDTH CONSTRAINTS             | 96  |
| 5.2.1 | Seismicity constraints                    | 96  |
|       | Great thrust earthquakes and aftershocks  | 96  |
|       | Intermediate magnitude thrust earthquakes | 97  |
|       | Tsunami constraints                       | 98  |
| 5.2.2 | Geodetic constraints                      | 98  |
|       | Geodetic Data                             | 99  |
|       | Elastic Dislocation Models                | 100 |
|       | Coseismic deformation                     | 102 |
|       | Interseismic deformation                  | 103 |
| 5.3   | CASCADIA                                  | 103 |
| 5.3.1 | Seismicity constraints                    | 103 |
|       | Tsunami constraints                       | 103 |
| 5.3.2 | Geodetic constraints                      | 104 |
|       | Levelling data                            | 104 |
|       | Tide gauge data                           | 107 |
|       | GPS data                                  | 109 |
|       | Coseismic deformation                     | 109 |
| 5.3.3 | Comparison with thermal model results     | 110 |
| 5.4   | SOUTH ALASKA                              | 112 |
| 5.4.1 | Seismicity constraints                    | 112 |
|       | 1964 Main event                           | 112 |
|       | 1964 Aftershock activity                  | 112 |
|       | Intermediate magnitude thrust earthquakes | 113 |
|       | Tsunami constraints                       | 113 |
| 5.4.2 | Geodetic constraints                      | 116 |
|       | Levelling data                            | 116 |
|       | Tide gauge data                           | 116 |
|       | Coastal data                              | 117 |
| 5.4.3 | Comparison with thermal model results     | 119 |
| 5.5   | CHILE                                     | 120 |
| 5.5.1 | Seismicity constraints                    | 120 |
|       | 1960 Main event                           | 120 |
|       | 1960 Aftershock activity                  | 123 |
|       | 1985 Main event                           | 123 |
|       | 1985 Foreshock & aftershock activity      | 124 |
|       | 1971 Main event & aftershock activity     | 125 |
|       | 1943 Main event & aftershock activity     | 126 |
|       | Intermediate magnitude thrust earthquakes | 126 |
|       | Tsunami constraints                       | 128 |
| 5.5.2 | Geodetic constraints                      | 129 |
|       | Levelling data                            | 129 |

|  |            |
|--|------------|
| Tide gauge data .....                              | 130        |
| Coastal data .....                                 | 130        |
| 5.5.3 Comparison with thermal model results .....  | 130        |
| 5.6 NANKAI .....                                   | 136        |
| 5.6.1 Seismicity constraints .....                 | 136        |
| 1944 & 1946 Main events .....                      | 136        |
| 1944 & 1946 Aftershock activity .....              | 136        |
| Tsunami constraints .....                          | 137        |
| 5.6.2 Geodetic constraints .....                   | 138        |
| Levelling data .....                               | 138        |
| Tide gauge data .....                              | 138        |
| 5.6.3 Comparison with thermal model results .....  | 140        |
| <br>   |            |
| <b>CHAPTER VI DISCUSSION AND CONCLUSIONS .....</b> | <b>143</b> |
| 6.1 SEISMOGENIC WIDTH PREDICTIONS .....            | 143        |
| 6.1.1 Thermal model .....                          | 143        |
| Constraints to seismogenic zones .....             | 143        |
| Uncertainty analysis .....                         | 143        |
| 6.1.2 Seismogenic width constraints .....          | 144        |
| Uncertainty analysis .....                         | 144        |
| 6.2 CONCLUSION .....                               | 145        |
| <br>   |            |
| <b>BIBLIOGRAPHY .....</b>                          | <b>148</b> |

## LIST OF TABLES

|           |  |     |
|-----------|--|-----|
| Table 1.1 | List of top 10 megathrust events over the last century . . . . .                               | 3   |
| Table 3.1 | List of parameters used in the 1-D thermal model . . . . .                                     | 37  |
| Table 3.2 | List of data sources used for the oceanic plate dip profile geometry . . . . .                 | 40  |
| Table 3.3 | List of physical parameters used to constrain the thermal models . . . . .                     | 50  |
| Table 3.4 | List of thermal parameters used to constrain the thermal models . . . . .                      | 52  |
| Table 6.1 | Comparison of thermal and dislocation model seismogenic widths to<br>seismicity data . . . . . | 167 |

## LIST OF FIGURES

|             |   |    |
|-------------|---|----|
| Figure 1.1  | Circum-Pacific seismicity map for the last 50 years . . . . .                 | 2  |
| Figure 1.2  | The seismogenic zone of subduction thrust faults . . . . .                    | 5  |
| Figure 2.1  | Map showing the tectonic regime for Cascadia . . . . .                        | 9  |
| Figure 2.2  | Cross-section for Vancouver Island profile . . . . .                          | 11 |
| Figure 2.3  | Map showing the geological setting for Cascadia . . . . .                     | 13 |
| Figure 2.4  | Map showing the tectonic regime for South Alaska . . . . .                    | 15 |
| Figure 2.5  | Cross-section for S. Alaska . . . . .   | 16 |
| Figure 2.6  | Geological setting for South Alaska . . . . .                                 | 18 |
| Figure 2.7  | Map showing the tectonic regime for Chile . . . . .                           | 20 |
| Figure 2.8a | Cross-section showing sediment thickness, 3 provinces, Chile . . . . .        | 22 |
| Figure 2.8b | Axial cross-section showing sediment thickness, Chile . . . . .               | 22 |
| Figure 2.9  | Map showing morphological units, Chile . . . . .                              | 24 |
| Figure 2.10 | Map showing the tectonic regime for Nankai . . . . .                          | 26 |
| Figure 2.11 | Cross-section for Nankai . . . . .  | 27 |
| Figure 3.1  | Velocity strengthening-velocity weakening behaviour around 350°C . . . . .    | 31 |
| Figure 3.2  | Frictional response to increasing temperature from Westerly granite . . . . . | 32 |
| Figure 3.3  | Smectite-illite transition with increasing temperature . . . . .              | 33 |

|              |  |    |
|--------------|--|----|
| Figure 3.4   | Porosity-depth curve for sediments near the deformation front . . . . .      | 36 |
| Figure 3.5   | 2-D finite element mesh . . . . .  | 44 |
| Figure 3.6a  | Multichannel seismic reflection cross-section for Van. Is. profile . . . . . | 47 |
| Figure 3.6b  | Interpretation of main reflections of Figure 3.6 (a) . . . . .               | 47 |
| Figure 3.6c  | Dip profile from Fig. 3.6 (a) & (b) and Wadati-Benioff earthquakes . . .     | 48 |
| Figure 3.7   | Dip profiles for Cascadia . . . . .  | 49 |
| Figure 3.8a  | Interpreted multichannel seismic reflection data for S. Alaska . . . . .     | 54 |
| Figure 3.8b  | Dip profile from Fig. 3.8 (a) and Wadati-Benioff earthquakes . . . . .       | 55 |
| Figure 3.9   | Two-way travel time vs. depth conversion curve . . . . .                     | 56 |
| Figure 3.10  | Dip profile for North Chile profile . . . . .                                | 59 |
| Figure 3.11  | Dip profile for Taltal profile . . . . .                                     | 60 |
| Figure 3.12  | Dip profile for Coquimbo profile . . . . .                                   | 61 |
| Figure 3.13  | Dip profile for Valparaiso profile . . . . .                                 | 62 |
| Figure 3.14a | Multichannel seismic reflection cross-section for South Chile profile . . .  | 63 |
| Figure 3.14b | Interpretation of main reflections of Fig. 3.14 (a) . . . . .                | 63 |
| Figure 3.14c | Dip profile from Fig. 3.14 (a) & (b) and Wadati-Benioff earthquakes . .      | 64 |
| Figure 3.15a | Multichannel seismic reflection cross-section for Nankaido profile . . . .   | 67 |
| Figure 3.15b | Dip profile from Fig. 3.5 (a) and Wadati-Benioff earthquakes . . . . .       | 67 |
| Figure 4.1   | 1-D temperature gradient for Cascadia . . . . .                              | 70 |
| Figure 4.2   | Model surface heat flow compared to heat flow data, Cascadia . . . . .       | 72 |
| Figure 4.3   | Temperature contours (isotherms) for Cascadia . . . . .                      | 74 |
| Figure 4.4   | Thrust plane temperatures vs. distance landward for Cascadia . . . . .       | 75 |
| Figure 4.5a  | Variation to model heat flow with a changing subducting plate age . . . .    | 77 |
| Figure 4.5b  | Thrust plane temperatures for changing oceanic plate age . . . . .           | 78 |
| Figure 4.6   | Variation to model heat flow with a changing subducting plate dip . . . .    | 79 |
| Figure 4.7a  | Variation to model heat flow with the addition of frictional heating . . . . | 82 |
| Figure 4.7b  | Variation to thrust plane temperatures with the frictional heating . . . .   | 82 |
| Figure 4.8   | 1-D temperature gradient for S. Alaska and Chile . . . . .                   | 83 |
| Figure 4.9a  | Model surface heat flow for S. Alaska and Chile . . . . .                    | 85 |

|              |  |     |
|--------------|--|-----|
| Figure 4.9b  | Model surface heat flow compared to heat flow data, Chile . . . . .                        | 85  |
| Figure 4.10a | Temperature contours for S. Alaska and northern Chile . . . . .                            | 87  |
| Figure 4.10b | Temperature contours for southern Chile . . . . .  | 88  |
| Figure 4.11  | Thrust plane temperatures vs. distance for S. Alaska and Chile . . . . .                   | 90  |
| Figure 4.12  | 1-D temperature gradient for Nankai . . . . .  | 91  |
| Figure 4.13  | Model surface heat flow compared to heat flow data for Nankai . . . . .                    | 92  |
| Figure 4.14  | Temperature contours for Nankai . . . . .  | 94  |
| Figure 4.15  | Thrust plane temperatures vs. distance landward for Nankai . . . . .                       | 95  |
| Figure 5.1   | Elastic half-space dislocation model . . . . .   | 102 |
| Figure 5.2   | Map of geodetic data sources for Cascadia . . . . .  | 105 |
| Figure 5.3a  | 2-D dislocation model fit to interseismic data, Van. Island profile . . . . .              | 106 |
| Figure 5.3b  | 2-D dislocation model fit to interseismic data, Olym. Pen. profile . . . . .               | 106 |
| Figure 5.3c  | 2-D dislocation model fit to interseismic data, Columbia R. profile . . . . .              | 107 |
| Figure 5.3d  | 2-D dislocation model fit to interseismic data, mid-Oregon profile . . . . .               | 108 |
| Figure 5.3e  | 2-D dislocation model fit to interseismic data, mid-Oregon profile . . . . .               | 108 |
| Figure 5.4   | Map showing locked and transition zone widths, Cascadia . . . . .                          | 111 |
| Figure 5.5a  | Aftershock and inverted tsunami rupture area, S. Alaska . . . . .                          | 114 |
| Figure 5.5b  | Coseismic surface deformation, S. Alaska . . . . .   | 115 |
| Figure 5.6a  | 2-D dislocation model fit to coseismic data, Kenai Pen. profile . . . . .                  | 118 |
| Figure 5.6b  | 2-D dislocation model fit to coseismic data, Kodiak Is. profile . . . . .                  | 118 |
| Figure 5.7   | Map showing locked and transition zone widths, S. Alaska . . . . .                         | 119 |
| Figure 5.8a  | Aftershock and inverted tsunami rupture area, S. Chile profile . . . . .                   | 121 |
| Figure 5.8b  | Coseismic surface deformation, S. Chile profile . . . . .                                  | 122 |
| Figure 5.9   | Aftershock seismicity from 1971 & 1985 events, Valparaiso profile . . . . .                | 124 |
| Figure 5.10  | Aftershock seismicity from 1943 event, Coquimbo profile . . . . .                          | 126 |
| Figure 5.11  | Aftershock seismicity from 1966, 1983, & 1987 events, Taltal & N. Chile profiles . . . . . | 128 |
| Figure 5.12a | 2-D dislocation model fit to coseismic data, S. Chile profile . . . . .                    | 131 |
| Figure 5.12b | 2-D dislocation model fit to coseismic data, Valparaiso profile . . . . .                  | 131 |

|              |  |     |
|--------------|--|-----|
| Figure 5.13a | Map showing locked and transition zone widths, S. Chile profile . . . .                | 132 |
| Figure 5.13b | Map showing locked and transition zone widths, Valparaiso profile . .                  | 133 |
| Figure 5.13c | Map showing locked and transition zone widths, Coquimbo profile . . .                  | 133 |
| Figure 5.13d | Map showing locked and transition zone widths, Taltal & N. Chile<br>profiles . . . . . | 135 |
| Figure 5.14  | Aftershock and inverted tsunami rupture area for Nankai . . . . .                      | 137 |
| Figure 5.15a | 2-D dislocation model fit to coseismic data, Tonankai profile . . . . .                | 139 |
| Figure 5.15b | 2-D dislocation model fit to interseismic data, Tonankai profile . . . . .             | 139 |
| Figure 5.15c | 2-D dislocation model fit to coseismic data, Nankaido (north) profile .                | 140 |
| Figure 5.15d | 2-D dislocation model fit to interseismic data, Nankaido (north) profile               | 140 |
| Figure 5.15e | 2-D dislocation model fit to coseismic data, Nankaido (south) profile .                | 141 |
| Figure 5.15f | 2-D dislocation model fit to interseismic data, Nankaido (south)<br>profile . . . . .  | 141 |
| Figure 5.16  | Map showing locked and transition zone widths for Nankai . . . . .                     | 142 |
| Figure 6.1   | Histogram plot showing thermal and dislocation model results . . . . .                 | 145 |

## ACKNOWLEDGMENTS

I would like to thank my supervisor, Dr. Roy Hyndman, for his guidance and dedication to this study of great thrust earthquakes. Dr. Hyndman was always approachable for questions, and has the ability of simplifying a problem into identifiable, well founded components from which a reasonable solution is obtained. I am particularly grateful for his reviews of the thesis near the end of the program. I extend my thanks to my graduate committee, Dr. George Spence, Dr. Garry Rogers, and Dr. Kathy Gillis who provided support and direction throughout this study. I also thank my external examiner, Dr. John Cassidy, for his time and review of this thesis.

I am also thankful for the opportunity to have worked as a co-op masters student. The academics at the University of Victoria and the working environment at the Pacific Geoscience Centre has been extremely helpful in promoting my understanding on how experienced geophysicists might discuss and offer solutions to outstanding problems. I extend my thanks to Garry Rogers, Herb Dragert, Kelin Wang for the numerous discussions related to tectonic and thermal modelling for the Cascadia Margin. I would also like to thank Richard Baldwin for his help with UNIX systems, Randy Enkin for discussions regarding his interesting paleomagnetic results, and the administrative staff at PGC.

I am also thankful for discussions with Joe Henton regarding the Western Canadian Deformation Array GPS network, world history and geography, Bernard Desmons and Paul Flueck for sharing computer time, and Cam Fink for working through MATLAB together. I am especially grateful to my family for their encouragement, and to my girlfriend, Sandra de Souza, whose perseverance and commitment to our relationship provided exceptional support towards this endeavour.

## CHAPTER I INTRODUCTION

### 1.1 SUBDUCTION THRUST EARTHQUAKES

The focus of this study is great subduction thrust ( $M > 8.0$ ) and megathrust ( $M > 9.0$ ) earthquakes produced by the abrupt release of strain accumulated along the interface between a subducting oceanic plate, and an overriding continental plate (e.g., Chen & Molnar, 1983; Savage, 1983; Rogers, 1988; Pacheco et al., 1993; Dragert et al., 1994). (Fig. 1.1). This interface is commonly referred to as the subduction thrust plane. The greatest concentration of subduction thrust events globally occurs along the Circum-Pacific Belt (Fig. 1.1). This seismic belt consists mainly of low magnitude thrust earthquakes of similar mechanism which occur very frequently. The depths to the thrust activity may be used to obtain an approximate top of the subducting plate, and thus the boundary to the seismic portion of the subduction thrust plane. The great thrust and megathrust earthquakes represent the abrupt release of hundreds of years of strain, and represent most of the global budget of seismic energy released annually. The largest 25 historical earthquakes are listed in Table 1.1, with corresponding magnitudes. The large magnitude is related to the large rupture area and to the amount of slip along the thrust plane. These great earthquakes are associated with the highest seismic risk globally, and are a primary concern in the economical and geographical growth and of coastal towns and cities. The seismic belt also is a product of a dipping group of earthquake foci which occur within the subducting plate referred to as Wadati-Benioff earthquakes, important in determining the position downdip and geometry of the subducting plate. Together, these very different types of earthquakes outline the subducting behaviour and fate of the Pacific Plate at its convergent boundaries.

The severity of great thrust and especially megathrust earthquakes is readily acknowledged by looking at the immediate and longer term consequences. Initially, with coseismic rupture, the toe of the overriding plate, which was coupled to the subducting plate, moves rapidly updip along the thrust plane, causing extension, subsidence, and strong ground motion for coastal areas. Flooding, slope failure, and heavily damaged or collapsed buildings may result, taking many casualties. At the same time, farther offshore, large continental shelf

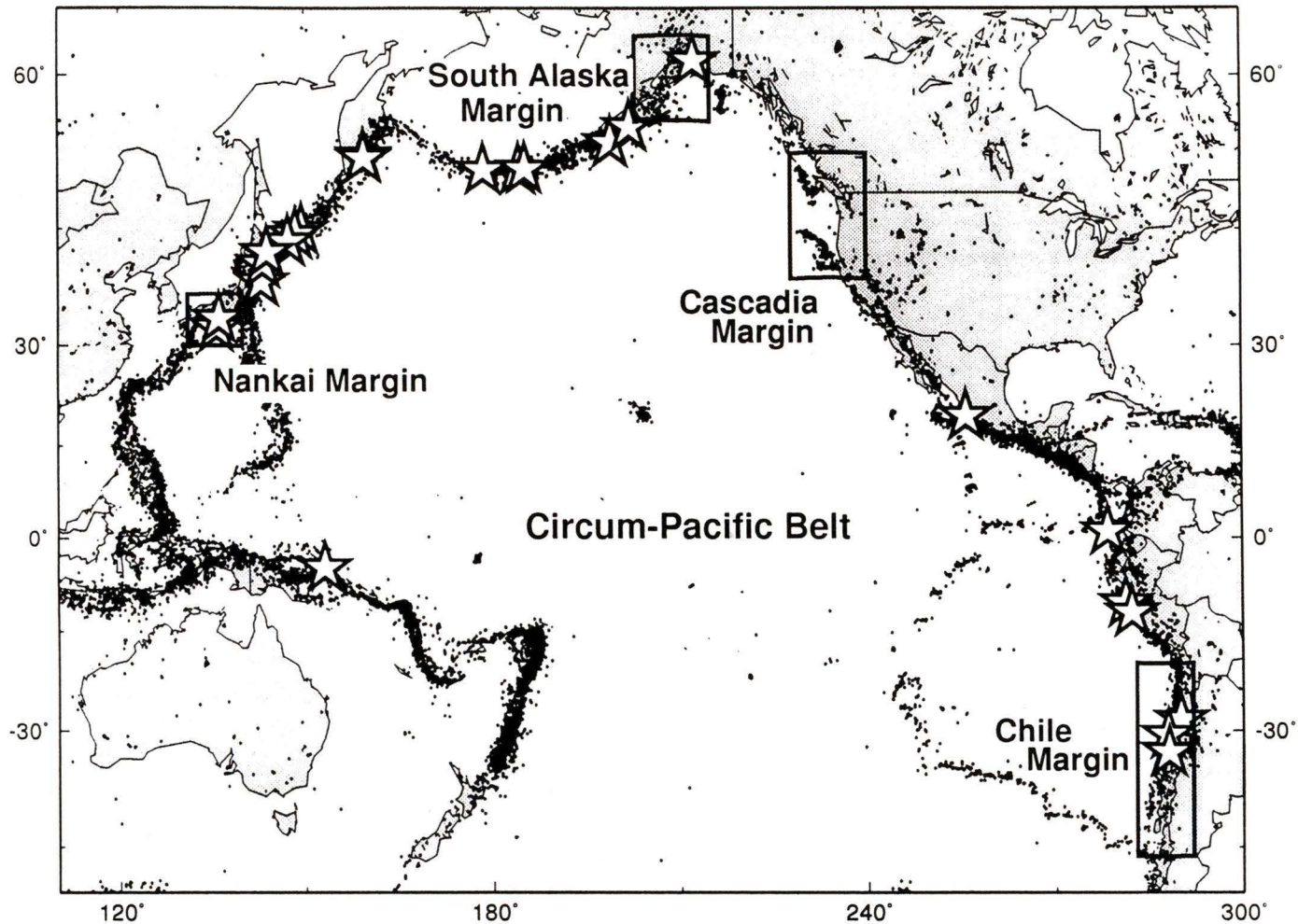


Figure 1.1. Map showing the shallow, low magnitude seismic activity (0-80 km;  $4.0 < m_b < 7.5$ ) along the Circum-Pacific Belt over the last 20 years. The seismic activity records mainly thrust and Wadati-Benioff earthquakes resulting from the subduction of the Pacific Plate and various east Pacific plates along the western, northern, and eastern boundaries. Great and megathrust earthquakes (large stars) have occurred less frequently but are distributed fairly uniformly along the belt. One notable exception is the absence of historical thrust events for the Cascadia Margin. Boxes indicate regions of study (USGS National Earthquake Information Centre sources, *Reagor et al.* [1994]).

| Date                     | Region                   | M <sub>s</sub> | M <sub>w</sub> |
|--------------------------|--------------------------|----------------|----------------|
| <b>May 22, 1960</b>      | <b>South Chile</b>       | <b>8.5</b>     | <b>9.5</b>     |
| <b>March 28, 1964</b>    | <b>South Alaska</b>      | <b>8.4</b>     | <b>9.2</b>     |
| March 9, 1957            | Aleutian                 | 8.1            | (9.1)          |
| November 4, 1952         | Kamchatka                | 8.3            | 9              |
| January 31, 1906         | Ecuador-Columbia         | 8.6            | (8.8)          |
| February 4, 1965         | Rat Is., Aleutian        | 8.2            | 8.7            |
| November 11, 1922        | Atakama, Chile           | 8.3            | (8.5)          |
| October 13, 1963         | Kurile Islands           | 8.1            | 8.5            |
| March 2, 1933            | Sanriku, Japan           | 8.5            | 8.4            |
| November 6, 1958         | Kurile Islands           | 8.1            | 8.3            |
| February 3, 1923         | Kamchatka                | 8.3            | (8.3)          |
| May 16, 1968             | Tokachi-Oki, Japan       | 8.1            | 8.2            |
| August 11, 1969          | Kurile Islands           | 7.8            | 8.2            |
| August 17, 1906          | Valparaiso, Chile        | 8.4            | (8.2)          |
| November 10, 1938        | Alaska                   | 8.3            | (8.2)          |
| <b>April 6, 1943</b>     | <b>Coquimbo, Chile</b>   | <b>7.9</b>     | <b>(8.2)</b>   |
| May 4, 1959              | Kamchatka                | 7.7            | (8.2)          |
| <b>December 20, 1946</b> | <b>Nankaido, Japan</b>   | <b>8.2</b>     | <b>8.1</b>     |
| <b>December 7, 1944</b>  | <b>Tonankai, Japan</b>   | <b>8</b>       | <b>8.1</b>     |
| March 4, 1952            | Tokachi-Oki, Japan       | 8.3            | (8.1)          |
| June 3, 1932             | Jalisco, Mexico          | 8.1            | (8.1)          |
| October 17, 1966         | Peru                     | 7.8            | 8.1            |
| July 26, 1971            | New Ireland              | 7.7            | (8.1)          |
| Oct 3, 1974              | Peru                     | 7.6            | 8.1            |
| May 7, 1986              | Andreanof Is., Aleutian  | 8              | 8.0            |
| <b>March 3, 1985</b>     | <b>Valparaiso, Chile</b> | <b>7.8</b>     | <b>8.0</b>     |

Table 1.1. Largest great and megathrust earthquakes (1906-1992). Parenthesis indicate that the  $M_w$  values were determined from aftershock distribution areas (after *Kanamori* [1977]; *Abe* [1979]). Events marked with bold lettering indicate earthquakes relevant to this study.

and seafloor areas are uplifted producing a large tsunami which causes additional, extensive coastal damage, inflicting many more casualties. A tsunami from the same source, but moving in the opposite direction, may also cause casualties and some damage at distant locations. Within the few months during the postseismic period, low magnitude aftershock activity may persist. This seismicity represents the readjustment response to strain release in the great thrust event, and usually occurs over a region representative of the area involved in the great earthquake rupture (e.g., Tichelaar & Ruff, 1991; Plafker et al., 1994). Heavily damaged and unstable buildings may collapse with this activity, compounding the problems of rescue operations, rebuilding, or personal healing. The repercussions of great thrust earthquakes are thus important not only on local or nearby coastal areas, but rather on global proportions, and provide the impetus for this study.

## **1.2 SLIP BEHAVIOUR OF THE SUBDUCTION THRUST**

The subduction thrust has been divided into three regions defined by the seismogenic behaviour between and during great thrust events (Fig. 1.2) (e.g., Vrolijk, 1990; Blackwell, 1991; Hyndman & Wang, 1993; Tichelaar & Ruff, 1991). There is stable sliding between the oceanic plate and the blanket of deep sea and turbiditic sediments at the seaward, updip end of the thrust near the trench (e.g., Scholtz, 1988; Hyndman & Wang, 1993). With the onset of subduction, the majority of the sediments are scraped-off the incoming oceanic plate and accreted to the continental margin. The interaction between the base of the accreted sediment section and the subducting oceanic plate is important to the thermal models. One component of the sediment section are fine clays. Laboratory sliding tests with the dehydration of similar are generally marked with a transition from stable to unstable sliding around 100-150°C, (e.g., Vrolijk, 1990; Hyndman & Wang, 1993). This is taken to mark the updip, seaward limit of the locked, seismogenic zone, within which earthquake failure may initiate (Fig. 1.2).

Farther downdip, the contact along the thrust plane undergoes a brittle to semi-brittle transition, and exhibits stable-sliding at around 350°C (Tse & Rice, 1986; Blanpied et al. 1991). A transition zone is suggested between 350°C and 450°C, where fault rupture propagates with decreasing offset downdip. Coseismic rupture may propagate into the upper

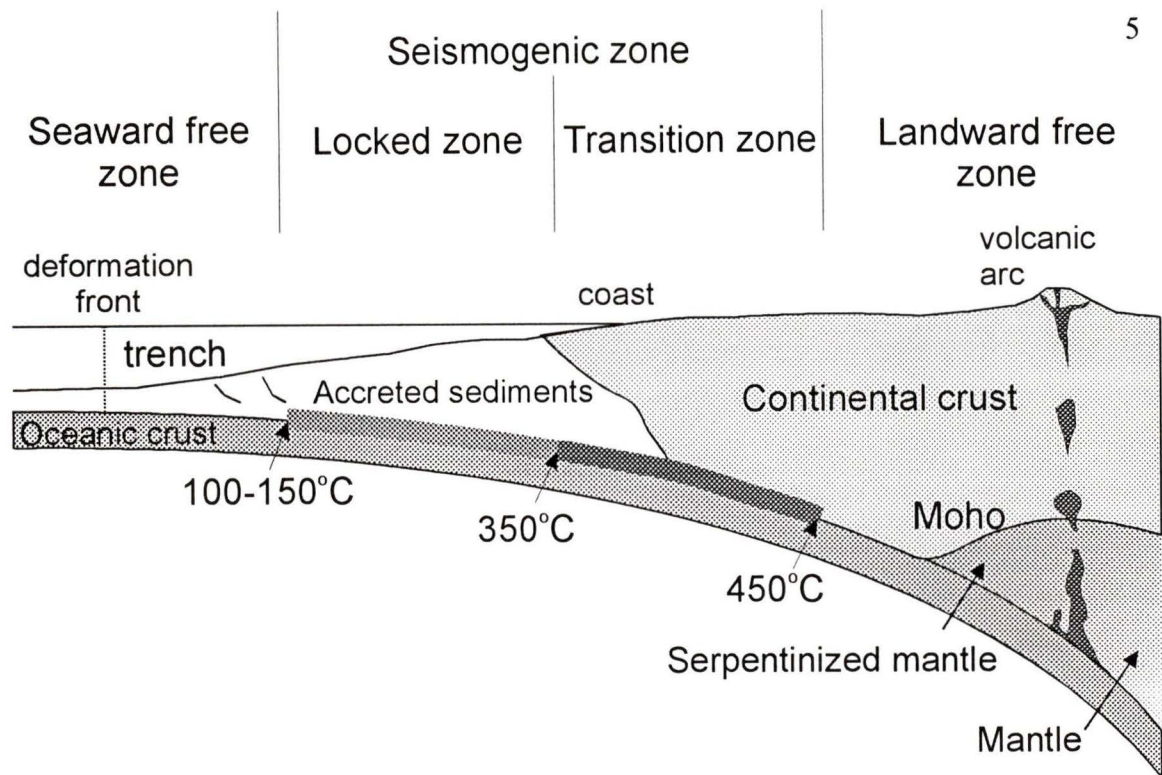


Figure 1.2. Division of the subduction thrust fault as given by thermal constraints of 100-150°C, 350°C, and 450°C. The updip limit to the earthquake-producing locked portion of the seismogenic zone may be where stable-sliding marine clays dehydrate sufficiently to initiate stick-slip behaviour, between 100-150°C. The downdip limit is likely where increasing temperature causes the contact rocks along the thrust plane to deform semi-plastically, around 350°C. The transition zone represents the region in which thrust fault rupture decreases to zero downdip. Beyond 450°C, plastic flow is believed to occur (modified from *Scholtz* [1988]).

portion of the transition zone, but earthquakes may not initiate with this region. Plastic flow is assumed to occur beyond 450°C (Tse & Rice, 1986). In the subduction of older oceanic plates which have had longer cooling periods, the 350°C landward downdip limit may not be reached until depths below which thrust earthquakes are observed globally. In these cases, serpentinized mantle below the continental Moho may act to lubricate the fault, and provide a mechanism for stable sliding (Fig. 1.2). Support for these limits will be discussed in greater detail in Chapter 3.

### 1.3 PURPOSE OF STUDY

The purpose of this study is twofold:

1. To calculate temperatures on subduction thrust plane and from this estimate the seismogenic zone width from detailed numerical thermal models, and;
2. To compare the proposed thermally controlled seismogenic zone with the downdip extent of observed seismic, tsunami, and geodetic data.

### 1.3.1 Regions of study

One notable exception to the megathrust distribution along the Circum-Pacific Belt is in the region of the Cascadia Margin (Fig. 1.1). Here, the subduction of the small Juan de Fuca Plate has produced no historically recorded large thrust earthquakes (e.g., Heaton & Kanamori, 1984; Rogers, 1988). This suggests that either the convergence with the overriding North America Plate is being accommodated aseismically, or the historical record is too short. As most subduction zones around the world have produced great thrust events, it is likely that the Juan de Fuca-North America convergence also produces such events. Interseismic uplift and shortening observed the length of the margin from geodetic data support the latter suggestion (e.g., Savage et al., 1991; Dragert et al., 1994; Atwater et al., 1995). Furthermore, numerous paleoseismic indicators show evidence of successive peat layers inferred to be the tops of old coastal marsh vegetation, rapidly buried from coseismic subsidence (e.g., Clague & Bobrowski, 1994; Atwater et al., 1995). Several of these peat layers are overlain by a thin layer of sand believed to be of tsunami origin. The intervals are irregular but average about 500 years between subsidence occurrence. This pattern is very similar to other coastal areas which have recently experienced great thrust earthquakes, and points to an earthquake cycle of interseismic tectonic uplift and sudden subsidence and tsunami flooding during coseismic rupture. Several deep sea turbidite sediment layers have also been interpreted to have their origin from marine landslides triggered by great earthquakes about every 590 years (e.g., Adams, 1990). There also exist historical records in Japan of a tsunami on January 26, 1700, which is suggested to have Cascadia as the origin (e.g., Satake, 1995). This coincides with isolated native legends that an earthquake occurred on a winter night, in which villages were lost to the sea. Initial thermal modelling of this margin was carried out by Hyndman & Wang (1993) and interseismic deformation modelling

by Dragert et al. (1994) and Hyndman & Wang (1995). Additional detailed modelling is part of this thesis study.

The other regions considered in this study include South Alaska, Chile, and Nankai (southwest Japan) margins (Fig. 1.1). They have all experienced historical, great thrust earthquakes, and have extensive geophysical data. The South Alaska Margin experienced a megathrust  $M_w=9.2$  event on March 27, 1964, which produced subsidence and uplift deformation and extensive damage (Plafker, 1969). One thermal model profile is included in this study. The Chile Margin has experienced great thrust earthquake activity over the last 300 years recorded from written records, and over the last 50 years from instrumental records (Nishenko, 1985). In the northern to central portion of the margin, numerous intermediate magnitude and great thrust earthquakes provide constraints on the maximum rupture depth along the thrust plane (Tichelaar & Ruff, 1993). Toward the southern portion of the margin, the megathrust  $M_w=9.5$  event of May 21, 1960, has substantial surface deformation and widespread damage, along with the generation of a large tsunami (Plafker & Savage, 1970). A series of thermal and coseismic deformation models have been produced for this study. The Nankai Margin off southwest Japan has regularly experienced great thrust earthquakes from written records over the past roughly 1000 years (Kanamori, 1972; Ando, 1975). These data record tsunami height run-up distances, the pattern of surface deformation, and the destruction along the southwest Japanese coast. The thermal regime and the downdip extent of the seismogenic zone of this margin studied by Hyndman et al. (1995) and Wang et al. (1995b) are included for discussion, but no new thermal models was done.

#### **1.4 OUTLINE OF THESIS**

This study examines the geological and tectonic setting for each of the margins described above (Chapter 2), followed by a discussion of the thermal constraints to the seismogenic zone and 2-D thermal model parameters (Chapter 3). The results of the thermal models for each margin are presented, with estimates to the seismogenic zone widths (Chapter 4), followed by a comparison to the seismic rupture and geodetic data deformation patterns (Chapter 5). Discussion and conclusion close the thesis (Chapter 6).

## CHAPTER II GEOLOGIC & TECTONIC SETTING

### 2.1 INTRODUCTION

The thermal model used in this study to constrain the seismogenic widths is dependent on the physical parameters of the subduction zone; structure, lithology, and geological history of the accretionary prism, overriding continental plate, and subducting oceanic plate. The model is also dependent on the thermal properties; the thermal conductivity, radiogenic heat generation, and thermal heat capacity. This chapter begins with a brief description of the tectonic and geological setting for the four areas of study, highlighting the accretionary prism and overriding plate composition and structure. Particular emphasis is placed on the South Alaska and Chile margins for which new thermal models were generated.

### 2.2 CASCADIA

The Cascadia subduction zone extends nearly 1200 km along the mid-latitude western margin of the North America Plate, and marks a break in the right lateral transform fault system which extends from southeast Alaska to southern California / northern Mexico. The northern end of the converging Juan de Fuca plate system comprises a complex series of small plates, the largest of which is the Explorer Plate, which may have stopped converging or greatly slowed very recently (Fig. 2.1) (Govers et al., 1996). The change in margin fault mechanism in this region from the right lateral Queen Charlotte fault to the Cascadia thrust fault is accommodated by discontinuous transform faults including the Nootka and Sovanco fracture zones (Fig. 2.1) (Riddihough, 1984). The Mendocino Triple Junction marks the southern end of the margin, at the intersection of the Mendocino fracture zone, the Cascadia megathrust, and the San Andreas Fault (Mooney & Weaver, 1989). The highly deformed Juan de Fuca Plate in this region, also known as the Gorda Plate, bears witness to the complex behaviour near the triple junction. The Juan de Fuca Plate overall is a remnant of a much older oceanic plate system which has since subducted beneath North America.

Seafloor magnetic anomaly data suggest that the Juan de Fuca plate has been converging at roughly present rates at an approximate azimuth of  $65^\circ$  since the Eocene

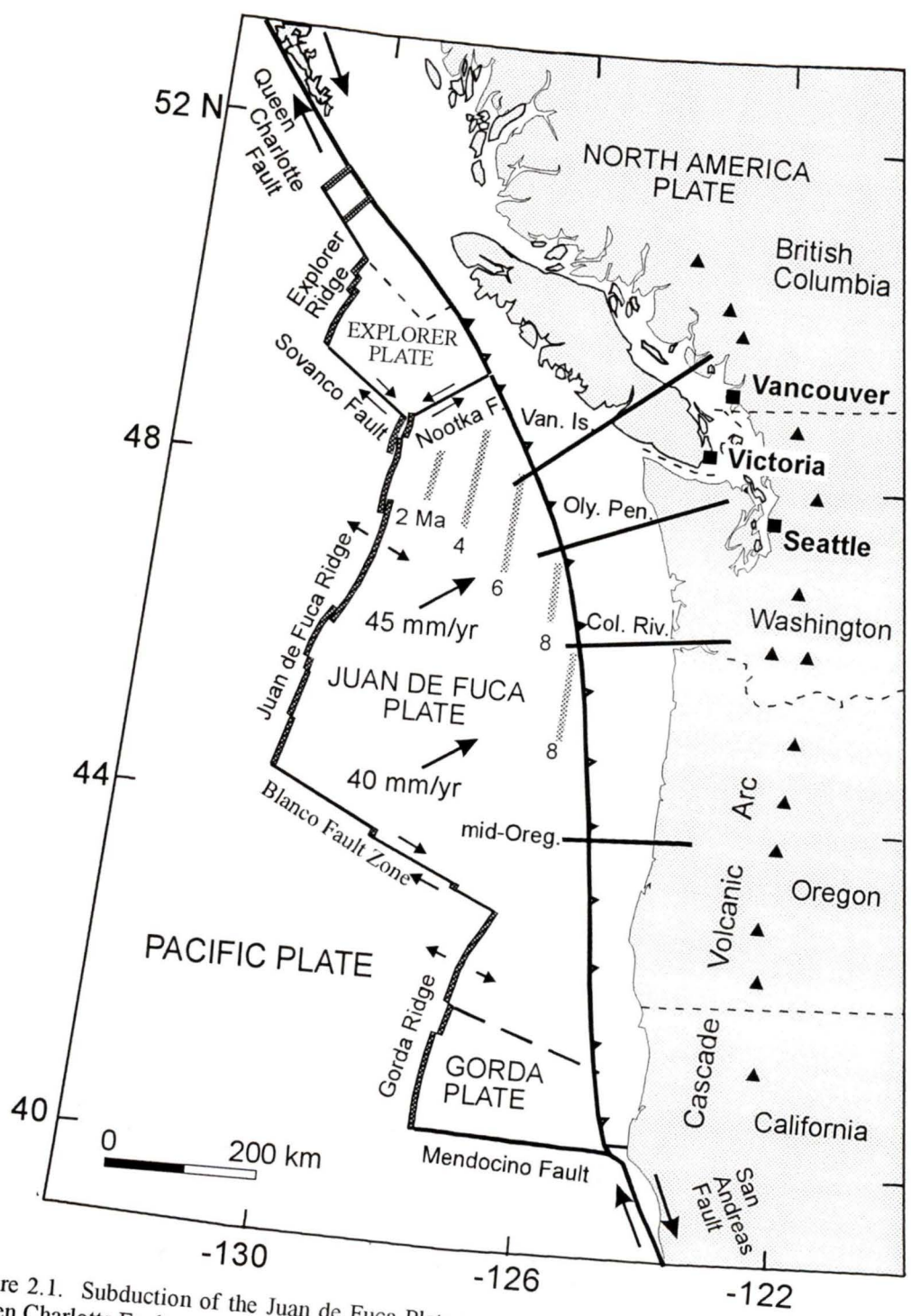


Figure 2.1. Subduction of the Juan de Fuca Plate separates the right lateral strike-slip San Andreas and Queen Charlotte Faults to the south and north of the subduction zone. Plate convergence decreases slightly and plate age increases slightly from north to south. The four thermal model profiles are shown as heavy lines perpendicular to the margin. Solid triangles show volcanic centres of the Cascade Volcanic Arc (modified from Davis & Hyndman [1989]).

(Riddihough, 1984). The present rate increases northwards along the margin from 40 mm/yr near 42°N (mid-Oregon) to 45 mm/yr near 48°N (Vancouver Island) (Davis & Riddihough, 1982; Riddihough, 1984; Engebretson et al., 1985; Riddihough, 1985; DeMets et al., 1990). The North America Plate absolute motion of 22 mm/yr relative to the deep mantle accounts for roughly half of the plate convergence rate (Riddihough, 1984). The fate of the Juan de Fuca plate upon subduction averages a dip of 10-12° 60 km landward of the deformation front in the northern and southern regions of subduction, separated by a region of flattening to 4-5° off the Olympic Peninsula. Here, the oceanic plate is geometrically constrained by a southwest facing embayment which acts to bow the subducting plate upwards. The Juan de Fuca Plate increases in age from north to south, from 6 Ma off Vancouver Island to 8 Ma off mid-Oregon (Riddihough, 1984), and is considered a relatively young, hot oceanic plate.

### **2.2.1 Sediment sections**

#### **Deep sea & trench-fill sediments**

The sedimentation history of the incoming sediments are important factors in the initial, seaward thermal gradient used in the thermal model. A 3 to 5 km thick succession of sediments covering the Juan de Fuca Plate near the deformation front consists of a lower, 1 to 2 km thick hemipelagic sequence of pre-Pleistocene age with relatively fine-grained sediments, and an upper, 2 to 3 km thick probably turbiditic layered sequence, rapidly deposited during the Pleistocene (Fig. 2.2) (Hayes & Ewing, 1970; Davis & Hyndman, 1989; Westbrook et al., 1994). The latter sequence includes coarse material interleaved with fine material associated with rapid deposition events associated with Pleistocene glaciation (Davis & Hyndman, 1989). Most of the sediments in this incoming section are accreted to the continental margin to form the large accretionary prism.

#### **Accretionary prism**

The off-scraping of the incoming sediment section and accretionary prism growth has been nearly continuous since the Eocene, with the volcanic Crescent Terrane forming a landward backstop (Fig. 2.2) (Clowes et al., 1987). Most of the continental shelf is covered

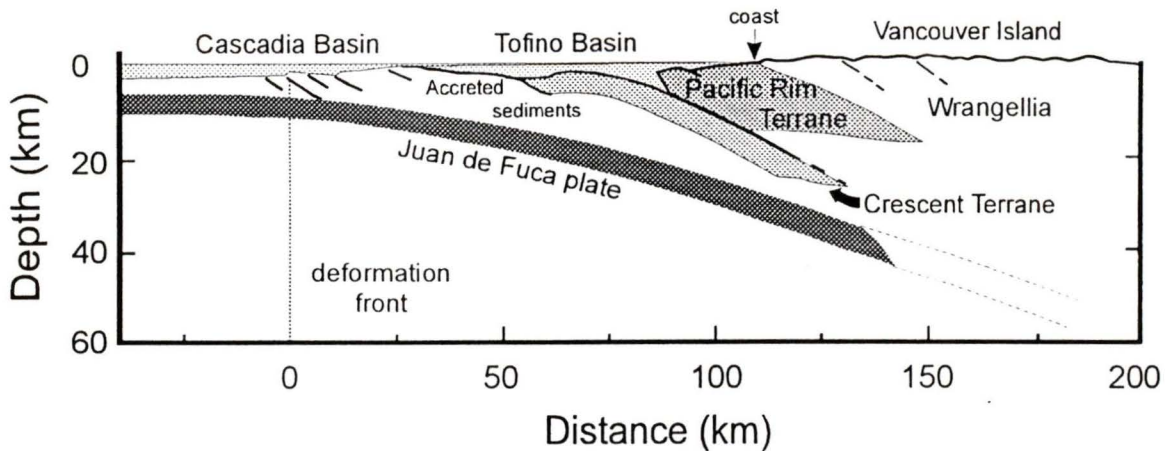


Figure 2.2. Cross-section of southern Vancouver Island showing the Pacific Rim and Crescent terranes, underthrusting Wrangellia to the east. The sediments which make up the accretionary prism are scraped off the incoming oceanic plate near the deformation front, and are backstopped by the Crescent Terrane rocks. The Tofino Basin sediments overlie both the accreted sediments and the terrane rocks (after Hyndman *et al.* [1990]).

by the active forearc Tofino Basin consisting of more than 3 km of Eocene to Holocene marine sediments, which lie on top of the modern accretionary prism (Yorath, 1987). From the deformation front to 20 km landward, the sediments within the Cascadia Basin are folded and faulted into anticlinal ridges oriented nearly parallel to the margin (Hyndman, 1995). These ridges have formed over thrust ramps that are rooted in a décollement which penetrates close to the top of the underlying oceanic crust as given by seismic reflection data, and support the off-scraping of a large portion of the incoming sediments.

To the south, off southern Washington and Oregon, the lower continental slope is also shaped by a series of thrust faults that are caused by Late Tertiary underthrusting of the oceanic crust (MacKay *et al.*, 1992). However, the landward dipping faults penetrate to a décollement which is located higher in the sediment section, permitting some of the incoming sediments to underplate the accretionary prism (e.g., MacKay *et al.*, 1992). This region is also characterized by the influx on terrigenous sediments via large submarine canyons and fans in the southern Cascadia Basin, accumulating nearly 4 km of turbidite sediments near the base of the continental shelf. The active accretionary prism off central Oregon is part of a larger and older subduction complex, partly exposed onshore on the Olympic Peninsula, and remarkably different than off Vancouver Island to the north (Snively, 1983).

### 2.2.2 Continental Geology

The continental geology is important to the thermal model in that the thermal conductivity and radiogenic heat generation of the onshore regions are estimated from nearby surface rock samples. If we assume much of the terrigenous sediment supplied to the accretionary prism comes from nearshore sites, then the thermal conductivity and radiogenic heat generation of these source rocks are important to the thermal model for the offshore regions as well. The origin and composition of these rocks for Cascadia are derived from the amalgamation of allochthonous, mainly oceanic, volcanic terranes which have successively accreted to the North American craton and adjacent miogeosyncline since the Middle Jurassic (Yorath, 1987; Gabrielse et al., 1991). For the Vancouver Island margin, the pre-Tertiary continental margin was established around the Late-Cretaceous when the Insular Superterrane, composed mainly of the morphologically distinct Wrangellia and Alexander terranes, accreted to the Intermontane Superterrane (Monger & Berg, 1984; Irving, 1985; Yorath, 1987). The Coast Plutonic Complex, a belt of mainly quartz diorite and granodiorite plutons, was formed along the suture between the two superterranes (Gabrielse et al., 1991), and likely provides much of the terrigenous source material to the adjacent accretionary prism.

The most recent terrane accretion includes the Mesozoic marine sedimentary Pacific Rim Terrane and the Eocene marine volcanic Crescent Terrane, which have been thrust beneath Wrangellia during the latest Eocene, about 42 Ma ago (Fig. 2.3) (Yorath, 1987; Hyndman et al., 1989). The Tofino Basin sediments off Vancouver Island and related shelf basins to the south overlie both terranes. The Pacific Rim Terrane is exposed along the west coast of Vancouver Island and comprises mudstone-chert-sandstone melange and calc-alkaline conglomerate, greywacke, and non-metamorphosed sediment and metavolcanic sections (Yorath, 1987). The Crescent Terrane is exposed along nearly the full length of the Cascadia Margin, and is named the Siletz Terrane in Oregon (Fig. 2.3), and is dominated by a succession of gabbro rocks, sheeted dikes, and pillow sheet flow basalts (Massey, 1986). Beneath the Vancouver Island margin, the terrane is estimated to be roughly 10-15 km thick (Yorath, 1987). In the Olympic Peninsula, the exposed Crescent/Siletz Terrane is roughly

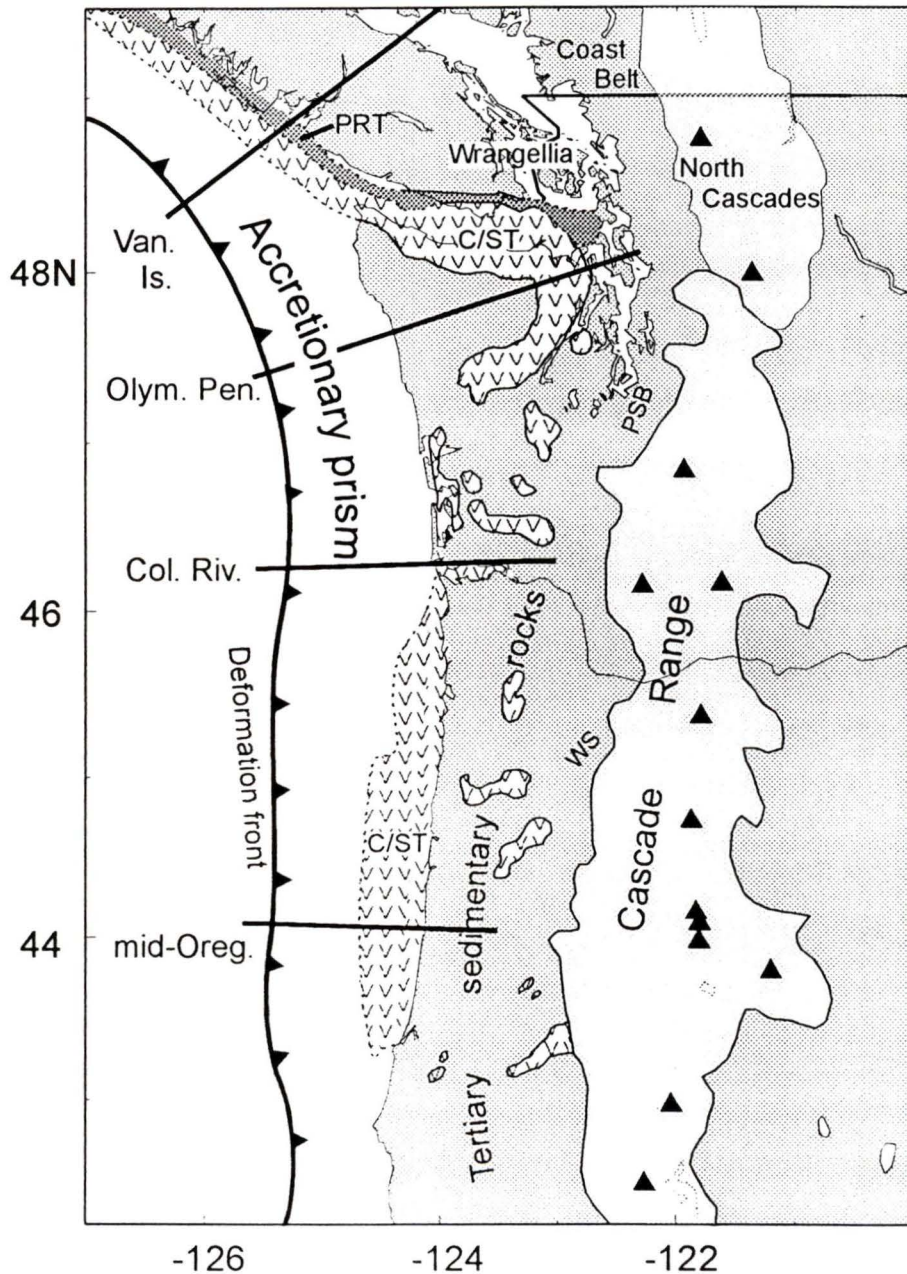


Figure 2.3. The Crescent/Siletz Terrane (C/ST) extends nearly the entire length of the Cascadia Margin, as evident from both offshore seismic and magnetic data and onshore surface exposure. Seismic reflection data throughout Oregon and Washington have shown the volcanic terrane as being thicker to the south and east. The landward extent of the terrane is not well resolved due to the presence of the Puget Sound (PS) and Willamette (WI) sediment basinal fills (after *Trehu et al.* [1994]). In the north, the accretion and proposed underthrusting of the C/ST and the Pacific Rim Terrane (PRT) to Wrangellia is delineated through surface faults (modified from *Hyndman et al.* [1990]). The new thermal models are along the Olympic Peninsula, Columbia River, and mid-Oregon profile lines. Solid triangles mark the active or dormant volcanoes of the Cascade Range magmatic arc (after *Mooney & Weaver* [1989]).

only 2 km thick, and consists mostly of pillow basalts (Snavely, 1983). The Crescent/Siletz Terrane outcrops intermittently throughout much of Washington and Oregon and is of varying thickness, blanketed by a thick succession of Miocene aged oceanic sediments (Fig. 2.3) (e.g., Mooney & Weaver, 1989; Trehu et al., 1994). The erosion of these volcanic and sedimentary rocks provides an additional source of land-derived material to the thick sediment blanket covering the Juan de Fuca plate.

### 2.3 SOUTH ALASKA

The Alaska-Aleutian Arc extends more than 3600 km from the Gulf of Alaska to the westernmost Aleutians. It has experienced 5 great subduction thrust earthquakes and numerous intermediate magnitude events within the past 60 years, forming a nearly continuous rupture zone, broken only by the Shumagin Gap for which there is no recent thrusting activity (Fig. 2.4) (Plafker et al., 1994). The eastern limit is marked by the complex system of transition faults which accommodate the fault mechanism change from subduction to strike slip. The western limit to the arc is marked by a change in convergence obliquity coincident with the Kamchatka Peninsula and the northern end of the Kurile Trench. The change is one of near trench-parallel convergence along the arc to one of near perpendicular convergence along the Kurile Trench.

In the Cook Inlet and Prince William Sound regions, relative plate motion is nearly perpendicular to the North American Plate in a northwesterly direction at a rate of roughly 60 mm/yr (Lahr & Plafker, 1980; DeMets et al., 1990; Page et al., 1989; Ambos et al., 1995). Convergence rates gradually increase westwards across the arc to 70 mm/yr (Fig. 2.4) (Lahr & Plafker, 1980; Plafker et al., 1994). The oceanic plate age at the trench off Prince William Sound is 50 Ma, increasing westward along the arc to 75-80 Ma (Kulm et al., 1971). The region of study for the thermal model profile (South Alaska) corresponds to the central part of the rupture zone of the great thrust March 28, 1964 event (Fig. 2.4). Plate dip is very gentle under the Cook Inlet, between 7-11° 170 km landward of the trench, and steepens farther landward. It is 3-5° steeper over a similar range to the north under Prince William Sound (Johnson et al. 1996).

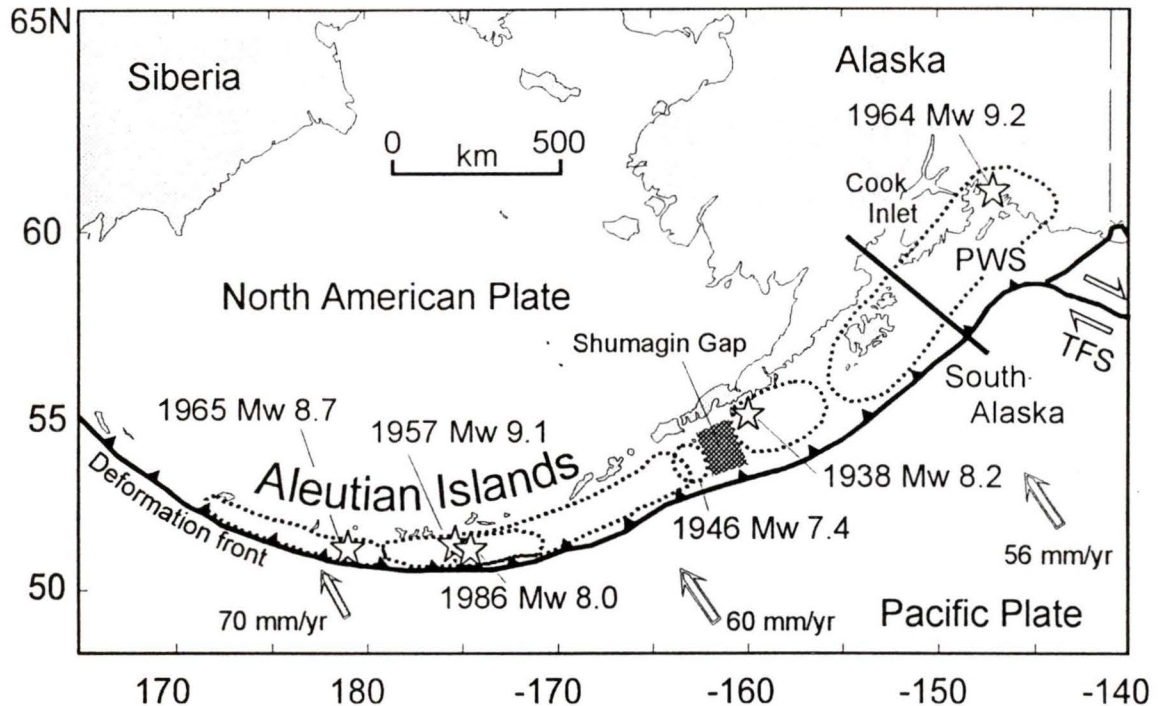


Figure 2.4. Rupture areas associated with great thrust earthquakes occurring within the last 60 years along the Alaska-Aleutian megathrust fault. The subduction of the Pacific Plate changes from near perpendicular convergence in the eastern regions to near parallel convergence in the westernmost Aleutians. The eastern end of the deformation front connects with the Transition Fault System (TFS) near Prince William Sound (PWS) (modified from *Davies & House [1979]* and *Johnson et al. [1994]*). The South Alaska thermal profile is shown by the straight heavy line midway through the 1964 rupture envelope.

### 2.3.1 Sediment sections

#### Deep sea & trench-fill sediments

The marine stratigraphy seaward of the trench has been examined with single- and multichannel seismic reflection data (e.g., TACT reflection lines, Brocher et al., 1994; EDGE transect, Moore et al., 1991). The top ~800 m of the seismic sections are well studied from DSDP wells (Kulm et al., 1971). The section consists of a thick, pelagic sediment blanket deposited from Early Miocene (20 Ma) to present, overlain by a sequence of silty clay with erratic, ice rafted pebbles, and changes progressively upwards to poorly sorted silty-sands and clay bearing oozes (Kulm et al., 1971). This sequence, also found in other deep sea drilled cores in the area (e.g., Creager et al., DSDP leg 19, 1973; Rea et al., ODP leg 145, 1993), is thought to be representative of the abyssal plain sedimentary stratigraphy. Closer to the deformation front, the sediment thickness swells to 1200 m. This upper part of the

sediment section consists of graded silt turbidites, interbedded muds, and ice-rafted debris resulting mostly from trench fill turbidites and ice rafted debris deposited during the Pleistocene (~1.8 Ma) (Kulm et al., 1971). Trench depths are about 4500 m just east of Prince William Sound, and increase westwards to 6400 m near the Shumagin Gap (Johnson & Monahan, 1984). Trench-fill turbidite sedimentation correspondingly decreases over a similar area with the reduction in continentally derived sediments along the narrow Alaska-Aleutian Arc (Kulm et al., 1971; Plafker et al., 1994).

### Accretionary prism

The continental shelf and slope are about 110 km wide in the area of the South Alaska profile, expanding to nearly 250 km to the northeast off Prince William Sound. Most of the shelf topography is gently undulating, and is periodically broken by submarine valleys carved by glaciers during the latest Pleistocene (Fig. 2.5) (Plafker et al., 1994). The accretionary prism in the region of the thermal model consists of an older wedge of Late Mesozoic to Eocene age accreted to the terrane rocks of the overriding plate, and a younger Cenozoic to

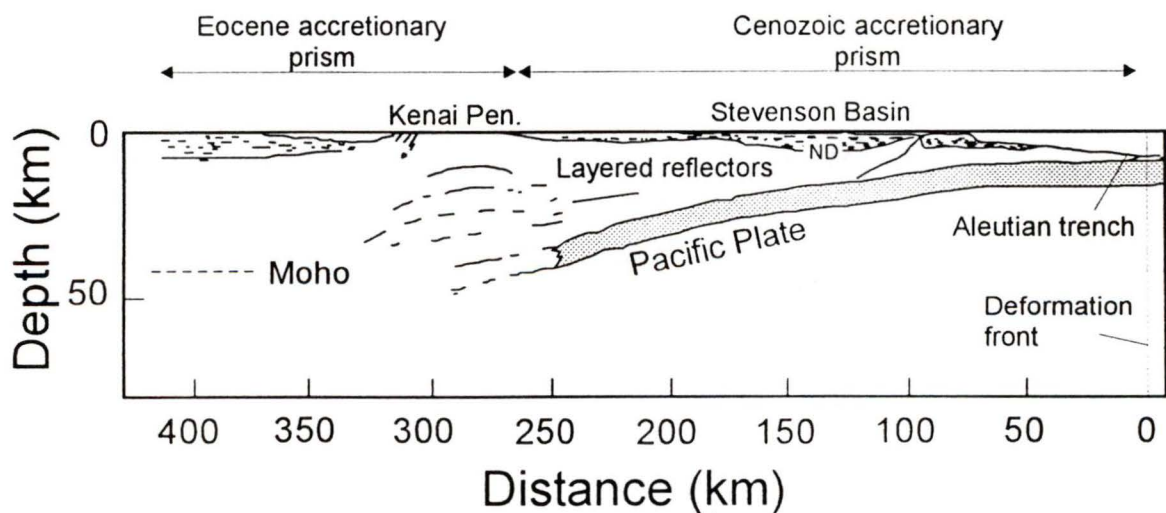


Figure 2.5. Cross-section of south central Alaska showing the seaward part of the thrust beneath the Cenozoic and Eocene accretionary wedge complex. The Neogene and shelf and slope deposits (ND) are contained within the Stevenson Basin. Numerous layered reflectors may indicate substantial lateral growth of the margin since the Eocene. A prominent reflector at about 40 km depth is believed to represent the continental Moho (modified from Moore et al. [1991]).

present accretionary prism (Fig. 2.5) (von Huene et al., 1987; Plafker et al., 1994). The older accreted wedge is exposed throughout the Kodiak Island and Kenai Peninsula areas. In a seaward direction, the older accreted wedge consists of a blueschist-greenschist sequence of Jurassic age, a mid-Cretaceous melange of siltstone and sandstones, and a sequence of Eocene turbidites (Moore et al., 1991; Plafker et al., 1994). Farther seaward to the shelf edge, the prism is characterized by undeformed Neogene basin deposits overlying accreted sediments of Eocene-Oligocene age (Fig. 2.5). Exploration wells drilled near the shelf edge (Turner, 1987) and surface dredging samples at a similar distances from the coast (Plafker & Claypool, 1979), define the seaward extent of the Eocene turbidites. Multichannel seismic reflection data further suggest ponding of unconsolidated fine Holocene muds which blanket the Eocene and Oligocene sedimentary sequences within the Stevenson Basin (Carlson et al., 1977; Moore et al., 1991). Continued wedge growth comes mainly from the thick sequence of turbidite sediments scraped-off the incoming plate (Plafker et al., 1994).

### **2.3.2 Continental Geology**

Southern Alaska is a collection of oceanic and continental fragments which have accreted to the continental margin during the Mesozoic to Cenozoic (Fuis et al., 1991; Plafker et al., 1994; Ambos et al., 1995). In the region of study, Jones et al. (1981, 1984) have identified up to 17 individual, fault bounded, stratigraphically distinct allochthonous terranes (larger terranes shown in Figure 2.6) (e.g., Plumley et al., 1983; Bol, 1993). The subduction zone forearc region is bounded to the northwest by the Alaska-Aleutian range volcanic arc, and to the southeast by Aleutian trench (e.g., Fisher & von Huene, 1980). The northern limit of the Aleutian megathrust is marked by the Transition Fault System and the Kayak Island Fault, separating the Southern Composite Terrane from the Yukatat Terrane (Fig. 2.6).

Within the area of study, the Border Ranges Fault system separates the northern Wrangellia composite terrane from the Southern Margin Composite Terrane (Plafker et al., 1989; Fuis & Plafker, 1991; Ambos et al., 1995). The Wrangellia Composite Terrane includes the Peninsular, Wrangellia, and Alexander terranes, of which the Peninsular Terrane

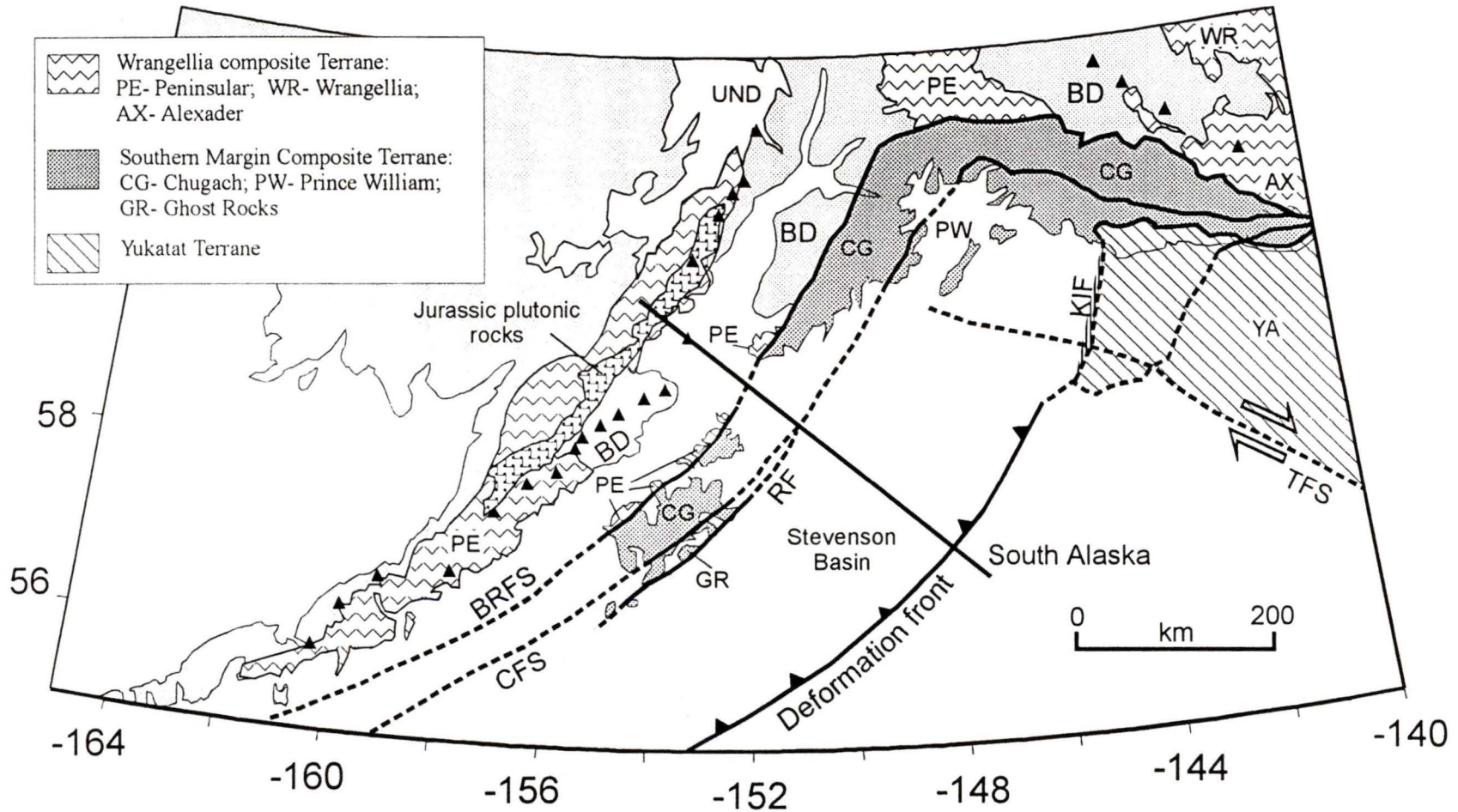


Figure 2.6. Coastal geology for south Alaska showing the accreted volcanic allochthonous terranes (stippled areas), separated by major cross-cutting faults (heavy lines). The South Margin Composite Terrane is comprised mainly of the Chugach, Prince William and Ghost Rocks terranes which underthrust the Wrangellia Composite Terrane to the north. Abbreviations are as follows: BD - Basinal deposits, includes sedimentary and volcanic rocks of Paleozoic to Tertiary in age and Jurassic plutonic rocks; UND - Undifferentiated terranes, includes Late Cretaceous to Tertiary plutonic rocks; BRFS - Border Ranges Fault System; CFS - Contact Fault System; RF - Resurrection Fault; TFS - Transition Fault System; KIF - Kayak Island fault. Dark triangles denote the Aleutian-Alaska volcanic arc range (modified from *Plafker et al.* [1994]).

is exposed along the coast (Plafker et al., 1994). The Southern Margin Composite Terrane includes four accreted terranes: the Chugach, St. Elias, Ghost Rocks, and Prince William Sound terranes. The Chugach Terrane comprises the greatest proportion of the South Margin Composite Terrane, and consequently these rocks supply the greatest volume of material for turbidite sedimentation.

The accreted rocks of Late Mesozoic age make up much of the Chugach Terrane rocks. The terrane is composed of three major fault-bounded assemblages ranging in age from Late Triassic to Early Paleocene. The most important of these assemblages to the thermal model are the Late Cretaceous to Early Paleocene volcanoclastic flysch and oceanic basaltic rocks exposed in extremely thick sequences (Roeske et al., 1991; Plafker et al., 1994). The flysch accounts for nearly 90% of the assemblage, extending the full length of the terrane and up to 80 km in width along the Kodiak Island and Prince William Sound areas (Roeske et al., 1991). The dominant flysch rocks come from metabasalts and consequently have a relatively high radiogenic heat generation value.

A secondary large source of sediments comes from the Jurassic to Eocene plutonic rocks of gabbroic to granitic composition (Fig. 2.6) (Reed & Lanphere, 1973; Reed et al., 1983). The older Jurassic plutons are made up of highly altered tonalite, diorite, and granodiorite (Reed & Lanphere, 1973; Reed et al., 1983; Plafker et al., 1994). The younger Paleocene to Eocene plutons are mainly metamorphosed calc-alkaline rocks. These younger plutons are considerably more abundant within the outcrop area, and provide a source of terrigenous sediment to the wedge development (Plafker et al., 1994).

## **2.4 CHILE**

The convergence of the Nazca Plate beneath the western edge of the South America Plate forms one of the longest subduction zones in which a single oceanic plate underthrusts continental lithosphere. Numerous large thrust earthquakes have been recorded along the margin recorded instrumentally and in written records back to the 1600's (Nishenko, 1985). The Nazca Plate is bounded by the Galapagos Rift to the north, the East Pacific Rise spreading ridge to the west, and by the Chile Rise spreading ridge to the south (Fig. 2.7). The

southern intersection of the Nazca, Antarctic and South America plates is marked by the Chile Triple junction. Several long fracture zones offset the Chile Rise, causing substantially differently aged oceanic crust, i.e., 0-50 Ma, to be subducted at the Chile trench (Fig. 2.7).

Relative plate convergence rates range from 85 mm/yr in the south near the Chile

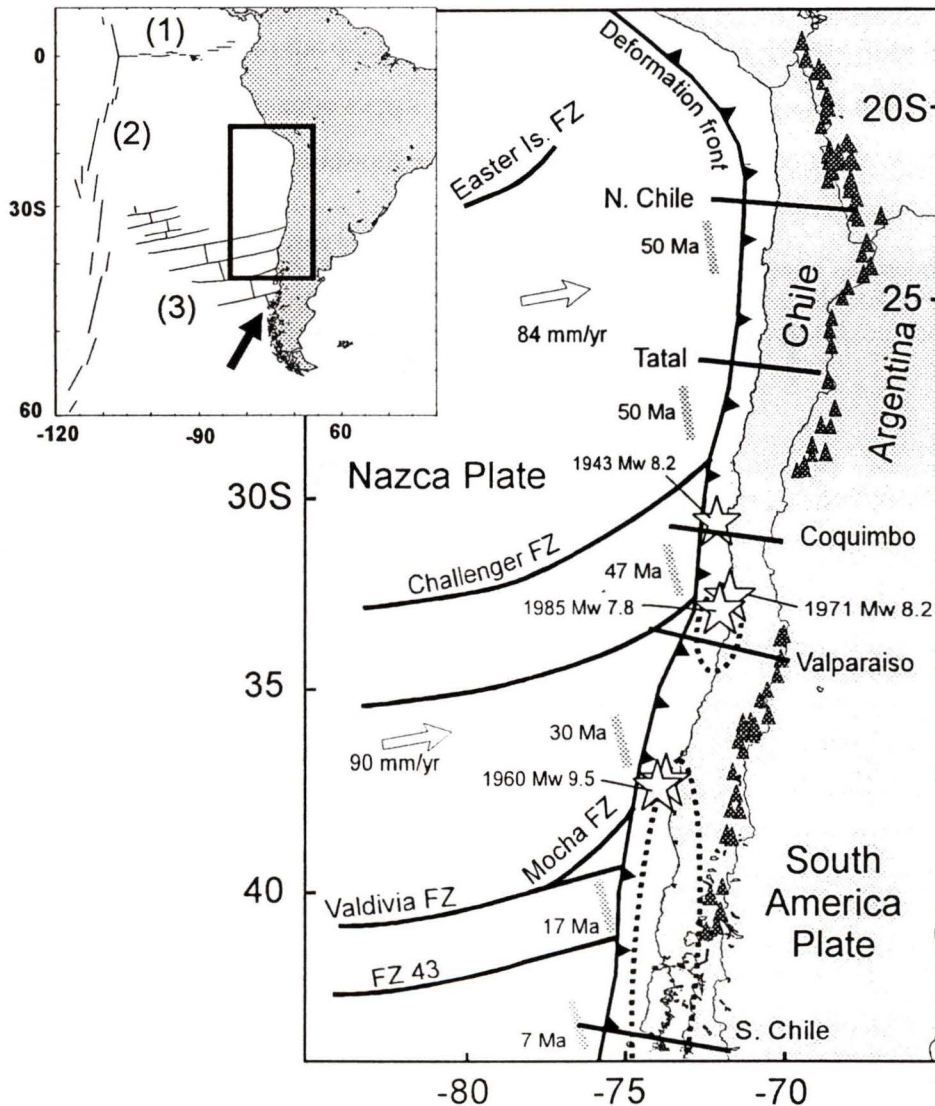


Figure 2.7. Map showing the subduction of the Nazca Plate beneath the continental South America Plate. Inset shows the Chile Triple Junction location (solid arrow) and major boundaries to the Nazca Plate: (1) Galapagos Rift; (2) East Pacific Rise; and (3) Chile Ridge. Convergence rate and plate age increase to the north along the Chile margin. The age of the subducting Nazca Plate at the deformation front (grey rectangles) increases discontinuously northwards across the main fracture zones (*Cifuentes* [1989]). Main seismic thrust events (large stars) and their associated aftershock envelopes (closed loops) relevant to the thermal models (solid lines) are also shown. Dark triangles denote Andean Volcanic Arc (modified from *Nishenko* [1985] and *Tichelaar & Ruff* [1991]).

Triple Junction to 95 mm/yr in the north. The convergence direction is at an azimuth of 85°NE, and is nearly perpendicular to the margin. Due to the extreme plate age, sediment thickness (see below), and tectonic variations existing along the trench, five thermal profiles have been constructed. The Nazca Plate increases in age from roughly 5 Ma in the area of the South Chile profile, to 50 Ma for the northern Taltal and North Chile profiles.

The plate dip profiles are fairly uniform within the top 100 km depth range 70 km landward of the deformation front, where they average 10-12° (Barazangi & Isacks, 1976; Bevis & Isacks, 1984; Tichelaar & Ruff, 1991). Between 28°-33°S, stratovolcanic centres are absent along the Andean volcanic arc; coincident with this, at a depth of 100 km, the Nazca Plate flattens to 4-5° 150 km landward of the deformation (Cahill & Isacks, 1992). Several suggestions, including aseismic ridge subduction (e.g., Barazangi & Isacks, 1976), alternating continental curvature (e.g., Wortel & Cloetingh, 1985; Cahill & Isacks, 1992), and westward jumping of the Chile trench (e.g., Moore, 1995) have been proposed to explain the absence of volcanic centres.

This study is concerned with the 1960 (Mw 9.5), the 1943 (Mw 8.2), the 1971 (Mw 8.1), and the 1985 (Mw 8.0) great thrust earthquakes, occurring within the southern half of the margin (Fig. 2.7).

#### **2.4.1 Sediment sections**

##### **Deep sea & trench-fill sediments**

Based on trench fill sediment volumes, the Chile Margin is divided into three distinct regions: 1- North Chile (22°-27.5°S), where trench sediments have negligible thickness consisting of isolated sedimentary basins, ponded within depressions of basaltic basement (also referred to as a 'starved' trench); 2- Central Chile (27.5°-33°S), where a more continuous sedimentary wedge 1000 m average thickness partially fills the trench; and 3- South Chile (33°-45°S), where excessive trench fill spills seaward of the trench lip and swells to greater than 25 km in width more than 2 km in thickness (also referred to as a 'swollen' trench) (Fig. 2.8a) (Thornburg et al., 1990). In the north, the deep sea sediment section at the deformation front is a very thin, 100 m thick, conformable drape of the pelagic and

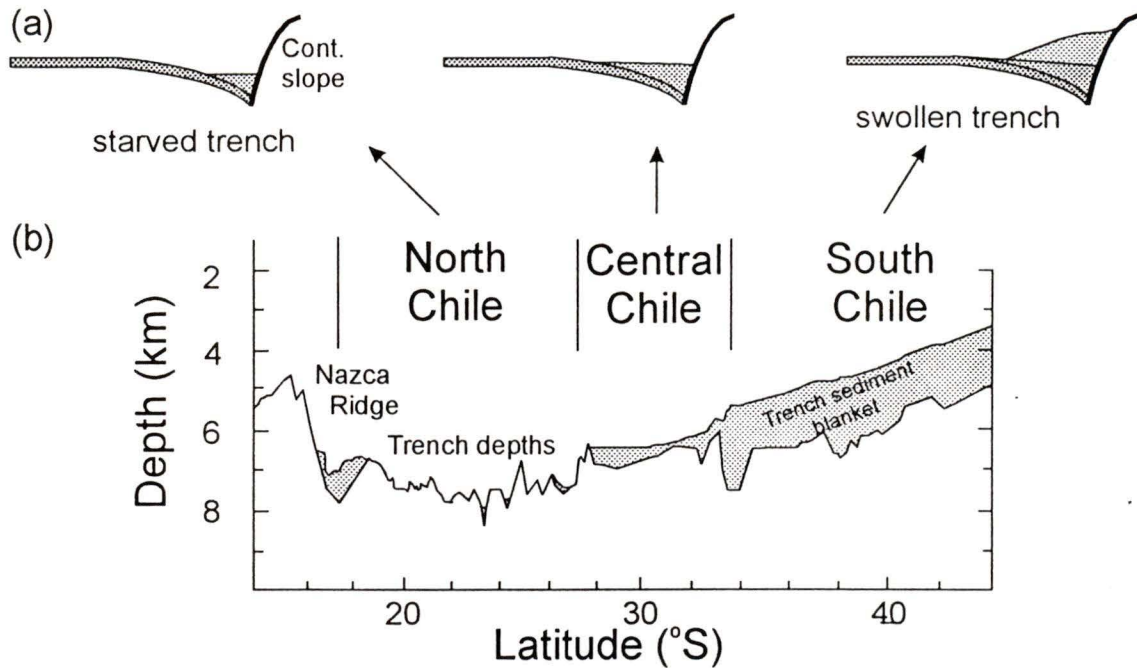


Figure 2.8. Trench sediment thickness for the Chile Margin. (a). Orthogonal cross-sections for 3 morphological provinces defined by the volume of sediment in the trench: a 'starved' region to the north with little trench-fill sediments; a partially filled region in mid-Chile; and a 'swollen' region to the south (b). Along trench axis cross-section, where the depth to the top of the oceanic crust and sediment thickness are plotted according to latitude (after Schweller *et al.* [1981]).

hemipelagic strata that overlies the basaltic basement (Yeats *et al.*, 1976; Schweller *et al.*, 1981). These sediments consist predominantly of oxidized clays and chinks as evident from deep sea sedimentation studies and drill core analysis (Berger, 1974; van Andel *et al.*, 1975; Yeats *et al.*, 1976). Toward the south, trench-fill turbidites consist of rapidly deposited coarse and fine sediments of glacial or fluvial origin, distributed seaward via submarine canyons and fans (Schweller *et al.*, 1981; Thornburg *et al.*, 1990). The volume of sediment in the trench matches the onshore climatic gradient: increasing precipitation and thus sediment supply southward contrasting with the desert climate and little erosion in the north (Thornburg & Kulm, 1987a; 1987b). Thus the extreme range in sediment thickness along the margin is mainly due to the presence or absence of trench fill turbidites and the intensity of terrigenous sediment supply.

### **Accretionary prism**

The size of the accretionary prism along the Chile Margin also varies in a similar manner as the trench-fill sediment thickness. In the north, where very little sediment is available for off-scraping, the accretionary prism is narrower. For the southern regions where extensive trench fan systems overlie the accreted sediments, there is a wider accretionary prism (Fig 2.8a). For the northern and southern Chile regions, the outer accreted prism sediments are derived primarily from Jurassic plutonic sources, and exhibit a high quartz and feldspar content (Thornburg & Kulm, 1987b). For the central regions, where the accreted sediments are derived mainly from dissected magmatic arc trench-fan lobes which transport the turbidites seaward, they are composed of heavily eroded sand and gravel. These are in turn overlain by fine grained turbidites (Thornburg & Kulm, 1987a). Provenance studies and geochemical analysis of deep sea cores suggest that the fine sediments were derived from granitoid sources, likely originating from the nearshore rocks (Thornburg & Kulm, 1987b). Much of the rapid and extensive accretionary prism growth occurred during repeated Pleistocene glacial activity.

#### **2.4.2 Continental Geology**

The geology of the Southern Andes in the region of study varies considerably over the length of the margin. Up to nine distinct morphological units are recognized within the Southern Andes, of which the Coast Range, PreCordillera, and Andean Range are of importance to the radiogenic heat production and thermal conductivity of the landward portion of the thermal models (Fig. 2.9). The geology of the Coast Range is of particular importance to the composition of the adjacent accretionary prism as discussed above. The pre-Andean Orogen basement in Chile is represented by metamorphic, sedimentary, and igneous rocks of Precambrian to Late Paleozoic age. The more abundant metamorphic rocks include granitoids which are predominantly calc-alkaline, granodiorites, and granites with granulated quartz (Aguirre, 1985; Vergara et al., 1995). They are believed to represent the deeper crustal layer of Late Paleozoic magmatic arcs that are also seen in the central and eastern high Andes (Aguirre, 1985). No low thermal conductivity and/or low radiogenic heat

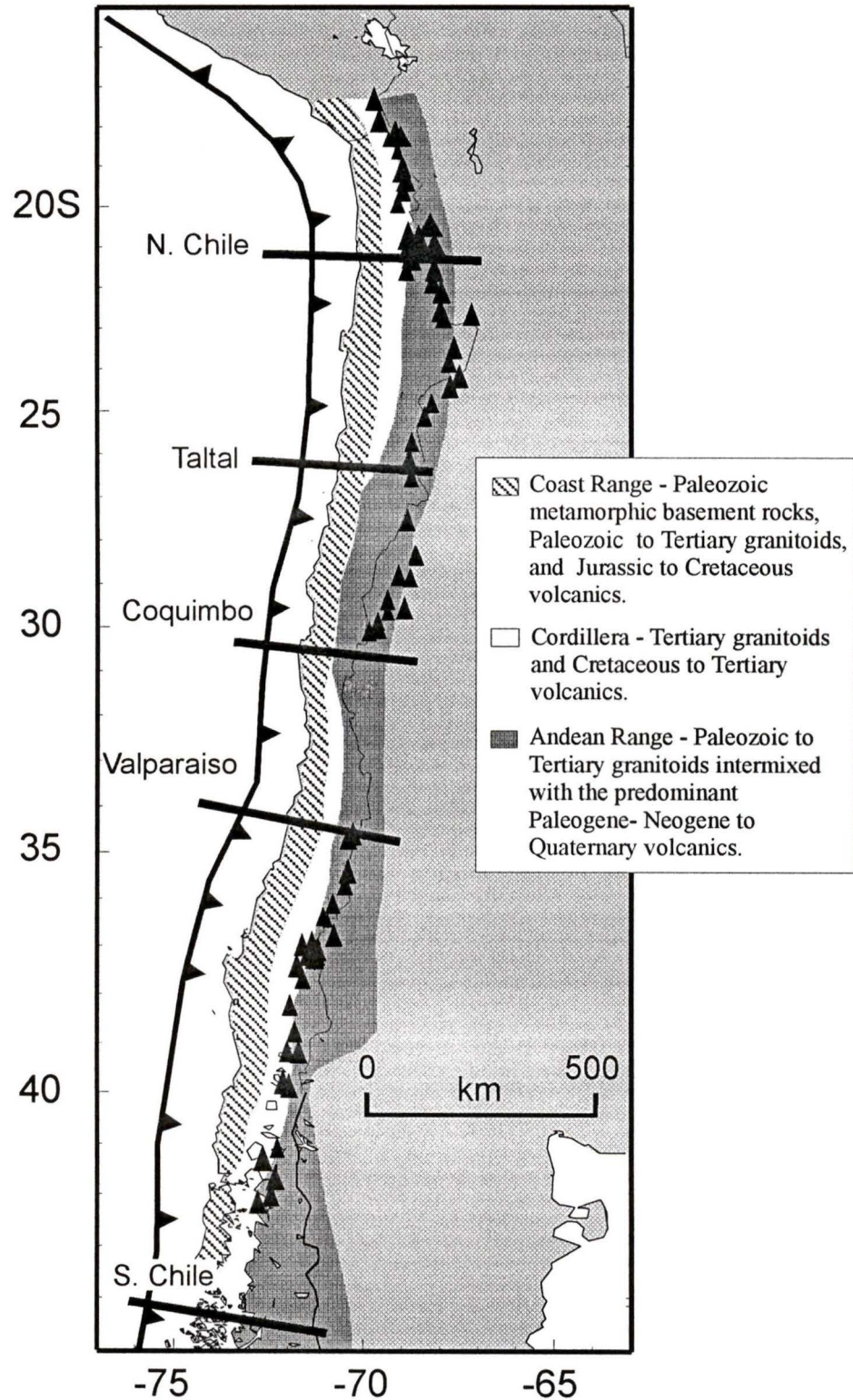


Figure 2.9. Principal morphological rock units and their general lithology for the Chile Margin. The geology of the Chile Margin is autochthonous and records superposition of younger plutonic (diagonal fill), granitoid, and volcanic (dark triangles, stipple fill) rocks on the older, basement metamorphic rocks. The Coast Range is the most important source for continental derived sediments supplied to the accretionary prism (modified from *Aguirre* [1985]).

generation terranes have been identified in the coastal geology (Forsythe, 1982; Irwin et al., 1987; Beck, 1988), and the thermal models applied for the Chile Margin therefore omit any such rocks.

Overlying the basement metamorphic rocks are the Jura-Cretaceous granitoids and volcanics. The Late Jurassic granitoids consist of granodiorite, quartz diorite, granite and tonalite (Fig. 2.9) (Aguirre, 1985). The volcanic rocks were extruded between the Late Jurassic and Early to mid-Cretaceous and constitute a major portion of the Coast Range. These volcanic rocks are well represented between 20-40°S, and are of high calc-alkaline character and silicic composition (Aguirre, 1985). Overlying the Jura-Cretaceous granitoids and volcanics are the Late Cenozoic volcanic belts, subdivided into the Coastal Volcanic Belt and the Andean Volcanic Belt. The volcanic centres form a continuous volcanic arc along the margin, separated by a volcanic gap between 30-33°S (Fig. 2.9). The highly eroded Coastal Volcanic Belt rocks are characterized by large andesitic lava flows and calc-alkaline intermediate lavas (Vergara, 1972; Vergara & Munizaga, 1974; Aguirre, 1985).

## 2.5 NANKAI

The Nankai Margin off southwestern Japan has developed from the Late Cenozoic tectonic interaction of the Eurasian, Philippine Sea, and Pacific plates which meet at the triple junction off central Japan (Fig. 2.10) (Ranken et al., 1984). On the northwestern boundary of the Philippine Sea Plate, the Shikoku Basin is bounded to the north by the Izu-Bonin Arc, and to the south by the Kyushu-Palau Ridge located off the southwest end of Japan. The Shikoku Basin has been subducting northwestward under southern Japan since the mid-Miocene, and possibly since its formation (Moore et al., 1990). A fossil spreading ridge within the Shikoku Basin is oriented perpendicular to the present day trench. The basin originally opened about this ridge at 26-20 Ma, and then stopped spreading around 15 Ma (Fig. 2.10) (Hibbard & Karig, 1990; Okino et al., 1994). The age of the subducting plate has therefore increased during the past 15 Ma from near zero to the present age of 15 Ma where the fossil spreading ridge meets the margin near Shikoku Island.

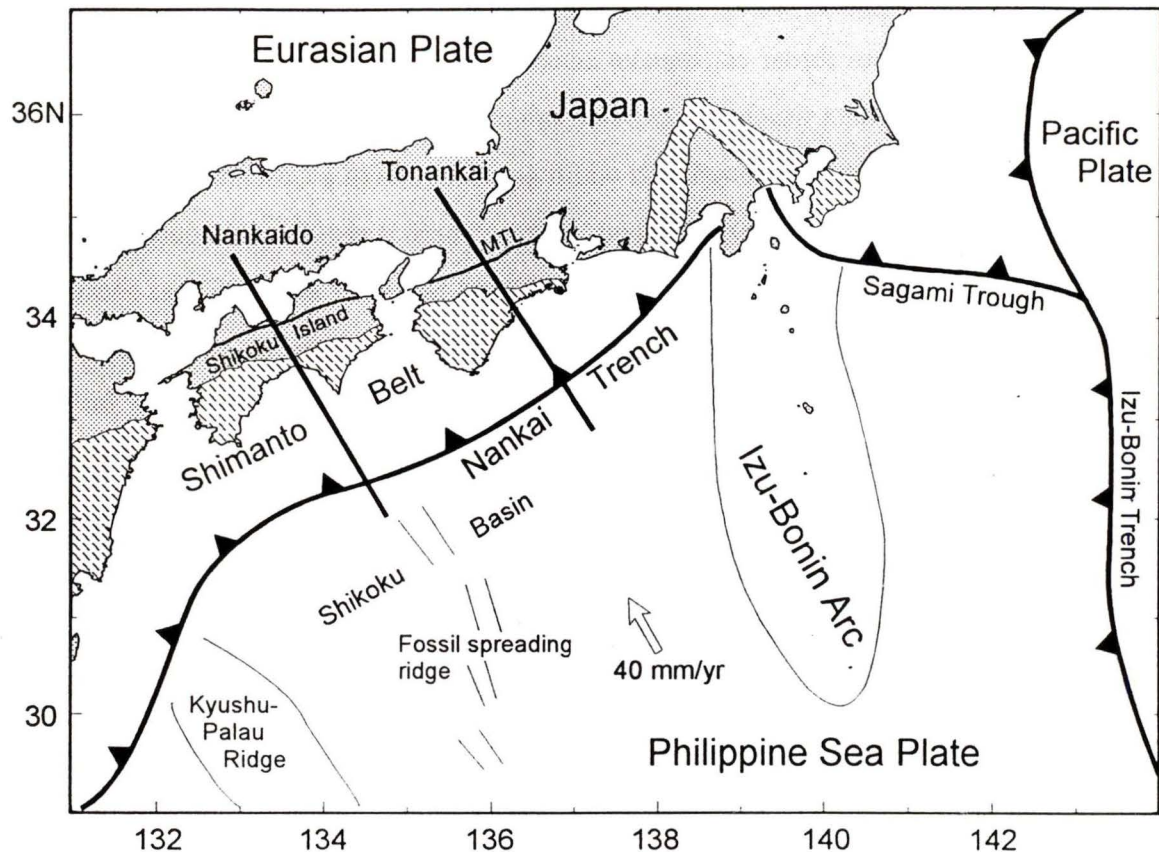


Figure 2.10. Tectonic setting and major geological units of southwest Japan. The Shikoku Basin is separated by a northwest trending fossil spreading ridge, bounded to the northeast by the Izu-Bonin Arc, and to the southwest by the Kyushu-Palau Ridge. The Shimanto Belt (pattern fill) represents the accreted Cretaceous to Miocene Shimanto accretionary prism, and continues offshore to merge with the active Nankai accretionary complex. The Median Tectonic Line (MTL) has been interpreted to show a history since the Cretaceous and divides the Jurassic accretionary belt (modified after *Hibbard & Karig [1990]; Taira et al. [1991]*).

The convergence direction and rate across the margin are not well constrained by magnetic reversals as the Philippine Sea plate is surrounded by subduction zones (Moore et al., 1990; Hibbard & Karig, 1990). Estimated convergence rates range from 17-57 mm/yr, and most recently 40 mm/yr at about azimuth 330° (Ranken et al., 1984; Moore et al., 1990). The latter value has been used in the thermal models. Along the Nankai Trough, the Philippine Sea Plate increases in age northeastward along the margin from 15 to 25 Ma (Seno et al., 1993).

## 2.5.1 Sediment sections

### Deep sea & trench-fill sediments

The Nankai trench extends 700 km from the Sagami Trough to the northern tip of the Kyushu-Palau Ridge (Hill et al., 1993). The trough off Shikoku Island is fairly shallow due to the young, buoyant Philippine Sea Plate crust, and because sediment cover on the subducting plate is fairly thick (Moore et al., 1990, Hill et al., 1993). The Shikoku Basin sediment section is of pelagic composition and is only about 100-200 m thick, due primarily to the fairly young age of the Philippine Sea Plate. This section has apparently thrust some distance under the accretionary prism (Fig 2.11) (Hill et al., 1993). There is evidence that the underthrust section is also underplated by a downward step in the décollement about 30 km landward of the deformation front (e.g., Moore et al., 1990). Overlying the deep sea sediments is a turbidite trench-fill section composed of reworked coarse and fine clays, approximately 750 m thick (Fig. 2.11) (Taira et al., 1992).

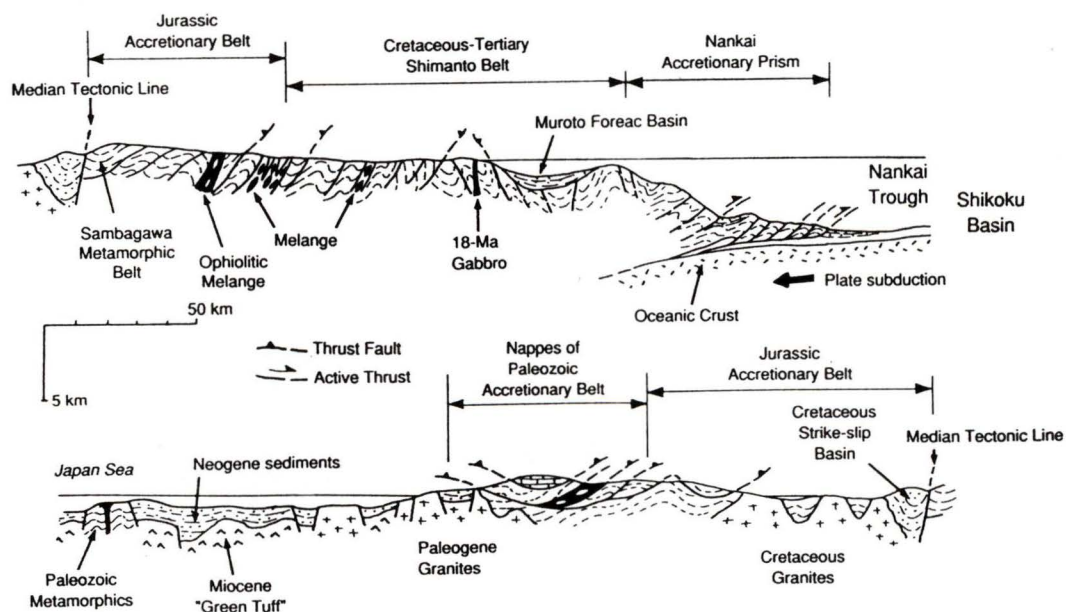


Figure 2.11. Cross-section of the Nankai Margin, southwest Japan, showing the thrust piles of the Paleozoic to Tertiary accretionary complex. The Shimanto Belt accretionary prism complex is backstopped by the older, Jurassic accretionary belt. The MTL from Figure 2.10 is also shown cutting the this latter Jurassic Belt (after Taira et al. [1991]).

### **Accretionary prism**

The accretionary prism consists of off-scraped and underplated sediments originating from the trough-fill turbidites and the Shikoku Basin hemipelagic sediments (Fig. 2.11). The accretionary prism is roughly 100 km wide and began forming with early Shikoku Basin spreading during the late Oligocene to middle Miocene (Hill et al., 1993). The prism section being deformed in the Nankai trough off the Shikoku Basin consists of a trench-fill roughly 750 m thick at the deformation front, supplied mainly by terrigenous turbidites which have been transported seaward by turbidity currents across the trench from Shikoku Island source rocks (Moore et al., 1990; Hill et al., 1993). The upper sections are mainly coarse clastic pebbles, rocks, and volcanic ash from the Kyushu and Bonin volcanic arcs, intermixed with shelf sands which crosscut the hemipelagic sequences of the accretionary prism (Hill et al., 1993).

#### **2.5.2 Continental Geology**

The present Nankai outer forearc overlies the older Shimanto Belt accretionary prism of Cretaceous to Tertiary age (Hill et al., 1993). The Shimanto Belt is roughly 1800 km long and 100 km wide and constitutes the largest structural block of the Japanese Islands (Fig. 2.10) (Taira et al., 1991). It is composed of two main lithologies which occur in a repeated fashion: a coherent turbidite sequence and a highly deformed melange belt in which most rocks have undergone zeolite to greenschist facies metamorphism (Taira et al., 1992). The consolidated turbidite facies has been interpreted to be of axial-transported trench-fill sequences. The melange zone includes bits of oceanic crust, i.e., pillow lavas and pelagic cherts, hemipelagic shales, and fine-grained turbidites (Taira et al., 1992; Hill et al., 1993). The Shimanto Belt is overlain by several sedimentary sequences from Cretaceous to Tertiary age, and is backstopped by the Median Tectonic Line (MTL) which may be traced across Shikoku Island and parts of southwest Japan (Fig. 2.10).

## CHAPTER III THERMAL MODELLING APPROACH

### 3.1 INTRODUCTION

The temperature on the subduction thrust plane is suggested to be the main constraint on the width of the locked seismogenic zone (e.g., Ruff & Kanamori, 1983; Savage et al., 1991; Hyndman & Wang, 1993; Tichelaar & Ruff, 1993). Accurate thermal models are therefore needed to produce estimates to the potential great earthquake rupture zone. In this chapter, the constraints on the slip behaviour along the subduction thrust are first discussed, followed by a discussion of model parameters used to constrain the thermal model subduction thrust temperatures. The effects of frictional heating, which may play some role in the sliding behaviour transition from brittle to plastic flow, are also considered.

### 3.2 LIMITS TO THE SEISMOGENIC ZONE

#### 3.2.1 Sliding behaviour

For the thrust earthquakes, the contact fault separating the subducting and overriding plates is believed to accommodate most of the strain accumulated between large events, as less shear stress is required to initiate contact failure. Along this contact, the sliding behaviour changes with increasing deviatoric stress and increasing temperature associated with increasing depth. Steady state sliding along a contact fault is described by the relationship between the shear resistance  $\tau^{ss}$ , i.e., also called the frictional stress, and the sliding velocity  $V$ , given by

$$\tau^{ss} = \sigma_n \mu^{ss} = \sigma_n \left[ \mu_o + (a-b) \ln \frac{V}{V^*} \right] \quad (1)$$

where  $\sigma_n$  is the normal stress,  $\mu^{ss}$  is the coefficient of friction,  $V^*$  is an arbitrary reference velocity (Ruina, 1983). Here,  $(a-b)$  is a strength factor which is dependent on the physical properties of the rock, i.e., rheology, pore space, chemical composition, etc. Laboratory tests of fault sliding behaviour have shown that, at a fixed sliding velocity  $V$ , the  $\tau^{ss}$  evolves toward the steady state value  $\tau^{ss}(V)$  (Tse & Rice, 1986). Changing the sliding velocity to a new value

involves only a transition from one steady state to another (Ruina, 1983; Tse & Rice, 1986).

To first order, i.e.,  $(a-b) \approx 0$ , the system reduces to the static friction law, i.e.,  $\tau = \sigma_n \mu$ , as observed in low loading experiments (Tse & Rice, 1986). For frictional stability analysis relevant to the thrust earthquake failure mechanism, second order effects, i.e.,  $(a-b) \neq 0$ , must be included. Equation (1) then gives

$$(a-b) = \frac{\partial \mu^{ss}}{\partial (\ln V)} \propto \frac{V}{\sigma_n} \frac{\partial \tau^{ss}}{\partial V} \quad (2)$$

The sign of  $(a-b)$  determines the stability of the fault: when  $(a-b) > 0$ , there is stable sliding as  $\tau^{ss}$  increases with increasing  $V$ . This case is referred to as velocity strengthening, and occurs within the stable-sliding zone described in Chapter 1. When  $(a-b) < 0$ , the fault becomes weaker, which may cause rapid and sudden rupture. This case is referred to as velocity weakening (e.g., Tse & Rice, 1986), and it is within this region only that earthquakes may initiate.

### 3.2.2 The downdip temperature limit

To test the velocity weakening/strengthening hypothesis, the temperature dependence of  $(a-b)$  has been studied in the laboratory for samples of dry and wet Westerly Granite (Stesky, 1975; 1978; Blanpied et al., 1991). In both cases,  $(a-b)$  increased with temperature. Around 300-350°C, a transition occurs from velocity weakening to velocity strengthening in both the wet and dry samples, although  $(a-b)$  is less sensitive to temperature for the dry samples (Fig 3.1) (Tse & Rice, 1986). This temperature also corresponds to the brittle to semi-brittle transition observed with the onset of quartz plasticity in deep continental rocks (Scholtz, 1990). It is also found to correspond to roughly the maximum depths of earthquakes in most continental areas (Tse & Rice, 1986; Rogers, 1983, 1988; Tichelaar & Ruff, 1991; Hyndman & Wang, 1993). The extent to which the rupture may propagate downdip into the stable sliding zone where  $(a-b)$  becomes increasingly positive is a topic of debate (e.g., Ruina, 1983; Tse & Rice, 1986; Tichelaar & Ruff, 1991; 1993; Hyndman &

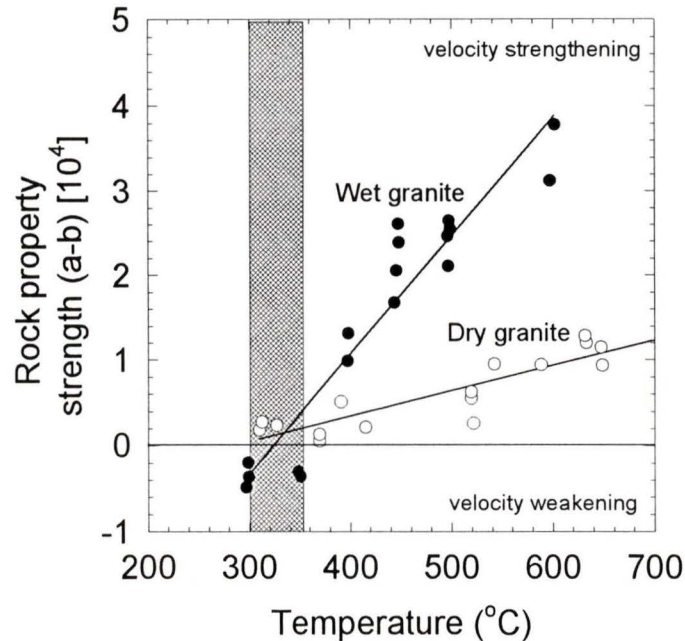


Figure 3.1. Velocity strengthening-velocity weakening behaviour around 300-350 $^{\circ}\text{C}$  (stippled area) after *Tse & Rice* [1986] using dry granite data from *Stesky* [1975] and wet data from *Blandpied et al.* [1991]. The steeper slope of the wet granite data shows stronger stable sliding behaviour with increasing temperature, and is likely closer to the behaviour of the hydrated downgoing oceanic crust (modified from *Hyndman & Wang* [1993]).

Wang, 1993), but great thrust earthquake rupture is believed to extend well into the velocity strengthening zone.

With increasing temperature downdip, there is a transition to plastic behaviour associated with the semi-brittle to plastic transition of bulk rock rheology for continental crustal materials at roughly 450 $^{\circ}\text{C}$  (Tse & Rice, 1986). This happens to correspond to a rapid increase in instantaneous shear stress for dry Westerly granite (Fig. 3.2). *Stesky* (1978) reported that an increase in mobility along the contact fault in the presence of water, which is likely with the subduction and dewatering of oceanic crust, may lower the 450 $^{\circ}\text{C}$  transition temperature. Although he had no experimental data to confirm by what factor it might be lowered, he acknowledged that temperatures around 450 $^{\circ}\text{C}$  mark an important transition to plastic flow.

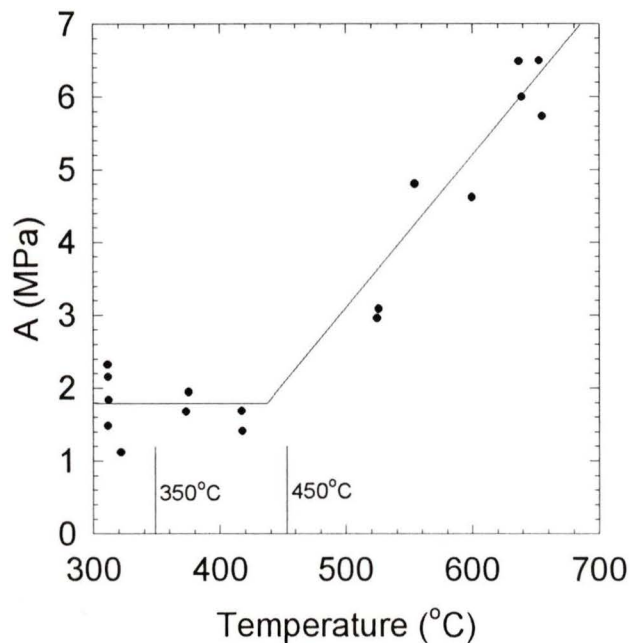


Figure 3.2. Near instantaneous frictional response to increasing temperature for "dry" Westerly granite. There is a rapid increase above about 450°C. Data includes response behaviour for both sudden loading rate increase and decrease from *Stesky* [1975] (modified from *Tse & Rice* [1986]). Although crustal rocks near the contact fault are likely hydrated from the dewatering of the downgoing plate, the "dry" data results are used to demonstrate the shear stress response for quartz-rich rocks. Similar data for "wet" samples do not exist, but may cause the stress response to be slightly lower than 450°C (*Stesky* [1978]). A (MPa): stress applied to the sample.

### 3.2.3 The updip temperature limit

At low temperatures and pressures at the seaward end of the seismogenic zone, the thrust plane undergoes a transition from updip, stable sliding, to downdip, unstable sliding. *Byrne et al.* (1988) have shown that an updip limit exists in many subduction zones, seaward of which little to no seismicity occurs on the thrust fault. One possible control to this updip limit comes from clays existing within the lower accretionary prism sediments that, when in sliding contact, lead to very low shear stress and effective stable-sliding behaviour (e.g., *Wang & Mao*, 1979; *Vrolijk*, 1990). With increasing temperature downdip, the clays dehydrate, transforming from expandable, lubricating smectite to non-expandable, mica-like, chlorite and illite which exhibit stick-slip or velocity weakening behaviour (*Vrolijk*, 1990; *Byrne et al.*, 1988; *Hyndman & Wang*, 1993). Field studies have shown that this transition occurs between

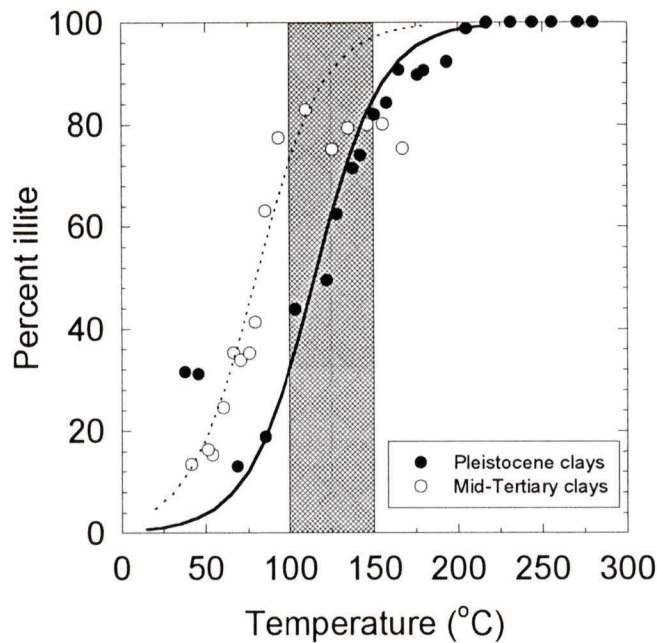


Figure 3.3. Transition of non-expandable marine clays with increasing temperature. The transition from stable sliding to stick-slip behaviour occurs between 100-150°C, as denoted by the shaded box. The younger Pleistocene sediments (*Jennings & Thompson [1986]*) show a stronger correlation to 150°C transition temperature than do the Middle Tertiary sediments (*Hower et al. [1976]*) [modified from *Hyndman & Wang [1993]*].

100-150°C for Pleistocene clays (*Jennings & Thompson, 1986*), and between 75-125°C for older, mid-Tertiary clays (*Hower et al., 1976*) (Fig. 3.3). Although other components of the sediment column are also likely important to the sliding behaviour e.g., carbonates which dehydrate at higher temperatures and therefore initiate stick-slip behaviour at only greater depths, the smectite to illite transition is used as a maximum width, updip limit of the seismogenic locked zone. Other factors that may control the updip limit are the pore pressure and degree of consolidation of the accretionary prism (e.g., see discussion in *Byrne et al., 1988*), but are not pursued in this study. The uncertainty on the updip limit is therefore probably around  $\pm 50^\circ\text{C}$ .

### 3.2.4 The serpentinization of mantle rocks: an alternative downdip limit

As discussed in Chapter 1, in the subduction of older oceanic plates, the downdip

350°C and 450°C thermal limits may occur only at depths greater than 60 km. There is little evidence for great thrust earthquakes extending below a depth of about 45 km, and the seismogenic zone likely does not extend below this limit (e.g., see discussion Pacheco et al., 1993; Tichelaar & Ruff, 1991; 1993). Another process, other than thermally controlled limit, must then set the downdip seismogenic limit. One possible process may be serpentinized forearc mantle below the Moho (e.g., Hyndman et al., 1996). It has been suggested that free water generated by the early dehydration of the subducting oceanic crust migrates updip until temperatures favour mineral precipitation (e.g., Hyndman, 1988). At greater depths, the subducting crust continues to dewater into the overlying crust rocks, acting to hydrate the overlying forearc mantle (Fig. 1.1) (e.g., Fyfe et al., 1978). The hydrothermal alteration of magnesium or iron-rich silicates, i.e., a major component of the mantle is olivine, produces a form of serpentinite which exhibits stable-sliding behaviour at convergent rates and which may exhibit stick-slip behaviour at rupture propagation rates (e.g., Rayleigh & Patterson, 1968; Reinen et al., 1991; Moore et al., 1995).

The serpentinite is expected to occur in contact with the thrust plane downdip of the intersection of the continental Moho with the subducting plate, and serpentinite within the forearc upper mantle has been confirmed by the presence of serpentinite diapirs between the trench and the volcanic arc (e.g., Fryer et al., 1992; Fryer, 1996). However, depth constraints to this intersection from seismic reflection data are particularly poor for several reasons: First, the intersection commonly occurs beneath the coastline (e.g., Ruff & Tichelaar, 1995), in the gap between marine seismic reflection studies and continental studies; Second, there are few interpretable continental Moho reflections due to structural deformation associated with the region of contact between the subducting plate and the overriding plate (e.g., Fuis & Plafker, 1991; K. Rohr, personal communication, 1995); and third, where reflection data are available, the serpentinization of the upper mantle reduces the mantle velocity and thus reduces the velocity contrast across the forearc Moho. However, the serpentinization of the continental forearc rocks provides the most likely cause limiting the downdip rupture propagation depth where the subduction of older oceanic crust occurs. An average depth between 40-45 km for the intersection of the continental Moho with the subducting plate is

chosen for all the studied regions, with an uncertainty of about 5 to 10 km (e.g., Goodwin et al., 1989; Tichelaar & Ruff, 1991; Beaudoin et al., 1994; Brocher et al., 1994, and references therein).

### 3.3 HEAT TRANSFER THEORY

The thermal models used to constrain the width of the seismogenic region along the thrust plane consist of a 2-D conductive and advective heat transfer model describing the subduction process, and a 1-D conductive heat transport model constructed at the deformation front that provides the initial temperature-depth profile. Each is discussed below as developed by Wang & Davis (1992) and by Hyndman & Wang (1993).

#### 3.3.1 The 1-D thermal model

Near the deformation front, the mechanism for heat transport within the sedimentary column overlying the nearly horizontal oceanic plate is taken to be vertical. It may therefore be approximated by a fixed temperature-depth profile obtained from a 1-D finite element model. The model incorporates the cooling history of an oceanic plate, and the effects of sedimentation, i.e. total sediment accumulation thickness, to derive a unique temperature gradient. Modified from Hutchinson (1985), the model employs a porosity-depth profile that is constant, regardless of sediment accumulation rate or thickness. The porosity of the sediment is therefore a function of depth only until near constant porosity at some depth, important for the conservation of solid and fluid mass of the sediment column (Fig. 3.4) (e.g., Wang & Davis, 1992; K. Wang, personal communication, 1995). Wang & Davis (1992) used an exponential porosity-depth function of the form

$$\phi = \phi_o e^{\left(\frac{-z}{L}\right)} \quad (3)$$

where  $\phi_o$  is the porosity value at the sediment surface, and  $L$  is a porosity depth scale. Both  $\phi_o$  and  $L$  are assumed known, but in practice they are derived from porosity estimates from

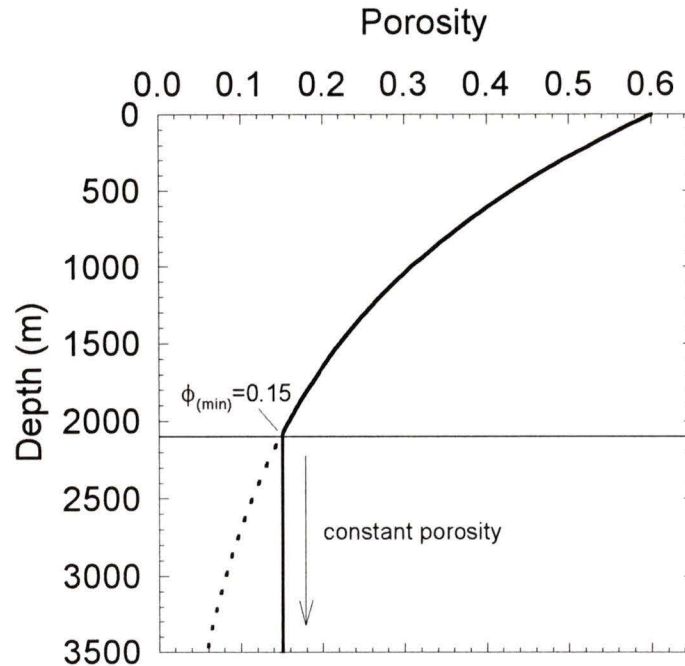


Figure 3.4. Porosity as a function of increasing depth for sediments blanketing the oceanic plate. The resulting curve is from the exponential relationship  $\phi = \phi_0 \exp(-Z/L)$ . Below roughly 2000 m, the porosity is inferred to remain at a nearly constant minimum value of  $\phi_{\min} = 0.15$ , as interpreted from seismic velocity data (modified from Wang & Davis [1992]).

seismic velocity data (e.g., Wang, 1994). This relationship determines the heat transfer via pore water flow and sediment compaction at any time. Typical 1-D model parameters are listed in Table 3.1.

### 3.3.2 The 2-D thermal model

A 2-D finite element scheme is applied to model the thermal regime of a subduction zone. It models the heat flux through the accretionary prism, the forearc continental rocks, and the subducting plate using the method described by Hyndman & Wang (1993) & Wang et al. (1995b). The steady state temperature field  $T$  is described in a depth ( $z$ ) and horizontal distance ( $x$ ) coordinate system by

$$Q = - \left[ \frac{\partial}{\partial x} \left( \lambda \frac{\partial T}{\partial x} \right) + \frac{\partial}{\partial z} \left( \lambda \frac{\partial T}{\partial z} \right) \right] + \left[ \rho c \left( v_x \frac{\partial T}{\partial x} + v_z \frac{\partial T}{\partial z} \right) \right] \quad (4)$$

where  $Q$  is the heat source term representing the radiogenic and frictional heat,  $\lambda$  is the

| Symbol        | Range | Units                            | Description                 |
|---------------|-------|----------------------------------|-----------------------------|
| $\lambda_w$   | 0.6   | $\text{Wm}^{-1} \text{K}^{-1}$   | water conductivity          |
| $\lambda_s$   | 2.74  | $\text{Wm}^{-1} \text{K}^{-1}$   | sediment grain conductivity |
| $\lambda_b$   | 2.79  | $\text{Wm}^{-1} \text{K}^{-1}$   | oceanic plate conductivity  |
| $\rho c_w$    | 4.3   | $\text{MJ m}^{-3} \text{K}^{-1}$ | water thermal capacity      |
| $\rho c_s$    | 2.65  | $\text{MJ m}^{-3} \text{K}^{-1}$ | sediment thermal capacity   |
| $\rho c_b$    | 3.3   | $\text{MJ m}^{-3} \text{K}^{-1}$ | basement thermal capacity   |
| $Q_s$         | 0.6   | $\mu\text{W m}^{-3}$             | sediment heat generation    |
| $\phi_o$      | 0.6   | --                               | surface porosity            |
| $\phi_{\min}$ | 0.15  | --                               | minimum porosity            |
| L             | 1.5   | km                               | porosity depth scale        |

Table 3.1. List of parameters used in the 1-D temperature gradient calculated at the deformation front. The range of values for the temperature gradient calculation were the same for all margins considered (see text for details) [modified after *Hyndman & Wang, 1993*].

thermal conductivity of the rock, assumed to be isotropic as a function of  $x$  and  $z$ , and  $\rho c$  is the thermal heat capacity of the oceanic plate, with density  $\rho$  and specific heat  $c$ . The first pair of square brackets encloses the conductive heat transfer term, and the second pair encloses the convective heat transport term which is assumed to take place only in the subducting oceanic plate. Where the subduction history is more complicated, a transient model having the subducting plate age change with time is required. For example, to model the condition for the Nankai Margin of the subduction with time of younger to older crust, a transient model was developed by Wang et al. (1995b). Their results are compared to other subduction zones in this study.

### 3.4 APPLICATION OF THE 2-D MODEL PARAMETERS

The 2-D geothermal gradient models have been applied to the four subduction zones. Discussed below are the constraints to the non-thermal and thermal parameters for the 1-D and 2-D models. The sensitivity of the models for each parameter is constrained by a comparison to the observed heat flow, presented in Chapter 4.

### 3.4.1 Non-thermal parameters

#### Sediment accumulation rate & prism structure

The deep sea sedimentation history, the sediment blanket covering the incoming plate at the deformation front, and the outer accretionary prism structure are all important parameters for the construction of the 1-D thermal model. A thick sediment cover acts to insulate the oceanic plate, resulting in high initial thrust plane temperatures. The porosity-depth relation shown in Equation (3) is estimated for the corrected sediment column height or thickness as a function of time during accumulation. A porosity of 60% is a common estimate for the sea floor porosity  $\phi_0$ . The porosity is taken to decrease exponentially to a depth of 2 km where  $\phi_{\text{min}}=0.15$ ; at greater depths, the porosity is maintained at this constant value (Fig. 3.4) (Davis & Hyndman, 1989; Wang & Davis, 1992). As the 15% porosity represents the maximum consolidation at 2 km, an average depth of 1.5 km with 25-30% porosity is used to better accommodate the listed uncertainties. The errors associated with these assumptions are necessarily large: the observed thickness of the sediment column is mainly estimated from seismic reflection data. Two-way travel time to depth conversions for thick sediment sequences, i.e. as for Cascadia 2-3 km, have an uncertainty of about 5-10%, or 100-150 m (Davis & Hyndman, 1989; Davis et al., 1990; E. Davis, personal communication, 1994). Any differences in sediment composition may introduce additional uncertainty. The sediment column thickness estimate within 150-200 m is therefore to be expected (e.g., Davis & Hyndman, 1989).

The prism structure is derived mainly from single- and multichannel seismic reflection data. In the models, the prism is bounded by the seafloor bathymetry and by the geometry of the subducting crust. The landward edge of the wedge is backstopped either by terrane rocks (Cascadia), older accreted sediments (South Alaska and Nankai), or by continental crustal rocks (Chile). The décollement is taken to coincide with the top of the oceanic crust. For some margins, it may lie a few hundred metres higher, which affects estimates of temperatures on the thrust near the prism toe. The interpretation of how much sediment is subducting and how far remains uncertain (e.g., Hyndman et al., 1993; Tichelaar & Ruff, 1993; Westbrook et al., 1994), and a common décollement level is chosen.

### **Plate dip profile**

Many earlier models of subducting plates approximated the dip with a single plane or, in a few cases, by a plane segmented into two differently dipping sections (e.g., James et al., 1989; Ponko & Peacock, 1995, and references therein). With an increased understanding of the structure underlying subduction zones over the past ten to fifteen years from seismic reflection, refraction, and seismicity data, more realistic, better constrained plate geometries can now be constructed. In this study, the dip geometry has been approximated by a third order polynomial which is assumed to be within  $\pm 10^\circ$  of the true dip.

The dip profile is constrained by five data sets: 1. single- and multichannel seismic reflection data; 2. seismic refraction data; 3. Wadati-Benioff earthquake data; 4. main thrust earthquakes; and 5. aftershock and intermediate magnitude thrust earthquakes. A list of references for the constraints for each margin used in this study is given in Table 3.2. The seismic reflection data define the top of the plate near the deformation front. For the deeper, more landward portion, Wadati-Benioff earthquakes occurring within 50 km of the selected profile are used to constrain the upper surface of the plate. These earthquakes are believed to occur at some depth below the top of the plate where plate bending stresses are greatest, favouring brittle fracture and failure (e.g., Bevis & Isacks, 1984; Apperson & Frohlich, 1987; Singh & Mortera, 1991; Protti et al., 1994; Rogers et al., 1990). For example, for South Alaska and Chile, the Wadati-Benioff earthquakes were estimated to be within 10-15 km of the upper surface of the subducting plate. This depth offset corresponded well to continuity with seismic reflection data. For the younger oceanic plates for Cascadia and Nankai, the distance chosen is 10 km. All five data sets were weighted according to their estimated accuracy: higher weighting was used for the seismic reflection data and larger magnitude thrust activity believed to be along the subduction thrust plane, and lower weighting for the smaller, intraplate events. The estimated uncertainties in the depth to the subduction thrust range from about  $\pm 0.3$  km near the deformation front, to about  $\pm 5$  km at 50 km depth.

| Data set                                      | Association |             | Reference source  |   |   |   |
|---|-------------|-------------|---|---|---|---|
|   | Inter-plate | Intra-plate | Cascadia  | South Alaska  | Chile   | Nankai  |
| multichannel seismic reflection & refraction  | ✓           |             | <ul style="list-style-type: none"> <li>• Hyndman et al. (1990)</li> <li>• Spence et al. (1991a; 1991b)</li> </ul>                           | <ul style="list-style-type: none"> <li>• Moore et al. (1991)</li> <li>• Brocher et al. (1994)</li> <li>• Ambos et al. (1995)</li> </ul>   | <ul style="list-style-type: none"> <li>• Berhmann et al., ODP leg 141 (1992)</li> <li>• von Huene et al., GEOMAR Cruise Report SO101, (1995)</li> </ul>                                 | <ul style="list-style-type: none"> <li>• Moore et al. (1990)</li> </ul>   |
| Wadati-Benioff earthquakes                    |             | ✓           | <ul style="list-style-type: none"> <li>• Rogers, (1983);</li> <li>• Crosson &amp; Owens, (1987);</li> <li>• Rogers et al. (1990)</li> </ul> | <ul style="list-style-type: none"> <li>• NEIC catalogue: (1970-1992) <math>m_b \geq 3.0</math>; 0-150 km depth; 100 km wide swath projected onto profile (Reagor et al., 1994)</li> </ul> |   | <ul style="list-style-type: none"> <li>• Hirahara (1981)</li> <li>• Mizoue et al. (1983)</li> <li>• Ito (1990)</li> </ul> |
| Main thrust earthquakes                       | ✓           |             | --  | <ul style="list-style-type: none"> <li>• Plafker (1969)</li> <li>• Moore et al. (1991)</li> <li>• NEIC catalogue 1964</li> </ul>  | <ul style="list-style-type: none"> <li>• Plafker &amp; Savage (1970)</li> <li>• Cifuentes (1989)</li> <li>• Barrientos et al. (1992)</li> <li>• NEIC catalogue: 1960-1968</li> </ul>    | <ul style="list-style-type: none"> <li>• Kanamori (1972)</li> <li>• Ando (1975)</li> </ul>                                |
| Aftershocks & intermediate thrust earthquakes | ✓           |             | --  | <ul style="list-style-type: none"> <li>• NEIC catalogue 1964</li> <li>• Tichelaar &amp; Ruff (1993)</li> <li>• Plafker (1969)</li> </ul>  | <ul style="list-style-type: none"> <li>• Choy &amp; Dewey (1988)</li> <li>• Tichelaar &amp; Ruff (1991)</li> <li>• Araujo &amp; Suarez (1994)</li> <li>• NEIC catalogue 1960</li> </ul> | <ul style="list-style-type: none"> <li>• Kanamori (1972)</li> <li>• Ando (1975)</li> </ul>                                |

Table 3.2. List of pertinent data sources used in the estimation of the subducting oceanic plate dip profile geometry: NEIC National Earthquake Information Centre.

### Convergence rate & plate age

The two remaining non-thermal constraints, the convergence rate and subducting plate age, are estimated from global plate motion models which use fairly well constrained magnetic anomaly data and average motions along the transform fault boundaries (DeMets et al., 1990). Additional constraints to the plate age come from deep sea DSDP and ODP

drill cores which penetrated the upper oceanic crust and to which reliable dating has been acquired. While the model is mostly insensitive to variations in the convergence rate, variations in the plate age by  $\pm 20\%$  were found to significantly affect the model results, as presented in the uncertainty analysis in Chapter 4.

### 3.4.2 Thermal parameters

#### Thermal Conductivity

The thermal conductivity of the accretionary prism sediments increases landward and downward with the corresponding decrease in porosity, which is both temporally and spatially a complex function of pore fluid expulsion, sediment composition, etc. For the thermal model, these processes are represented with a linear increase in surface thermal conductivity from the toe of the prism to the landward backstop. A linear increase with depth was also applied to correspond to the increasing consolidation with depth. The conductivity of the oceanic and overriding plates was assumed constant with depth. Where conductivity data were unavailable, values were assumed to be similar to that obtained from surface samples for the northern Cascadia Margin (Lewis et al., 1984; Lewis et al., 1988).

#### Radiogenic heat generation

The radiogenic heat generation through the decay of the radioactive isotopes of uranium, thorium, and potassium, i.e.,  $U^{235 \& 238}$ ,  $Th^{232}$ , and  $K^{40}$  provides a major component of the surface heat flow. The relation between the average radioactivity of the surface rocks and the heat generation is given by  $(aU + bTh + cK\%)*D$ , where both the uranium (U) and thorium (Th) element concentrations given in parts per million (ppm) by weight, and potassium (K) in percent atomic weight; D is the rock density. The coefficients a, b, and c are factors determined from laboratory samples, and the contributions from all three are of similar magnitude (Turcotte & Schubert, 1982; Lewis et al., 1984). Unfortunately, there is limited information on the uranium and thorium concentrations for surface rocks. The contribution from potassium, for which there is a greater data availability, was therefore used.

The heat generation of the accretionary prism sediments was taken from analysis on

drill core samples. In the absence of such data, the heat generation was assumed to be an average for the continental coastal rocks from which the prism sediments were derived. Plutonic rocks were generally chosen based on their widespread distribution and high erodability. For all margins, the heat generation of the subducting oceanic crust was assumed negligible (Dumitru, 1991).

### 3.4.3 Frictional heating

Based on the conclusions of Wang et al. (1995a), frictional heating has been neglected in the preferred thermal models. However, for the uncertainty analysis discussion in the following chapter, the effect of frictional heating along the thrust plane has been examined. The simplified frictional behaviour along the thrust plane used in this study is based upon the theory by van den Beukel & Wortel (1987), as applied by Wang et al. (1995a). The amount of frictional and shear heating along the thrust plane is directly related to the magnitude of the shear stress, which has been estimated to be between near zero to 120 MPa (Turcotte & Schubert, 1982; Wang et al., 1995a). This variation comes from several factors: first, near the seaward end of the thrust fault, the high pore fluid pressures may be near-lithostatic, inducing a very low coupling shear stress on the thrust plane interface (Wang & Davis, 1992; Wang et al., 1993; Westbrook et al., 1994). Second, the transition from brittle behaviour to plastic flow is not well constrained, and thus the shear stress may vary depending on the conditions along the thrust plane for a given depth.

The thrust plane is divided into upper and lower frictional regimes. In the brittle regime, the frictional strength at low deviatoric stress is best described by Byerlee's law. The shear stress on the fault plane depends on depth and the pore to lithostatic pressure ratio. The frictional heating per unit fault width downdip is given by  $Q_{fi} = \tau v$ , where  $v$  is the sliding velocity. In the lower plastic region the frictional shear heating per unit volume is given by  $Q_{fi} = \tau \dot{\epsilon}$ , where  $\dot{\epsilon}$  is the deformation strain rate along the fault. The strain rate is dependent on the shear stress and on the thrust plane temperature (van den Beukel & Wortel, 1987). In the thermal model, frictional heating is incorporated by assigning a thin, 500 m thick layer above the subducting plate. This layer represents the region which experiences the

shear stress associated with the subduction thrust. Hyndman & Wang (1993) and Wang et al. (1995a) showed that the surface heat flow data for Cascadia agree with the model values only if there is negligible frictional heating. Wang et al. (1995a) suggested that high pore pressure might account for the low shear stress and therefore low frictional heating along the thrust plane. This study confirms their findings that with the addition of significant heating along the thrust plane, large changes to the temperatures and inferred seismogenic zone widths are produced. Thus, in the preferred models, frictional heating was neglected.

#### 3.4.4 The effect of volcanic arcs

The effects of high temperatures near the arcs has been examined through a very simple model. The surface heat flow above the volcanic arc is crudely estimated from  $T = T_o + [Q/\lambda]z$ , where the temperature gradient  $([T - T_o]/z)$  to a depth of 80 km below the volcanic arc is proportional to a surface heat flow of  $80 \text{ mWm}^{-2}$  and inversely proportional to the conductivity  $\lambda$ . Here,  $T_o$  is the initial surface temperature and  $z$  is the depth in km. This additional constraint to the landward boundary acts to increase the subduction thrust temperatures downdip, narrowing the brittle to plastic flow transition zone. However, it appears that the effect from the volcanic arc is too far landward to change the thrust plane temperatures important to the seismogenic region.

#### 3.4.5 Finite element grid

In the 2-D thermal model, Equation (4) is solved using a quadrilateral finite element mesh with preset boundary conditions. Each element consists of eight nodes: four corners nodes and four mid-point nodes (Fig. 3.5). Within each element, the thermal properties are uniform, but the temperature may vary quadratically. The average heat flux is calculated at the centre of each element. For each margin, a finite element mesh was created based on a few control lines, i.e., the top of the accretionary prism, the dip profile of the subducting plate, the bottom asthenosphere boundary. The density of elements was increased where greater computation is required, e.g., the accretionary prism, modelled with elements  $10 \text{ km}^2$ , and decreased where reduced computation will suffice, e.g., continental regions, elements

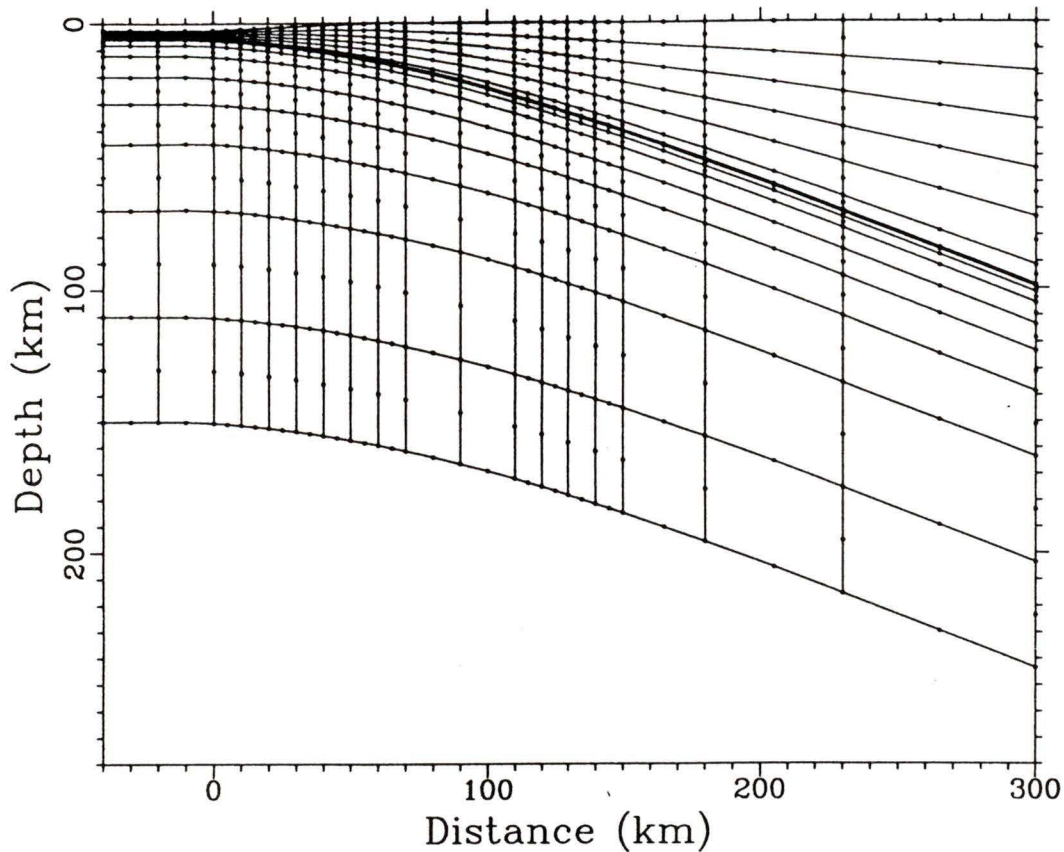


Figure 3.5. Example of the finite element mesh constructed for each margin. The mesh consists of a skeleton frame composed of control lines between which additional divisors are equidistantly spaced. Element size is correlated to the thermal gradient of a particular area: the accretionary prism from 0 km to roughly 100 km landwards of the deformation front has tight element spacing to represent the more dynamic thermal gradients in the sediments; the continental rocks from 100 km to 300 km landwards have larger element spacing representing the more uniform thermal conductivity and heat generation averaged over the entire area. The control line representing the top surface of the subducting plate (thick line across middle of mesh) is derived from the Wadati-Benioff and seismic reflection data as fit by a third order polynomial. The thermal model is insensitive to the subducting plate thickness, and a generous thickness down to 150 km is chosen to avoid bottom edge effects.

are typically  $50 \text{ km}^2$  (Fig 3.5). The mesh extends from about 40 km seaward of the deformation front to 300 km landward, and to a vertical depth of 300 km. These dimensions extend well beyond the seismogenic region, seaward and landward, to avoid edge effects. The upper boundary approximates the surface topography of the accretionary prism with a gently upwards sloping curve to the coast. Landward of the coast, the surface is taken to be at sea level as the model is insensitive to surface topography of less than 2 km, small compared with the depth to the thrust plane (10's of kilometres). A thin band of elements is included along the top of the mesh to calculate the surface heat flux with greater precision.

The boundary at the top and bottom of the grid are fixed at 0°C and 1400°C, approximating the temperature at the earth's surface and in the mantle respectively. Velocity vectors are assigned to all nodes below the line representing the top of the subducting plate. Trial runs with subducting plate thickness of 15-20 km, as given by the simple cooling-thickening relationship  $7\sqrt{L}$ , where L is the age of the plate, showed no significant change in the surface heat flow profile. The seaward edge of the model is constrained by the temperature-depth profile gradient developed from the 1-D thermal model and the landward end is assumed to be in conductive and thermal equilibrium with the continental rocks of the overriding plate, i.e., no horizontal heat transport occurs across the landward boundary.

### 3.5 CASCADIA

This section reviews the results from Hyndman & Wang (1993) and Wang et al. (1995a), and presents new results of modified and improved thermal models to the southern portions of the margin.

#### 3.5.1 Non-thermal parameters

##### **Sediment accumulation rate & prism structure**

The deep sea Cascadia Basin sedimentation history used in the thermal model has been described by Davis & Hyndman (1989) for offshore Vancouver Island. There were three main sedimentation phases: from the time of ocean crust formation at the Juan de Fuca ridge to 4 Ma, there was slow deposition due to the elevation of the spreading Juan de Fuca Ridge (this deposition has been neglected); from 4 to 2 Ma there was more rapid hemipelagic and pelagic sedimentation (1.1 mm/yr); and from 2 Ma to present, there was rapid turbiditic sedimentation in a broad ponding against the margin in the Cascadia Basin (1.2 mm/yr).

The accreted sediments form a fairly uniform wedge from the deformation front to the coast. The base of the accretionary prism matches the gentle initial dip of the subducting oceanic crust (Spence et al., 1991a). The prism increases in thickness from 2-3 km at the deformation front to 12-15 km thick at the coast, forming an average 10-12° tapered wedge at the coast. As discussed in Chapter 2, deeply rooted thrust faults which penetrate close to

the top of the oceanic crust suggest that most of the sediment is scraped-off. For the southern regions of the margin, some seismic sections show the detachment is around 500 m above the oceanic crust (e.g., MacKay et al., 1992). The assumption that the décollement is at the base of the sediment section may overestimate the temperatures on the thrust by about 15-20°C.

### **Low conductivity and low heat generation terranes**

The Crescent/Siletz Terrane that lies along the whole margin and the Pacific Rim Terrane off Vancouver Island have unusually low thermal conductivity and heat generation, and are treated separately from the remaining continental crust in the model. The cross-sections are derived from offshore and onshore multichannel seismic reflection and refraction data (e.g., Hyndman et al., 1990; Trehu & Nakamura, 1993; Trehu et al., 1994). The Crescent/Siletz Terrane beneath Vancouver Island is about 6 km thick, and between 25-30 km thick beneath the Oregon Coast Range. There is eastward thickening by 15 km at 100 km landward of the Oregon coast (e.g., Trehu et al., 1994). Farther inland, seismic refraction resolution becomes poor, and the terrane is undefined. Variations in thickness and location of the terrane were considered in the thermal model. The Pacific Rim Terrane is imaged only beneath Vancouver Island, and is roughly the same size as the Crescent Terrane for this region.

### **Plate dip profile**

Multichannel seismic reflection data provided the main definition of the top of the oceanic plate (Hyndman & Wang, 1993; Hyndman, 1995a, and references therein). The top surface was traced intermittently 120 km landward of the deformation front (Fig. 3.6a & b) (e.g., Hyndman, 1995a). The subducting plate beneath northern Cascadia, i.e., Vancouver Island and the Olympic Peninsula, was also constrained by relatively few but well constrained Wadati-Benioff earthquakes located by the dense seismograph station network in southwest British Columbia and northwest Washington state (e.g., Rogers, 1983; Crosson & Owens, 1987; Rogers et al., 1990). This seismicity is limited to a maximum depth of roughly 70 km,

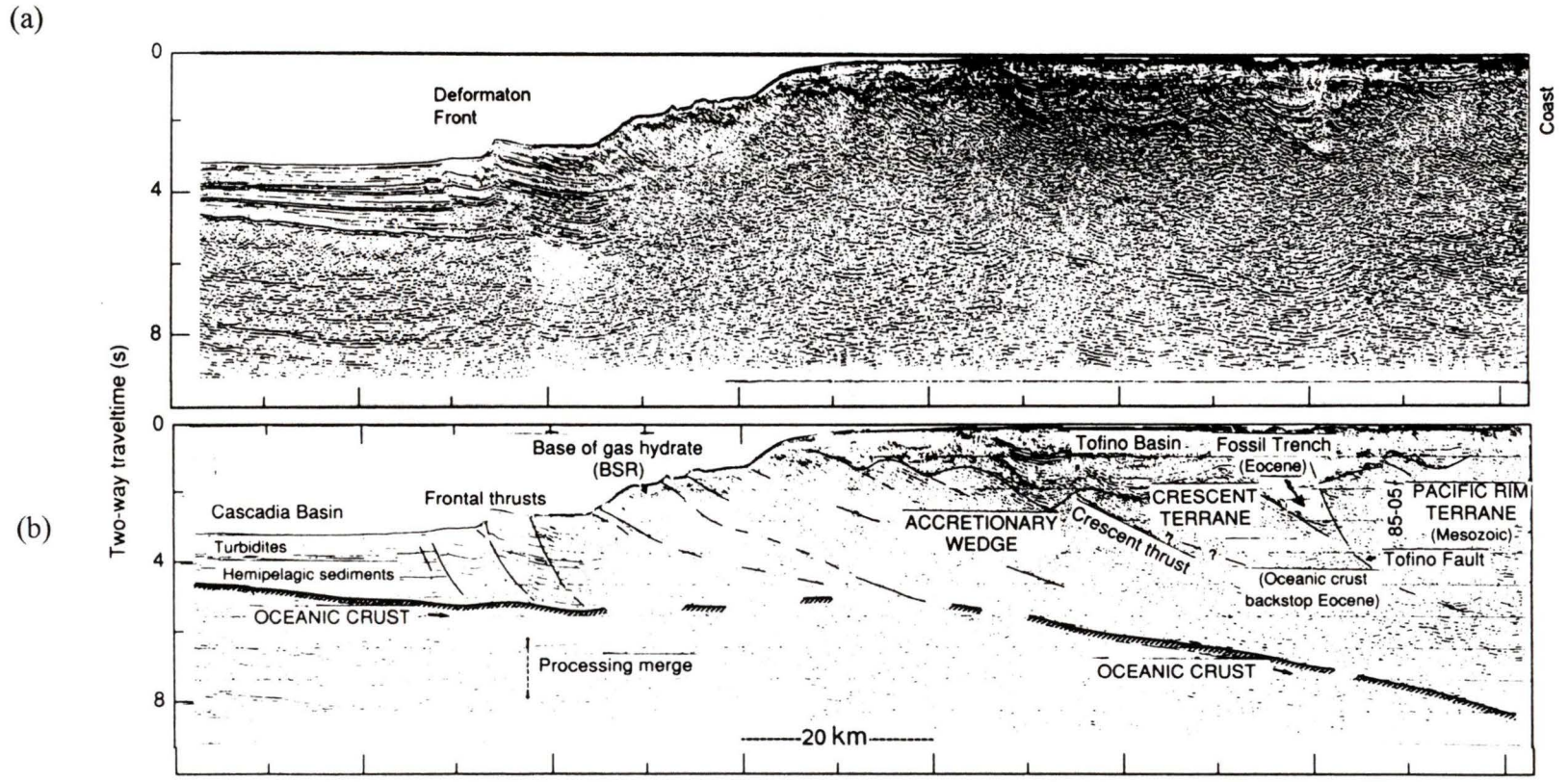


Figure 3.6. Dip profile geometry for the Vancouver Island margin. (a) Multichannel seismic reflection data acquired from by the Geological Survey of Canada. Vertical exaggeration is about 3:1 for the upper sedimentary section, and 1:1 at the landward end. (b) Interpretation of main reflectors underlying Vancouver Island. The Crescent Terrane which acts as a backstop to the accretionary prism. The top of the Vancouver Island. The Crescent thrust marks the outer edge of the Crescent front (after Hyndman et al. [1990]).

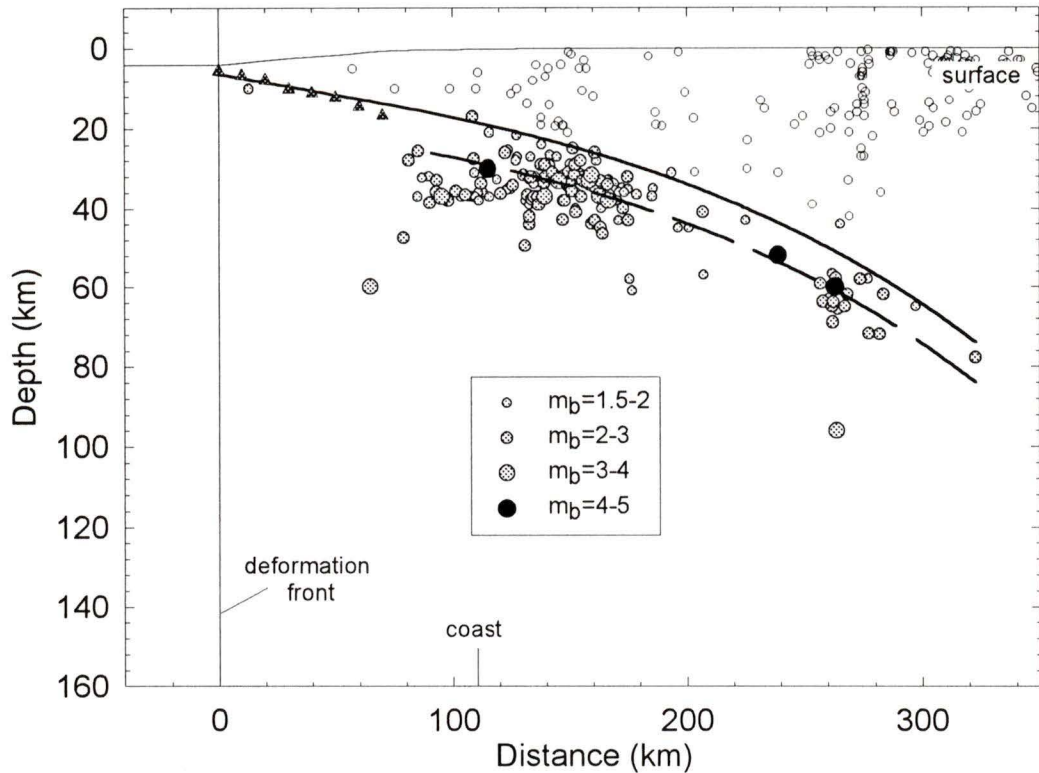


Figure 3.6. (continued) (c). Dip profile for the Vancouver Island profile, Cascadia Margin. The addition of Wadati-Benioff data, combined with the seismic reflection data from (a) and (b), are fit by a third order polynomial which represents the top of the oceanic crust (solid line). The subduction thrust is taken to be 10 km above the fit to the Wadati-Benioff data (dashed line).

below which the hot Juan de Fuca plate rapidly exceeds the maximum temperature for mantle earthquakes of about  $750^{\circ}\text{C}$  (Fig 3.6c) (Riddihough & Hyndman, 1976).

Separate and readily identifiable are the overlying continental crustal earthquakes, limited to a depth of about 30 km by the maximum temperature for continental crustal earthquakes of about  $350^{\circ}\text{C}$  (Fig. 3.6c) (Rogers, 1983; Rogers et al., 1990). Seismic refraction studies also provided additional constraint to the top of the subducting slab beneath Vancouver Island (Spence et al., 1985) and Oregon (Trehu et al., 1994). There is little Wadati-Benioff seismicity beneath southern Washington and Oregon, and poorer seismic reflection data, so the landward part of the thrust geometry is less well constrained (e.g.,

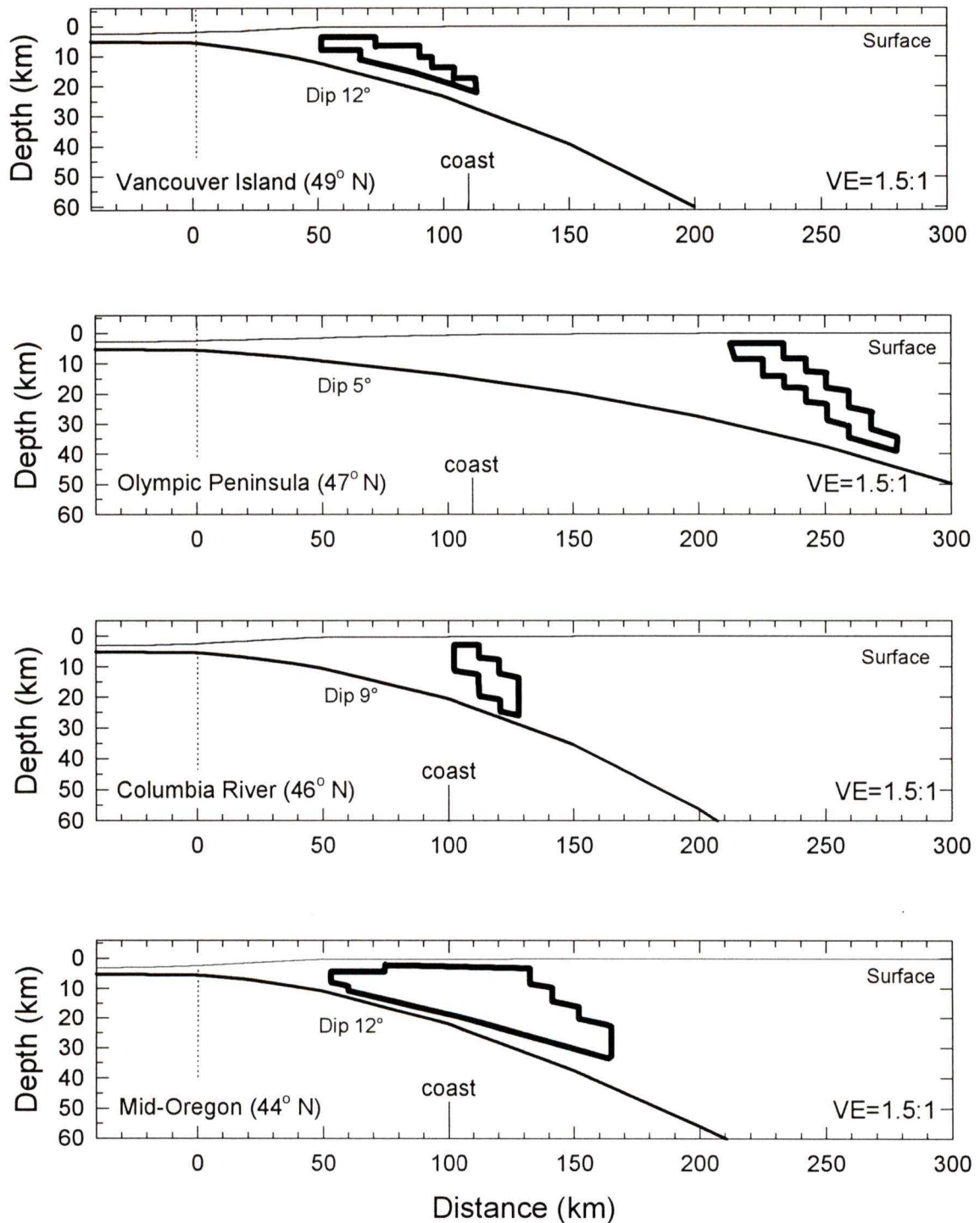


Figure 3.7. Dip profile geometries from north to south along the Cascadia Margin. The plate geometries were derived in similar fashion as described in Fig. 3.6. The dip angles shown are estimated from the top of the subducting plate 60 km landward of the deformation front (vertical dashed line). The low thermal conductivity Crescent/Siletz Terrane is modelled from seismic reflection and refraction data (see text for details) (modified from Hyndman & Wang [1995]).

Crosson & Owens, 1987; Hyndman & Wang, 1995). The main constraint for the landward part is the seismic refraction data of Trehu et al. (1994). The dip profile and Crescent/Siletz Terrane geometries for the four profiles constructed across the Cascadia Margin are given in Figure 3.7.

### Convergence rate & plate age

Convergence has remained relatively constant in rate and direction since the Eocene, and perhaps earlier (Riddihough, 1984; Engerbretson et al., 1985). Present convergence rates increase south to north across the margin, while Juan de Fuca Plate age decreases in the same direction (Table 3.3) (Riddihough, 1984; DeMets et al., 1990). The corresponding decrease in convergence obliquity from south to north as outlined in Chapter 2 is resolved into a trench

| Area of study |                      | Convergence rate (mm a <sup>-1</sup> ) | Sediment thickness* (km) | Plate dip profile** (°) | Subducting plate age (Ma) |
|---------------|----------------------|--|--------------------------|-------------------------|---------------------------|
| Margin        | Profile              |  |                          |                         |                           |
| Cascadia      | Vancouver Is. (49°N) | 45 <sup>†</sup>                        | 3500                     | 13                      | 6.5                       |
|               | Olympic Pen (47°N)   | 45 <sup>†</sup>                        | 3500                     | 8                       | 8                         |
|               | Columbia Riv. (46°N) | 40 <sup>†</sup>                        | 3500                     | 12                      | 8                         |
|               | mid-Oregon (44°N)    | 40 <sup>†</sup>                        | 3500                     | 13                      | 8                         |
| South Alaska  | South Alaska (58°N)  | 65 <sup>‡</sup>                        | ~1500                    | 11                      | 50                        |
| Chile         | North Chile (22°S)   | 84 <sup>‡</sup>                        | 100                      | 13                      | 50                        |
|               | Taltal (26°S)        | 84 <sup>‡</sup>                        | 100                      | 12                      | 50                        |
|               | Coquimbo (31°S)      | 84 <sup>‡</sup>                        | 500                      | 14                      | 48                        |
|               | Valparaiso (33°S)    | 90 <sup>‡</sup>                        | 2500                     | 19                      | 45                        |
|               | South Chile (41°S)   | 90 <sup>‡</sup>                        | ~200                     | 14                      | 20                        |
| Nankai        | Tonankai (33°N)      | 40 <sup>¥</sup>                        | 1500                     | 11                      | 0-15                      |
|               | Nankaido (32°N)      | 40 <sup>¥</sup>                        | 1500                     | 20                      | 0-15                      |

Table 3.3. List of physical parameters used to constrain the thermal models. The latitude assigned to each profile marks the seaward end of the transect. \* Sediment thickness at the deformation front; \*\* calculated at the downdip limit of the locked zone. The following superscripts denote reference sources applicable to both the convergence rate and the plate age: † Riddihough [1984]; Hyndman & Wang [1993]; ‡ DeMets et al. [1990] & Plafker et al. [1994]; ¥ Seno et al. [1993].

normal and trench parallel component. As the thermal model uses a 2-D half space, only the trench-perpendicular component is considered. This introduces little error if the subduction zone is sufficiently uninterrupted along strike, as is the case of Cascadia.

### 3.5.2 Thermal parameters

#### Thermal conductivity

The conductivity profiles were estimated from grain matrix conductivity and porosity estimates from seismic velocity and down-hole logs of petroleum exploration wells (e.g., Lewis et al., 1988; Lewis et al., 1991; Hyndman et al., 1993). In northern Cascadia Basin, surface sediment thermal conductivity values are about  $1.5 \text{ Wm}^{-1}\text{K}^{-1}$  near the seafloor. The sediment conductivity matches the increasing consolidation landward and with depth by increasing linearly to  $2.5 \text{ Wm}^{-1}\text{K}^{-1}$  at 10 km depth (Table 3.4). Farther south along the margin, off Oregon, average surface sediment thermal conductivity values are between 1.3 and  $2.0 \text{ Wm}^{-1}\text{K}^{-1}$ , and increase landwards and with depth similar to the northern Cascadia Basin (e.g., Hyndman & Wang, 1993).

The thermal conductivity of the overriding continental crust landward of the margin on Vancouver Island was estimated at  $3.0 \text{ Wm}^{-1}\text{K}^{-1}$  from numerous surface samples (Lewis & Bentkowski, 1988; Blackwell et al., 1990). The same value was used for the Washington and Oregon models. The thermal conductivity of the subducting oceanic plate is taken to be  $2.9 \text{ Wm}^{-1}\text{K}^{-1}$  (Table 3.4) (e.g., Dumitru, 1991). The thermal conductivity of the Crescent/Siletz and the Pacific Rim terranes are sufficiently different from either prism sediments or continental rocks that they must be represented separately in the thermal model. Thermal conductivity measurements on the Crescent/Siletz volcanic terrane rocks from land boreholes in Washington and Oregon average  $1.59 \text{ Wm}^{-1}\text{K}^{-1}$  (Blackwell et al., 1990). Surface samples from the landward extension of the Pacific Rim Terrane on Vancouver Island give an average value of  $2.5 \text{ Wm}^{-1}\text{K}^{-1}$  (Table 3.4) (Lewis & Bentkowski, 1988).

| Margin       |                    | Thermal conductivity<br>$\lambda$ ( $\text{Wm}^{-1}\text{K}^{-1}$ ) | Radiogenic heat generation<br>$Q$ ( $\mu\text{Wm}^{-3}$ ) | Thermal heat capacity<br>$\rho c_p$ ( $\text{MJ m}^{-3}\text{K}^{-1}$ ) |
|--------------|--------------------|---|---|---|
| Cascadia     | accretionary prism | 1.5 - 2.5   | 0.6   | --  |
|              | volcanic terrane   | 1.59  | 0.05 <sup>†</sup>   | --  |
|              | continental crust  | 2.5 */ 3.0  | 0.2-0.6   | --  |
|              | oceanic plate      | 2.9   | 0.01 <sup>†</sup>   | 3.3   |
| South Alaska | accretionary prism | 1.5-2.5   | 0.8   | --  |
|              | continental crust  | 2.0-3.0   | 0.2-1.0   | --  |
|              | oceanic plate      | 2.9   | 0.01 <sup>†</sup>   | 3.3   |
| Chile        | accretionary prism | 1.5-2.5   | 0.8   | --  |
|              | continental crust  | 3.0   | 0.2-1.0   | --  |
|              | oceanic plate      | 2.9   | 0.01 <sup>†</sup>   | 3.3   |
| Nankai       | accretionary prism | 2.0-2.5   | 1.9-2.4   | --  |
|              | continental crust  | 2.5   | 0.4-1.9   | --  |
|              | oceanic plate      | 2.9   | 0.01 <sup>†</sup>   | 3.3   |

Table 3.4. Thermal property constraints used for input to the thermal models calculated for each region depending on sediment source history and tectonic regime. Values for Cascadia are modified from *Hyndman & Wang* [1993], and are extrapolated where necessary for South Alaska and Chile where constraints are poor from the lack of data. \*: thermal conductivity is given for both the Crescent Terrane ( $1.59 \text{ Wm}^{-1}\text{K}^{-1}$ ) and for the Pacific Rim Terrane ( $2.5 \text{ Wm}^{-1}\text{K}^{-1}$ ); †: radiogenic heat generation of the volcanic terranes and of the oceanic plate is considered to be negligible, and taken to be near zero.

### Radiogenic heat generation

The accretionary prism heat generation is very low, estimated to be about  $0.6 \mu\text{Wm}^{-3}$  from well samples on the Vancouver Island continental shelf (Table 3.4) (Lewis et al., 1988). This is similar to the surface crustal rocks from which the Tofino Basin sediments presumably were derived. Radiogenic heat production of the continental crust rocks was assumed to decrease from  $0.6 \mu\text{Wm}^{-3}$  at the surface to a constant value of  $0.2 \mu\text{Wm}^{-3}$  below about 10 km depth (Table 3.4) (Lewis & Bentkowski, 1988; Lewis, et al., 1988).

The radiogenic heat generation of the Crescent/Siletz and Pacific Rim terranes was estimated to be very low, at  $0.05 \mu\text{Wm}^{-3}$  from surface samples in southern British Columbia (e.g., Lewis & Bentkowski, 1988) and from mid-Oregon (Blackwell et al., 1990). The

combination of low heat generation and low thermal conductivity refract the heat away causing a pronounced decrease in the surface heat flow over this terrane. The thermal heat capacity for the oceanic crust was taken to be  $3.3 \text{ MJ m}^{-3} \text{ K}^{-1}$  for all margins.

### **3.6 SOUTH ALASKA**

#### **3.6.1 Non-thermal parameters**

##### **Sediment accumulation rate & prism structure**

Offshore South Alaska, there were four main sedimentation phases: from the time of ocean crust formation (50 Ma) to 20 Ma, there was very slow abyssal plain sedimentation (this deposition has been neglected); from 20 to 2 Ma, there was slightly faster pelagic sedimentation (0.04 mm/yr); from 2 to 0.2 Ma, there was hemipelagic deposition to a thickness of about 750 m (0.90 mm/yr); and from 0.2 Ma to present, a final and extremely short phase of deposition occurred (9.0 mm/yr), consisting mainly of trench fill turbidites (Kulm et al., 1971; Carlson et al., 1977; Plafker et al., 1994).

The Late Cenozoic to present accretionary prism sediments form an  $8^\circ$  wedge taper. The wedge has grown laterally during the emplacement of off-scraped sediments as suggested from numerous seaward dipping layered reflectors (e.g., Moore et al., 1991). For the thermal model, the prism increases in thickness from 2 km at the deformation front to 15 km roughly 100 km landward. The Eocene to Middle Cenozoic accreted sediments increase further to 40 km thickness at 250 km landward of the deformation front. The top surface of the accretionary complex is from seafloor bathymetry (e.g., Fisher and von Huene, 1980).

##### **Plate dip profile**

The South Alaska dip profile is well constrained as it is seismically active and has had numerous multichannel seismic reflection studies within the area of study (e.g., Brocher et al., 1994). The initial dip geometry is constrained by the EDGE transect extending from just seaward of the Aleutian trench to the magmatic arc (e.g., Moore et al., 1991). The oceanic crust dips gently near the base continental shelf, and is traceable for roughly 200 km landward from the trench to the shelf edge, where it is at a depth of about 30 km (Fig. 3.8). Depth-time

(a)

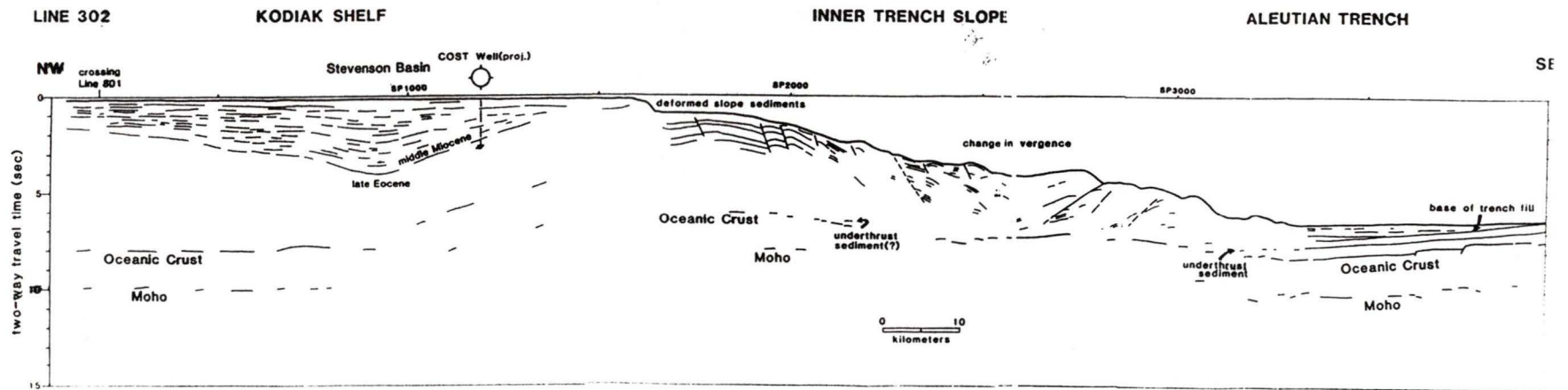


Figure 3.8. Dip profile geometry for South Alaska. (a). Interpretation of main reflectors for the outer accretionary prism from EDGE multichannel time-section seismic reflection data after Moore *et al.* [1991]. Depth-migration was achieved using the depth-time relationship modified from Bruns & Schwab [1983] (see text for details).

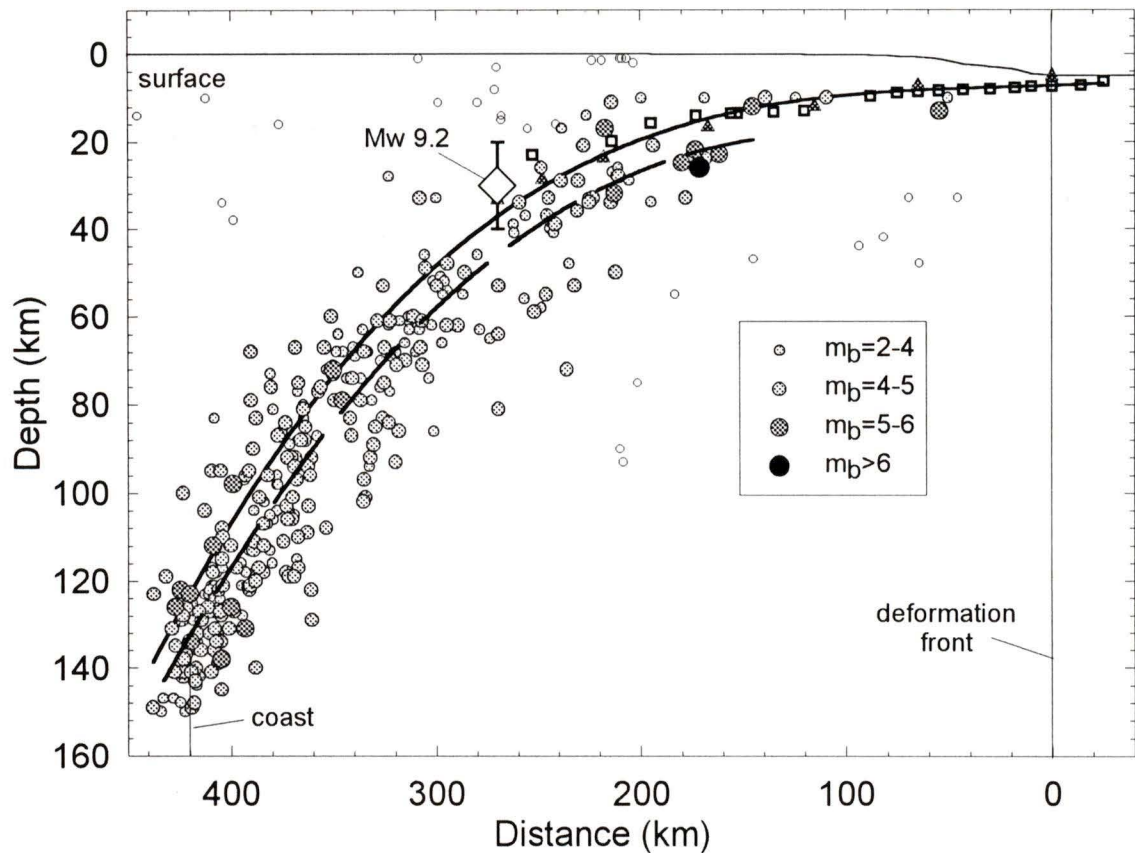


Figure 3.8. (continued) (b) Shape of the subducting plate (solid line) derived from Wadati-Benioff earthquake data, EDGE transect data (black triangles) chosen from selected points along the thrust plane in (a), seismic reflection data as interpreted from *Bruns & Schwab* [1983] (open squares), and the main thrust event of 1964 Prince William Sound earthquake (large diamond) from the NEIC catalogue. Earthquakes excluded from the dip profile analysis are interpreted either to belong to the overriding plate or to occur sufficiently deeply to be considered unreliable (small open circles). VE:2:1.

conversions for the seismic reflection data to a two-way travel time ( $t$ ) of 4 seconds are derived from the relationship of *Bruns & Schwab* (1983), i.e.,  $z=0.17t^2 + 0.85t$ , where  $z$  is the depth in kilometres. From 4 to 12 seconds, a constant, velocity of 5 km/sec was assumed (Fig. 3.9).

Farther landward the geometry of the subducting Pacific Plate was constrained by the Wadati-Benioff earthquake data (Fig. 3.8b), which was taken from the USGS National Earthquake Information Centre (NEIC) database was used (Reagor et al., 1994). More than 500 events occurred with  $m_b \geq 3.0$  between 0-150 km depth, in a 100 km wide swath centred

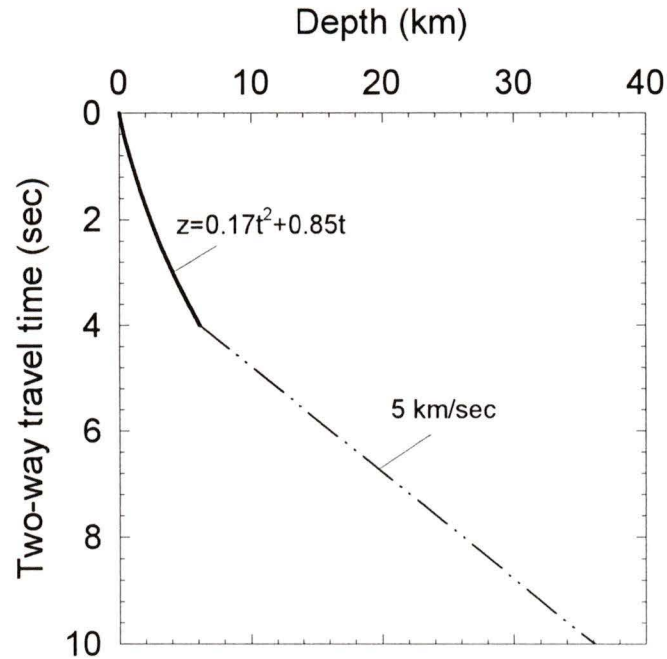


Figure 3.9. Two-way travel time conversion to depth (km). The conversion curve consists of two parts: up to 4 two-way second traveltimes (solid curve) from multichannel seismic reflection data, i.e.,  $z=0.17t^2 + 0.85t$  (Bruns & Schwab [1983]); from 4-10 two-way seconds (dashed line), a 5 km/sec approximation based on data for accretionary prisms elsewhere.

on the model profile. All events corresponding to fixed depths of 10, 22, 33, 40, and 100 km were excluded, as were continental earthquakes. The 1964 event is above the model thrust plane as it is located slightly to the north of the model profile where the subducting Pacific Plate dips more gently. The calculated dip profile is in good agreement with other recent studies (e.g., Page et al., 1989; Stephens et al., 1990; Abers, 1992; Zhao et al., 1995).

### Convergence rate & plate age

The Pacific Plate convergence with the North America Plate off south-central Alaska is between 57 and 62 mm/yr (e.g., DeMets et al., 1990; Brocher et al., 1994; Plafker et al., 1994). An average rate of 60 mm/yr was used in the model (Table 3.3). The subducting plate age is well constrained and has changed little with time as evident from the long history of steady northwestwards plate motion since the Early to mid-Tertiary.

### 3.6.2 Thermal parameters

#### Thermal conductivity

Thermal conductivity values of the South Alaska Margin are poorly constrained: no measurements from land boreholes and marine shelf wells are available. The accretionary prism conductivity was assumed to range from 1.5 to 2.5  $\text{Wm}^{-1}\text{K}^{-1}$  in similar fashion to Cascadia. For the overriding, Eocene accreted wedge for South Alaska, a conductivity of 3.0  $\text{Wm}^{-1}\text{K}^{-1}$  was assigned (Table 3.4). Thermal conductivity for the subducting Pacific Plate was taken to be the same as for the subducting Juan de Fuca plate at 2.9  $\text{Wm}^{-1}\text{K}^{-1}$ .

#### Radiogenic heat production

The sedimentary wedge is derived both from off-scraping of the incoming sediment blanket and from the continental erosion of nearshore moderately felsic plutonic and volcanic rocks, mainly of the Prince William and Chugach terranes (Reed et al., 1983; Barker et al., 1992). The larger Eocene accreted wedge contains relatively high percent potassium from the continental erosion of plutonic and volcanic rocks extruded seaward of the Alaska-Aleutian range, and consequently has a slightly higher surface radiogenic heat production, taken to be 1.0  $\mu\text{Wm}^{-3}$  (e.g., Reed et al., 1983; T. Lewis, personal communication, 1994). For the thermal model, this older prism also represents the important part of the overriding continental plate. Farther seaward, based on the potassium content of the Prince William Terrane source rocks, a heat generation of 0.8  $\mu\text{Wm}^{-3}$  was chosen (Table 3.4). The continental crust heat generation was assumed to decrease linearly downward from 1.0 to 0.2  $\mu\text{Wm}^{-3}$  at 10 km depth (Table 3.4).

## 3.7 CHILE

### 3.7.1 Non-thermal parameters

#### Sediment accumulation rate & prism structure

Due to the rapid variations of sediment supply along the Chile Margin, the sedimentation history and structure is described in general for each profile. Northern Chile sedimentation rates, i.e., North Chile and Taltal profiles, are the lowest along the entire

margin, with appreciable deposition only starting in the interval from 2 Ma to 0.1 Ma (0.1 mm/yr). Maximum sedimentation occurred from 100 ka to present as trench fill turbidites and hemipelagic sedimentation (0.6 mm/yr) (Yeats et al., 1976; Thornburg et al., 1990). A very thin sediment blanket averaging 100 m was assumed for these two profiles. This sediment thickness has a very small effect on the thermal models.

The southern profiles have sediment histories strongly influenced by fan migration across the trench. The bulk of sedimentation is from turbidite submarine flows from 100 ka to present (2.5 mm/yr). The sediment blanket within the Chile trough progressively increases in thickness from about 1000 m at 28°S to over 2500 m between 33 and 45°S (e.g., see Figure 2.11). The corresponding adjacent accretionary prisms are wider and to some degree thicker in the south than in the north. The top of the prism is based on singlechannel seismic reflection data (e.g., Schweller et al., 1981).

### **Plate dip profile**

For the Taltal and North Chile profiles, the thin sediment blanket infers a seafloor close to the top of the subducting plate. Constraints on the initial geometry of the underthrusting plate thus may be derived from bathymetry profiles across the trench where the trench-fill sediments are thin, i.e., northern Chile (e.g., Schweller et al., 1981). There are also singlechannel shallow seismic reflection lines which penetrate the upper few 10's of m of the sediment section to the top of the oceanic crust (e.g., Fig. 3.10 to 3.13). Farther south, multichannel seismic reflection data for the Valparaíso and Coquimbo profiles were collected in the recent GEOMAR CONDOR project. Some lines extended seaward of the deformation front to roughly 200 km from the coast (e.g., von Huene et al., 1995). Although the top surface of the oceanic plate can be traced landwards only a few 10's of kilometres from the deformation front, the data constrain adequately the seaward portion of the thrust plane. Farther south toward the Chile Triple Junction, in the area of the South Chile profile, ODP 141 line 745 provided excellent constraints on the upper surface of the subducting plate to 15-20 km landward of the trench (e.g., Fig. 3.14a & b). Plate dips at the trench are small and increase farther landward (e.g., Behrmann et al., 1992).

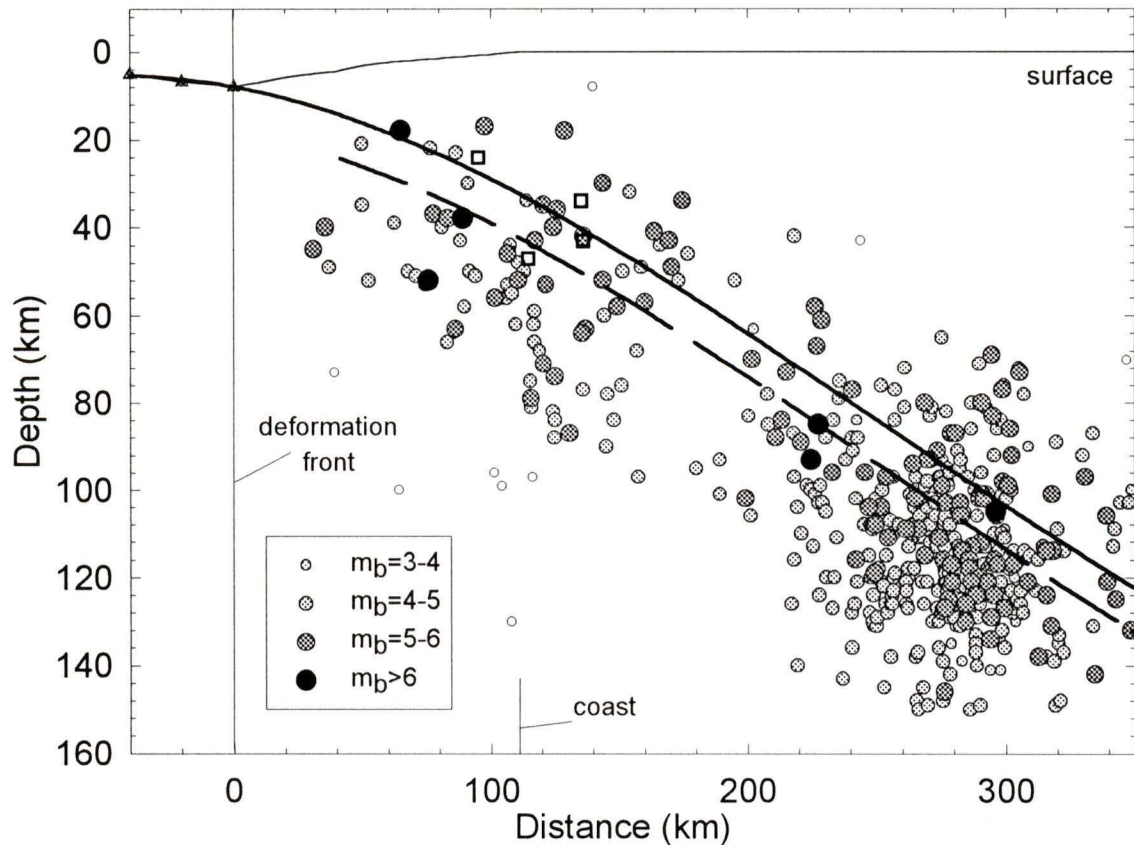


Figure 3.10. Dip profile geometry for North Chile profile. Wadati-Benioff earthquake data constrain the regressional analysis, with preferential weighting for larger events. The top of the oceanic crust (solid line) is assumed to be 10 km above the fit to the Benioff-Wadati data (dashed line). Symbols are: top of crust at trench (open triangles) after Schweller *et al.* [1981]; relocated thrust events (open squares) after Tichelaar & Ruff [1991] and Araujo & Suarez [1994]. The shelf surface topography is taken from single channel seismic reflection data after Schweller *et al.* [1981]. VE:1.5:1.

Abundant Wadati-Benioff seismicity exists for all profiles as given by the USGS NEIC database, with the exception of the South Chile profile (Fig. 3.10-3.14). Between 100-500 events are used to constrain the plate dip profile for the four northern profiles, while only 23 events were available for the South Chile profile. A similar selection of Wadati-Benioff events as for South Alaska, i.e., the constrained depth events, crustal earthquakes, etc., was applied. The depths are very scattered, more than Alaska and much more than Cascadia, producing a larger depth uncertainty of about  $\pm 10$  km to the top of the plate.

Across a large portion of the Chile Margin, between 27-32°S, the Nazca Plate dips

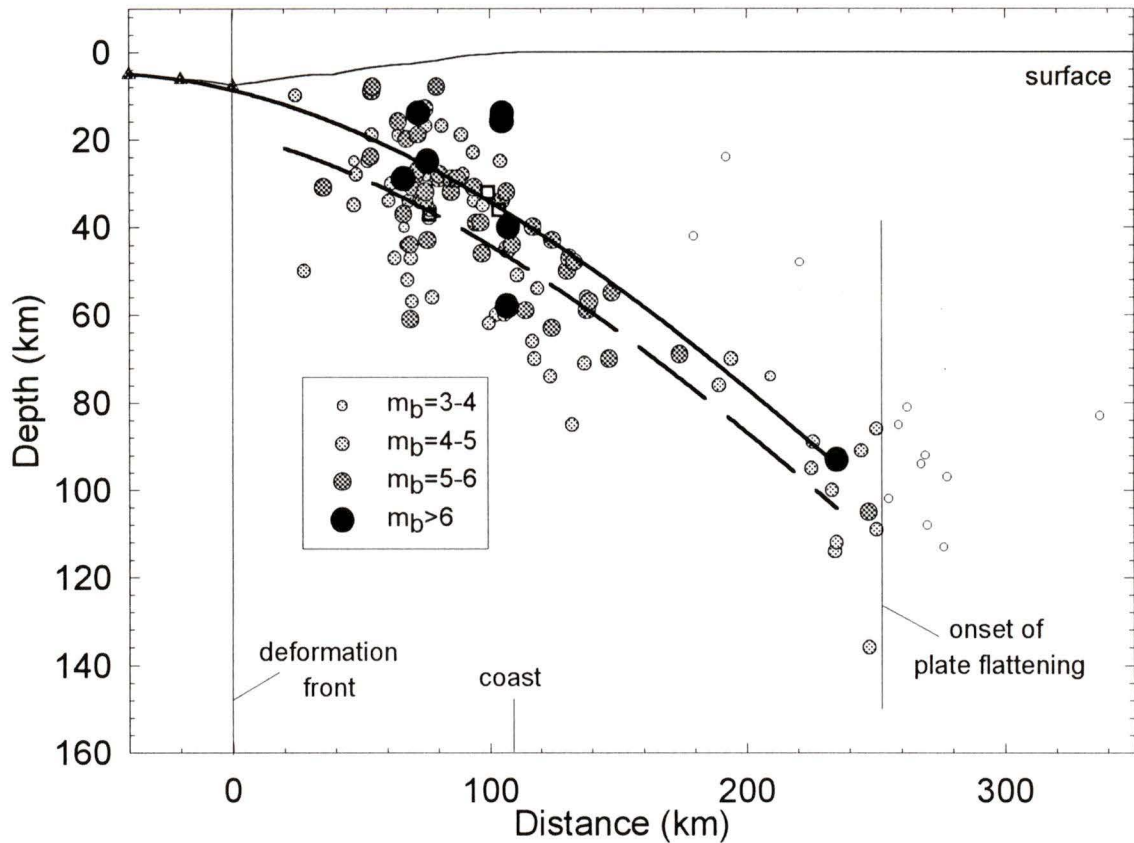


Figure 3.11. Dip profile geometry for Taltal profile. Symbols are as given in Fig. 3.10. The onset of plate flattening is defined by Wadati-Benioff seismicity and from subducting plate behaviour arguments (e.g., Cahill & Isacks [1992]). VE:1.5:1.

change drastically at about 100 km depth, flattening to shallow angles of 4-5° for roughly 100 km landwards, before resuming steeper values. This region separates the northern and southern regions of uniform dip geometry over the same depth interval, and coincides with an absence of Quaternary volcanism along the Andean magmatic arc (Barazangi & Isacks, 1976; Bevis & Isacks, 1984; Cahill & Isacks, 1992; Fuenzalida et al., 1992; Norabuena et al., 1994; Tichelaar & Ruff, 1991; Tichelaar & Ruff, 1993; Araujo & Suarez, 1994). Although well removed from the area of study, events landward of the onset of plate flattening were rejected to avoid affecting the regression fit describing the shallower dip profile (e.g., Fig. 3.11 & 3.12).

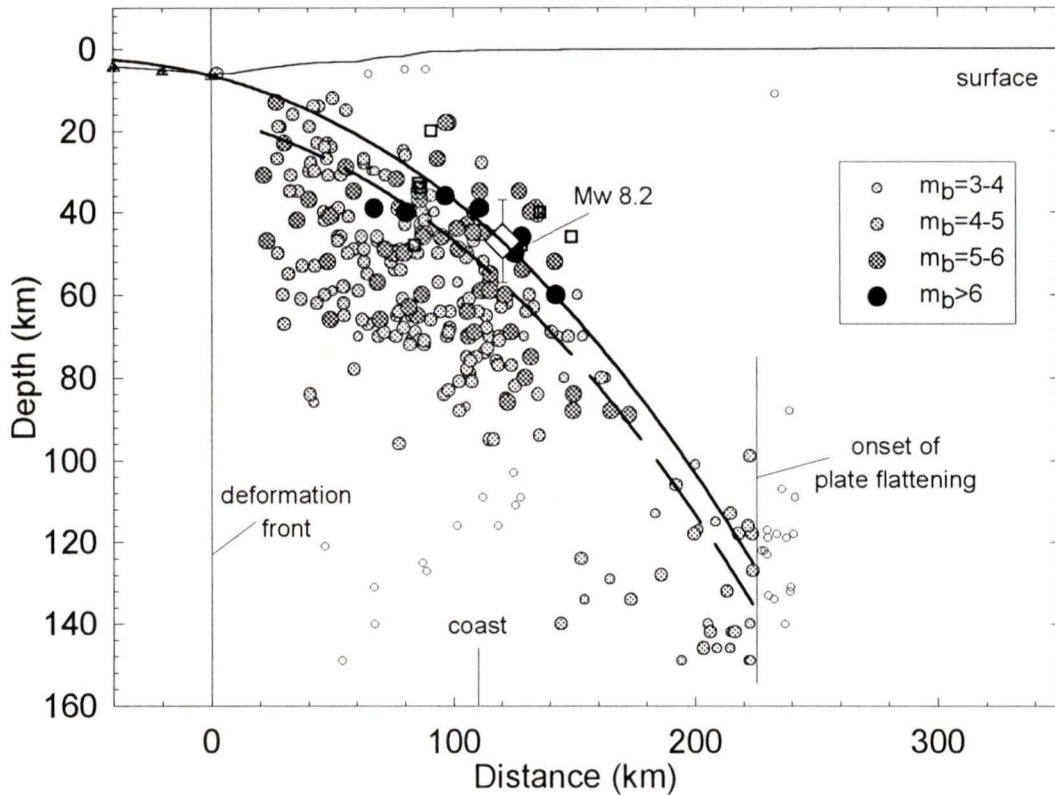


Figure 3.12. Dip profile geometry for Coquimbo profile. Symbols are as given in Fig. 3.10. Main thrust event for 1943  $M_w$  8.2 is also shown (large open diamond). VE: 1.5:1.

### Convergence rate & plate age

Nazca Plate convergence rates are 78 mm/yr at 20°S, 84 mm/yr at 35°S (e.g., DeMets et al., 1990), and up to 90-110 mm/yr immediately north of the Chile Triple Junction at roughly 45°S (e.g., Minster & Jordan, 1978; Cande et al., 1987). A rate of 84 mm/yr was used for the North Chile, Taltal, and Coquimbo profiles, while a slightly faster, 90 mm/yr convergence rate was used for the Valparaiso and South Chile profiles. Plate age decreases from 50 to 45 Ma for the North Chile, Taltal, Coquimbo, and Valparaiso profiles respectively (Table 3.3). A sharp decrease in plate age to 20 Ma for the South Chile profile is due to the proximity to the Chile Triple Junction and numerous fracture zones which intersect the Chile Trench.

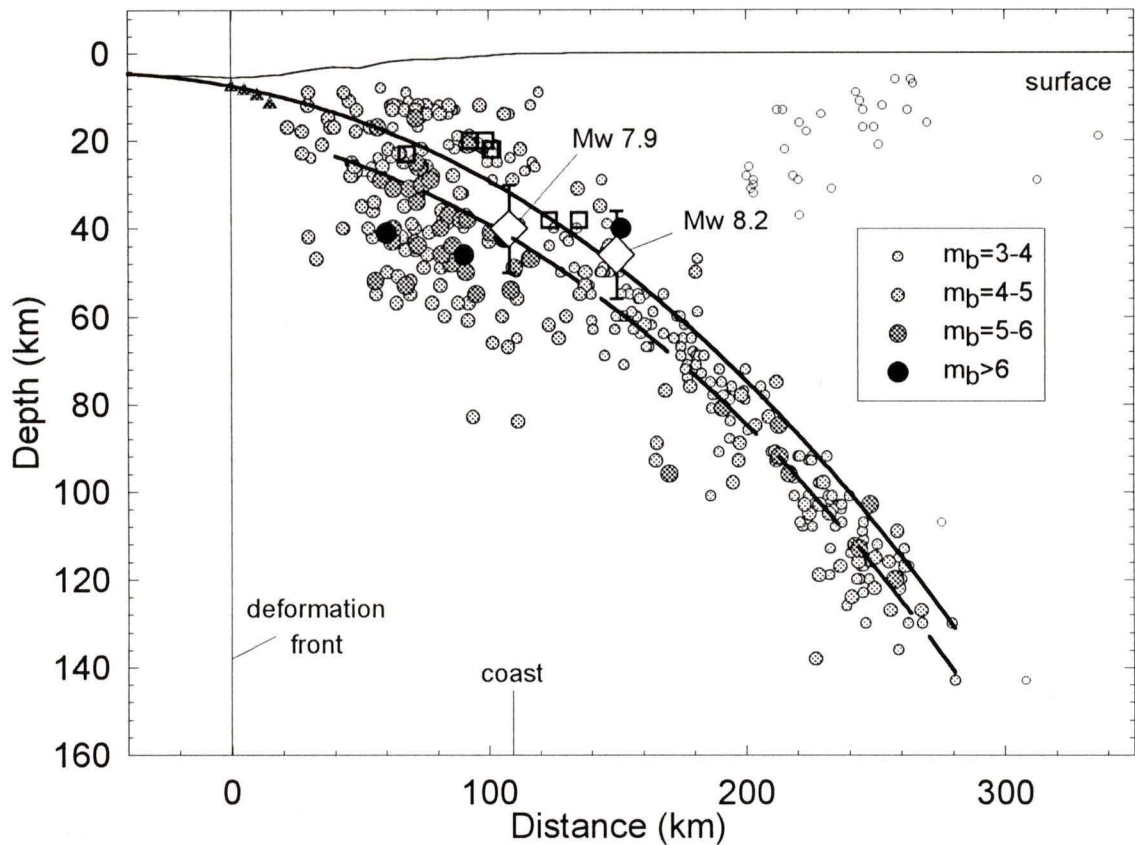


Figure 3.13. Dip profile geometry for Valparaiso. Symbols are as given in Fig. 3.10. Main thrust events of the 1971  $M_w$  8.2 and 1985  $M_w$  7.9 are also shown (large open diamonds). VE:1.5:1.

### 3.7.2 Thermal parameters

#### Thermal conductivity

The conductivity for the accretionary prism is poorly constrained: the only borehole measurements from slope or shelf wells come from ODP 141 near the Chile Triple Junction. However, these measurements are from very near the toe of the accretionary prism, close to the Chile Ridge. A thermal conductivity of  $1.75 \text{ Wm}^{-1}\text{K}^{-1}$  from site 890 was obtained (Behrmann et al., 1992). The conductivity was assumed to increase landward and with depth, and a similar value to that for Cascadia of  $2.5 \text{ Wm}^{-1}\text{K}^{-1}$  was used as the landward limit. The overriding South America Plate was assigned a conductivity value of  $3.0 \text{ Wm}^{-1}\text{K}^{-1}$  (Table 3.4).

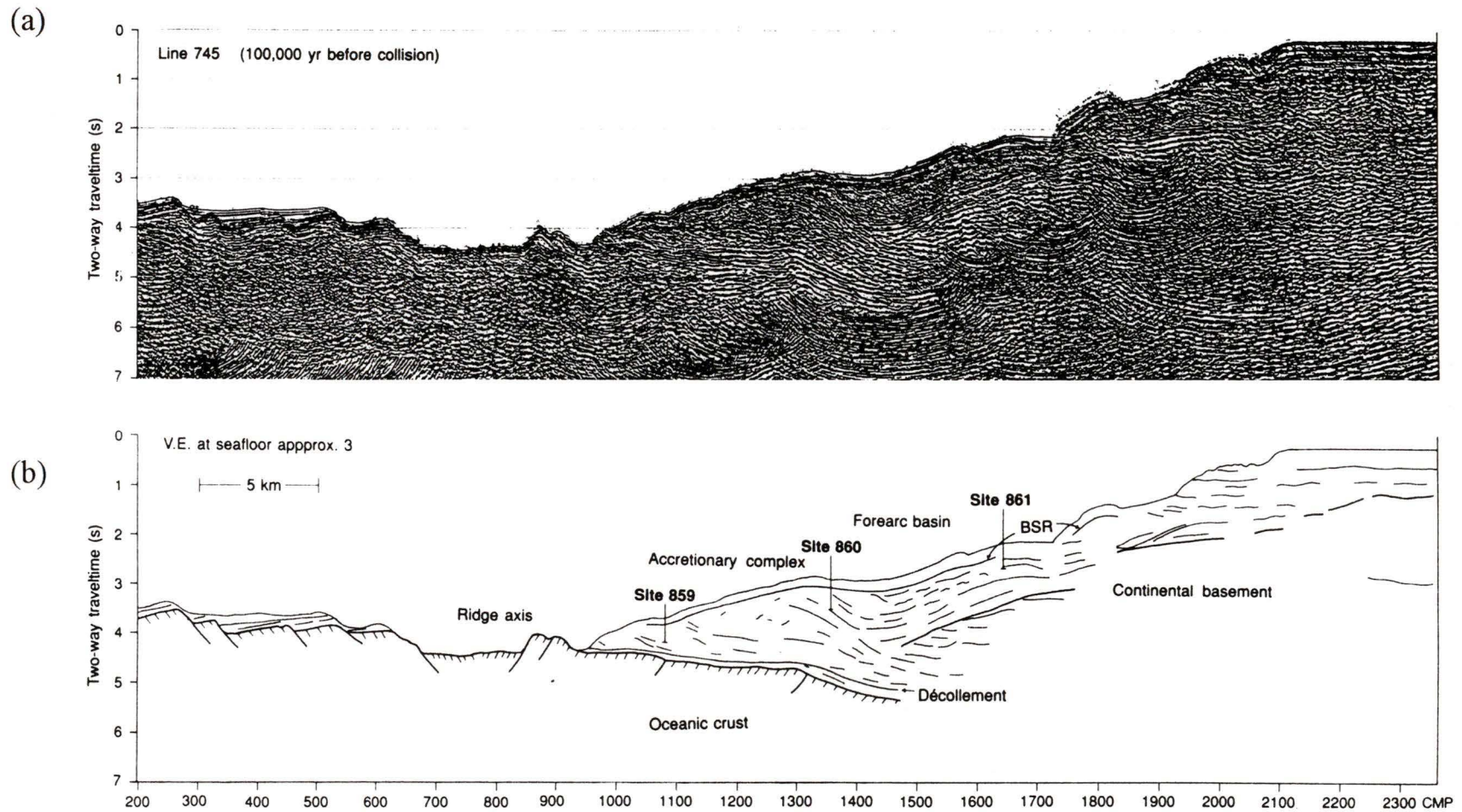


Figure 3.14. Initial dip profile for the South Chile profile, Chile Margin. (a). Seismic reflection data acquired from ODP leg 141. The trace of the top of the plate may be followed roughly 15 km landward of the deformation front. (b). Reflection data interpretation over the same cross-section, showing good constraint to the initial dip profile geometry (after *Berhmann et al.* [1992]).

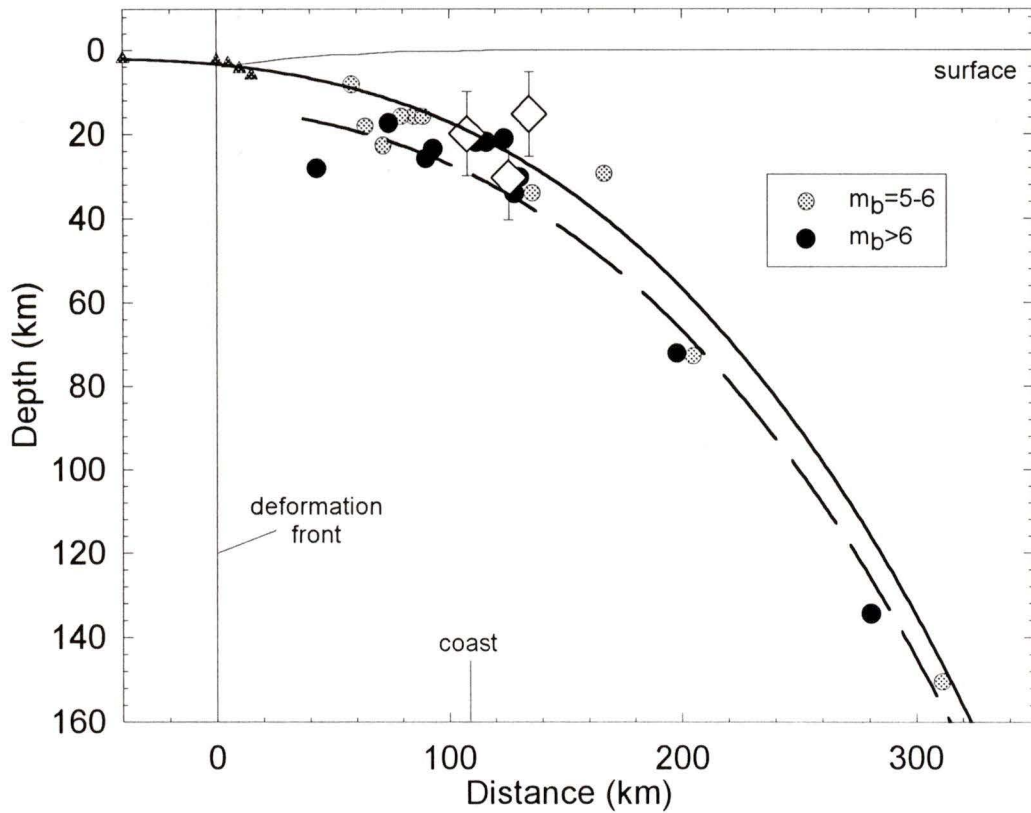


Figure 3.14 (continued) (c). Dip profile for South Chile profile. Geometry is calculated from earthquake distribution after *Barazangi & Isacks* [1976] and from static deformation models after *Plafker* [1972], *Barrientos & Ward* [1990], and *Barrientos et al.* [1992], and seismic reflection data from ODP leg 141 (*Berhmann et al.* [1992]). The three main shocks of the great 1960 event are also shown (large open diamonds). VE:1.5:1.

### Radiogenic heat production

Variation in sediment thickness within the trench from north to south has been proposed as the direct result of the varying sediment supply from continental sources (Thornburg et al, 1990). The plutonic and volcanic rocks that are widespread on the margin have a similar potassium concentration as for the South Alaska coastal Jurassic plutons (Vergara & Munizaga, 1974; Vergara et al., 1995; Reed et al., 1983). As the nearshore plutonic rocks are the dominant geology in the area, a radiogenic heat production for the accretionary prism of  $0.9 \mu\text{Wm}^{-3}$  was used. Onshore analysis of drill hole potassium logs for site 860, ODP leg 141 indicate, however, a slightly lower percent potassium content than

would be expected if derived from the pluton source rocks (Behrmann et al., 1992). However, the log is close to the spreading Chile Ridge, where the trench-fill is much thinner than at the South Chile profile, situated 150 km to the north. As the margin is further complicated by the intersection of fracture zones which may have altered the sediment distribution, the closer plutonic source rock heat generation values were used. The heat generation for the continental rocks as a unit was chosen to decrease linearly from  $1.0 \mu\text{Wm}^{-3}$  at the surface to  $0.2 \mu\text{Wm}^{-3}$  at 10 km depth.

### **3.8 NANKAI**

This section reviews the constraints applied to the thermal models from previous work by Hyndman et al. (1995) and Wang et al. (1995b). No new modelling has been done, but this margin is included for comparison to the other margins of this study.

#### **3.8.1 Non-thermal parameters**

##### **Sediment accumulation rate & prism structure**

The sediment accumulation rates for Nankai are more complicated due to the presence of the fossil ridge within the Shikoku Basin and to the complex history of convergence of the Philippine Sea Plate. The sedimentary section being deformed in the Nankai Trough consists of a Miocene hemipelagic sequence roughly 500 m thick of Miocene age which accumulated at an estimated rate of 0.025 mm/yr. This underlies a younger, 1000-1500 m thick terrigenous sediment wedge, which accumulated at a rate of 0.04 mm/yr from Pliocene to present (Moore et al., 1990; Taira et al., 1991). For Nankai, the thermal model was modified to account for the change in subducting plate age with time as the incoming plate age changing with time affected the thermal model results more than small variations in sediment blanket thickness at the deformation front (see details in Wang et al., 1995b).

The accretionary prism has a gentle taper from the deformation front to the coast. This pattern was formed by off-scraping much of the incoming sediment section with an older Cretaceous to Miocene accreted wedge acting as a backstop (Taira, 1988; Taira et al., 1991). As indicated by landward dipping thrust faults, most of the present shortening of the prism

is occurring over the seaward few 10's of kilometres. For the thermal model, the prism is assumed to increase in thickness from 1.2 km at the deformation front to 15 km thick roughly 100 km landward. The Cretaceous to Miocene accreted sediments are taken to increase further to 20 km thickness at 130 km landward of the deformation front. The top surface of the finite element mesh is taken from multichannel seismic reflection data across Nankai (Moore et al., 1990)

### **Plate dip profile**

Multichannel shallow seismic reflection data across the Nankai Trench were collected in site surveys for ODP leg 131 (Taira et al., 1991). Excellent reflection data define the top of the oceanic crust dipping gently over 20-30 km landwards from the deformation front (Moore et al., 1990). As in the other profiles, the décollement was assumed to coincide with the top of the subducting plate, although it may be higher for the outermost 25 km section (Fig. 3.15a). Over this latter region, both the Tonankai and Nankaido profiles were assigned the same initial geometry (Fig. 3.15b).

Farther landward, the oceanic plate was defined by Wadati-Benioff seismicity (Hirahara, 1981; Ito, 1990). The subduction thrust was taken to be about 5 km closer to the uppermost Wadati-Benioff earthquakes (e.g., Hyndman et al., 1995) than for the South Alaska and Chile margins. The subduction of younger, thinner oceanic crust for Nankai suggests a thinner region within the subducting plate where intraplate earthquakes may occur. The subduction of the Philippine Sea Plate beneath the Eurasian Plate is at a shallower angle for the Nankaido profile than for the Tonankai profile, and it has been argued that warping or tearing may occur between the two segments to accommodate the change in dip (Sato & Matsu'ura, 1992).

### **Convergence rate & plate age**

Deformation within the overriding Eurasian Plate, coupled with extension within the surrounding backarcs bordering the Philippine Sea Plate, makes the interpretation of plate convergence ambiguous (Seno et al., 1993). Most recent estimates place the convergence

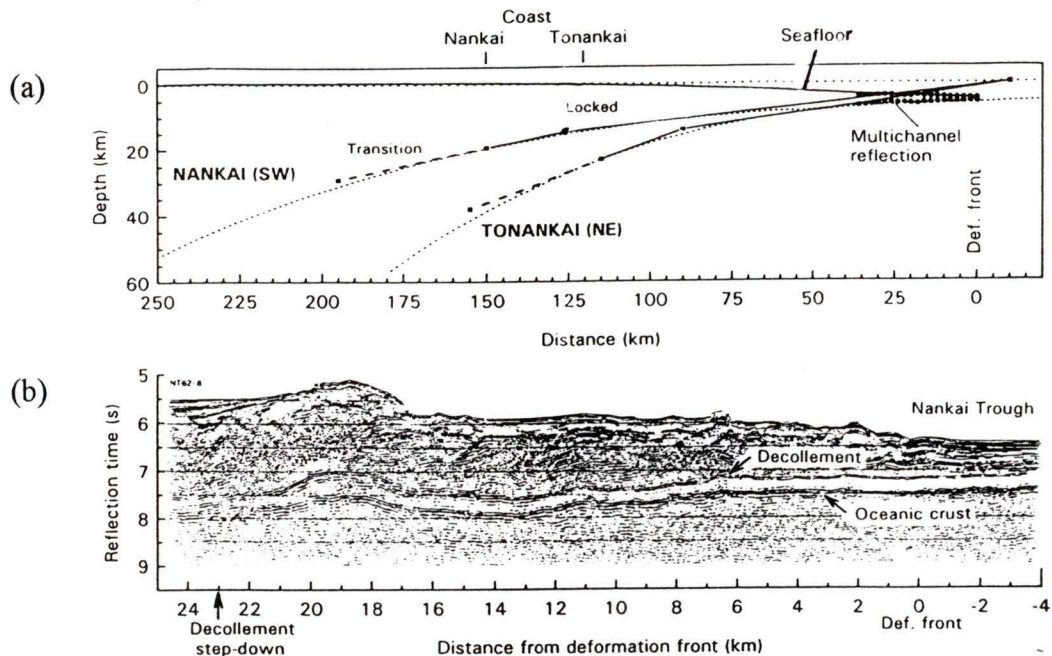


Figure 3.15. Dip profile geometry for Nankai Trough. (a). Multichannel seismic reflection section along the southern Nankaido profile showing clear reflection trace corresponding to the top of the subducting plate. (b). Dip profiles from Wadati-Benioff data (not shown) and from seismic refraction data. The seafloor approximation is also from seismic reflection data (after *Hyndman et al.* [1995]).

between the Philippine Sea Plate and the Eurasian Plate at 43-46 mm/yr (Seno et al., 1993). An average rate of 40 mm/yr was used for modelling purposes (Table 3.3) (e.g., Wang et al., 1995b).

The plate age is also difficult to constrain as the submarine fossil spreading ridge separating the Shikoku Basin is being subducted. Spreading of the ridge is believed to have ceased at about 15 Ma, at which point the subducting plate southeast of the Nankai Trough increased in age from 0 to the present 15-17 Ma (Table 3.3) (Hibbard & Karig, 1990). Wang et al. (1995b) apply a time-dependent boundary condition at the seaward end of the model to the steady state thermal model to accommodate the ageing Philippine Sea Plate.

### 3.8.2 Thermal parameters

#### Thermal conductivity

The average thermal conductivity of the accretionary prism is slightly higher than for the other margins discussed in this study. Values of  $2.0 \text{ Wm}^{-1}\text{K}^{-1}$  were chosen at the seaward

toe of the prism and  $2.5 \text{ Wm}^{-1}\text{K}^{-1}$  at a distance roughly 90 km farther landward (Table 3.4) (Hyndman et al., 1995). The surface thermal conductivity of the overriding continental rocks, assumed to be  $2.5 \text{ Wm}^{-1}\text{K}^{-1}$  (Kanaya & Ishirara, 1975), was determined mainly from core samples within the Shimanto Belt on Shikoku Island. The thermal conductivity of the subducting Philippine Sea Plate is assumed to be  $2.9 \text{ Wm}^{-1}\text{K}^{-1}$  (Dumitru, 1991).

### **Radiogenic heat production**

The radiogenic heat generation of the accretionary sedimentary prism at its seaward extreme is  $1.9 \mu\text{W m}^{-3}$ , as determined from measurements uranium, thorium, potassium concentrations in ODP drill cores (Taira et al., 1991; Hill et al., 1993). Data on the heat generation of the plutonic rocks along the Shimanto Belt of southwest Japan range from 0.86 to  $2.4 \mu\text{Wm}^{-3}$  (Table 3.4). This is in good agreement with the accretionary prism values, allowing for the porosity difference landward across the accretionary prism (Taira et al., 1991). Hyndman et al. (1995) employed an average value of  $1.9 \mu\text{Wm}^{-3}$  for the upper 10 km of the continental crust, and an average value of  $0.4 \mu\text{Wm}^{-3}$  for the lower crust from 10 to 20 km (Table 3.4).

## CHAPTER IV THERMAL RESULTS

### 4.1 INTRODUCTION

This chapter first discusses the temperature gradient calculated at the deformation front based on the cooling history of the subducting plate and on the sediment accumulation history. Second, the surface heat flow profiles from the models are presented and compared to heat flow data. Third, isotherm plots are presented for each profile cross-section, highlighting the thermally constrained locked and transition zones along the thrust plane. The position and influence of the continental forearc Moho is also included in this discussion. Fourth, plots of the thrust plane temperatures versus distance landward from the deformation front are presented to compare the seismogenic zone widths between margins. These widths will in turn be compared to those predicted by the pattern of inter- and coseismic deformation and other studies described in Chapter 5.

For each model, estimated uncertainties (usually about  $\pm 20\%$ ) are imposed on the thermal and non-thermal parameters important to the model, and the effect on surface heat flow and thrust plane temperature determined. It was found that the model was most sensitive to the plate age, the dip geometry, and to the frictional heating. Results for these parameters are presented graphically.

### 4.2 CASCADIA

#### 4.2.1 Thermal model results

##### Temperature-depth profiles

The 1-D thermal model calculation based on the cooling rate of the oceanic crust and the sediment accumulation rate gives the temperature versus depth curves shown in Figure 4.1. Curves are labelled with the age of the subducting crust. The subducting crust for the Vancouver Island profile is the youngest for the models, and has a slightly higher temperature gradient compared to the Olympic Peninsula, Columbia River, and middle-Oregon profiles. As we are concerned with the top 20-30 km of the gradient, this difference is important in the estimate of the seaward limit of the seismogenic zone.

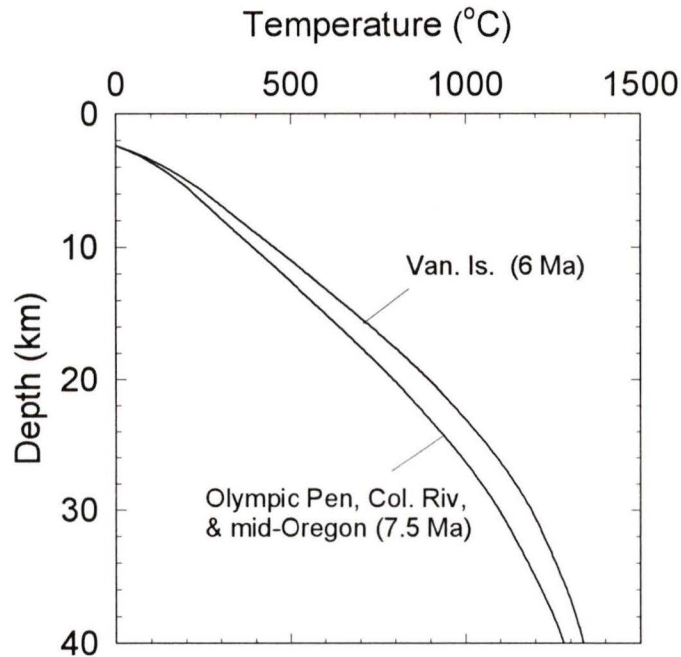


Figure 4.1. Temperature versus depth from the 1-D temperature gradient profile calculated at the deformation front based on sedimentation rate and cooling history of the subducting plate. Initial temperatures are slightly higher for the younger material subducting beneath Vancouver Island.

### Surface heat flow data

From the 2-D model, we may obtain surface heat flow profiles which may be compared to observed surface heat flow data. For the Vancouver Island profile, model surface heat flow decreases from  $120 \text{ mWm}^{-2}$  near the deformation front, to  $60 \text{ mWm}^{-2}$  over the continental shelf, to  $45 \text{ mWm}^{-2}$  at the coast (Fig. 4.2a). This heat flow profile is compared to heat flow data offshore Vancouver Island in the deep sea basin and on the continental slope (Davis et al., 1990), and to continental shelf exploratory well and land borehole heat flux data (Lewis et al., 1988; Lewis, 1990; summary in Hyndman & Wang, 1993; Wang et al., 1995a). Errors estimated for these measurements are  $\pm 20\%$  ( $\pm 30 \text{ mWm}^{-2}$ ) in the marine data, and between  $\pm 10\%$  and  $15\%$  ( $\pm 5$  to  $10 \text{ mWm}^{-2}$ ) for the land data. The larger uncertainty in the marine data is due to the shallow penetration of slope sediments, i.e., 1-3 m, compared to land boreholes, i.e., 200-500 m (Davis et al., 1990), and to the poor quality temperature and thermal conductivity data in shelf wells. The error bars are omitted for clarity. There are also

borehole heat flow measurements on the mid-continental slope from ODP leg 146, sites 889 and 890 (Fig. 4.2a) (Westbrook et al., 1994). A thermally controlled gas-hydrate reflector, i.e., bottom simulating reflector or BSR, also allows heat flow estimation (Hyndman et al., 1993). The BSR heat flow data has errors between  $\pm 15\text{-}20\%$  due to uncertainties in the hydrate stability fields and in the properties of the sediments above the reflector (see discussion of Hyndman et al., 1993). Both the ODP and BSR heat flow data have been corrected for fluid expulsion effects (Wang et al., 1995a).

Marine heat flow values off Washington was determined from shallow penetrating probe measurements by Langseth & Hobart (1984) and Shi et al. (1988), while southern Washington and Oregon marine heat flow data come from Korgen et al. (1971) and Trehu et al. (1994) (Fig. 4.2b). ODP leg 141, site 892 is also allows heat flow estimation (Westbrook et al., 1994). Land data for Washington and Oregon come from the Decade of North American Geology (DNAG), volume of North American heat flow (Blackwell et al., 1989). All the southern offshore data for Washington and Oregon have been projected onto a single profile around  $46^\circ\text{N}$  as there is inadequate data to resolve variations along the margin associated with variations in the subducting plate dip geometry.

### **Low conductivity/radiogenic heat generation terranes**

The pronounced drop in the predicted surface heat flow along the margin marks the seaward edge of the low thermal conductivity and very low radiogenic heat generation of the Crescent/Siletz Terrane (Fig. 4.2). Although the modelling approximation of the terrane may somewhat enhance the surface heat flow change, the region of lower surface heat flow does correspond to observed lower heat flow for the middle-Oregon, Columbia River, and Vancouver Island profiles (Fig. 4.2a & b). The latter profile also incorporates the effects of the Pacific Rim Terrane, but owing to its smaller dimension has a smaller thermal conductivity contrast, and the effect is less pronounced. Compared to the surface heat flow of Hyndman & Wang (1993) which used a more detailed finite element model, a slightly accentuated surface heat flow change associated with the Crescent/Siletz Terrane is observed, but otherwise matches their results very well. This shows that a uniform finite element mesh

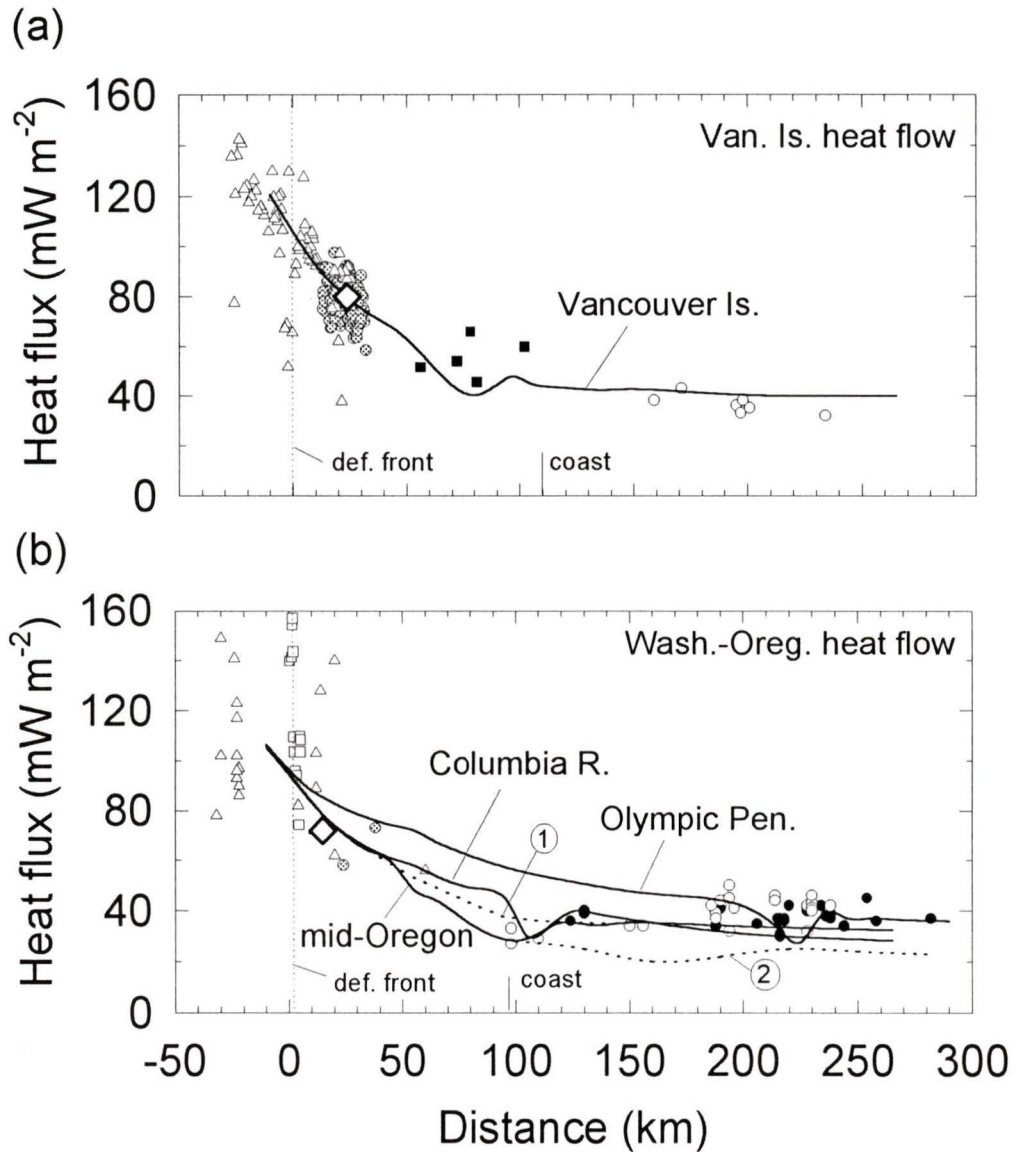


Figure 4.2. Heat flow data compared with predicted heat flow from thermal models for profiles along the Cascadia Margin for: (a) Vancouver Island; and (b) Olympic Peninsula, Columbia River, and mid-Oregon. Dashed lines are the predicted heat flow curves for the mid-Oregon profile for no terrane (labelled "1"), and for terrane extension landward to the Cascade Mountains (labelled "2"). Errors on the heat flow values for the marine data are roughly  $\pm 15\%$ , and  $\pm 5\text{-}10\%$  for the land borehole data. The BSR and ODP heat flow data have been corrected for fluid expulsion effects as given by Wang *et al.* [1995a]. Error bars are excluded to avoid confusion for the tightly spaced data sets. Symbols are as follows: for (a) - marine probe data (open triangles) after Davis *et al.* [1990], BSR data (grey circles) after Hyndman & Wang [1993], ODP Site 889 & 890 (large open diamond) after Westbrook *et al.* [1994], shelf wells (solid squares) and land boreholes (open circles) both after Lewis *et al.* [1988]; for (b) - marine probe data (open triangles & squares) after Shi *et al.* [1988] & Langseth & Hobart [1984] respectively, BSR data (grey circles) after Trehu *et al.* [1994], ODP Site 892 (large open diamond) after Westbrook *et al.* [1994], and land bore hole data for Washington (solid circles) and for Oregon (open circles) after Blackwell *et al.* [1989].

may adequately represent the underlying structures for a given profile. Finally, for the Olympic Peninsula profile, the terrane is located well landward and shows a similar drop but is less well constrained (Fig. 4.2b).

### **The effects of a shallow dipping plate**

The difference in the model surface heat flow for the Olympic Peninsula profile relative to the other 3 Cascadia profiles is mainly a result of the more gentle dip of the plate for the Olympic Peninsula profile (Fig. 4.2b). A higher temperature gradient exists above the subducting plate as it descends more gradually than for a steeply dipping plate. The downward component of convective heat transport is consequently less, and the surface heat flow is higher (Hyndman & Wang, 1995). Unfortunately, there is no heat flow data offshore or onshore the Olympic Peninsula to test the model prediction.

### **4.2.2 Temperature fields**

The preferred model temperature contour or isotherm plots for each profile for Cascadia, showing the locked zone, transition zone, and continental Moho depth, are shown in Figure 4.3. For the subduction of the young Juan de Fuca plate, the temperature limits of 350°C and 450°C are reached at relatively shallow depths, well above the depth of the Moho, located at 36-40 km depth beneath the Strait of Georgia (Cassidy, 1995). Thus, the seismogenic zones along the entire margin are believed to be thermally controlled. The widest seismogenic locked zone is for the Olympic Peninsula profile, and the narrowest is for the Vancouver Island profile (Fig. 4.3). The high temperature Cascade Volcanic Arc is not included in these models as it occurs well landward of the narrow seismogenic zones.

The temperatures along the four profile thrust planes may also be plotted as a function of distance landward from the deformation front, divided downdip into the four regions presented in Chapter 1: a seaward stable-sliding zone downdip until 100-150°C; an unstable, stick-slip locked zone from 150°C to 350°C; a stable sliding transition zone from 350°C to 450°C; and a landward plastic flow regime above 450°C (Fig. 4.4). As the initial thrust plane temperatures are very high for the Juan de Fuca plate, the onset of the locked zone is taken

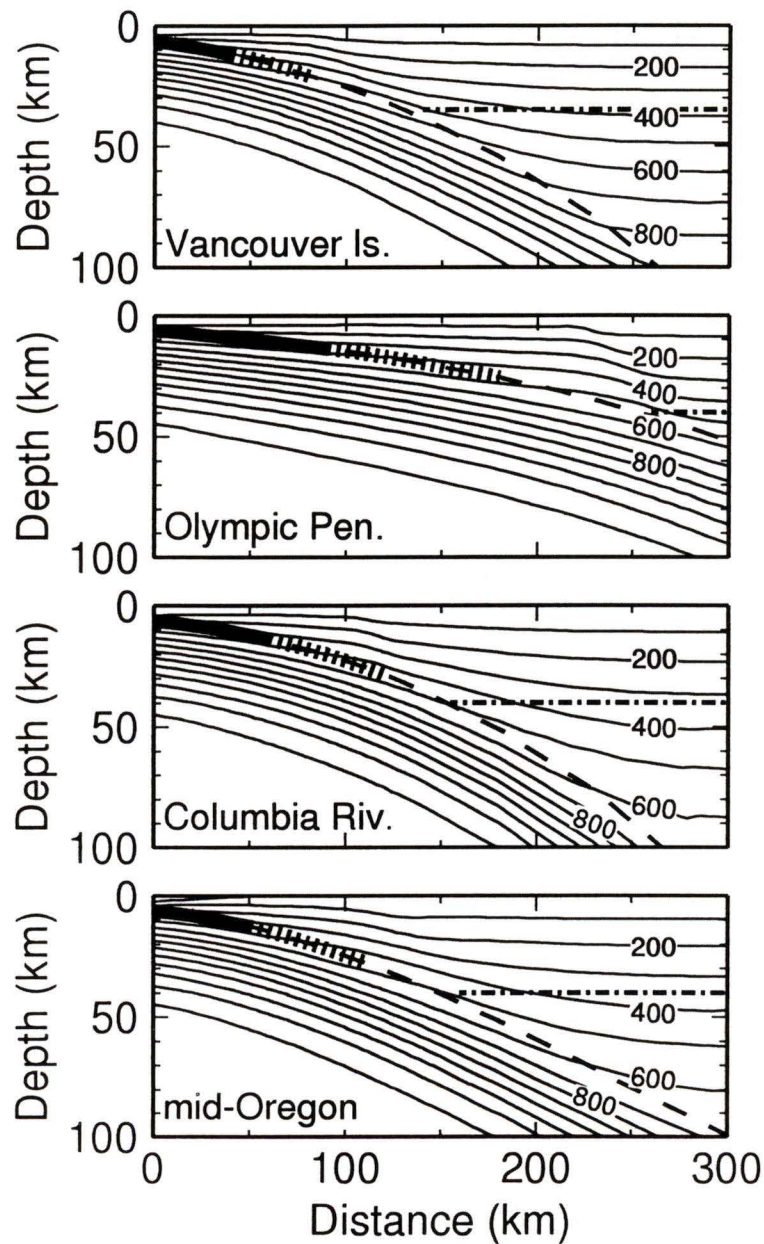


Figure 4.3. Temperature contours (isotherms) of the preferred models for the four profiles along the Cascadia Margin. The thermally constrained locked (solid thick line) and transition (broken thick line) zones are estimated from where the thrust plane (broad dashed line) crosses the 350 and 450°C isotherms. The continental Moho (horizontal dash-dot lines) intersection with the subducting plate is shown for each profile. Isotherms are given in 100°C intervals. Distance is landward from the deformation front.

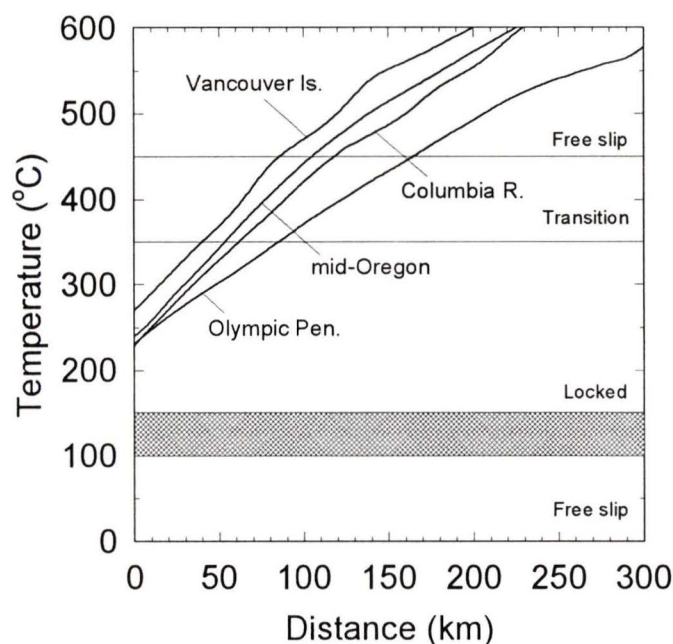


Figure 4.4. Model temperatures on the subduction thrust plane versus landward distance from the deformation front. The downdip limits of 100-150 (shaded area), 350, and 450°C correspond to the seismogenic thermal constraints developed in Chapter 3.

to be very near, i.e., within 10 km, of the deformation front (the 100-150°C boundary is included for comparison to the other margins). The Vancouver Island profile, although similar in dip geometry and incoming sediment thickness to the Columbia River and mid-Oregon profiles, has highest initial temperature and thrust plane temperatures for the entire margin because of the ~1 Ma younger plate (Fig. 4.4). The Olympic Peninsula profile has the lowest thrust plane temperatures due to the gentle plate dip as discussed above. Slight variations in the thrust plane temperatures are in part due to the presence of the Crescent/Siletz Terrane which extends down close to the thrust plane and affects the heat transfer process between the prism sediments and the subducting plate.

#### 4.2.3 Uncertainty analysis

The predicted surface heat flow curves and thrust plane temperatures are sensitive to a number of model parameters described previously. Error analysis is provided to show how

the positions downdip of 350°C and 450°C change with a range of values. Only the uncertainty analysis for the plate age and dip profile, which affected the model most significantly, are presented graphically for Cascadia only. The errors constrained by the abundant surface heat flow data for Cascadia are expected to be similar for the profiles across the other margins. The analysis for the remaining parameters is quoted in the text.

### **Non-thermal parameters**

The effect of variations of the non-thermal parameters (the convergence rate, the sediment thickness at the deformation front, the plate age, and the thrust plane dip profile) were examined. The error analysis was done for each parameter independently, and the combined error from all the parameters is estimated to be about  $\pm 20$ -25 km on the location of both 350 and 450°C thermal limits.

Convergence velocities varying by  $\pm 40\%$ , between 24 mm/yr and 56 mm/yr, give surface heat flow changes of  $\pm 3$  mWm<sup>-2</sup> and a shift of  $\pm 5$  to 10 km for the 350°C limit. The model heat flow profile shape across the area of interest remains very similar to the preferred model.

Changing the thickness of the insulating sediments directly affects the initial 1-D temperature profile calculated at the deformation front. Thinner sediment cover translates into a more rapid cooling of the upper oceanic plate prior to subduction. Changes of  $\pm 20\%$  or roughly 600 m of the thickness of trench-fill sediment produces negligible effects to the surface heat flow, less than  $\pm 2$  mWm<sup>-2</sup>, with a change to seismogenic widths of  $\pm 5$  km.

Variations in subducting plate age of  $\pm 25\%$  produced a  $\pm 10$  mWm<sup>-2</sup> variation at the seaward end of the predicted heat flow profiles, decreasing to less than  $\pm 5$  mWm<sup>-2</sup> variation at the landward end (Fig. 4.5a). The scatter in available surface heat flow data covers this range. However, the changes to the temperatures along the thrust plane are much greater. An age uncertainty of  $\pm 25\%$  corresponds to  $\pm 25$  km and  $\pm 40$  km changes in the position of the downdip limit of the locked and transition zones respectively (Fig. 4.5b).

Variations in the thrust dip angle were produced by multiplying the coefficients to the regression fit for each profile by a factor of  $\pm 20\%$  (Fig. 4.6). This translates into depth

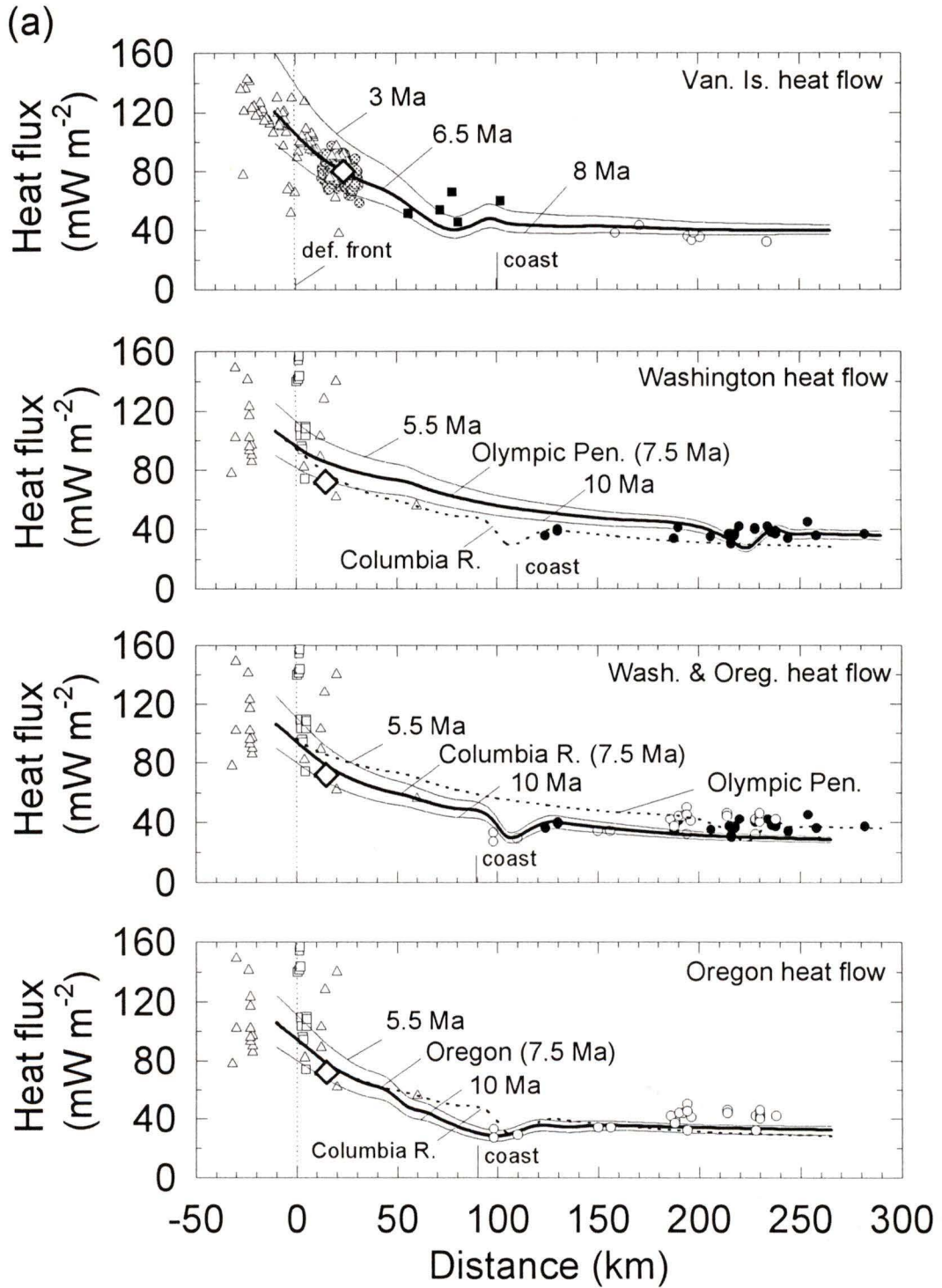


Figure 4.5. (a). Heat flow data for the Cascadia Margin compared to the predicted heat flow from the thermal model for each profile over a range of  $\pm 25\%$  of the preferred subducting plate age. The preferred model is shown in the heavy line for each profile. The drop in the surface heat flow profiles with increasing age for a given sediment blanket thickness at the deformation front reflects the cooler nature of the subducting plate, and consequently lower initial thrust plane temperatures. Symbols are as given in Figure 4.2.

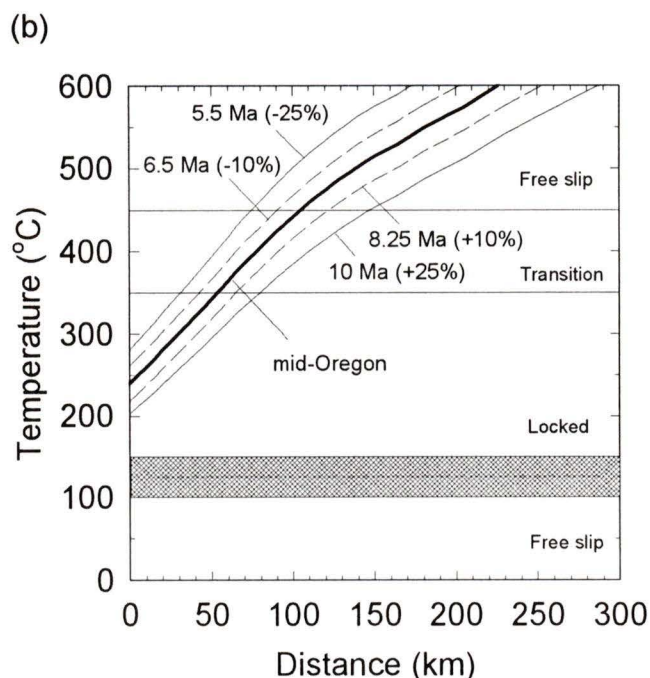


Figure 4.5 (continued) (b). The thrust plane temperatures for the mid-Oregon profile. The  $\pm 10\%$  plate age uncertainties (thin lines) demonstrate the sensitivity of the model to a small change in plate age (preferred model-heavy line). The  $\pm 10\%$  uncertainty translates into width differences of  $\pm 10$  km and  $\pm 25$  km for the locked and transition zones respectively; the  $\pm 25\%$  uncertainty translates into  $\pm 25$  km and  $\pm 40$  km respectively.

changes of roughly  $\pm 10$  km, 60 km landward of the deformation front. This is a reasonable uncertainty limit as the dip profile geometry is well constrained for the northern profiles by numerous Wadati-Benioff earthquakes, i.e., within 10 km depth location (Rogers, 1988; G. Rogers, personal communication, 1996), and by shallow seismic reflection data, i.e., within 100-200 m for good velocity two-way traveltimes conversions (Spence et al., 1991a; 1991b).

### Thermal parameters

In addition to the main physical parameters, the sensitivity of the thrust temperatures to the thermal properties were also tested for the accretionary prism, the continental crustal rocks, and the oceanic crust. The thermal properties of the overriding low thermal conductivity structures (volcanic terranes) were also investigated.

The effect of varying the radiogenic heat production for the prism sediments by  $\pm 30\%$

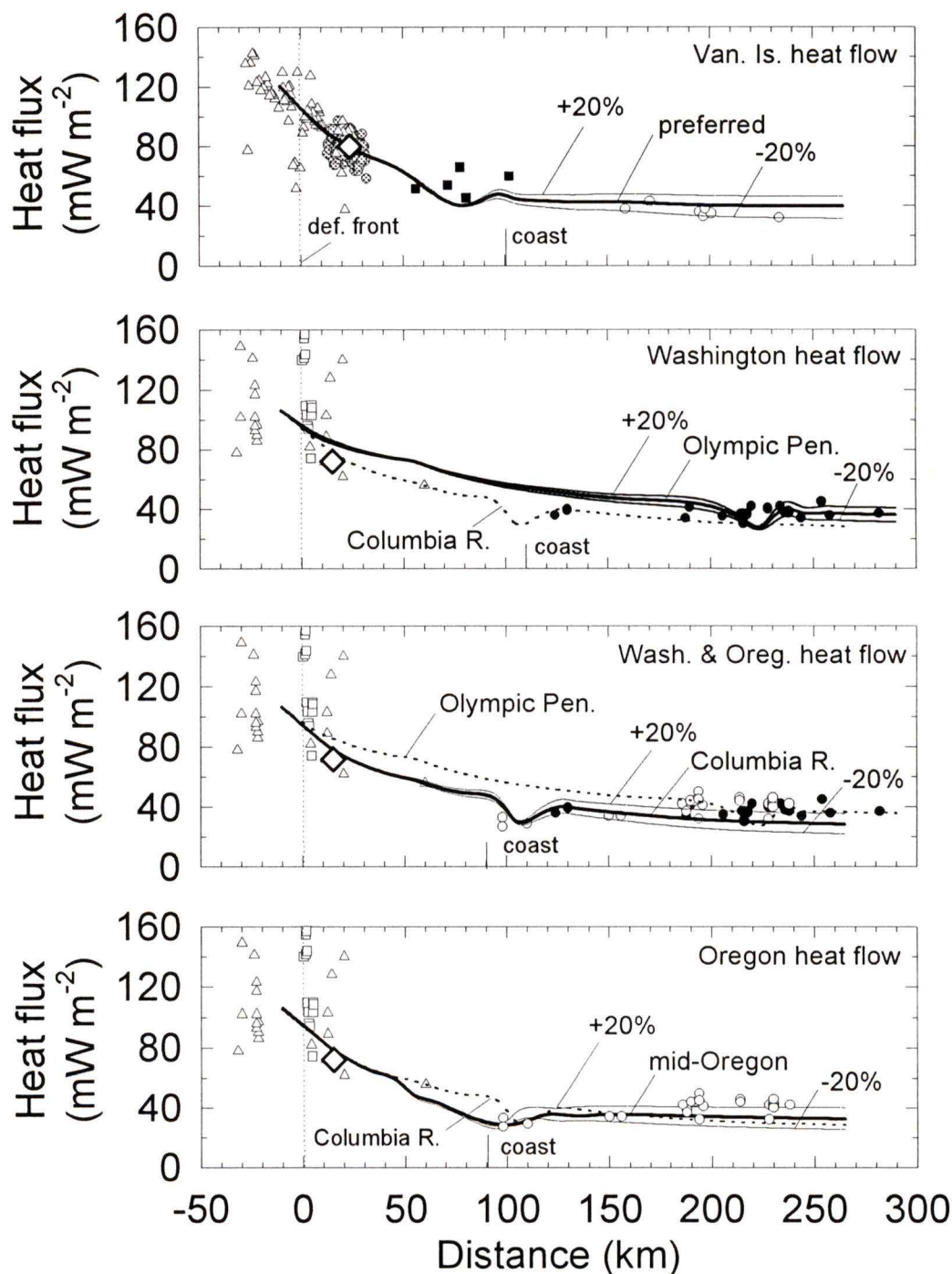


Figure 4.6. Heat flow data for the Cascadia Margin compared to the predicted heat flow from the thermal model for each profile over a range of  $\pm 20\%$  of the preferred dip profile geometry, which translates into roughly  $\pm 10$  km thrust plane depth uncertainty at the  $350^\circ\text{C}$  thermal limit. The preferred model is shown in the heavy line for each profile. Whereas the plate age variance in Figure 4.5 mainly affects the heat flow profiles near the deformation front, changes in dip geometry affect regions closer to the seismogenic zones and further landwards. For this reason, it is one of the most important constraints to the thermal model. Symbols are as given in Figure 4.2.

from the preferred value of  $0.6 \mu\text{Wm}^{-3}$  has only a small effect on the surface heat flow, less than  $\pm 5 \text{ mWm}^{-2}$  and a small change to the computed thrust temperatures and inferred seismogenic width. The effect of varying the conductivity within the prism was examined by changing the range of conductivity values from the deformation front to the continental backstop. Varying the conductivity by  $\pm 30\%$  produces surface heat flow variations of  $\pm 8 \text{ mWm}^{-2}$ , and changes the inferred seismogenic widths by  $\pm 5\text{-}10 \text{ km}$ .

For the landward, overlying continental rock, the model radiogenic heat production decreases with depth over the top 10 km, from  $0.6$  to  $0.1 \mu\text{Wm}^{-3}$ . Varying the upper limit by  $\pm 30\%$  produces surface heat flow variations of  $\pm 5\text{-}6 \text{ mWm}^{-2}$ , with negligible effects on the thrust temperatures and position of the downdip end of the seismogenic zone. The effect of varying the conductivity by  $\pm 0.5 \text{ Wm}^{-1}\text{K}^{-1}$  affects the surface heat flow by  $\pm 5 \text{ mWm}^{-2}$ , but again negligibly affects the thrust plane temperatures.

The effect of varying the thermal of the oceanic plate by  $\pm 0.5 \text{ Wm}^{-1}\text{K}^{-1}$  from the preferred value of  $2.9 \text{ Wm}^{-1}\text{K}^{-1}$  is to change the  $350^\circ\text{C}$  point on the thrust by roughly  $\pm 7 \text{ km}$ . The effect of varying the heat capacity of the oceanic plate by  $\pm 10\%$  or  $\pm 0.3 \text{ MJm}^{-3}\text{K}^{-1}$  from the preferred value of  $3.3 \text{ MJm}^{-3}\text{K}^{-1}$  is negligible. Finally, variations to the slab thickness were examined by allowing only a thin, 15 km thick sliver to subduct between steady state units above and below. This has very little effect on the resulting surface heat flow or thrust plane temperatures.

The importance of the low thermal conductivity Crescent/Siletz Terrane is characterized in two ways: 1. What are the consequences to the surface heat flow and thrust plane temperatures in the absence of the terrane?; and 2. Given that the volcanic terrane is a factor, how important are the thermal properties and dimension assigned to the terrane? The first question was examined by modelling with no terrane. A constant heat production similar to that of the accretionary prism sediments was assigned across the entire profile, with a gradual increase in thermal conductivity from the deformation front to the landward model boundary. The pronounced dip in the surface heat flow profile is absent with little other change in the model heat flow (Fig. 4.2). Some support for the terrane comes from the drop in surface heat flow values in the region of the terrane in Oregon. Secondly, the dimensions

of the terrane were varied to explore the suggestion that the landward extent of the Crescent/Siletz Terrane for the mid-Oregon profile may reach the Cascade Volcanic Arc (e.g., Trehu et al., 1994; A. Trehu, personal communication, 1995). Extension of the terrane to the Cascade arc produced low landward surface heat flow values of less than  $25 \text{ mWm}^{-2}$ . Slightly higher surface heat flow resulted if there was progressive thinning of the terrane with increasing distance landward (Fig. 4.2). However, the model heat flow remains well below the regional average of  $40\text{-}45 \text{ mWm}^{-2}$  for 100 km landward of the volcanic arc. It is thus unlikely that the terrane extends so far inland based on heat flow data.

All the uncertainties listed above account for a total landward distance uncertainty of about  $\pm 20\text{-}25$  km in the position of the  $350^\circ\text{C}$ . For the  $450^\circ\text{C}$  intersection, the variation is similar. An additional source of error comes from laboratory and field measurement uncertainties, estimated to be  $\pm 25^\circ\text{C}$  ( $\pm 10$  km distance along dip), for a total uncertainty of 25-35 km distance landward of the deformation front.

### **Frictional heating**

The addition of moderate frictional heating results in predicted surface heat flow profiles to be higher than the preferred model and a seaward shift in the  $350^\circ\text{C}$  and  $450^\circ\text{C}$  boundaries by 10 km and 20 km respectively (Fig. 4.7a & b). However, the predicted surface heat flow profile is relatively insensitive to frictional heating along the thrust plane, and the surface heat flow data does not provide adequate constraint on whether to include or exclude such heating. Regional coupling stress directions from focal mechanism solutions for earthquakes occurring within continental forearc support low shear stress along the thrust plane for southwestern British Columbia (Wang et al., 1995a). Wang et al. (1995b) suggest similarly low frictional heating for southwest Japan. Although closer to the outer coast, the focal mechanisms might indicate greater coupling between the overriding and subducting plates (e.g., Rogers, 1995), frictional heating was neglected in the preferred model.

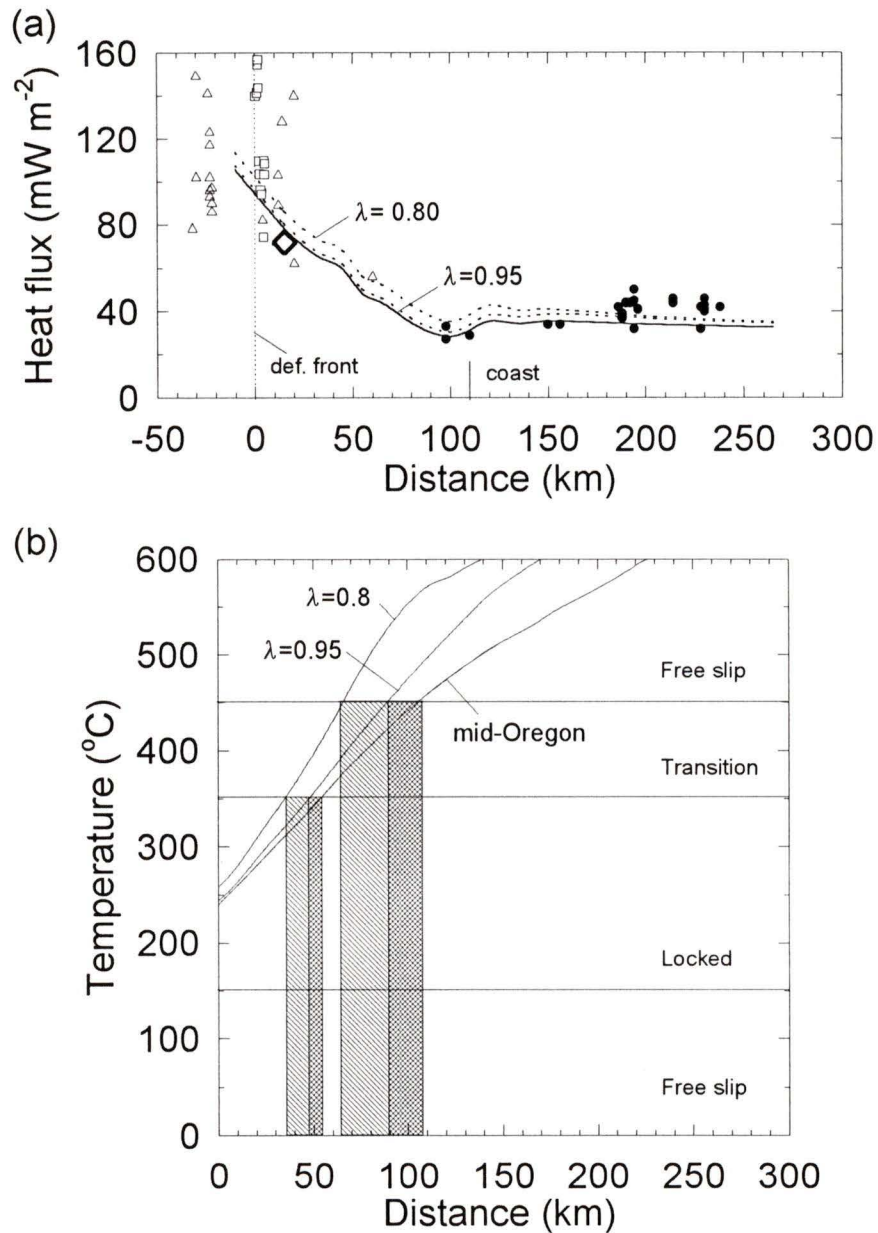


Figure 4.7. The effects of frictional heating for the mid-Oregon profile. (a) Surface heat flow profiles from the preferred model (solid line) and for models including frictional heating along the thrust plane compared with available surface heat flow data. The higher surface heat flow is observed with the low pore pressure ratio given by  $\lambda=0.8$ , which implies a high shear stress. (b) Thrust plane temperatures for the same three models. With high pore fluid pressures, and hence low shear stress given by  $\lambda=0.95$  (cross-hatched fill), the locked and transition zones were narrowed by about 10 and 20 km respectively. The effects are even more accentuated for the lower, more reasonable pore pressure ratio of  $\lambda=0.8$  (diagonal fill), with changes in width on the order of 20 km and 50 km for locked and transition zones respectively.

### 4.3 SOUTH ALASKA & CHILE

#### 4.3.1 Thermal model results

##### Temperature-depth profiles

The results for the South Alaska and Chile margins are presented together because there are limited thermal data and because they have similar plate age and subduction history. Temperature versus depth curves at the deformation front for both margins compared to the mid-Oregon profile, Cascadia Margin, are shown in Figure 4.8. The curves are again labelled according to the plate age at the deformation front. The pronounced differences between the mid-Oregon profile and the South Alaska and Chile profiles are mainly from to the difference in plate age. The Pacific and Nazca plates subducting beneath the South Alaska and Chile margins are much older, and consequently are much colder at the onset of subduction. The

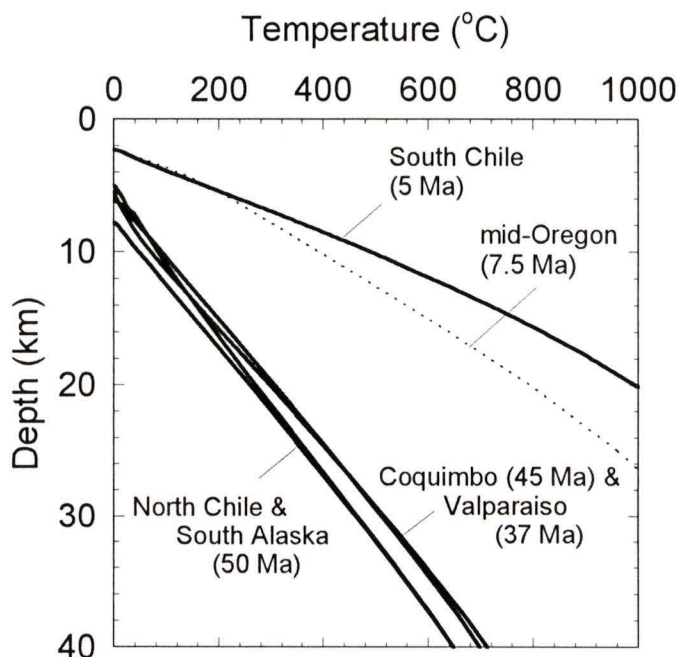


Figure 4.8. Temperature-depth profiles at the seaward boundary of the thermal model for the south Alaska and Chile margins. The South Alaska is most similar in age to the North Chile and Taltal. Differences in the temperature profile are produced by the effects of sediment blanket thickness at the deformation front, over 2 km of sediment for Alaska versus a few hundred meters for North Chile and Taltal. The Coquimbo and Valparaiso profiles are very similar; small differences are caused by variations in sediment thickness. The considerably younger and hotter plate off the South Chile profile produces a considerably more shallow curve, comparable to the young mid-Oregon profile of the Cascadia Margin.

one exception is the South Chile profile being in close proximity to the Chile Triple Junction, where very young crust subducts (~5 Ma). In addition, the South Alaska and northern Chile margins have roughly 1 km less sediment at the trench axis. The greater plate age and thinner sediment blanket for the Taltal and North Chile profiles account for the slightly lower temperature gradients for these profiles within the Chile Margin (Fig. 4.8).

### **Surface heat flow data**

Except for the South Chile profile, low initial thrust plane temperatures translate into low predicted surface heat flow curves for both margins, about 30-40 mWm<sup>-2</sup> near the deformation front, decreasing landwards across the continental shelf to 20-25 mWm<sup>-2</sup> (Fig. 4.9a). The seaward portion of the South Chile heat flow profile is high due to the young age of the plate, and remains slightly higher than the mid-Oregon heat flow to roughly 120 km landward due to the absence of low thermal conductivity and low heat generation terranes (Fig. 4.9b). The slight rise in South Alaska predicted heat flow between 120-180 km is due to the higher heat generation assumed for the seaward portion of the older, Eocene prism. For the South Alaska Margin, there is only one heat flow value within the study area, but it is landward of the volcanic arc (Blackwell et al., 1989). The predicted South Alaska heat flow profile is therefore presented for future reference. The Chile Margin also has limited surface heat flow data, applicable to only the near coast region of the middle two profiles, Valparaiso and Coquimbo (Uyeda & Watanabe, 1982). Encouragingly, the model heat flow profiles bisect the four land borehole values (Fig. 4.9b).

Offshore, regional heat flow data extracted from the depth to the BSR was determined from shallow seismic reflection data from the ODP leg 141, lines 743 & 745 (Lewis et al., 1995). Unfortunately, the complicated tectonic environment associated with the subduction of several fracture zones separates the ODP results from the South Chile profile 150 km to the north. These data thus cannot be used as reliable constraints on the predicted surface heat flow for the model profile, but are instead included as a general, landward decreasing heat flow pattern expected across the outer shelf (Fig. 4.9b).

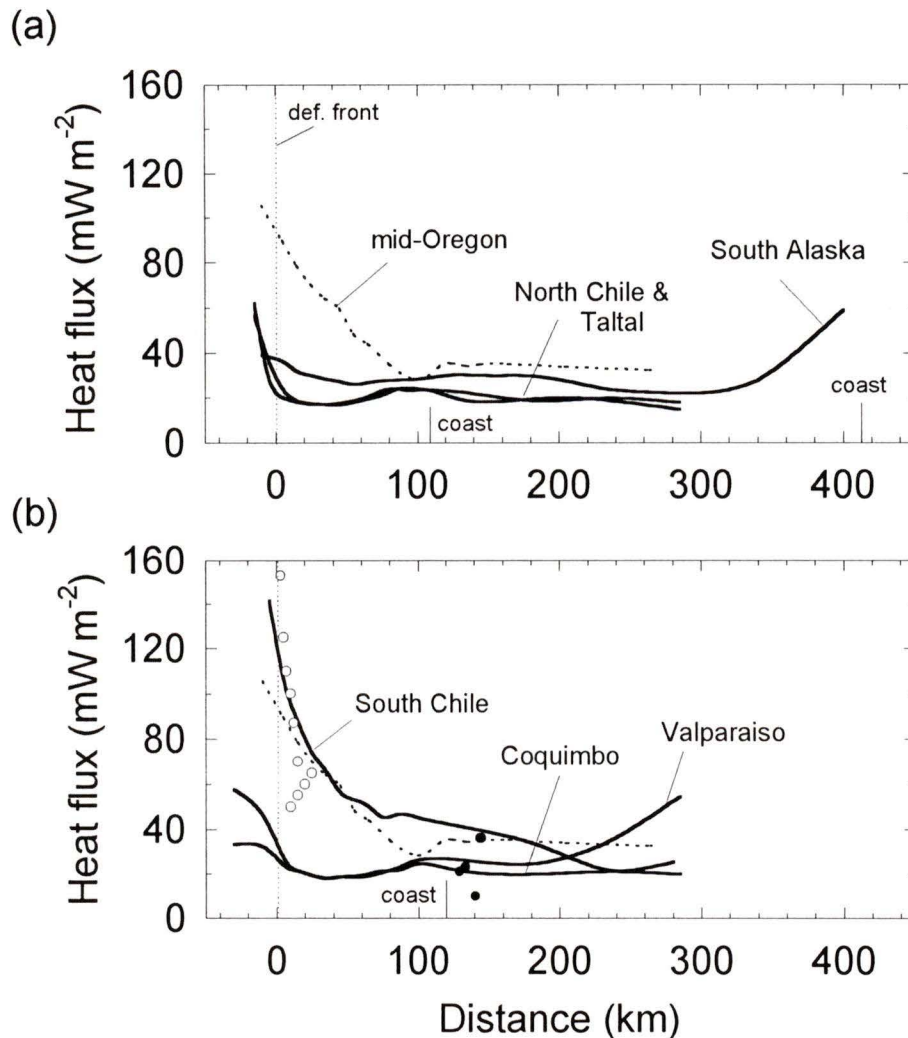


Figure 4.9. Predicted surface heat flow profiles plotted against distance landwards from the deformation front. (a) Similarly aged subducting plates (50 Ma) for the South Alaska and for the two northernmost profiles along the Chile Margin - North Chile and Taltal, compared with the surface heat flow results for the young, hot, mid-Oregon profile presented in Figure 4.2. The low surface heat flow is a result of the very cool Pacific and Nazca plates which subduct beneath South Alaska and Chile margins respectively. (b) Same as (a), but for the southern profiles along the Chile Margin. The slight rise in the South Alaska, Valparaiso and South Chile heat flow profiles is the result of the proximity of the volcanic arc. Observed heat flow from site 860, ODP leg 141 (grey circles) are included for comparison to the model heat flow curves.

### Low conductivity/radiogenic heat generation terranes

Although the South Alaska Margin is one of allochthonous terrane accretion, there is no evidence from the EDGE transect (e.g., Moore et al., 1991) for the existence of any

terrane structures downdip. For the Chile Margin, there is likewise no evidence within the continental crust for large structures with low thermal conductivity or low radiogenic heat generation. For both margins, these effects were therefore omitted.

### **The effect of volcanic arcs**

The sharp rise in model heat flow at the landward end for the South Alaska, Valparaiso, and South Chile profiles is the result of the simplified model representation of the thermal effect of the Aleutian and Andean volcanic arcs (Fig. 4.9a & b). The volcanic arc has the effect of supplying an additional heat to the landward surface heat flow. There is, however, no observed heat flow data to provide constraint. Although this area is landward of the locked and transition zones, it was included on the basis that the volcanic arcs for these two margins are closer to the seismogenic zone than for Cascadia and may be important to the deeper portion along the thrust plane (see next section).

### **4.3.2 Temperature fields**

The isotherm plots for the preferred models along each profile, along with the inferred locked and transition portions of the seismogenic region, are shown in Figure 4.10. The greater age of the subducting plates for South Alaska and Chile indicates that the oceanic plate has low initial temperatures at the deformation front, i.e., 50°C compared to 230°C for Cascadia, moving the seaward limit of the locked zone landward. The downdip thermal limit of 350°C is therefore reached only at very great depths, nearly 100 km (Fig. 4.10). This depth is inconsistent with the maximum depth of aftershocks for the great 1964 Alaska earthquake of about 40 km (e.g., Davies & House, 1979), and to similar aftershock data from other great thrust earthquakes near the Chile profiles (e.g., Plafker & Savage, 1970; Nishenko, 1985; Tichelaar & Ruff, 1991; Araujo & Suarez, 1994). Thus the downdip limit of the seismogenic locked zone is not likely to be thermally controlled.

As discussed above, for older, colder subducting plates, the continental Moho may mark the downdip limit to the locked zone. The Moho intersection with subducting lithosphere is taken to be roughly 40 to 45 km, based on deep seismic refraction

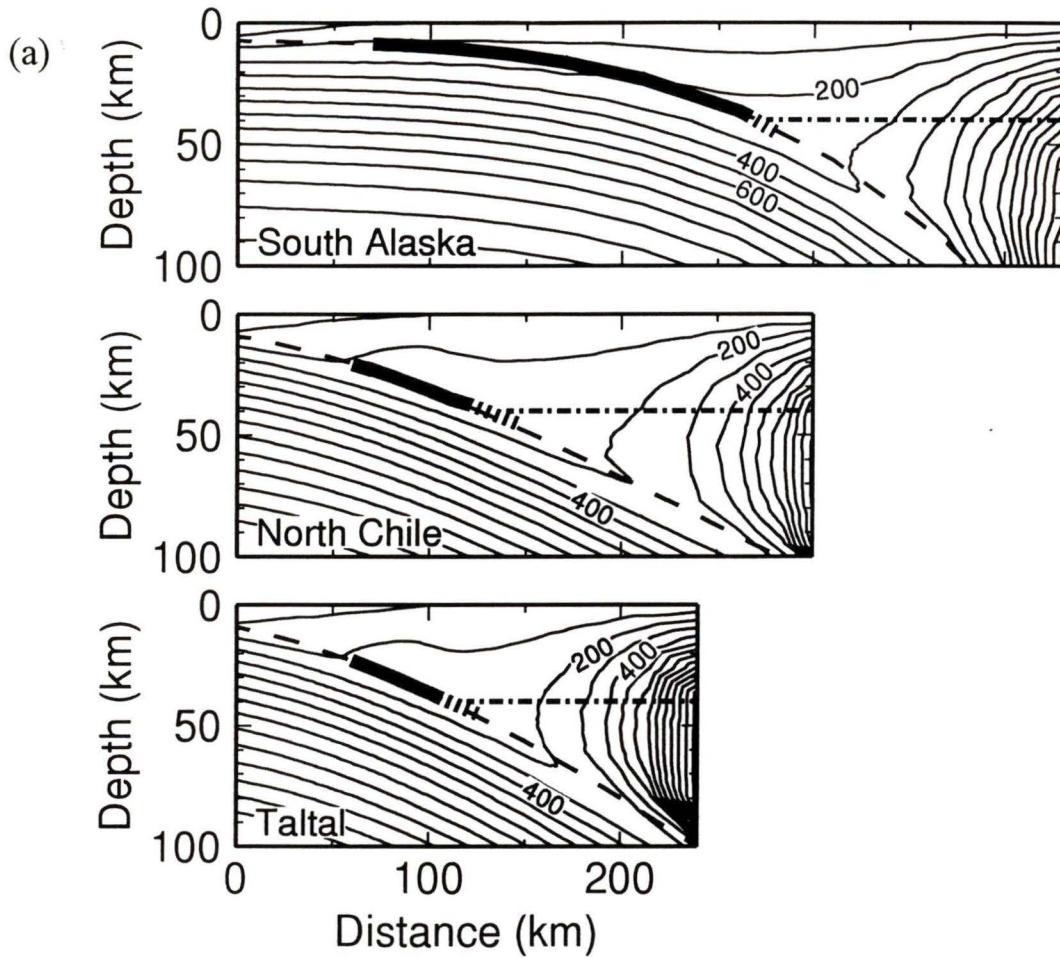


Figure 4.10. Isotherms of the preferred thermal models for the South Alaska and northern Chile margins. (a) Similarly aged subducting plates show considerably different locked zones (thick lines), mainly due to different plate dip geometry: A much more shallow dip profile yields a potentially wider locked zone as with the South Alaska profile, contrasting with the relatively steeply dipping North Chile and Taltal profiles. The transition zone (broken thick line) is taken to straddle the continental Moho (horizontal dash-dot line) by  $\pm 10$  km. The volcanic arcs associated with each margin are included to demonstrate the thermal effect on the downdip portion of the thrust plane (broad dashed line). Isotherms are given in  $100^{\circ}\text{C}$  intervals. Distance is landward from the deformation front.

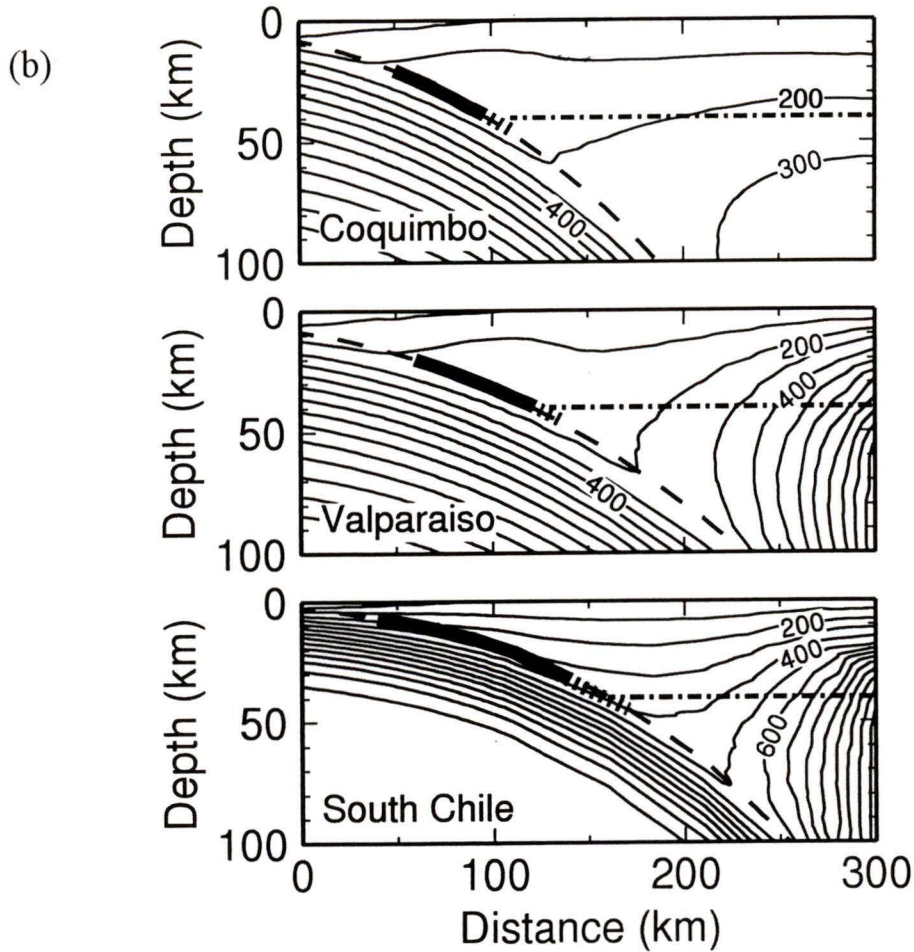


Figure 4.10 (continued) (b). Isotherm plots for the southern three profiles, Chile Margin.

measurements in south-central Alaska (e.g., Page et al., 1989; Fuis & Plafker, 1991; Brocher et al., 1994; Plafker et al., 1994) and in northern Chile (e.g., Scheffels, 1990; Schmitz, 1994; Wigger et al., 1994). The exception to the constraint provided by the Moho for these profiles is the South Chile profile, where the subduction of young oceanic material results in elevated thrust plane temperatures. For this profile, as for Cascadia, the downdip seismogenic limit is thermally controlled.

Taking the base of the crust as the seismogenic cutoff, the locked zone widths vary from 50 km in northern Chile to 60 km in central Chile (Coquimbo and Valparaiso profiles). The similarity of results for the four northern Chile Margin profiles is a consequence of the similarity in plate dip geometry to roughly 100 km depth (Fig. 4.11). Slightly cooler thrust

plane temperatures along the Taltal and North Chile profiles are due to the thinner sediment cover and a 5 Ma greater plate age. The change in convergence rate from 84 mm/yr in the south to 90 mm/yr in the north may also account for the slightly cooler thrust plane temperatures. For South Alaska, the locked zone width is 3-4 times as wide as that for central and northern Chile (Fig. 4.11). Sediment thickness and plate age are similar for the South Alaska, Valparaiso, and Coquimbo profiles, and the width difference is mainly due to the gentle dip of the Pacific Plate compared to that of the Nazca Plate. The volcanic arc for the Chile Margin is also closer to the deformation front by about 100 km, and this may also affect thrust plane temperatures downdip, narrowing the seismogenic widths.

#### 4.3.3 Uncertainty analysis

A test of the model parameters through a comparison of predicted and model heat flow was not possible for either the South Alaska and Chile margins due to the lack of surface heat flow data. The uncertainty analysis for the thermal properties assigned to the accretionary prism and subducting plate for these margins were taken to be similar to the Cascadia and Nankai margins. However, special attention was given to the effect of differences in radiogenic heat generation of the prism and of the overriding continental plate. For South Alaska, a higher measured percent potassium content from near-coastal plutonic rocks compared to Cascadia suggests higher radiogenic heat production for prism sediments derived from these sources. Higher heat generation was also taken for the Chile Margin through similar arguments. As the land heat flow is directly dependent on the continental crust heat production, a range  $\pm 25\%$  was applied to each of these margins. The result changes the predicted surface heat flow by about  $\pm 10 \text{ mWm}^{-2}$  and the position of the  $350^\circ\text{C}$  limit by  $\pm 10 \text{ km}$  distance landward of the deformation front.

Frictional heating, although argued to be negligible for the for Cascadia and Nankai, could play a significant role in the thrust temperatures for older subducting plates (e.g., Tichelaar & Ruff, 1993). The addition of high frictional heating, i.e.,  $\lambda=0.75$ ,  $\tau=50\text{-}100 \text{ MPa}$ , elevated thrust plane temperatures by about  $30^\circ\text{C}$ , and moved the  $350^\circ\text{C}$  seaward by 50 km. For South Alaska, this is about 20 km landward of the proposed Moho cutoff which

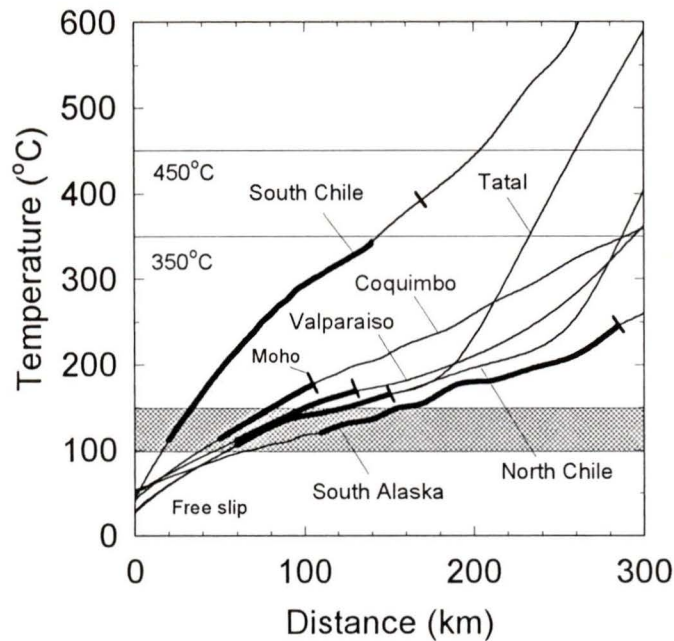


Figure 4.11. Thrust plane temperatures plotted against distance landwards from the deformation front for the South Alaska and Chile margins. The locked portion along the thrust plane is represented by the heavier line for each profile. The landward cutoff (thick, short lines) is based on approximate continental Moho depths (see Figure 4.9 and text for details). The continental Moho may act as the landward limit to the locked zone for these older, colder plates, where the 350°C thermal limit only occurs at depths from the surface of 80-100 km, well below normal subduction thrust earthquake depths of 40-45 km. The sharp rise in thrust plane temperatures is meant to demonstrate the effects of the volcanic arc. For the South Alaska profile, a similar rise occurs around 400 km landward distance, in conjunction with the nearshore Aleutian Volcanic arc.

is within reasonable error for this limit. As seen for Cascadia, such a low pore pressure and high frictional heating are unlikely along the thrust plane from coupling stress arguments (Wang et al., 1995b). As there is no surface heat flow data to support or refute the corresponding increase in the predicted surface heat flow profiles, negligible frictional heating has been assumed in the preferred South Alaska and Chile models.

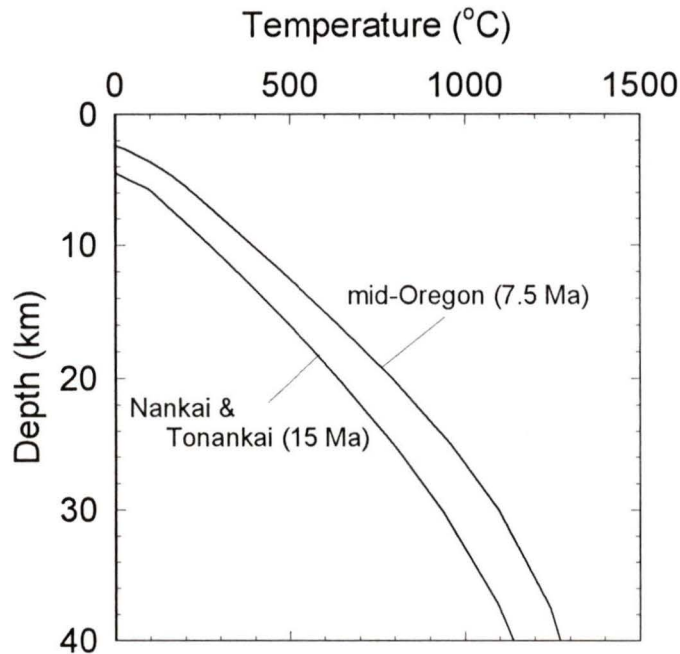


Figure 4.12. Temperature versus depth curve calculated at the deformation front for both the Nankai and Tonankai profiles, southwestern Japan. The mid-Oregon profile from the Cascadia Margin is included for comparison. The curves are labelled with time since the oceanic lithosphere at the deformation front was created, which is also the time since the model begins (modified from *Wang et al.* [1995b]).

#### 4.4 NANKAI MARGIN

##### 4.4.1 Thermal model results

###### Temperature-depth profiles

The initial temperature gradient returned from the 1-D thermal model gives the temperature versus depth curve shown in Figure 4.12. As discussed above for this margin, the initial temperature-depth profile was changed with time to match the increasing subducting plate age, from 0 to 15-17 Ma, and only the present subducting crust age of 15 Ma at the deformation front is shown.

###### Surface heat flow data

The predicted surface heat flow profiles for both the Nankaido and the Tonankai profiles of southwestern Japan are compared to extensive surface heat flow data which are

available across the continental margin of southwest Japan (Fig. 4.13). The offshore marine and onshore borehole data have been summarized by Yamano et al. (1984), Yamano et al. (1992), and Hyndman et al. (1995). Surface heat flow from the prism decreases landward towards the southwest coast of Japan, from about 120-130  $\text{mWm}^{-2}$  to 60  $\text{mWm}^{-2}$  (Yamano et al., 1992). The seaward portion of the model heat flow profile is mainly constrained by the depth to the BSR (grey circles, Fig. 4.13) (Ashi & Taira, 1993). The appreciable scatter in the remaining marine probe data has been attributed to active hydrothermal circulation within the prism sediments (Yamano et al., 1992). The heat flow measurements from land boreholes have been summarized by Li et al. (1989) and Yamano (1995), and have been superimposed onto one profile midway between the two thermal modelling profiles. The considerable scatter observed within the data is assumed to be caused by local groundwater flow effects (Li et al., 1989). The surface heat flow is higher compared to Cascadia mainly because of higher radiogenic heat generation (e.g., Hyndman et al., 1995). Crustal radiogenic heat production variation may also account for more regional discrepancies.

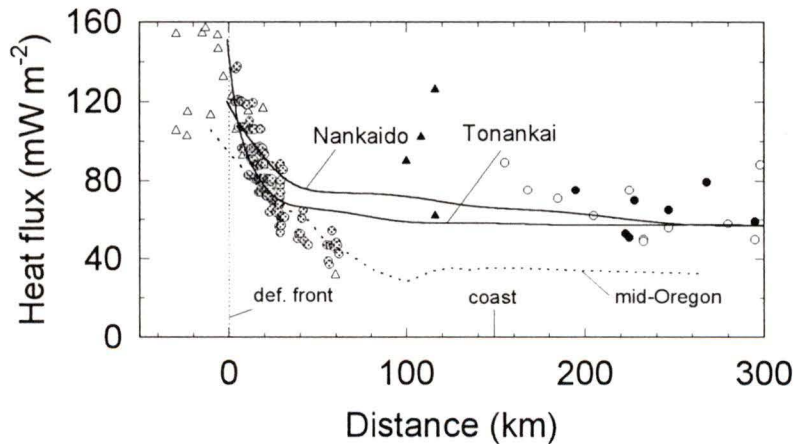


Figure 4.13. Heat flow data for the southwest Japan margin compared with predicted heat flow from thermal models for the Nankaido and Tonankai profiles. Errors on the heat flow values for the marine data are roughly  $\pm 15\%$ , and  $\pm 5\text{-}10\%$  for the land borehole data, but are excluded to avoid confusion for the tightly spaced BSR data. Symbols are as follows: marine heat flow data (open and solid (less reliable) triangles) after Yamano et al. [1992], BSR heat flow data (grey circles) after Yamano et al. [1984] and Ashi & Taira [1993], land borehole heat flow data (open and solid circles for Tonankai and Nankaido profiles respectively) after Li et al. [1989] and Yamano [1995]. The slightly higher heat flow curve for the Nankaido profile is due to a more shallow dip profile compared with the Tonankai dip geometry (modified after Wang et al. [1995b]).

The preferred model for Nankai is transient, with a landward migration of an initial thermal pulse generated by the subduction of very young ( $\sim 0$  Ma), very hot oceanic plate material (Wang et al., 1995b). These authors support their preferred transient model by comparing regular steady state models to the time-dependent models: the steady state models produced surface heat flow profiles well below the observed surface heat flow, similar to the mid-Oregon profile (Fig. 4.13). The higher model surface heat flow for the Nankaido profile compared to Tonankai profile is due to the more shallow dip of this portion of the Philippine Sea Plate. There is as yet an unexplained discrepancy between the model and BSR heat flow for the upper continental slope (Fig. 4.13) (Wang et al., 1995b).

#### 4.4.2 Temperature fields

The isotherm plots for the Nankaido and Tonankai profiles are presented in Figure 4.14. The plate age is similar for both profiles, and the difference in locked and transition zone widths is due to the more shallow dipping Nankaido profile. This is similar to the results for Cascadia, between the Olympic Peninsula and mid-Oregon profiles which have substantially different dip profiles (e.g., Fig 4.2). The estimated depth to the continental Moho is at greater depths than the  $450^{\circ}\text{C}$  downdip thermal limit for both the Nankaido and Tonankai models.

The thrust at the onset of subduction is between  $70\text{-}90^{\circ}\text{C}$ , so that the seaward limit of the locked zone is 20-40 km landward of the deformation front (Fig. 4.15). The thrust plane temperatures returned from the preferred thermal models are roughly twice the width than for northern and southern Cascadia profiles, around  $90 + 40$  km and  $80 + 30$  km locked plus transition respectively.

#### 4.4.3 Uncertainty Analysis

A number of tests to the thermal model were undertaken by Hyndman et al. (1995) and Wang et al. (1995b) to examine the effects of uncertainties of the complicated tectonic and thermal history. Small variations in time of  $\pm 2\text{-}3$  Ma since ridge spreading stopped produced changes between  $\pm 10$   $\text{mWm}^{-2}$  to the model surface heat flow, well within the scatter

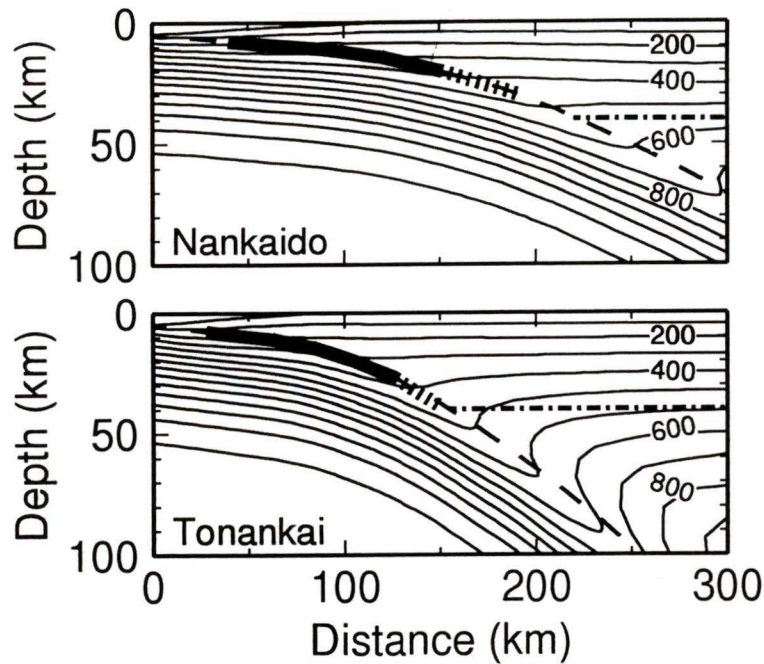


Figure 4.14. Present-day isotherms of the preferred models for the Nankai Margin off southwestern Japan. Nankaido, having a more shallow dip profile from 100 km and landward from the deformation front yields a wider locked zone (thick line). The downdip limit of the Tonankai profile transition zone (broken thick line) may approach the continental Moho (horizontal dash-dot line) abutment with the subducting plate. Isotherms are given in 100°C intervals. Distance is landward from the deformation (modified from *Wang et al.* [1995b]).

of the surface heat flow data, or 10-15 km width differences of the locked and transition zones (Hyndman et al., 1995). Reasonable wedge growth and convergence velocity variations produced small changes to the seismogenic zone widths,  $\pm 7$  and  $\pm 15$  km respectively (Hyndman et al., 1995). The amount of frictional heating for the margin is assumed to be low, but it is not constrained by the available thermal data (Wang et al., 1995b). In all, the error analysis suggested a  $\pm 20$  km uncertainty in the width of the seismogenic zones. The similar results to Cascadia provide support to the validity of the analysis.

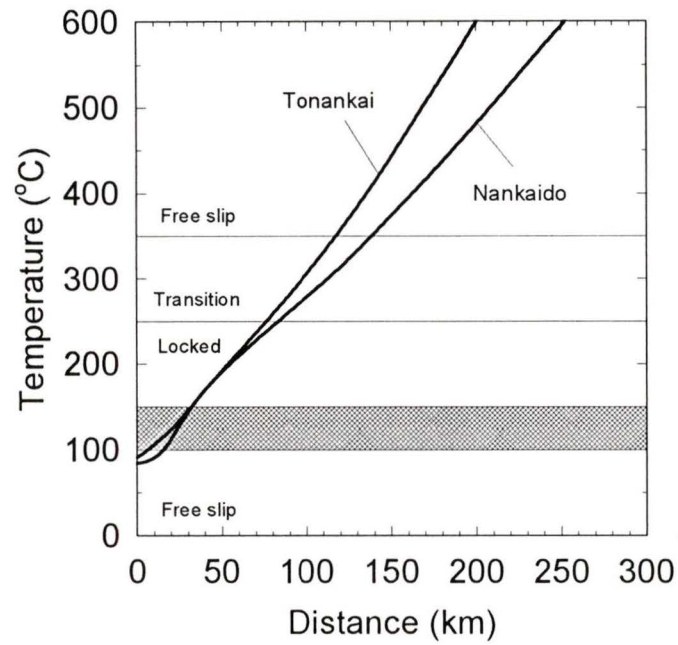


Figure 4.15. Thrust plane temperatures plotted against distance landwards from the deformation front for Nankai (SW Japan). The locked portion along the thrust plane is represented by the thermal constraints between 100-150°C to 350°C. The more narrow locked zone for the Tonankai profile reflects the steeper dip profile geometry associated with this portion of the subducting Philippine Sea Plate of southwestern Japan (modified from *Hyndman et al.* [1995]).

## CHAPTER V SEISMOGENIC WIDTH CONSTRAINTS

### 5.1 INTRODUCTION

The locked and transition zone widths predicted from the thermal models developed in the previous chapter are here compared to the coseismic rupture widths and interseismic locked zone widths estimated from three types of data: seismic, tsunami, and geodetic. The constraints provided by the seismic data are derived mainly from recent great thrust events, aftershock activity, and intermediate magnitude thrust events. With the exception of Cascadia, each margin considered in this study has experienced recent great thrust and intermediate magnitude thrust activity. Included in the seismic data discussion is the updip extent of the coseismic rupture provided by tsunami modelling of tide gauge data through waveform and wave propagation modelling.

The geodetic constraints to the width of the seismogenic zones come from 2-D elastic dislocation models fit to precise survey levelling and tide gauge data collected from both interseismic and coseismic periods. These data provided the most reliable estimate to the downdip extent of the seismogenic zone. Horizontal strain data interpreted from the geodetic data provided weaker constraint on the seismogenic width for Cascadia and Nankai, but are not considered in this study (e.g., see discussions in Hyndman et al., 1993; Dragert et al., 1994; Hyndman et al., 1995).

### 5.2 SEISMOGENIC WIDTH CONSTRAINTS

#### 5.2.1 Seismicity constraints

##### **Great thrust earthquakes and aftershocks**

Great thrust earthquakes ( $M_w > 8.0$ ) and their associated aftershock activity provide a direct comparison of coseismic rupture width to the maximum seismogenic zone width as predicted by the thermal models. The aftershock events are assumed to rupture localized areas along the thrust plane in response to the stress released along the thrust plane during the main event. An envelope can then be traced around the region with significant one day or up to two month aftershock activity, and is taken to approximate the rupture area. In the

analysis, it has been assumed that each great earthquake studied has ruptured the full seismogenic width, thus ignoring variations in rupture magnitude which likely occur over several earthquake cycles. Three of the four margins in this study have experienced instrumentally recorded great thrust events allowing this comparison.

Observations of the aftershock activity within a few months of the main event typically show a slow, outward propagation from the main shock asperity, and may represent aseismic creep along the thrust plane (Kanamori, 1977; Byrne et al., 1988). As the predicted seismogenic widths from the thermal model represent the maximum coseismic rupture, one day aftershock envelopes are preferred. However, the limited aftershock data may require the use of a longer period, up to two months in duration. Cascadia is excluded from the comparison to coseismic rupture as there has been no large historical thrust events.

### **Intermediate magnitude thrust earthquakes**

The seismogenic width estimates as obtained from great thrust earthquakes and aftershocks may be supplemented by well located intermediate magnitude thrust events. Whereas great thrust earthquakes usually rupture nearly all of the downdip portion of the thrust believed to be locked, intermediate thrust events rupture smaller regions. Often, such intermediate magnitude thrust events occur near the downdip end of the otherwise inferred seismogenic zone, and provide a constraint on the downdip limit. This study uses the intermediate magnitude relocated thrust events from Tichelaar & Ruff (1991; 1993). The following criteria were required for their events: 1. a minimum magnitude of  $M_w > 6.0$  (sufficiently accurate depth determination becomes increasingly difficult for lesser magnitudes); 2. a fault plane strike within  $\pm 30^\circ$  of the margin strike; and 3. a fault plane dip less than  $36^\circ$  (the cutoff of  $36^\circ$  was chosen as there is a gap in earthquake mechanism dips between roughly  $36^\circ$  and  $45^\circ$  for events which adhere to the other criteria). Tichelaar & Ruff (1991; 1993) speculate that this gap separates the interplate thrust events from the intraplate downdip compressional events. These deeper earthquakes may therefore also reflect the downdip limit of thrust events along the upper, more shallow dipping thrust interface.

The intermediate magnitude thrust earthquakes used in this study are for the time

period between 1977 to 1987 from the Harvard catalogue, with focal mechanism solutions compiled by Dziewonski & Woodhouse (1983). Prior to the Hazard catalog, from 1961 to 1976 the World-Wide Standard Seismograph Network (WWSSN) was used, but the focal mechanism solutions are of much poorer quality. Focal mechanism solutions from relocated events after Stauder (1973), Kadinski-Cade (1985), Malgrange et al. (1981), and Choy & Dewey (1988) taken from the International Seismological Centre (ISC) catalogue supplement the WWSSN catalog. For this study, intermediate magnitude events provide additional downdip constraint for the South Alaska and Chile margins only.

### **Tsunami constraints**

Far-field tsunami run-up height data from the Pacific Tsunami Warning System array supplemented local tide gauge readings to constrain simple rectangular tsunami source areas associated with great thrust events relevant to this study. Such models exist for the South Alaska, Nankai, and Chile margins. Paleotsunami evidence was used as an indirect constraint on the last great thrust earthquake for Cascadia.

### **5.2.2 Geodetic constraints**

Interseismic geodetic data allow estimates to the downdip extent of the thrust fault that is locked and storing elastic strain. Coseismic data acquired immediately after a main thrust event allow estimates on the magnitude of coseismic slip and rupture width. The interseismic period is assumed to occur from roughly 10-20 years following a thrust event up to the next main rupture (Savage et al., 1991). During this period, there appears to be approximately linear buildup of elastic strain, taken to be fully released during the coseismic rupture. A postseismic transient period may last for a few months following the main event to one or two decades, depending on the extent of rupture along the thrust plane (e.g. Plafker, 1971; Scholtz, 1988; Brown et al., 1977). This period is complicated by viscoelastic creep effects, and any data acquired during this period are excluded in this study.

The geodetic data from the coseismic and interseismic periods are compared with an elastic 2-D dislocation model approximating the elastic strain accumulation and release

associated with the earthquake cycle. The 2-D dislocation model assumes that the net deformation associated with the thrust event is zero so that the coseismic subsidence accommodates all the interseismic uplift. Although a more realistic model might include viscoelastic effects which occur on spatial scales of different magnitudes than the earthquake strain response cycle (e.g., Savage & Thatcher, 1992; Wang et al., 1994; Wang, 1995), the landward limit of the locked zone and the overall long term pattern of surface deformation do not change substantially. The dislocation model technique is described in greater detail below.

### **Geodetic Data**

The geodetic data includes precise repeat levelling, long term tide gauge records, horizontal strain laser ranging, and GPS networks. Uncertainties associated with the repeated levelling come from: 1. error propagation along the levelling line (landward end taken as fixed) which varies as  $\pm 4 \text{ mm K}^{1/2}$  for first order surveys, where K is the distance in kilometres between benchmarks (Vanicek et al., 1980; Dragert et al., 1994); 2. short repeat interval times which produce error estimates ranging from 0.7 mm/yr for 100 km long lines with repeat intervals around 50 years, to 3.6 mm/yr for 100 km long lines with repeat intervals of 10 years (Dragert et al., 1994; Hyndman & Wang, 1995); 3. postglacial rebound effects which may add up to  $\pm 2 \text{ mm/yr}$  (Dragert et al. 1994). Further, repeat levelling measurements yield relative height changes, and are therefore typically referenced to tide gauge records to obtain absolute uplift rates.

Application of tide gauge data requires a continuous or nearly continuous record of up to 50 years, but using relative differences applied to long term records allow sea-level trends from as little as 10 years of recording (Holdahl et al., 1989). The continuity of the data is important for corrections of long term atmospheric related effects, i.e., atmospheric loading, storm surges, El Niño effects, and global temperature increase (Chelton & Enfield, 1986). Two corrections which must be applied to the tide gauge data are the global eustatic sea-level rise (around 2 mm/yr) (Douglas, 1991; Peltier & Jiang, 1996), and the glacial isostatic rebound (around 3 mm/yr) (Savage et al., 1991). The rebound rates vary over

distances of 10's of kilometres for the northern margins, and are more difficult to quantify. Corrected tide gauge uplift rates provide a reference to which the relative height changes obtained from repeat levelling may be tied. They therefore provide an important absolute reference for the interseismic uplift rate across the margin. Tide gauge data is only given for the Cascadia and Nankai margins, where long, continuous data records exist. For unreliable or in the absence of tide gauge data, the levelling data is tied to a landward, near-zero reference point.

Horizontal strain data supplement the levelling and tide gauge data are . Early strain networks involved only triangulation between selected points over limited areas (10's km). These were followed by very accurate laser ranging distance measurements over much larger areas (100's km) (Savage et al., 1991), and most recently by global positioning surveys (GPS) (up to 1000's km). Within a few years of continuous operation, differential GPS stations referenced to a stable site several hundred kilometres landward of the subduction margin can yield relative uplift and shortening rates , and provide information relating larger plate tectonic movement (Dragert & Hyndman, 1995). Such data are available for Cascadia only.

For Cascadia, where no great thrust earthquakes have been recorded, the interseismic geodetic data provide the main constraint to the location and downdip extent of the seismogenic zone. For South Alaska and Chile, where great thrust earthquakes have occurred, the coseismic surface deformation data constrain the portion and total slip of the rupture area. Where both interseismic and coseismic data are available, as for Nankai, dislocation modelling to both the locked zone and rupture width is possible.

### **Elastic Dislocation Models**

The simplest model describing the deformation behaviour between great thrust earthquakes is purely elastic in which the strain accumulates at a constant rate during the interseismic period. This accumulated strain is in turn completely released during the coseismic rupture. This study applies the first-order assumption of an elastic deformation cycle using a 2-D edge-dislocation in an elastic half space (Savage, 1983). The model calculates the surface deformation from a fault dislocation which depends on the magnitude

of slip, the dip angle, and the downdip width over which slip occurs (Savage, 1983). All the energy is assumed to be released during the coseismic rupture, yielding a zero net deformation. The earthquake rupture area is therefore that portion of the thrust plane which is locked between earthquakes, and the interseismic deformation rate at any point is the negative of the coseismic deformation divided by the time between events (e.g., see discussion by Hyndman et al., 1995). There may be a spatial scaling problem with the accumulation of strain through tectonic loading and the release of such by the earthquake rupture cycle (e.g., Wang, 1995), but a zero net deformation cycle is apparently adequate to a first-order approximation.

The subduction thrust zone is approximated by a dislocation in a simple Earth model represented by an elastic half space. A right-handed coordinate system is used with the y-axis along the surface trace of the thrust zone, the x-axis horizontal in the plate convergence direction, and the z-axis directed vertically downwards (Savage, 1983). A line or edge dislocation is taken to be parallel to the y-axis. By making the line dislocation infinite, the subduction is assumed to be uniform along strike, and the problem becomes two dimensional. The surface deformation in such a model is described by two quantities: the uniaxial strain  $e_{xx}$  perpendicular to the margin and the vertical displacement  $w$  produced by the edge dislocation component (Savage, 1983). These components are given by

$$e_{xx} = \frac{2b_x \pi s \sin \alpha (s - x \cos \alpha)(x - s \cos \alpha)}{D^4} \quad (1)$$

$$w = \frac{1}{\pi} (b_x \sin \alpha) \left[ \frac{x s \sin \alpha}{D^2} + \arctan \left( \frac{x - s \cos \alpha}{s \sin \alpha} \right) - \frac{\pi}{2} \right] \quad x > 0 \quad (2)$$

where  $D^2 = x^2 + s^2 - 2xs(\cos \alpha)$ ,  $x$  being the distance landward from the surface trace of the deformation front,  $s$  being the downdip distance along the thrust plane,  $\alpha$  being the dip angle

of the thrust plane, and  $b_x$  being the dip slip Burgers vector (Savage, 1983). Maximum uplift occurs at the downdip edge of the main thrust zone.

### Coseismic deformation

Application to the coseismic deformation involves prescribing a slip width along a planar thrust fault (Fig. 5.1). A single planar fault was assumed to be an acceptable approximation to the dip profile if the widths of the seismogenic zones were narrow. Where the dip profile changes considerably, a superposition of two planar segments was used. The model ignores the many details associated with real subduction systems which may combine to produce variations to the seismogenic width along the thrust plane, such as a non-homogeneous plate rheology, a complicated Earth surface, a rough or smooth subducting plate surface. Further, strain accumulation may vary with time during the interseismic period, and not all the interseismic deformation is necessarily released during the coseismic rupture. Thus the magnitude of coseismic slip as input to the elastic model is that required to produce

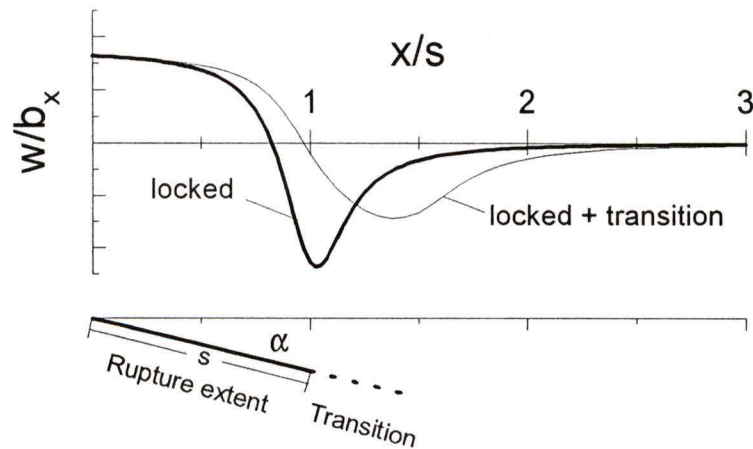


Figure 5.1. The elastic half-space dislocation model of strain accumulation applied to the various subduction zones in this study. The upper diagram shows the vertical uplift generated by a the simple planar locked zone of length  $s$ , dipping at angle  $\alpha$  for locked (heavy line) and locked plus transition (light line) zones. The peak uplift from both scenarios occurs approximately over the downdip limit of the locked zone for no transition zone, and at the middle of the transition zone when it is included.

the observed surface deformation.

### **Interseismic deformation**

Dislocation modelling constrained by the interseismic deformation is applicable providing: 1. the net vertical displacement over the earthquake cycle was assumed to be zero; 2. the interseismic uplift rate was assumed constant over the duration of the interseismic period; and 3. the earthquake released all of the elastic strain accumulated continuously during the interseismic period. A modification to the simple elastic locked / unlocked dislocation model is the addition of a transition zone in which strain accumulation decreases linearly downdip below a certain point, avoiding an unrealistic strain singularity where the system goes from fully locked to free slip (e.g., Plafker & Savage, 1970; Dragert et al., 1994; Hyndman & Wang, 1995). By changing the width of the locked and transition zones, the peak amplitude and width of the dislocation model curve may be changed to fit the available geodetic data (Fig. 5.1).

Although there remain theoretical problems with application of the dislocation model to the interseismic period as discussed by Wang (1995), the simplification into an elastic response cycle is validated by more complicated viscoelastic models. These models include temporal variations in early deformation rates (e.g., Rundle, 1978; Thatcher & Rundle, 1984, Barrientos et al., 1992). For longer, later, interseismic rates, however, the seismogenic width estimated from the viscoelastic models were in good agreement with the purely elastic models (Wang et al., 1994). Thus by excluding a 10-30 year period following a great thrust earthquake, the elastic model provided good constraint to the width of the seismogenic zone.

Below are the seismic, tsunami, and geodetic data for each margin fit to elastic dislocation models, which in turn are compared to the thermal results from Chapter 4.

## **5.3 CASCADIA**

### **5.3.1 Seismicity constraints**

#### **Tsunami constraints**

The Cascadia Margin is the only margin in this study which has not experienced great

or intermediate thrust earthquake activity in historical times. There are, however, local paleotsunami data which may provide some constraint to the maximum magnitude and thus the maximum rupture length and width associated with a Cascadia great thrust earthquake (e.g., Atwater et al., 1995; Nelson, 1996). There is also far-field descriptive tsunami data available from Japan. Satake et al. (1995) and Satake et al. (1996) has shown that tsunami reports along the east coast of Japan in 1700 AD have no corresponding local large earthquake. Historical earthquake records and paleoseismic evidence for this time also indicate the absence of large earthquakes in Alaska, South America, or Kamchatka (e.g., Satake et al., 1996). This leaves Cascadia as the only likely source. Wave propagation models suggest that  $M \sim 9$  is required to produce the widespread 2-3 m high waves reported, inferring that almost the entire Cascadia Margin must have ruptured in a single, very large event (Satake et al., 1996). This places a minimum limit on the length of a potential megathrust event for Cascadia. For a rough estimate on the downdip width, an average slip along the thrust plane of 20 m is taken, with a 1000 km long by  $\sim 100$  km downdip width to produce a  $M \sim 9$  event.

### 5.3.2 Geodetic constraints

#### Levelling data

Analysis of repeated levelling data by the Geodetic Survey of Canada and the US National Geodetic Survey on profiles along the Cascadia Margin pertinent to this study have been previously presented by several authors (e.g., Reilinger & Adams, 1982; Dragert & Liskowski, 1990; Holdahl et al., 1989; Dragert et al., 1994; Mitchell et al., 1994; Hyndman & Wang, 1995). Only the better data near the thermal models are presented here (Fig. 5.2). Propagation errors associated with the repeated levelling are to first order, i.e.  $3 \text{ mm } K^{1/2}$ , or better (Dragert et al., 1994). The postglacial rebound effects may be up to  $\pm 1.5 \text{ mm/yr}$  for Vancouver Island (James, 1996), and tilting over the length of most lines is about  $1 \text{ mm/yr}$  (Dragert et al. 1994).

Corrected levelling data for the Tofino-Parksville (TO-PA) and Bamfield-Port Alberni (BA-PA) lines (Dragert et al., 1994) are presented in Figure 5.3a. Based on the thermal

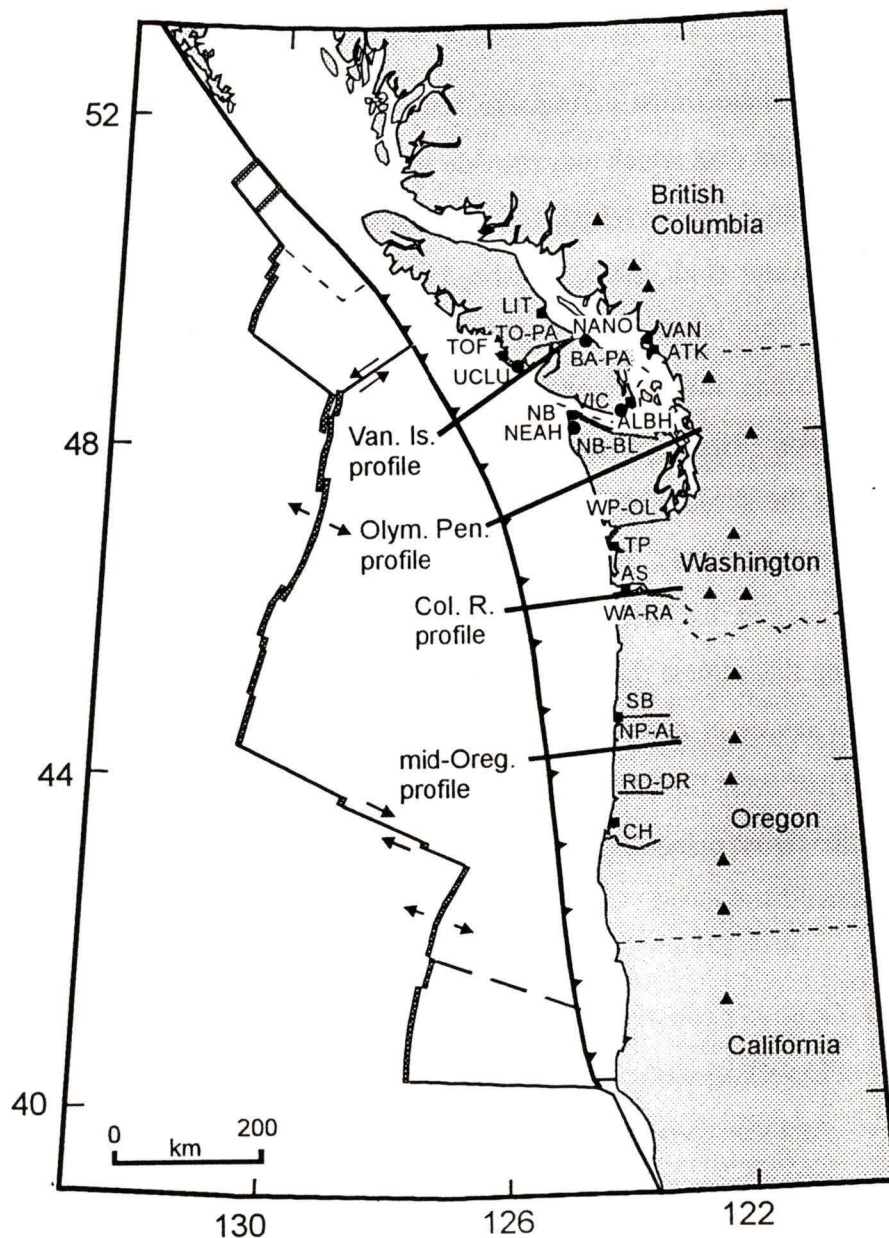


Figure 5.2. Levelling lines, tide gauge, and GPS sites used as constraints to the interseismic uplift rate for the 2-D dislocation modelling for the Cascadia Margin. Data within 50-100 km are projected onto the appropriate profile(see text for details). The Vancouver Island and Olympic Peninsula dislocation models are the best constrained models of the four profiles along the margin.

results, the locked and transition zones are assumed to have the same widths. The estimated locked and transition zone widths are  $60+60$  km respectively. In the model, the  $12^\circ$  dip angle chosen is a tangent to the dip profile 60 km landward of the deformation front. The relevant tide gauges and GPS station further constrain the 2-D dislocation model (Fig. 5.3a).

To the south, for the Olympic Peninsula, Columbia River, and mid-Oregon profiles,

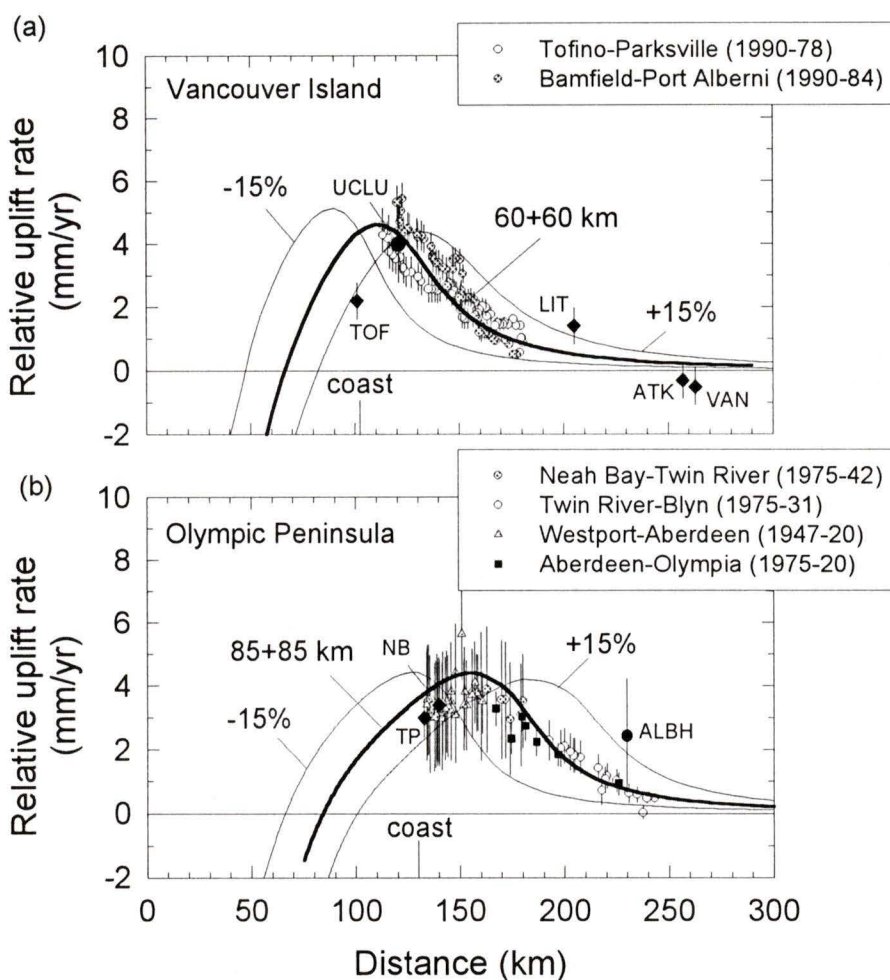


Figure 5.3. Profiles of interseismic vertical deformation from repeat levelling and tide gauge data. (a) The data are compared with the preferred simple 2-D dislocation model (heavy line) for the Vancouver Island profile. Errors to the model widths are on the order of 10-15 km, or roughly  $\pm 15\%$ . Error propagation along the levelling lines indicates the increasing uncertainty with distance, with the landwardmost point taken as being fixed. All levelling and tide gauge data not orthogonal to the margin have been projected onto the nearest profile along the margin to which they are applicable. (b) Same as for (a), but for the Olympic Peninsula profile (modified after Hyndman & Wang [1995]).

the longer repeat interval times between surveys reduces the error somewhat along the levelling lines. For the Olympic Peninsula, the Westport-Aberdeen and Neah Bay-Twin River data constrain the seaward and central portion of the uplift maxima respectively, while the

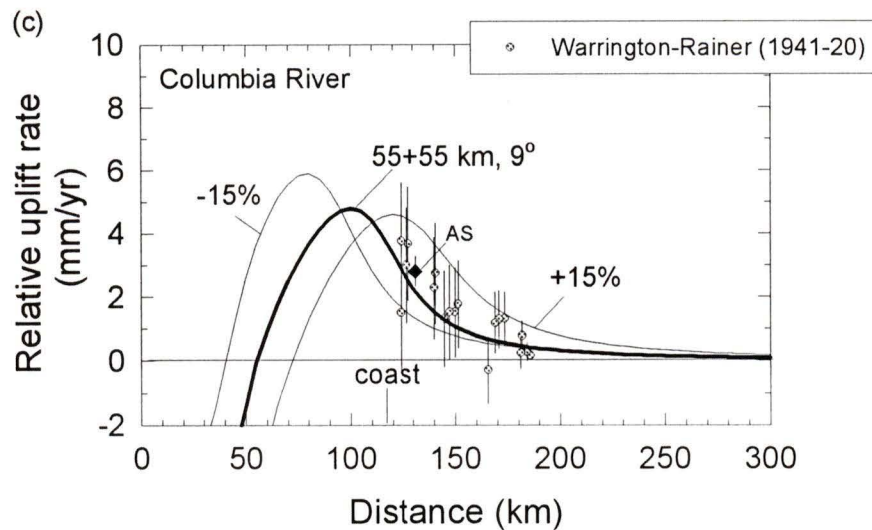


Figure 5.3 (continued) (c) Same as for (a) but for the Columbia River profile.

more landward Twin-River-Blyn and Aberdeen-Olympia constrain the landward, decreasing uplift portion of the dislocation profile (Fig. 5.3b). A preferred model of 85+85 km locked plus transition zone best matches the available data (Fig. 5.3b). The Columbia River model profile very closely follows the Warrington-Rainer (WA-RA) levelling line. A 55+55 km locked plus transition zone dislocation model (Fig. 5.3c). For the mid-Oregon profile, a repeat levelling line from the Reedsport-Drain (RD-DR) and Newport-Albany (NP-AL) lines constrain the dislocation model. Larger errors in this line may be associated with earlier levelling techniques (e.g., see discussion Reilinger & Adams, 1982). The best fit for the two lines is a 35+35 km wide locked plus transition zone (Fig. 5.3d & e).

### Tide gauge data

Extensive tide gauge data in operation since the early 1900's are available over the length of the Cascadia Margin (e.g., Fig. 5.2). Holdahl et al. (1989), Savage et al. (1991) and Dragert et al. (1994) have presented summaries of the tide gauge data applicable to the Vancouver Island and Olympic Peninsula profiles, and Mitchell et al. (1994) have presented

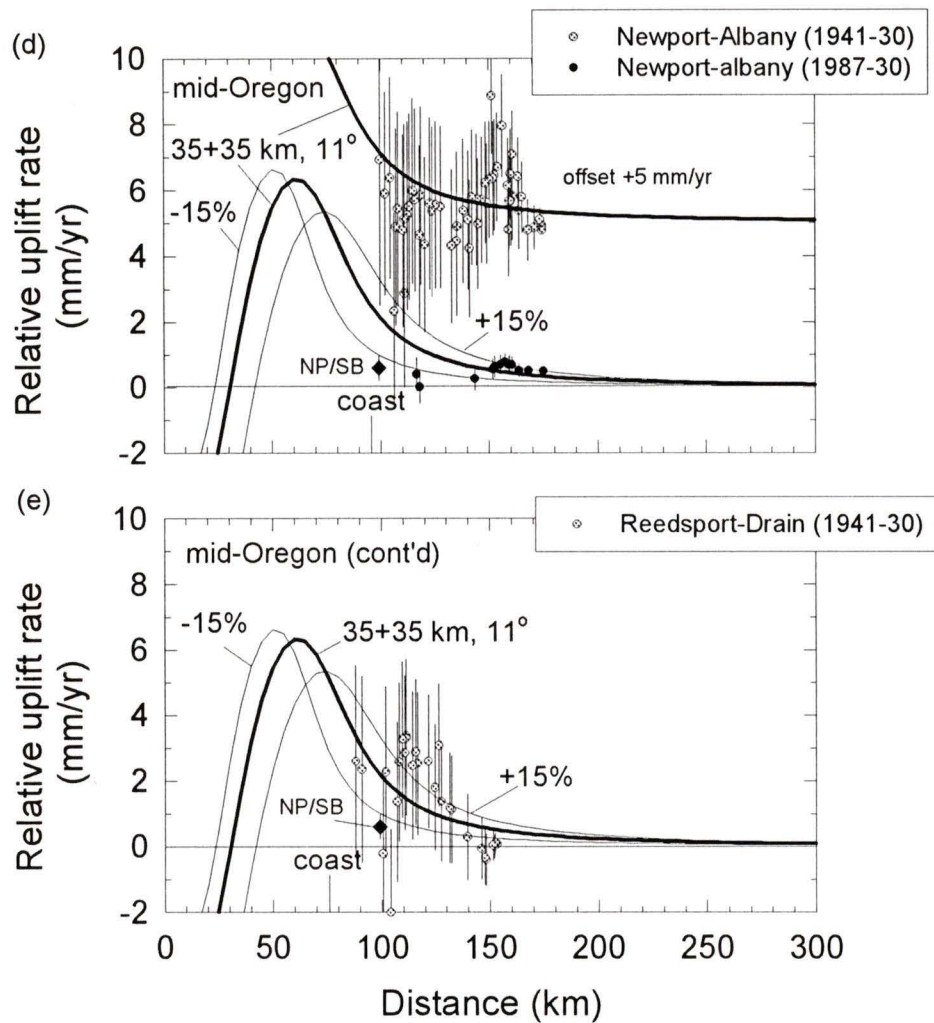


Figure 5.3 (continued) Same as for (a), but for the mid-Oregon profile. (d) Levelling and tide gauge data to the north of the profile. (e) Similar geodetic data to the south of the profile.

a summary for the regions of the Columbia River and mid-Oregon profiles. Dragert et al. (1994) and Hyndman & Wang (1995) present further details on the correction analysis of individual tide gauge stations applicable to the four profiles along the margin. Corrected tide gauge uplift rates from these authors are included with the precise levelling data in Figures 5.3a-d.

### **GPS data**

Four GPS sites have been in operation for at least one year for the northern region of the margin (Fig. 5.2). Uplift rates are referenced to Penticton located about 300 km inland where tectonic deformation associated with the subduction process is considered negligible. Only the Ucluelet (UCLU) and Albert Head (ALBH) stations are included as additional constraints to the dislocation models based on longer acquisition times and greater reliability of the available data. UCLU agrees well with the predicted dislocation model widths for the Vancouver Island profile (Fig. 5.3a), but ALBH predicts a slightly wider seismogenic zones (Fig. 5.3b). The latter GPS station may be complicated by the corner in the subducting plate (see discussion in Dragert et al., 1994; Dragert & Hyndman, 1995).

### **Coseismic deformation**

The strongest evidence for past great earthquakes along the Cascadia Margin comes from buried coastal marsh strata which is indicative of an abrupt lowering of the land. Such evidence is found nearly the entire length of the margin (e.g., Atwater et al., 1995). There is strong evidence for at least six subsidence events in the last ~7000 years (e.g. Clague et al., 1982; Darienzo & Peterson, 1990; Nelson & Kashima, 1993; Clague & Bobrowski, 1994). The subsidence events are marked by a sharp contact between peat and overlying intertidal mud. Sometimes the peat layers are overlain by layers of tsunami-generated sand (Atwater, 1987). This submergence and slow shoaling evident along Cascadia is similar to the observed submergence and postseismic shoaling in other subduction zones with historical great earthquakes (e.g., Plafker, 1969; Plafker & Savage, 1970).

Precise carbon-dating of peat and woody fragments in the buried marsh tops suggests that the most recent event occurred around 1700 AD. Similar carbon dates elsewhere support a sudden, large rupture rather than localized, isolated effects (Atwater et al., 1995). The coseismic deformation for Vancouver Island, Washington, and northern Oregon is all subsidence, ranging from 0.3 to 1.2 m (Atwater, 1987; Atwater et al., 1995). Assuming the coseismic deformation was caused by the most recent rupture, and assuming an interval of 300 years from the previous event (e.g., Adams, 1990), the predicted coseismic deformation

for northern Cascadia is roughly 1.6 m (based on the current uplift rates), decreasing towards the south to 0.7 m. These values are within 0.4 m of the observed values, and are considered to be well within error (Hyndman & Wang, 1995).

Visible secondary evidence in support of coseismic subsidence deformation comes from landslide and liquefaction evidence (these data are difficult to date with sufficient accuracy to determine whether the events were all coincident) and from offshore deep sea turbidite data showing regular submarine landslides roughly every 590 years, the last about 300 years ago (Adams, 1990). It should be noted that the 690 year event recorded in the turbidity flows is not clear in the coastal data (e.g., Atwater et al., 1995), and that the recurrence interval may be longer than 300 years. Tree ring patterns that show several years of narrowed growth rings before death may indicate stressed conditions likely coincident with submergence into intertidal salt water, and there is some evidence to support the 1700 AD event (Jacoby et al., 1992).

### **5.3.3 Comparison with thermal model results**

Only the interseismic deformation rates are presented as constraints to the dislocation models (e.g., Fig. 5.3a-e). The paleoseismic data provide evidence for the regular recurrence of great thrust events along the margin, but provide only a weak constraint on the maximum landward limit of the locked zone. The interseismic deformation matched that predicted by the dislocation models for a 60+60 km wide locked +transition zone for Vancouver Island, 85+85 km for Olympic Peninsula, 55+55 km for southern Washington and northern Oregon, and 35+35 km for mid-Oregon. Increasing locked zone widths beyond 80 km in the southern regions predicted coseismic uplift rather than the subsidence observed along the coastal regions, thus limiting the coseismic fault slip to beneath the continental shelf. There is very good agreement between the simple elastic dislocation results constrained by the interseismic geodetic data and the thermal results (Fig. 5.4). The width of the transition zone is assumed to match the changing width of the locked zone along the length of the margin, and is in good correspondence with the 450°C thermal limit. The thermal model results agree to within  $\pm 20$  km with those obtained from the dislocation models.

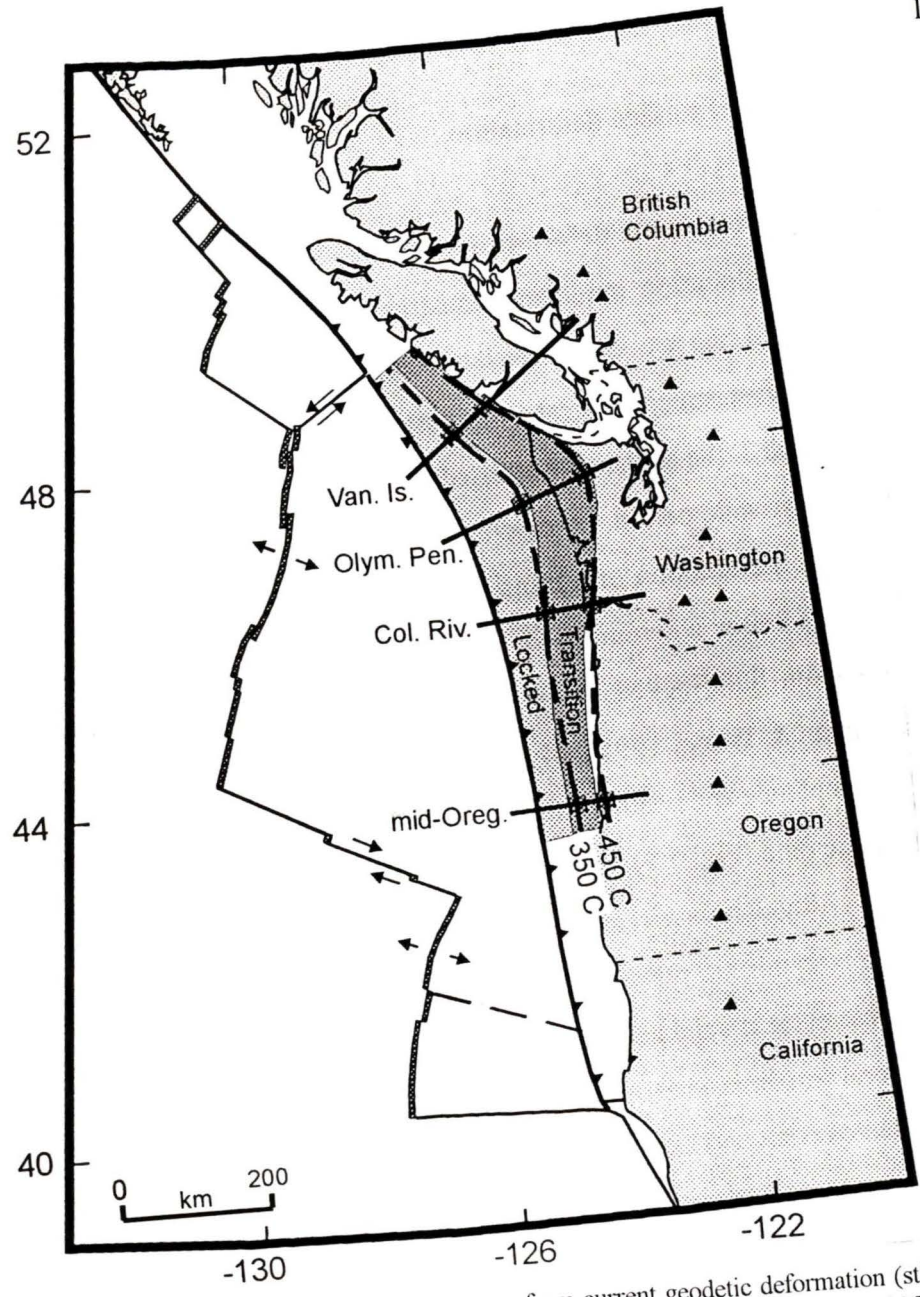


Figure 5.4. The widths of the locked and transition zones from current geodetic deformation (stippled areas) compared to those from the thermal analysis (thick short lines). The bands on the thermal limits of 350 and 450°C indicate estimated uncertainties.

## 5.4 SOUTH ALASKA

### 5.4.1 Seismicity constraints

#### 1964 Main event

The hypocentre for the great March 27, 1964 thrust earthquake was at  $61.06^{\circ}\text{N}$ ,  $147.44^{\circ}\text{W}$ ,  $25 \pm 10$  km depth (Fig. 5.5a) (Plafker, 1969), and the seismic moment was estimated at  $8.2 \times 10^{22}$  Nm ( $M_w$  9.2) (Kanamori, 1977). Rupture propagation was  $30 \pm 5^{\circ}$  SW for roughly 800 km. Source time functions determined from teleseismic P-waves indicated two major pulses of moment release: a first pulse initiated close to the epicentre which spread southward, initiating a second pulse, located in the Kodiak Island area, 600 km to the south (Christensen & Beck, 1994). The fault plane matches the dip geometry from Wadati-Benioff data (e.g., Plafker, 1969; Sykes, 1971; Miyashita & Matsu-ura, 1978; Davies & House, 1979; Page et al., 1989; Tichelaar & Ruff, 1993; Christensen & Beck, 1994; Johnson et al., 1996). The focal mechanism solution suggests a dip of  $7^{\circ}$  in a northwesterly direction with a slip of about 20-25 m in the Prince William Sound area (Stauder, 1973; Christensen & Beck, 1994). To the south around the Kodiak Island area, the fault plane dip increases to  $25^{\circ}$  in the same direction with a dislocation of about 18 m.

#### 1964 Aftershock activity

The one day aftershock envelope covers roughly  $385\,000$  km<sup>2</sup>, from near Kodiak Island to northern Prince William Sound (Fig. 5.5a). The aftershock zone was slightly broader to the east in the region of the main shock epicentre (Plafker, 1969). This broader rupture boundary was probably the result of a the shallow dip of the subducting plate, which caused an increase in coupling between overriding North America Plate and the subducting Yukatat Terrane / Pacific Plate (e.g., Brocher et al., 1994). The seaward limit of the one day aftershocks was 80-100 km landward of the deformation front. Most of the larger aftershocks with  $m_b \geq 5.0$  were situated seaward of the Kodiak Island and Kenai Peninsula outer coasts, while the intermediate aftershocks with  $4.0 \leq m_b \leq 5.0$  spread inland into the Cook Inlet (Plafker, 1969). The smaller  $m_b \leq 4.0$  events spread equally over both regions. The aftershock sequence diminished rapidly shortly after the main event (Plafker, 1969).

Associated with the rapid drop in the number of events was the continued outward spreading of the aftershock envelope by 50 km landward and seaward (Reagor et al., 1994). Little further increase in envelope size over the following 2 month period was reported (e.g., Fig. 5.5a) (Plafker, 1969). Algermissen et al. (1969) and Matumoto & Page (1969) reported that most of the aftershocks with  $m_b > 5.0$  occurred between 5-40 km in depth, with a mean depth of 12 km. Only 25 aftershocks with  $m_b > 4.4$  occurred deeper than 35 km. The aftershocks did not fall into a well defined planar zone, but there was a tendency of increasing depth for the lower limit landward beneath the continent (Algermissen et al., 1969; Matumoto & Page, 1969). For comparison to the thermal model results, only the one day aftershock envelope was considered. Aftershocks occurring in the following weeks may be in response to the slow creep re-adjustment of the strained focal region, and may exaggerate the estimated rupture area.

### **Intermediate magnitude thrust earthquakes**

Tichelaar & Ruff (1991) found only five interplate events along the eastern portion of the south Alaska margin, only one of which was located within the 1964 aftershock region. It occurred on September 4, 1965 at a depth between 36-38 km (Fig. 5.5a). This depth agreed well with the maximum depths of the majority of aftershocks, which occurred where the thrust plane is less than 40 km deep. Combined with the 4 other events immediately to the south of the 1964 rupture region, Tichelaar & Ruff (1991) obtained a downdip limit between 37-41 km depth.

### **Tsunami constraints**

The 1964 event uplift of the continental shelf in the Gulf of Alaska was responsible for the generation of a large tsunami (Pararas-Carayannis, 1976; Hatori, 1981). Joint inversion of tsunami wave and geodetic data has been used to determine the fault dislocation area as a large but variable slip dislocation near Prince William Sound, with a distinct separate slip distribution to the south around Kodiak Island (Fig. 5.5a) (Johnson & Satake, 1993; Johnson et al., 1996). This conclusion of two sub-events was supported by the pattern of two

(a)

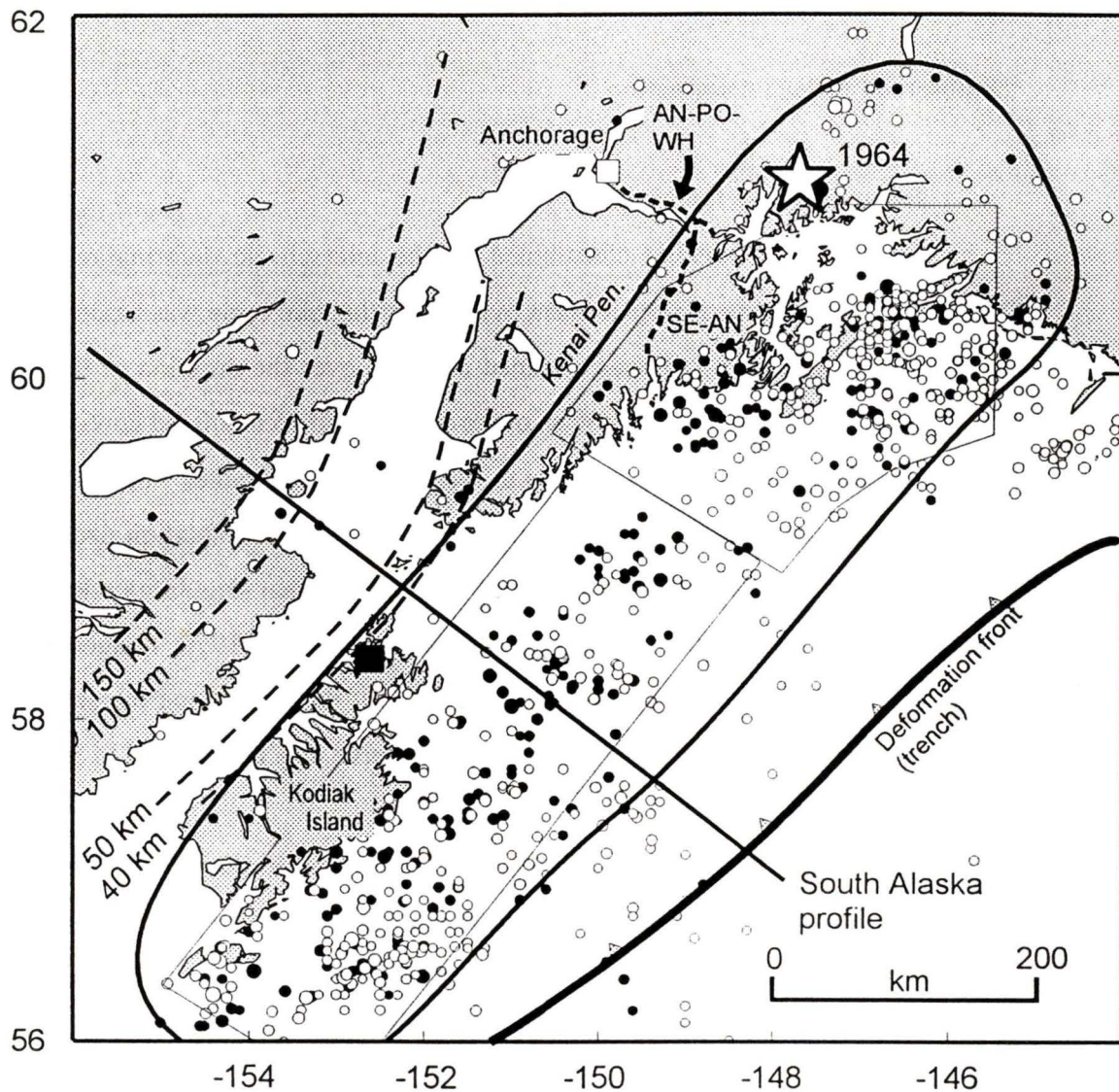


Figure 5.5. Regional map for South Alaska Margin. (a). Epicentre (large star) and rupture area (closed loop) from one day aftershocks (solid circles) for the Good Friday, March 27, 1964, Mw 9.2 megathrust event, after *Plafker* [1969]. Shallow events are excluded from the envelope as they are poorly constrained in depth and location. Progressive creep in the two months following the main event is concentrated in the northern Prince William Sound and southern Kodiak Island areas (open circles). Relocated intermediate thrust event (solid square) after *Tichelaar & Ruff* [1993] further constrain the downdip limit. The rectangular areas are the earthquake dislocation regions from inversion of geodetic and tsunami data after *Johnson et al.* [1996]. Repeat levelling data surveyed after the main event is along the Seward-Anchorage (SE-AN) and Anchorage-Portage-Whittier (AN-PO-WH) lines. Depth contours are to the top of the subducting Pacific Plate.

(b)

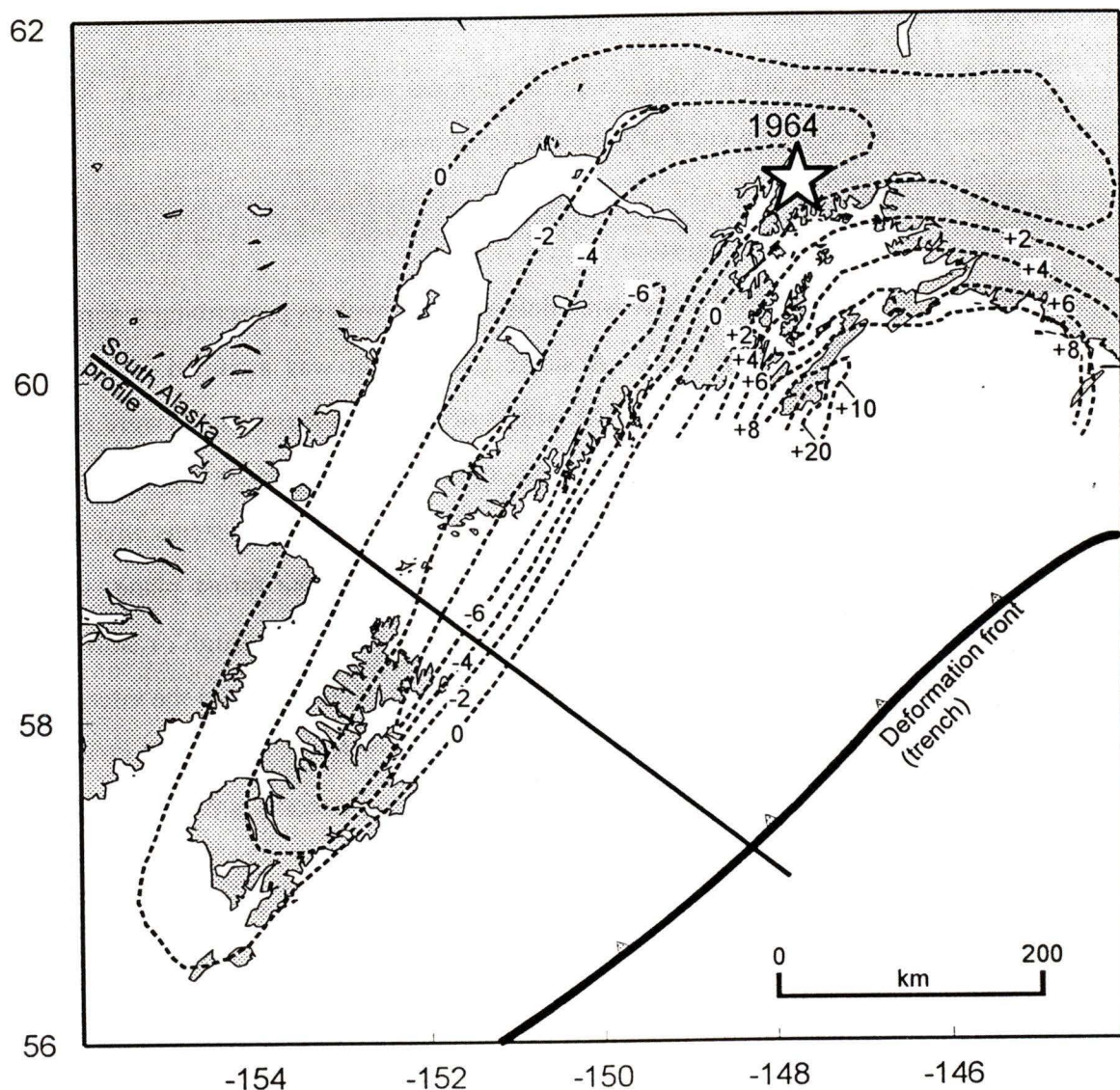


Figure 5.5 (continued). (b). Contour map showing the coseismic uplift and subsidence associated with the 1964 great thrust earthquake. Contours are given in feet (after *Plafker* [1969]).

periods of intense ground shaking separated by a short period of subdued shaking as reported in accounts from Kodiak Island (*Plafker*, 1969). There was a slight difference on the landward limit from the joint inversion estimate compared to the aftershock seismicity. These latter data extended an additional 30-40 km across Kodiak Island and somewhat less across the Kenai Peninsula (Fig. 5.5a). The rupture area estimated from the two week aftershock data extended an additional 20-30 km, about 50 km wider the joint inversion estimate.

## 5.4.2 Geodetic constraints

### Levelling data

Dislocation modelling was applied to the 1964 coseismic surface deformation to obtain the amount and distribution of slip along the thrust plane. Repeat levelling in the area of study was first carried out between Seward and Palmer in 1922 (e.g., Brown et al., 1977). Following the 1964 event, re-levelling was done in 1964, 1965, 1968, and most recently in 1975 across the Kenai Peninsula. All levelling was performed to first order specifications as described above. Only the 1922 and 1964 levellings covering the coseismic period were used to determine the coseismic rupture area. Successive re-levelling during the post-1964 10 year period suggested that the position of maximum uplift had migrated trenchward (e.g., Brown et al., 1977). These latter data were, however, complicated by the postseismic, transient viscoelastic effects described above, were not used for interseismic dislocation modelling.

As many of the 1922 levelling bench marks were lost, the 1964 repeat levelling required new bench marks which were not tied into the original line (Brown et al., 1977; Cohen et al., 1995; S. Cohen, personal communication, 1995). The relative heights of each bench mark referenced to the Anchorage tide gauge station were therefore transposed onto a profile between Whittier and Anchorage, following the general direction of both lines (AN-PO-WH line, Fig. 5.5a). Bench mark elevations from the two surveys near the profile were compared to obtain relative height changes, and tied into the Anchorage tide gauge station.

### Tide gauge data

In the area affected by the 1964 event, corrected tide gauge data showed postseismic uplift had occurred where coseismic subsidence was recorded, and postseismic subsidence where coseismic uplift was recorded (Savage & Plafker, 1991). Rapid postseismic deformation had elevated rates which were considerably damped out in a 10 year period. Savage & Plafker (1991) hypothesized that these elevated rates were not likely to be sustained over the recurrence interval, and that a 30-50 year relaxation period likely would accommodate the elevated rates, with much of the relaxation occurring within 5-10 years. Longterm interseismic tide gauge uplift rates were therefore only available for preceding the

1964 event. Only two tide gauges satisfy this criteria: the Kodiak Island tide gauge station (nearly continuous operation since 1950); and the Seward tide gauge station (intermittent operation since 1925, no data from 1938-45) (Savage & Plafker, 1991). The Kodiak Island pre- and post-earthquake uplift rates were  $4.8 \pm 1.6$  and  $17.5 \pm 0.8$  mm/yr respectively, while the Seward rates were  $2.8 \pm 1.5$  and  $13.3 \pm 3.7$  mm/yr respectively (Brown et al., 1977; Savage & Plafker, 1991). The discrepancy between the two pre-earthquake interseismic rates, although at roughly the same distance landward of the deformation front, has been attributed to the difficulty in determining uplift rates from short, discontinuous intervals. Although inadequate to constrain the 2-D elastic dislocation model, the tide gauge data provide a weak constraint for a  $\sim 350$  year recurrence rate (assuming constant interseismic deformation) since the last great thrust event.

### **Coastal data**

Coastal coseismic vertical deformation used to constrain the 2-D dislocation model includes changes to the upper growth limit of marine seaweeds and mussels, differences in the lower growth lower limit between the pre- and post-earthquake terrestrial vegetation, changes in the extreme high tide line, changes in the heights of tidal bench marks relative to sea level, and differences in heights of the pre- and post-earthquake storm beaches (Plafker, 1969). These data were used to constrain the 2-D elastic dislocation models along two profiles roughly 100 km distant from and running parallel to the thermal model profile (Fig. 5.6). Historical indicators of coseismic deformation include raised marine terraces (Nishenko & Jacob, 1990; Plafker et al., 1992), peat layers in intertidal muds (Bartsch-Winkler & Schmoll, 1992; Combellick, 1991), and buried coastal forests (Reimnitz, 1972; Plafker et al., 1992; Mann & Crowell, 1996). More than 800 coseismic deformation data points were recorded along the rocky coastlines of Prince William Sound, Kenai Peninsula, and Kodiak Island (Plafker, 1969). Based on these data, an isocontour map, indicating zones of uplift and subsidence, was constructed (Fig. 5.5b). The zero isobase, where little to no deformation was inferred, was traced along the outer coastline of the Kenai Peninsula and Kodiak Island. Uplift seaward of the zero isobase was particularly well constrained immediately southwest

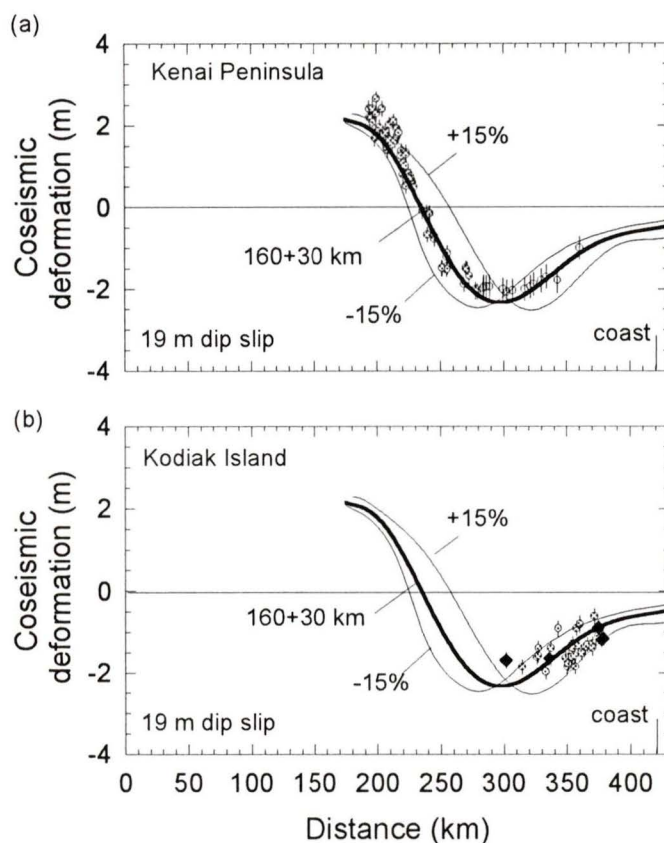


Figure 5.6. Profiles of coseismic vertical motion across the South Alaska Margin from lower and upper marine growth limits (solid circles), relative levelling bench mark (open circles) and tide gauge station height changes (solid diamonds). (a) Observed coseismic deformation across the Kenai Peninsula, in line with the Anchorage-Portage-Whittier levelling line, i.e., see Figure 5.1. Height change errors associated with marine growth limits are on the order of 20-50 cm after *Plafker* [1969], while levelling errors are greater due to projection onto the profile from different bench marks chosen during the re-levelling survey after the 1964 event (see text for details). (b). Same as in (a), but for height changes across Kodiak Island, supplemented by tide gauge bench height changes. Locked zone width is given from the seaward, updip limit.

of Prince William Sound, where numerous islands provided ample recording sites. These data had a peak vertical displacement of up to 10 m uplift along several surface faults (*Plafker*, 1969). The zone of subsidence landward of the zero isobase included nearly all of Kodiak Island and the Kenai Peninsula (Fig. 5.5b). Tidal bench marks and precise levelling provided additional constraints to this zone where intertidal growth levels were more difficult to measure.

### 5.4.3 Comparison with thermal model results

The models across both the Kenai Peninsula and Kodiak Island predict a 160+30 km locked plus transition zone, taken from the seaward limit (Fig. 5.6). This agrees remarkably well with the thermal-Moho limit model predictions of 180+20 km (Fig. 5.7). These results also agree favourably with the one day aftershock envelope and the tsunami source area. The

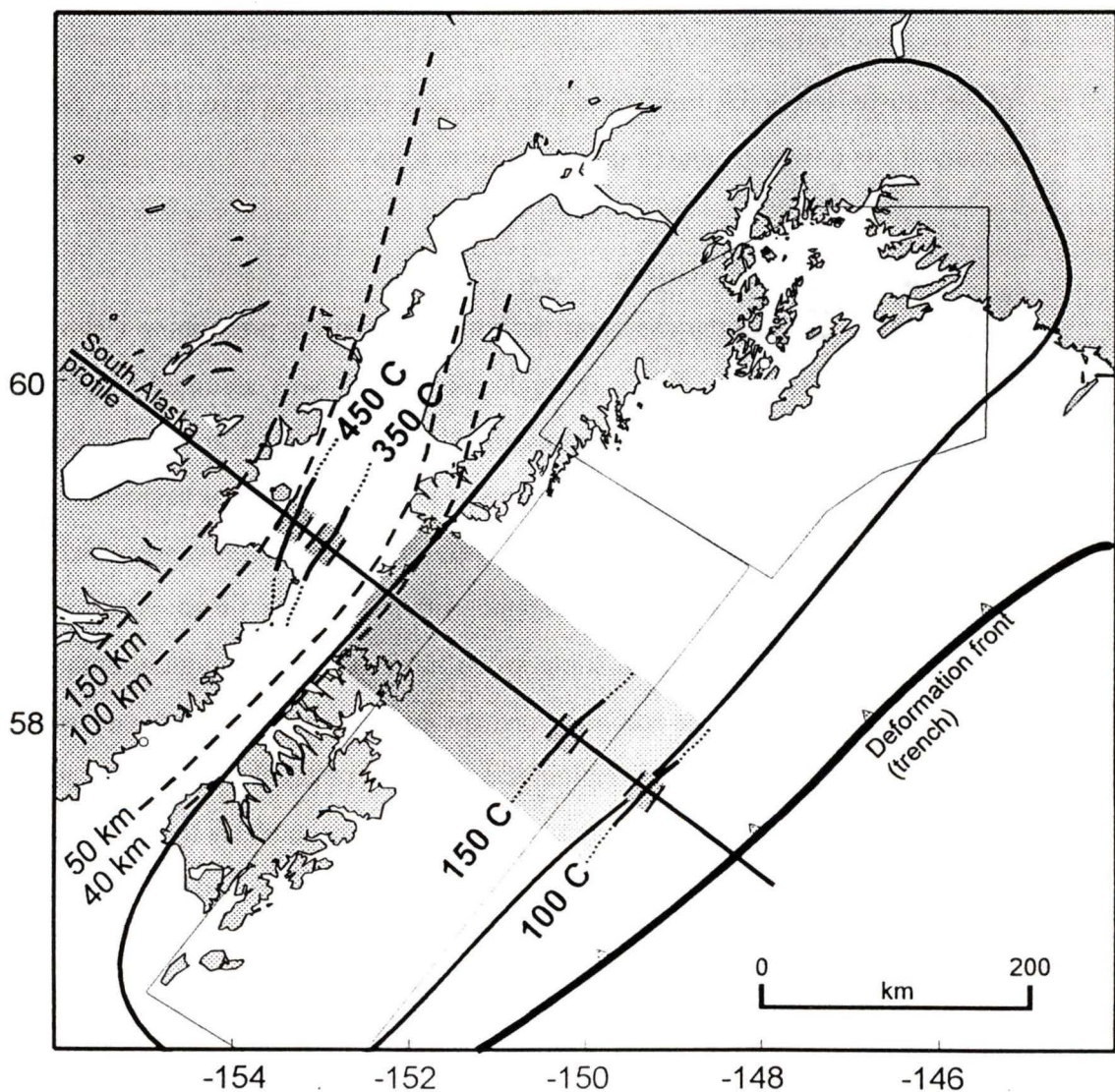


Figure 5.7. The widths of the locked and transition zones from the thermal analysis (thick short lines) compared to those from the 1964 coseismic deformation (stippled areas). The one day aftershock envelope (closed loop) from Figure 5.5. is also included for comparison. Bands on the thermal limits are as for Figure 5.4.

350°C and 450°C thermal limits are only encountered at greater depths, and the continental Moho intersection with the subducting plate between 40-45 km is assumed to mark the downdip limit of the seismogenic zone. A narrow, 20 km wide transition zone is assumed to represent the onset of stable sliding occurring farther downdip.

## **5.5 CHILE**

### **5.5.1 Seismicity constraints**

Great earthquake data for the Chile Margin combines a 300 year written history and a 50 year modern instrument record (Nishenko, 1985). Three of the five model profiles in this study are in the regions of great thrust events. From south to north, these include the 1960 megathrust, South Chile profile, the 1971 & 1985 great thrust events, Valparaiso profile, and the 1943 thrust event, Coquimbo profile. The most recent great thrust earthquakes for the Taltal and Northern Chile profiles to the north occurred prior to instrument recording and were therefore excluded.

#### **1960 Main event**

Plafker & Savage (1970) report that the great 1960 earthquake had sub-events spread over two days, starting on May 21, near the northern end of the rupture zone, followed by a second shock the following day, followed 16 minutes later by the culminating shock at 38.5°S, 74.5°W (Fig. 5.8a). The precursor event was preceded by 6 large foreshocks that came progressively closer in time, and defined a SW trend in the direction of the rupture initiation of the main event (Lomnitz & Hax, 1966; Plafker & Savage, 1970; Cifuentes, 1989). The total seismic moment of the shock sequence range from  $M_w$  9.4 (Kanamori & Cipar, 1974; Sykes & Quittmeyer, 1981; Nishenko, 1985) to a more recent estimate of  $M_w$  9.6 (Cifuentes, 1989; Cifuentes & Silver, 1989). Early fault models from teleseismic data suggested nearly 20 m of slip along the preferred 35°E dipping thrust plane, 60 km in width perpendicular to the margin (e.g., Press et al., 1961; Benioff et al., 1961; Kanamori & Cipar, 1974). More recent dislocation estimates yielded a preferred solution of a 17 m of slip with a dip of 20°E over a 130 km in width (e.g., Barrientos & Ward, 1990).

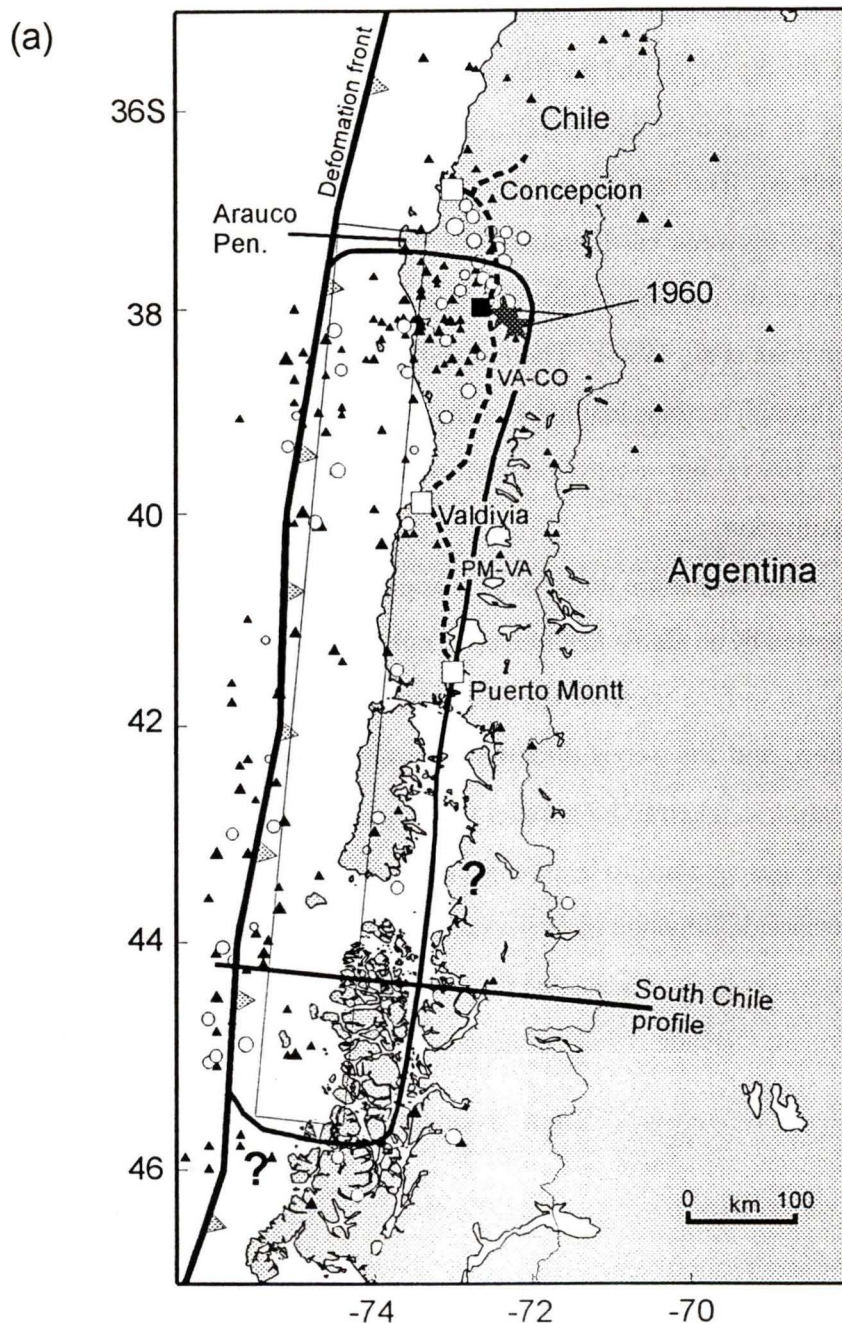


Figure 5.8. Region map for south Chile. (a) Aftershock seismicity for the great 1960 Mw 9.5 Chilean megathrust earthquake. The tight cluster of seismic activity (open circles) immediately to the north of the culminating large shocks (large stars) includes foreshock and one month aftershock activity. The aftershock envelope (closed loop) is poorly constrained both on the seaward and landward limits due to the small data set and poor depth and epicentre locations. Progressive creep associated events in the 8 years following the main event (solid triangles) concentrated around the main event, but their seaward boundary is also poorly constrained. The rectangle is the earthquake dislocation area defined by the tsunami data after *Hatori* [1966]. Its landward limit is essentially unconstrained. Repeat levelling data (dashed line) were surveyed along the Puerto Montt-Valdivia (PM-VA) and Valdivia-Concepcion (VA-CO) lines, running nearly parallel to the coastline (after *Plafker & Savage* [1970]).

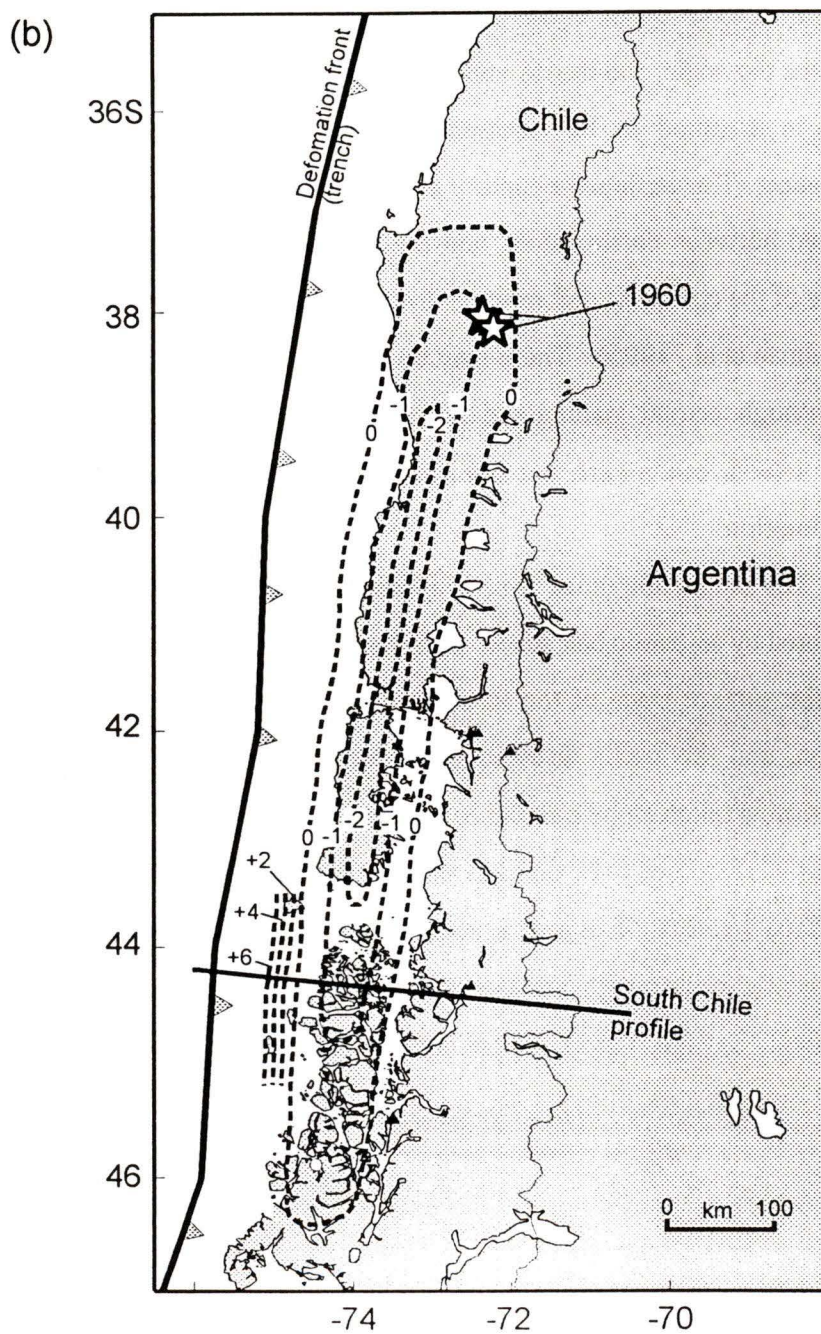


Figure 5.8. (continued) (b). Map showing coseismic uplift and subsidence associated with the 1960 great thrust earthquake. Contours are given in metres (after *Plafker & Savage* [1970]).

### **1960 Aftershock activity**

The one month aftershock envelope for the 1960 event is shown in Figure 5.8a. The scarcity of aftershock data reflects the lack of local seismograph stations rather than low aftershock activity. The distribution shows a concentration in the northern region near the main shock, and the average width of the envelope was about 140 km (Cifuentes, 1989). Aftershocks with body wave magnitude  $m_b \geq 6.0$  occurred primarily offshore, with the exception of 7 large aftershocks close to the region of rupture initiation (Barrientos & Ward, 1990). For aftershocks with  $4.0 < m_b < 6.0$ , there was a fairly equal distribution to offshore and onshore regions (Fig. 5.8a) (Barazangi & Isacks, 1976). The rupture length of the main shock determined from the one month aftershock distribution was around 950 km, north-south. The southern limit is supported by the southern extent of surface deformation (Fig. 5.8b) (Plafker & Savage, 1970), and by the probable physical barrier of the intersection of the Chile Ridge with the Chile Trench (Cifuentes, 1989). Barrientos & Ward (1990) included up to eight years of seismicity to increase the number of aftershock events believed to be associated with the 1960 thrust event. Although the 8-year aftershock envelope did not provide a marked improvement on the constraint to the rupture area, there was a noticeable seaward spreading that probably reflected slow aseismic creep along the thrust plane.

### **1985 Main event**

The most recent rupturing of the Valparaiso asperity was the 1985 thrust event. It occurred on March 3, 1985, with an epicentre located at lat  $33.24^\circ\text{S}$ , long  $71.85^\circ\text{W}$  (Fig. 5.9) (Comte et al., 1986). Analysis of long period teleseismic waves showed the main event consisted of three sub-events, and the seismic moment has been estimated at  $1.15 \times 10^{21}$  Nm ( $M_w$  8.0) (Choy & Dewey, 1988). The focal mechanism of the main shock was estimated to be a shallow plane dipping  $18^\circ\text{E}$  (Barrientos, 1988). The rupture extended approximately 90 km to the south, and the average displacement on the fault was estimated at 1.2 m, with a maximum of 3 m in the southern half of the rupture area (Choy & Dewey, 1988). Slip is believed to have extended down to a variable depth between 50 km in the north to less than 30 km in the south: updip extended within 10 km of the surface (Mendoza et al., 1994).

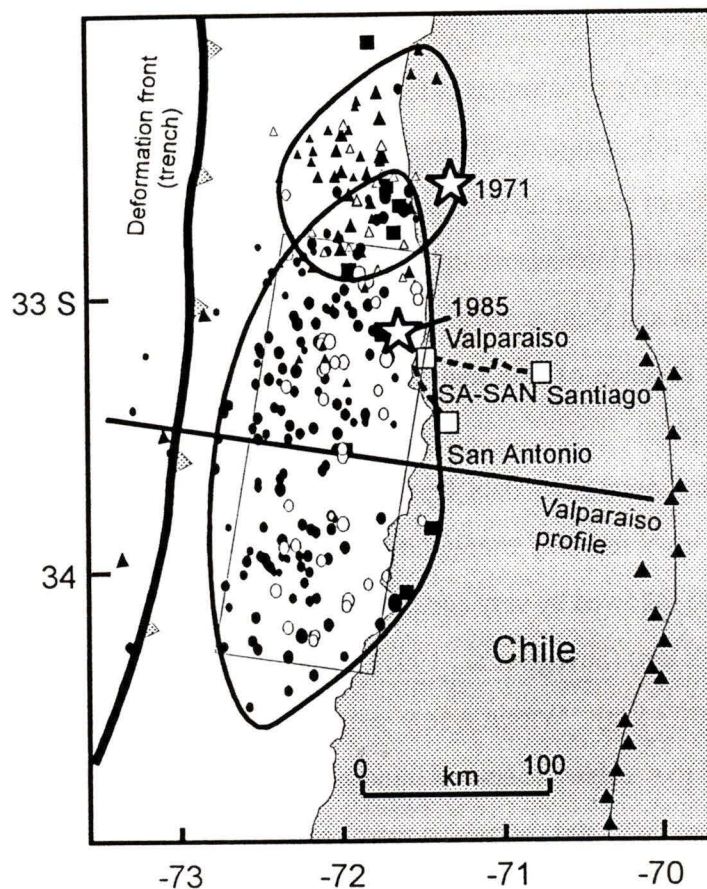


Figure 5.9. Seismic activity associated with the Ms 8.1 1971 and Ms 7.8 1985 great thrust earthquakes (large stars) with associated one day aftershocks (solid triangles and solid circles respectively) and envelopes (closed loops) after Choy & Dewey [1988]. Two month aftershock activity (open triangles and circles respectively) do not differ significantly from the one day distribution. Shallow events are again omitted from the rupture area due to poor depth and location constraints. Relocated intermediate thrust events (solid squares) after Tichelaar & Ruff [1991] provide additional constraint to the downdip rupture limit. Repeat levelling data was acquired along the San Antonio-Santiago (SA-SAN) levelling line (dashed line).

### 1985 Foreshock & aftershock activity

The main shock was preceded by high foreshock activity, which began 10 days prior to the main event, reaching a maximum of about 120 events per day (Comte et al., 1986). Their epicentres defined a tightly constrained patch on the thrust interface about 20 km long in a ENE-WSW direction, centred between the three sub-events of the main sequence (Choy & Dewey, 1988). The one day aftershock distribution suggested a region of slip extending roughly 140 km to the south and roughly 80 km wide (Fig. 5.9) (Barrientos, 1988; Mendoza et al., 1994). The two month aftershock envelope expanded the slip region an additional 30

km parallel to the margin, for a total length of 200 km, and increased the width to 100 km (Choy & Dewey, 1988). This behaviour is similar to most great thrust events examined in this study which have increasing slip area with time following the main event. A general increase in aftershock depth with increasing distance landward from the main shock was also observed.

### **1971 Main event & aftershock activity**

Although smaller in magnitude than the numerous historical earthquakes to the immediate south (e.g., Nishenko, 1985), the 1971 event provided valuable information on the nature of the thrust plane for this region of the Nazca Plate. The July 8, 1971 earthquake, occurred at lat 32.54°S, long 71.15°W, at a depth of 40 km at the northern end of a very seismically active region along the Chile Margin (Fig. 5.9) (Comte et al., 1986). Malgrange et al. (1981) reported a seismic moment of  $5.6 \times 10^{20}$  Nm ( $M_w$  7.7), although the source area for the main event was relatively small compared with other underthrusting events of similar size elsewhere along the Chile Margin. First motion analysis results are consistent with a low angle, reverse fault, dipping at roughly 24° to the east with a north-south strike. Slip ranged between 1.6 m and 5.7 m in the north and south regions of the rupture area respectively (Malgrange et al., 1981).

The 1971 event may have been a foreshock to the larger 1985 earthquake (Fig. 5.9) (McCann et al., 1979). In the historical earthquake record, events have occurred every  $83 \pm 7$  years, placing the 1985 great thrust earthquake as the successive event, and not the smaller 1971 event. Further, the 1971 event occurred entirely within the last great thrust (1906) source area, and the former was partially ruptured again in the 1985 event. This suggested it did not rupture a significant portion of the Valparaiso asperity, and was rather a 15 year precursor to the 1985 event. The aftershock distribution extended about 50 km north and south of the epicentre, and spread westward over several months (Fig. 5.9) (Eisenberg et al., 1972, Malgrange et al., 1981). The depths of the aftershocks were poorly constrained, but are believed to occur along the thrust plane mainly updip from the main shock hypocentre (Malgrange et al., 1981).

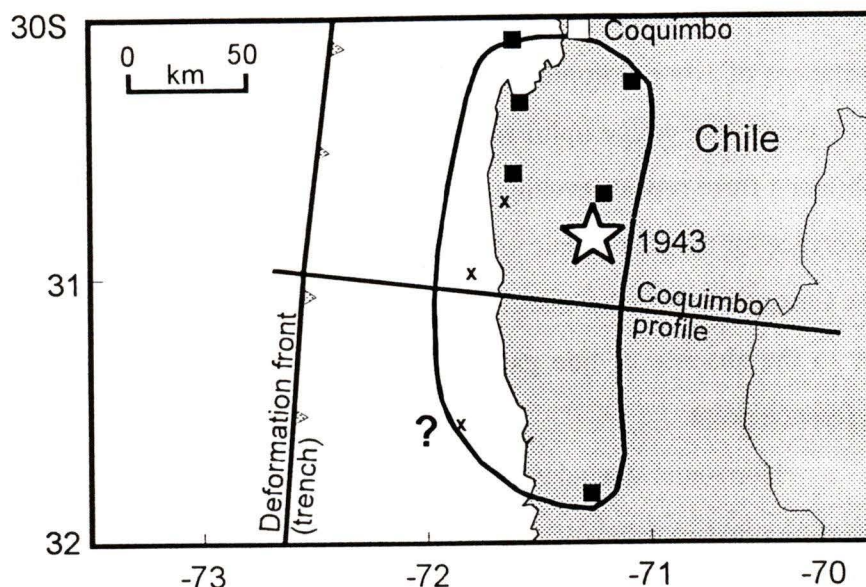


Figure 5.10. Seismic activity for the Coquimbo region, showing the 1943 main thrust (large star) and aftershocks (small crosses) after *Kelleher* [1972]. The aftershocks are too small for accurate depth determination, and consequently the aftershock envelope (closed loop) is poorly constrained on the seaward limit. Relocated intermediate thrust events (solid squares) from 1965-1987 further constrain the presumed 1943 rupture area inferred from reports of damage to coastal villages following the main event (after *Tichelaar & Ruff* [1991]).

### 1943 Main event & aftershock activity

The great thrust earthquake of April 6, 1943 had an epicentre at lat  $30.75^{\circ}\text{S}$ , long  $72^{\circ}\text{W}$ , but had poorly defined rupture area and aftershock zone due to the limited number of seismograph stations operating at that time (Fig. 5.10) (*Kelleher*, 1972). Heavy damage reports from coastal villages north and south of the epicentre suggested that the rupture propagated equally in both directions, limited by historical great thrust earthquake rupture areas north (1922) and south (1906) (*Nishenko*, 1985). The magnitude for the 1943 event was estimated at  $M_w$  8.3 (*Kelleher*, 1972). The few located aftershocks extended from  $30.42^{\circ}$  to  $31.78^{\circ}\text{S}$ , an along-strike distance of about 150 km (Fig. 5.10). An updip and downdip extent of 30 km and 120 km landward from the deformation front respectively have been estimated based on these data (*Tichelaar & Ruff*, 1991).

### Intermediate magnitude thrust earthquakes

Relocated intermediate magnitude thrust events after *Tichelaar & Ruff* (1991) were

used to supplement the downdip extent of the rupture area for earthquakes relevant to this study. Such events seem to commonly occur near the maximum depth of the seismogenic zone, and are important in the comparison to the seismogenic widths predicted from the thermal and Moho limit models. For the South Chile profile, intermediate magnitude thrust activity within the 1960 great thrust rupture zone has been low except for a small cluster between 37° and 39°S, near the Arauco Peninsula (Fig. 5.8a) (Tichelaar & Ruff, 1993). The largest event occurred between 32 km (Kadinski-Cade, 1985) and 41 km (Tichelaar & Ruff, 1991). Although loosely constrained, these data suggested coupling to a depth of 35-40 km.

A constraint to the maximum depth of coupling in the Valparaiso region was provided by two 1985 event aftershocks at 44-47 km and 40-41 km deep respectively (Fig. 5.9) (Tichelaar & Ruff, 1991). The 1971 great thrust earthquake, with hypocentre at 45 km depth, may mark the maximum coupling depth as rupture propagation was predominantly updip, and the relocated intermediate magnitude events occurred at shallower depths (Fig. 5.9). The maximum coupling depth in the Coquimbo region was constrained by 6 relocated events, the deepest two occurring between 48-49 km and 50-53 km (Fig. 5.10) (Tichelaar & Ruff, 1991). Combined with the 1943 great thrust event, the seismic coupling was taken to extend down to  $53 \pm 5$  km.

The Taltal profile ruptured in two intermediate magnitude earthquakes in 1966 and 1983 (Tichelaar & Ruff, 1991). Combined with the aftershocks of the 1983 event and two smaller relocated events, the maximum coupling depth was constrained to 30-38 km (Fig. 5.11). Although Tichelaar & Ruff (1991) reported that the source dimension for the 1966 and 1983 events were larger than 25 km, the aftershock distribution suggested the rupture propagation was mainly along-strike. For the Northern Chile profile, the last great thrust earthquake occurred in 1877, and this region is recognized as a gap in great earthquake occurrence along the Chile Margin (Kelleher, 1972; McCann et al., 1979). Maximum coupling depth constraints are provided by only three relocated intermediate thrust events. The 1970 event has been relocated at depths of 42-43 km, and the 1967  $M_w$  7.1 slightly deeper at 45-48 km (Fig. 5.11) (Tichelaar & Ruff, 1991). It is concluded that this region is coupled at least to 45 km, and perhaps to 48 km.

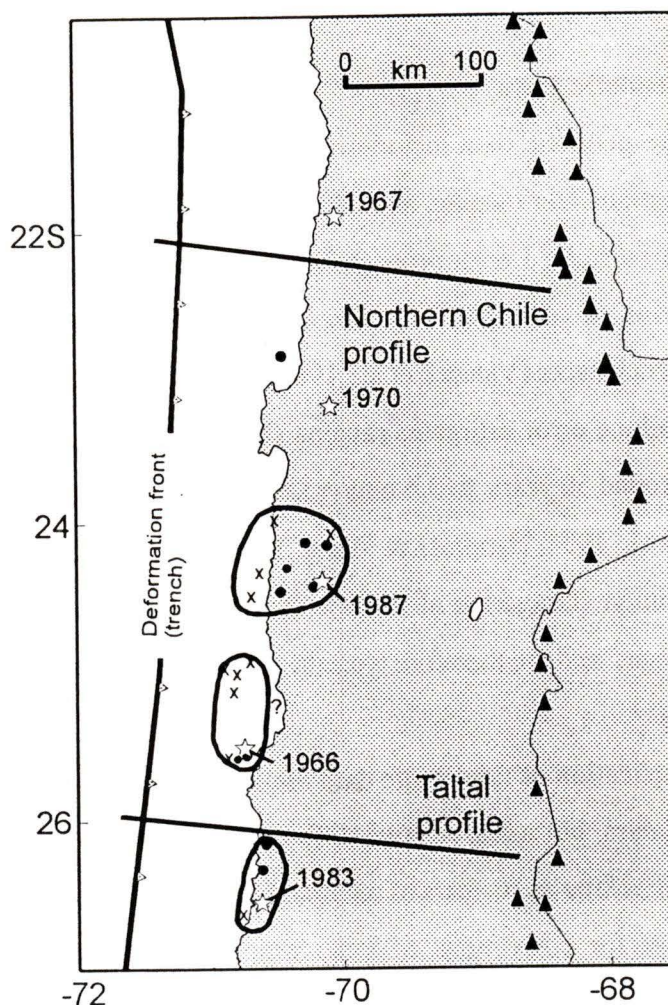


Figure 5.11. Intermediate magnitude thrust earthquakes for the Taltal and North Chile profiles after *Kelleher* [1972]; *Tichelaar & Ruff* [1991]). The aftershock rupture envelopes for the 1966, 1983, and 1987 thrust events are only poorly constrained (small crosses). Relocated intermediate events (solid circles) provide additional constraint to the downdip limit.

### Tsunami constraints

Tsunami source areas were only available for the 1960 and 1985 events as insufficient runup height data for the 1971 and 1943 events do not allow tsunami models. For the 1960 event, Hatori (1966) constructed wave-front diagrams based on initial tsunami wave amplitude at three northern Chile tide stations and from eyewitnesses data. Typical runup heights of 10-20 m were reported along the margin, requiring a source area  $138\,000\text{ km}^2$  vertically displaced 6 to 10 m. Abe (1979) reported a  $M_t$  9.4 from runup heights at numerous distant, tide gauge recordings, and estimated a source area of  $210\,000\text{ km}^2$ . The latter, better

defined area was used in this study (Fig. 5.8a). The seaward limit of the tsunami was taken to be within 10 km of the deformation front. The northern and eastern limits of the tsunami source associated with the 1960 event correspond roughly to the limit of coastal uplift (Fig. 5.8b) (Plafker & Savage, 1970).

The 1985 event rupture has been modelled from tsunami wave height data from numerous far-field tide gauge stations which were not in place for the 1960 event (Burton & Person, 1985). Nearshore coastal damage associated with the main event was caused by a tsunami of 1.2-1.8 m in height in the north, increasing southwards up to 3 m for some exposed beaches (G. Plafker, reported by Comte et al., 1986). Nakamura (1992) reported a the rupture length of about 150 km from nearby and far-field tsunami runup heights. The seaward limit was again taken to be within 10 km of the deformation front. A slightly shorter envelope of 140 km results if aftershocks occurring at less than 20 km depth are rejected based on large location errors. This latter length more closely matches the rupture length suggested by Nakamura (1992), and was used for this study.

### 5.5.2 Geodetic constraints

#### Levelling data

For the 1960 event, pre-earthquake levelling was performed during 1957-1959 along a line running 150 km northeast from Concepcion to Parral, and 600 km south from Concepcion to Puerto Montt (Fig. 5.8a) (Barrientos & Ward, 1990). A repeat survey was performed from 1963-1964. The levelling line was nearly parallel to the coast, so the data provided very little constraint to the 2-D dislocation model (Fig. 5.12a). Coseismic deformation for the 1985 event was inferred from first-order levelling line from San Antonio to Santiago, with 30 km between San Antonio and Valparaiso being parallel to the coast line (Fig. 5.9) (Barrientos, 1988). The initial survey was carried out in 1981 and the repeat survey in 1985. Levelling data plotted as function of distance landward from the coast shows roughly 0.5 m of relative uplift near San Antonio, decreasing to 0.1-0.2 m relative subsidence about 60 km inland (Fig. 5.12b) (Barrientos, 1995).

### **Tide gauge data**

No tide gauge data were used to constrain dislocation models along the Chile Margin: the only relevant tide gauge station for the 1960 event was operational since 1942, but had no data from 1954-1964, and records analyzed since 1964 showed a rapid postseismic deformation (Wyss, 1979); for the 1985 event, relevant tide gauge data was continuous for only 3 years prior to the event, and the short tidal record since does not exclude postseismic effects (Barrientos, 1995); and for the 1943 and 1971 thrust events, no tide gauges were located in the rupture areas.

### **Coastal data**

Measurable coseismic deformation data for the 1960 event include similar sources listed for South Alaska (Plafker & Savage, 1970). These data consist of some 155 post-earthquake coastal points located in the middle and southern regions of the rupture area. The general pattern of coseismic uplift and subsidence is shown in Figure 5.8b. A band 100 km wide perpendicular to the trench was projected onto the South Chile profile to constrain the 2-D dislocation model (Fig. 5.12a).

### **5.5.3 Comparison with thermal model results**

For the 1960 great thrust earthquake, a 110+20 km locked plus transition zone width dislocation model best matched the available coseismic deformation pattern (Fig. 5.12a). This compares very well with thermal model of 120+30 km locked plus transition (Fig. 5.13). Unlike the South Alaska and remaining Chile Margin profiles, where there is subduction of older plate material and the seismogenic zones are limited downdip by the continental Moho, the South Chile profile may be thermally controlled downdip due to the young (~5 Ma) plate age. Unfortunately, the landward extent of the coseismic rupture area is unconstrained because of the limited number and poorly located aftershocks and the lack of good tsunami model limit. An important consideration in fitting the dislocation model to the 1960 coseismic deformation data is that it was collected 8 years after the event, and thus includes postseismic rebound effects. The model accuracy is further limited because the dip profile geometry is

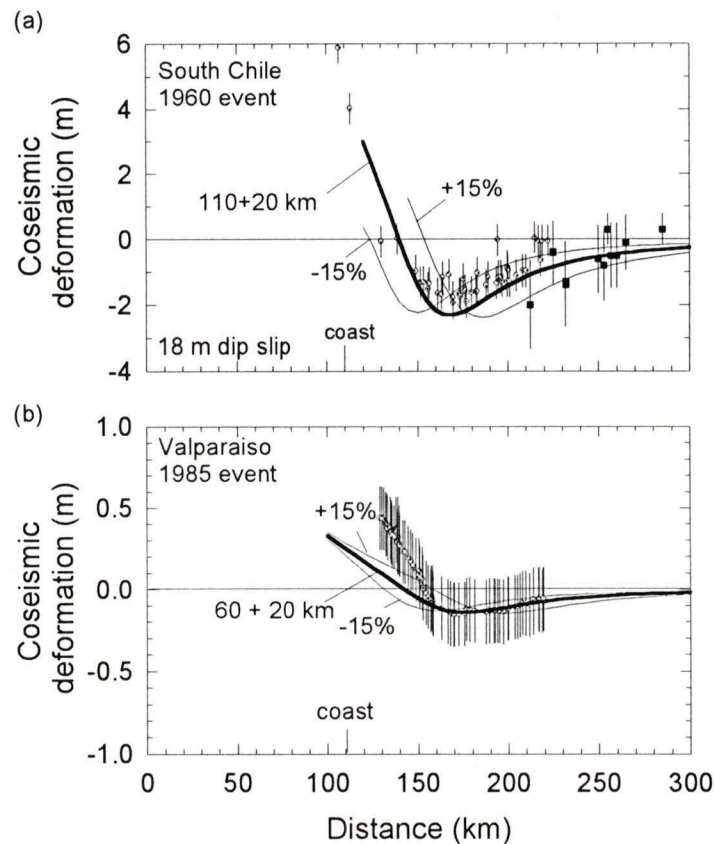


Figure 5.12. Profile of coseismic vertical motion across the southern Chile Margin. (a). Observed deformation from lower and upper marine growth limits (solid circles) and from repeat levelling along the Puerto Montt-Concepcion line for the 1960 event (after *Plafker & Savage* [1970]). The data presented above were collected 8 years following the 1960 event, and have likely been influenced by postseismic effects. This may effect the magnitude of the deformation, but does not significantly affect the pattern of deformation. (b) Observed deformation from repeat levelling for the 1985 event. Discontinuous slip models (e.g., *Barrientos* [1988]) render a better match to the rupture area, which is highly variable along the thrust plane and is poorly fit by elastic dislocation models (see text for details).

poorly constrained by Wadati-Benioff seismicity which occurred 500 km to the north. A conservative error estimate in the width of the seismogenic zone is roughly  $\pm 40$  km. The fact that the coseismic rupture width reported by *Plafker & Savage* (1970) was apparently insensitive to the change in subducting plate age (2-3 Ma to 20-25 Ma, south to north) along the rupture area may be an artifact of the poorly constrained source area analysis, and not the actual.

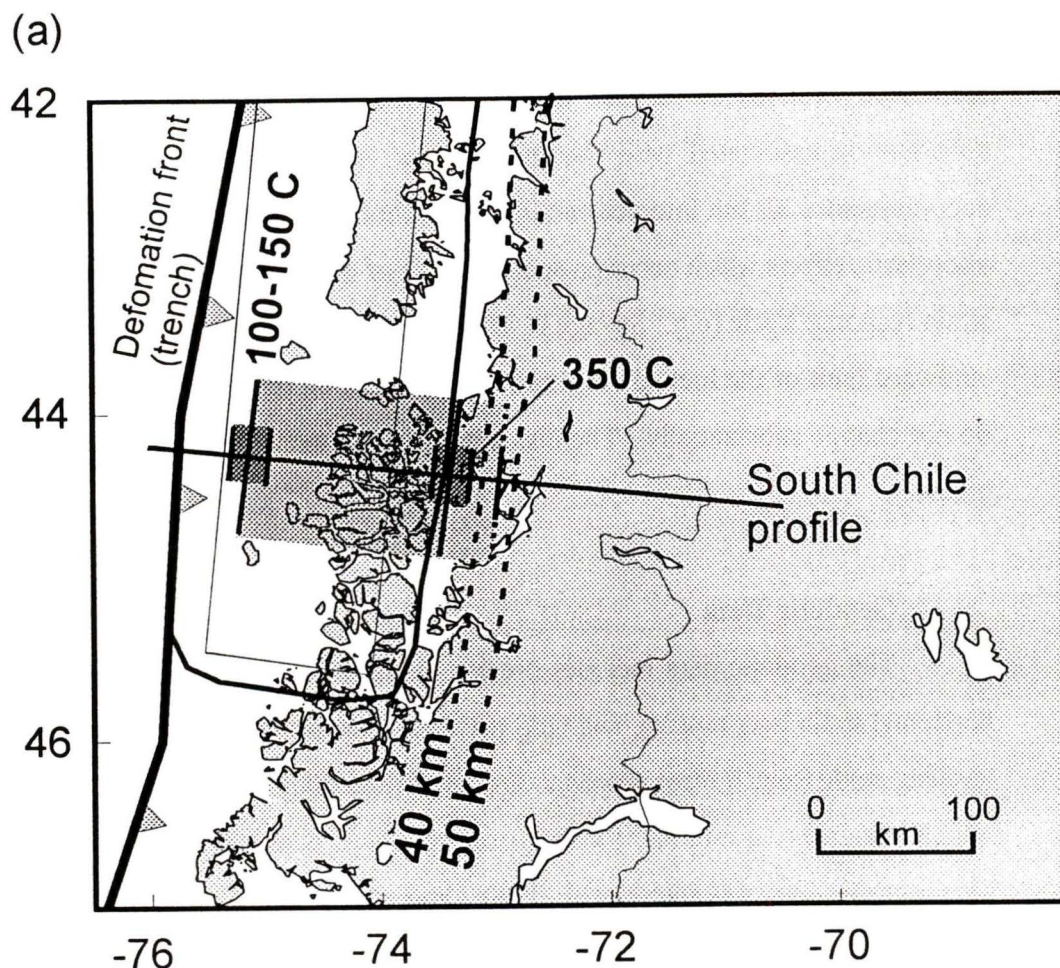


Figure 5.13. (a) The widths of the locked and transition zones from the thermal analysis (short thick lines) compared to those from the dislocation model (stippled areas) for the South Chile profile. The tsunami (rectangle) and aftershock envelope (closed loop) are also included from Figure 5.8. The bands on the thermal limits indicate the estimated uncertainties.

The coseismic dislocation model applied to the 1985 event constrained by the relative levelling along a profile predicts a  $60+20$  km locked plus transition zone width (Fig. 5.12b). This is similar in width to the estimates obtained from the thermal model of  $60+20$  km. However, the one day aftershock envelope width and the relocated intermediate thrust events were roughly 60 km further downdip than the thermal model limit (Fig. 5.13b). The surface deformation pattern has a peak coseismic subsidence roughly 140 km landward of the deformation front or a 90 km wide locked zone, and therefore requires the downdip limit of the corresponding locked zone to be around 140 km landward. This limit corresponds to a

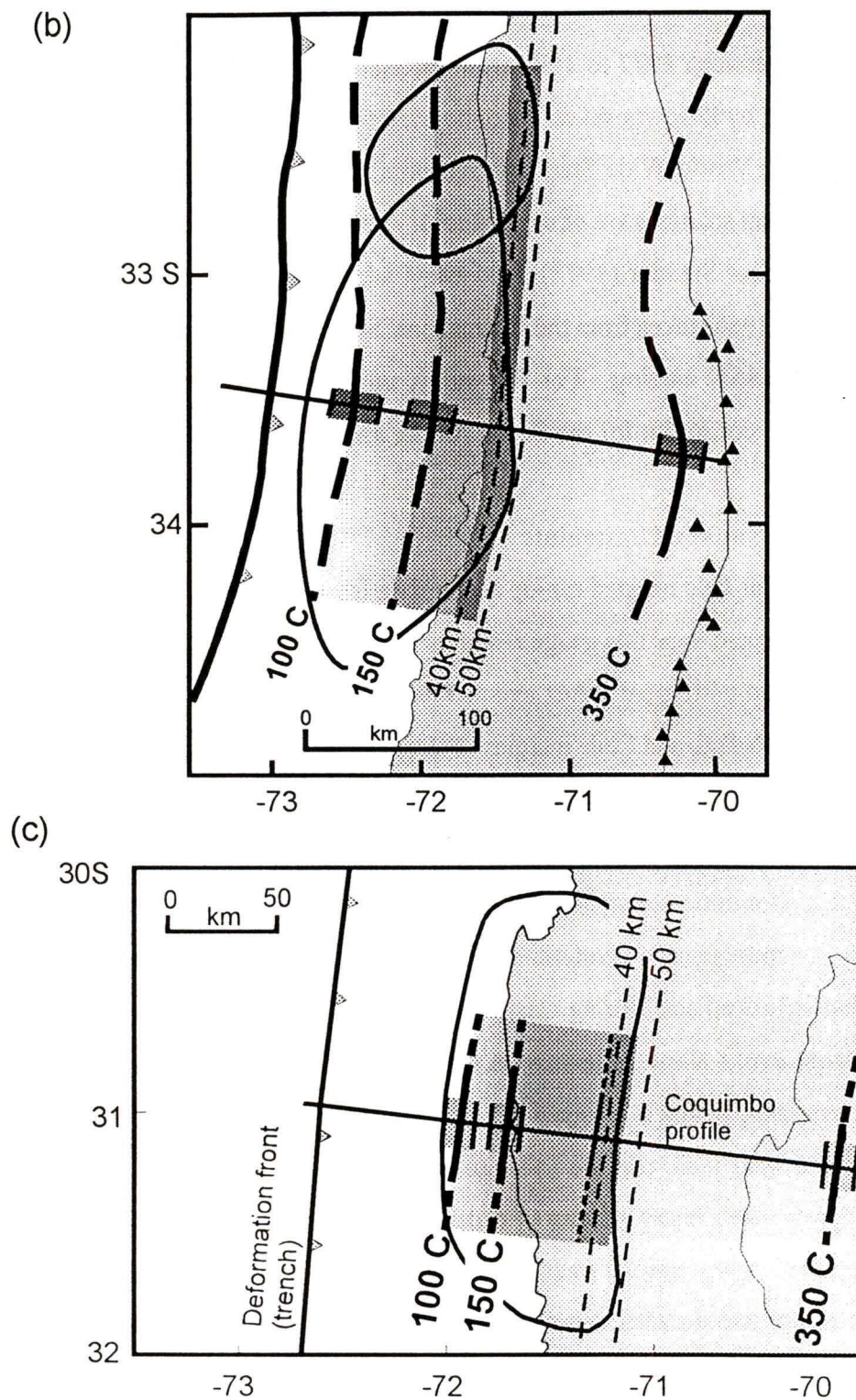


Figure 5.13 (continued). Seismogenic width estimates from thermal model and from the continental Moho downdip constraint for (b) the Valparaiso profile and for (c) the Coquimbo profile. In both cases, the continental Moho occurs above the 350°C thermal limit along the thrust plane, and constrains the downdip limit in good agreement with the aftershock envelopes. A narrow, 10 km wide transition zone is divided by the inferred 40 km Moho depth.

depth of 50-55 km, below the average estimated depth to continental Moho of 40-45 km (Schmitz, 1994; Schwarz et al., 1994; Wigger et al., 1994). The addition of the transition zone does not change this downdip limit substantially.

Barrientos (1988) described the inadequacy of numerous simple planar fault dislocation models, which range from  $20^\circ$  to  $35^\circ$  in dip and  $\pm 3$  m in slip to obtain a reasonable match to the levelling data. However, a better fit was given by a variable or gradient slip model which concentrated the slip deficit along a dip profile of  $18^\circ$  at a depth of 30-40 km in two patches, north and south of the levelling line. The northern asperity was coincident with the southern rupture limit of the 1971 event and with the 1985 foreshock sequence, while the southern patch was coincident with a smaller thrust event (Tichelaar & Ruff, 1991). The intervening region of the levelling line may therefore have been a region of greater slip during the interseismic period (Barrientos, 1988), and may explain the poor match obtained from the elastic models. It failed to explain, however, the landward distribution of the levelling data, and this misfit problem remains unresolved.

For the remaining three profiles, Coquimbo, Taltal, and North Chile, there is neither interseismic, coseismic, nor tsunami data with which the dislocation model may be constrained. The only comparison comes from the updip, seaward thermal limit to the seaward extent of aftershock envelope, and the downdip, landward limit to the continental Moho depth of roughly 40-45 km (Fig. 513c & d). Although these three profiles are more poorly constrained, the aftershock distribution provide support for the updip seaward thermal limit.

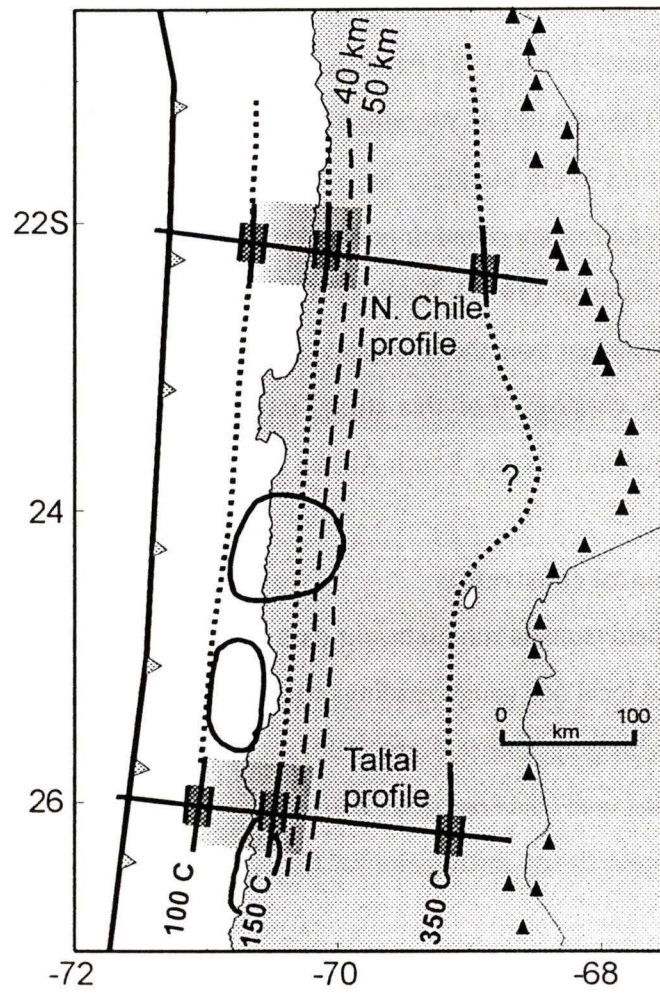


Figure 5.13 (continued) (d). Same as for (b) and (c), but for the Taltal and North Chile profiles.

## 5.6 NANKAI

Most of this analysis has been given by Hyndman et al. (1995), but it is presented here for comparison with the other margins studied.

### 5.6.1 Seismicity constraints

#### 1944 & 1946 Main events

The southwest margin of Japan is unique from the other margins pursued in this study in that a historical earthquake record exists for the past 1300 years (Ando, 1975). The 6 most recent earthquakes suggest a recurrence interval of  $111 \pm 21$  years, and the most recent interval was 90-92 years ago (Kanamori, 1972). The two most recent earthquakes were December 7, 1944 (Tonankai) with an epicentre at  $33.70^\circ\text{N}$ ,  $136.05^\circ\text{E}$ , and the more southern December 20, 1946 (Nankaido) with an epicentre at  $33.13^\circ\text{N}$ ,  $135.84^\circ\text{E}$  (Fig. 5.14). The rupture initiation occurred at roughly  $30 \pm 10$  km depth for both events, and a seismic moment of  $1.5 \times 10^{21}$  Nm ( $M_w$  8.0) has been estimated for both events (Ando, 1982) (Kanamori, 1972; Ando, 1975). The absence of modern seismograph stations excludes accurate determination of fault plane solutions, but first-motion data has been interpreted with a preferred dip between  $10$ - $30^\circ$  approximately in the direction of plate motion (Kanamori, 1972). Average estimated dislocations along the thrust plane are on the order of 3 m.

#### 1944 & 1946 Aftershock activity

The one day aftershock distributions for both events suggest the earthquake rupture initiated to the north and propagated toward the southwest, covering a surface area of approximately 80 km wide by 120 km long (Fig. 5.14) (Kanamori, 1972). The one month aftershock distribution for the Tonankai event remained similar in size to the one day pattern, whereas for the Nankaido event the envelope doubled in width and extended an additional 100 km southwestwards (Fig. 5.14) (Kanamori, 1972). The seaward limit of the aftershocks for both events was about 50 km landwards of the deformation front (Kanamori, 1972). As has been observed for all other cases in this study which have experienced thrust events, the increase in the envelope with time may suggest aseismic strain release along the thrust plane.

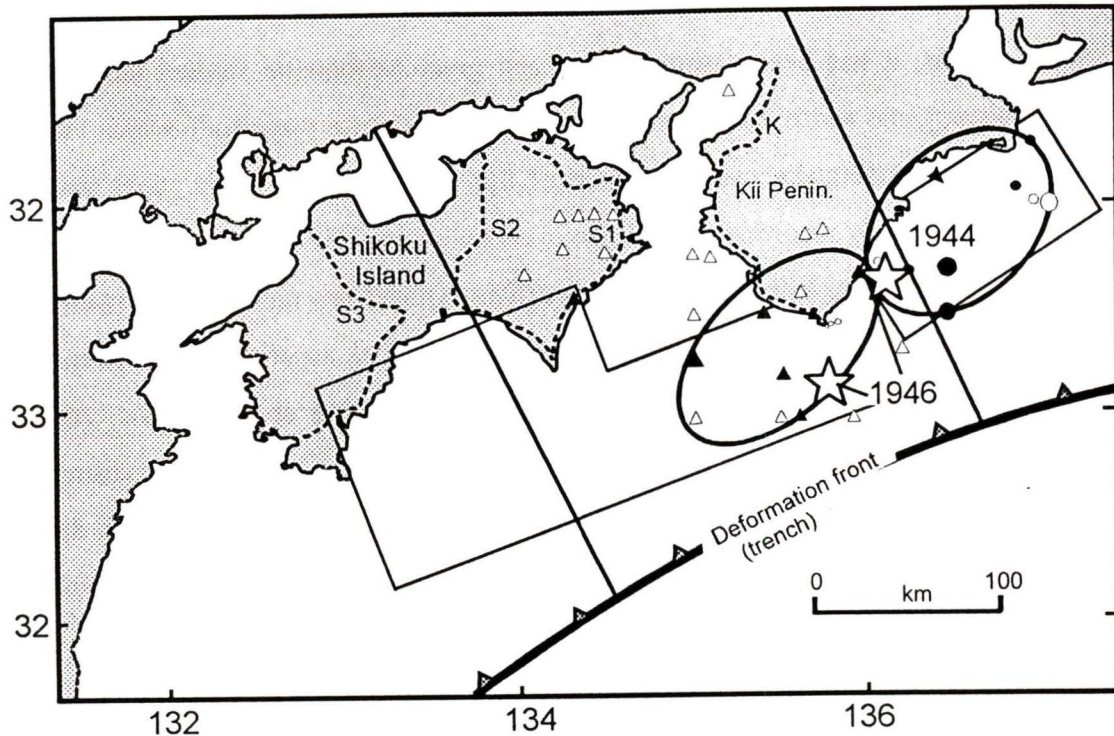


Figure 5.14. Seismic activity for the Nankai Margin, showing the Mw 8.0 1944 and 1946 main thrust events (large stars) and one day aftershocks (solid circles and triangles respectively). The small ellipses denote the one day aftershock envelopes after *Kanamori* [1972]. Progressive creep landwards is evident from the two month aftershock distribution, particularly for the 1946 Nankaido event (open triangles). Depth contours (dashed lines) are inferred from the top of the subducting Philippine Sea Plate. The rectangular areas are the earthquake dislocation areas defined by tsunami and geodetic data after *Aida* [1981] & *Ando* [1982]. Repeat levelling data was acquired from the four levelling lines, S1, S2, S3, & K.

### Tsunami constraints

*Ando* (1975) reports that two distinct waves sources were associated with the Nankaido great earthquake. The source area of the larger, initial wave corresponded well to the one day aftershock distribution, while the source area for the smaller wave extended to the south, in the direction of the expanded aftershock distribution. Most of the tsunami wave dislocation was associated with the main fault rupture (*Ando*, 1982). In similar tsunami wave studies, *Aida* (1981) obtained a total fault dislocation widths of 70 km for Tonankai and 120 km Nankaido (Fig. 5.14). These estimates extend to within 70-100 km of the deformation front, and support the hypothesis that the initial rupture occurred in the short time interval of the main shock followed by the slower rupture to the south.

## 5.6.2 Geodetic constraints

### Levelling data

Numerous repeat levelling surveys have been carried out over the past 100 years, providing both interseismic and coseismic deformation data. The S1, S2, S3, and K lines are of interest to this study (Fig. 5.14) (Thatcher, 1984; Hyndman et al., 1995). Levelling was accurate to first-order requirements, and has been corrected for isostatic and tectonic deformation (Thatcher, 1984). The landward ends of the levelling lines were fixed to near-zero interseismic deformation rates as indicated by the coseismic deformation data (Hyndman et al., 1995). This resulted in a slight difference between the coseismic and interseismic deformation profiles at their seaward ends, but does not affect the estimated width of the locked zone (see discussion in Hyndman et al., 1995). No re-levelling was done between the 1944 and 1946 earthquakes, and therefore the coseismic displacements are for the two events combined (Thatcher, 1984).

Dislocation models were used to investigate coseismic deformation (1947-1929/39) and early to middle interseismic (1979-1964) (Fig. 5.15a-f). The 10-15 year postseismic data are a factor of two greater in uplift rates than the interseismic deformation, and were neglected for this study. The coseismic deformation was also inverted and divided by the most recent strain accumulation period since the last event 90-92 years ago for comparison to the interseismic data (Fig. 5.15b, d, & e). Of the three levelling lines to which the Nankaido profile was compared, lines S2 and S3 provided the tightest constraint to the locked and transition zone widths. The S1 line, closer to the shoreline line, may have been subject to regional tectonic deformation unrelated to the earthquake cycle (see discussion Hyndman et al., 1995), and provides a weaker constraint. The K line constrained the coseismic and interseismic models for the northern Tonankai profile (Fig. 5.15a & b).

### Tide gauge data

Twenty seven tide gauges operating from 1950-1985 are situated around the southern half of Japan, 16 of which occur near the Nankaido and Tonankai model profiles. The data show a spatial pattern of uplift that matches the general pattern of the levelling data (Fig

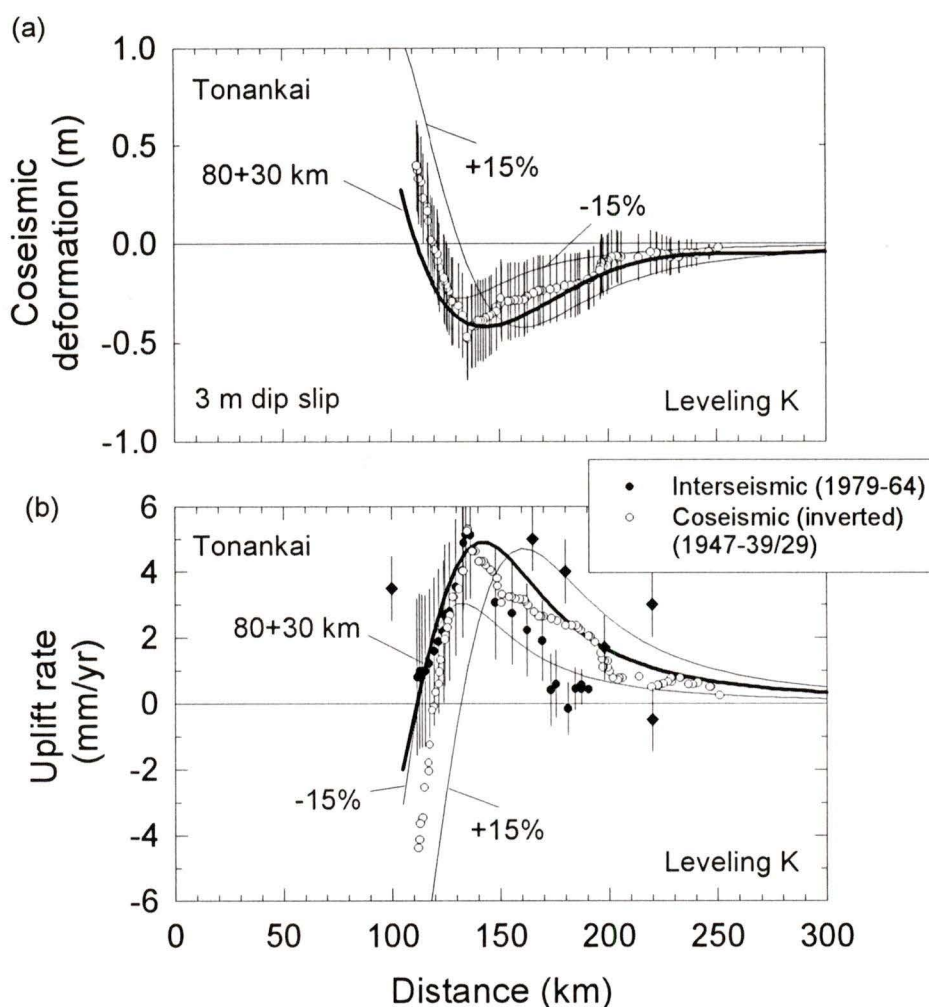


Figure 5.15. Repeat levelling data for the Nankai Margin after *Hyndman et al.* [1995]. (a) Coseismic deformation in metres along the levelling line K. The dislocation model predicts between 3-4 m dip slip associated with the 1944/46 events. (b) Interseismic repeat levelling (solid circles), interseismic tide gauge (solid diamonds), and inverted coseismic repeat levelling (open circles) deformation data for the Tonankai profile as fit by the simple 2-D dislocation model. The inverted coseismic deformation is compared to the interseismic deformation by dividing its magnitude by the time since the last great events, 90-92 years ago (*Ando* [1982]).

5.15a-f). However, the noticeable poorer constraint provided by the tide gauge data may be due to differential strain accumulation along the thrust plane as there is a considerable change in dip between the Nankaido and Tonankai profiles (e.g., *Savage & Thatcher*, 1992).

### 5.6.3 Comparison with thermal model results

For the Nankai Margin, the product of the rate of interseismic deformation and the recurrence interval since the two most recent events approximately equals the inverse of the coseismic deformation (e.g., Fig. 5.15b, d, & f) (Hyndman et al., 1995). It is also found that the interseismic locked zone closely matches the coseismic rupture zone (Fig. 5.16). Thus

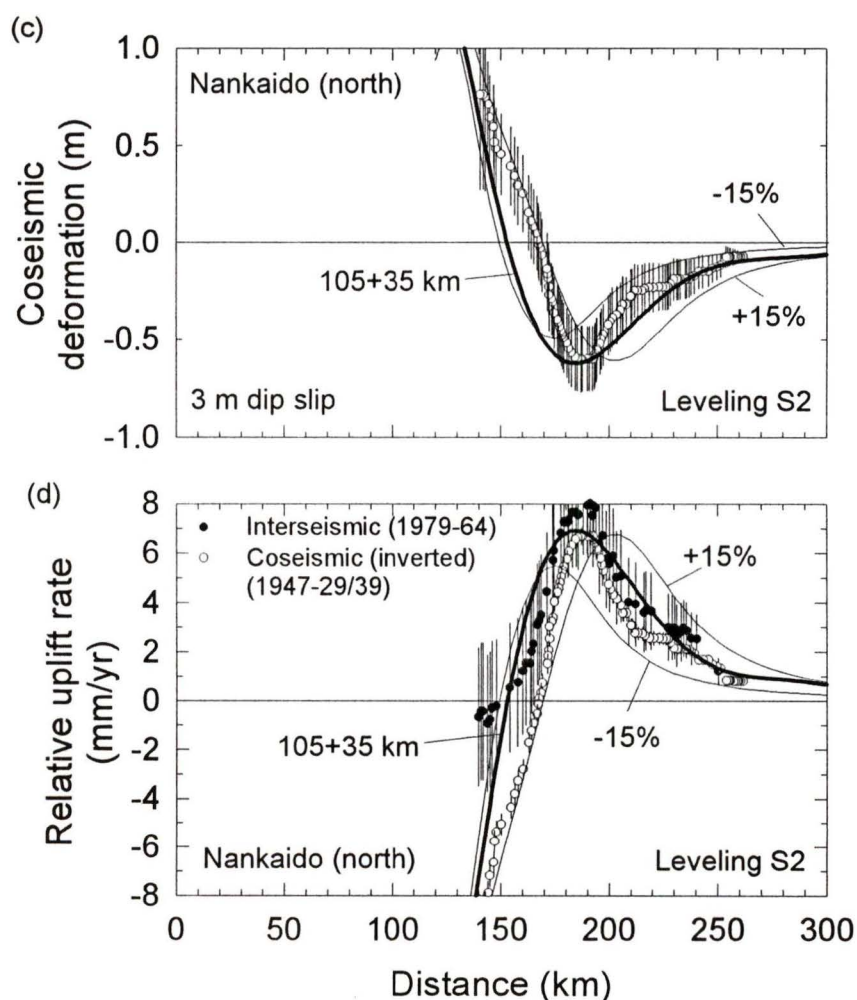


Figure 5.15 (continued). Repeat levelling for the southern Nankaido profile across the Nankai Margin after Hyndman et al. [1995]. (c) Coseismic deformation along levelling line S2, situated to the north of the Nankaido profile. (d) Interseismic levelling, tide gauge, and inverted coseismic deformation data for same levelling line. The preferred dislocation model was constrained by both the coseismic deformation and by the interseismic strain rate along the length of the levelling line. Symbols are as given in (b).

the earthquake cycle is, to a first order, elastic. The dislocation models for Nankaido give a 150+35 km locked plus transition zone width, compared with the thermal estimate of 120+55 km, and a 90+40 km compared with 80+30 km width for the Tonankai profile (Fig. 5.16). The levelling lines S2 and S3 are best constrained by dislocation models roughly 5-10 km wider than predicted by the thermal models. Uncertainties to the width of seismogenic zones correspond to a total error of roughly  $\pm 15$ -20 km.

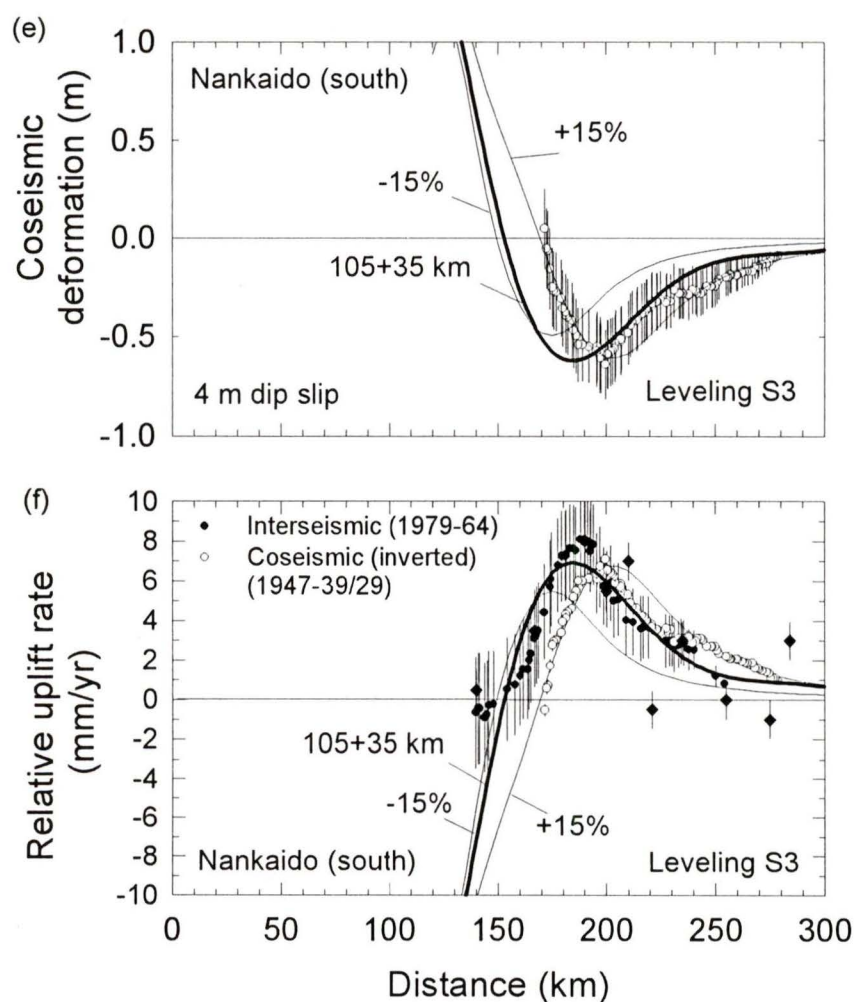


Figure 5.15 (continued). Repeat levelling for the southern Nankaido profile across the Nankai Margin after *Hyndman et al.* [1995]. (e) Coseismic deformation along levelling line S3, situated to the south of the Nankaido profile. (f) Interseismic (open circles) and inverted coseismic (grey circles) deformation data for same levelling line.

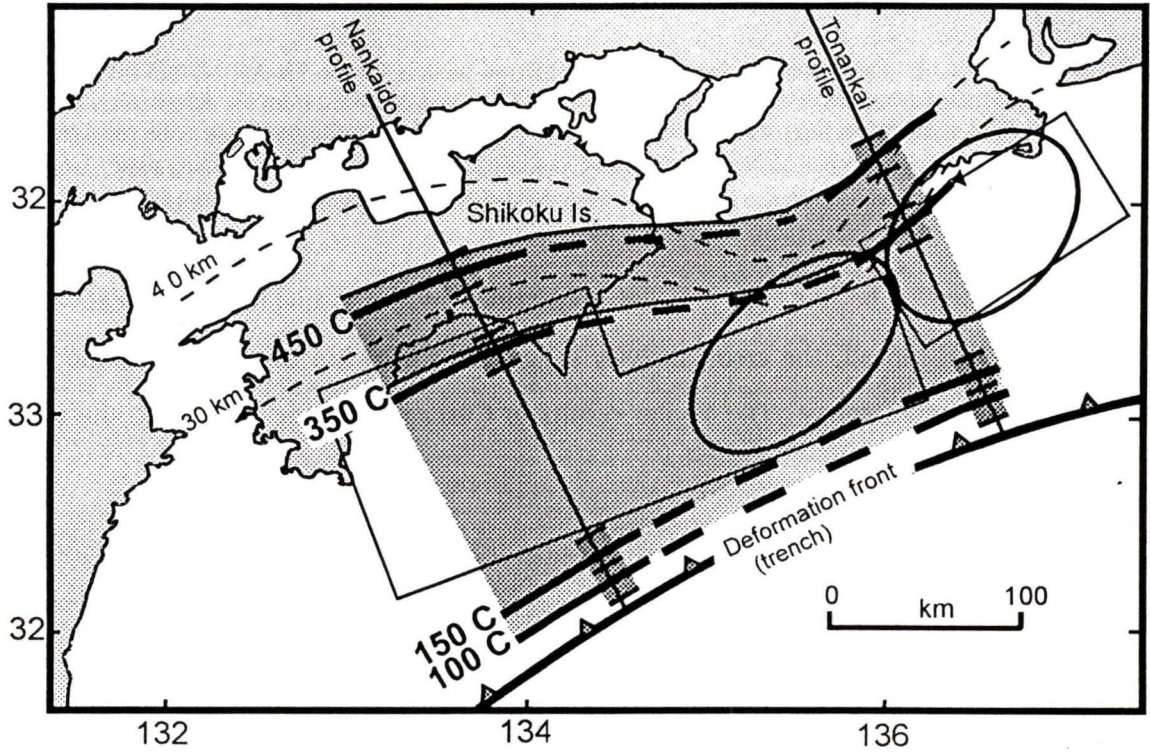


Figure 5.16. The widths of the locked and transition zones from the thermal analysis (short thick lines) compared to those from the interseismic and coseismic deformation (stippled areas). Included are the tsunami (rectangle) and one day aftershock envelopes (closed loop) from Figure 5.5. Error bands on the thermal limits are the same as for Figure 5.13.

## CHAPTER VI DISCUSSION AND CONCLUSIONS

### 6.1 SEISMOGENIC WIDTH PREDICTIONS

#### 6.1.1 Thermal model

##### **Constraints to seismogenic zones**

Thermal constraint modelling has been applied to 4 subduction zones with the aim of determining the downdip limits to the seismogenic zone responsible for the generation of great thrust earthquakes. The updip and downdip limits of the seismogenic zone may be thermally controlled: the updip thermal limit may correspond to the dehydration of marine clays, changing from stable-sliding to stick slip at about 100-150°C; the downdip limit may correspond a brittle to ductile transition of the contact rocks, changing from stick slip to stable-sliding downdip. The limit for crustal rocks is inferred to coincide with an increase in shear stress around 350°C. Thus from 100-150°C to 350°C, velocity weakening along the contact thrust fault is said to occur, producing the region of potential earthquake generation. The landward position of this limit is important to the earthquake hazard for coastal cities: the closer the downdip limit of the locked zone is to the coast, the greater intensity the shaking will be felt. A transition zone is taken to occur downdip of the locked zone, in which the earthquake rupture decreases to zero. For the subduction of young, hot oceanic crust, these thermal limits are believed to apply. For subduction of old, cold crust, stable-sliding serpentinite may provide the downdip limit.

##### **Uncertainty analysis**

Temperatures on the subduction thrust were found to be sensitive to several parameters. The non-thermal parameters include the convergence rate, the oceanic plate age, the sediment thickness at the deformation front, and the dip profile geometry of the subducting plate. The thermal models were most sensitive to the oceanic plate age and to the dip profile geometry. The uncertainty associated with the décollement level is poorly constrained, but may add an additional  $\pm 10$  km. The combined uncertainty in the position of the critical temperatures is about  $\pm 25$  km. The thermal parameters assigned to the accretionary prism, the continental plate, and the subducting oceanic plate include the thermal

conductivity, the radiogenic heat generation, and the thermal heat capacity. The uncertainty in these values was constrained by surface heat flow data, mainly for Cascadia and Nankai (SW Japan). The uncertainty in the position of the 100-150°C and 350°C temperatures from the thermal parameters was about  $\pm 5$  km. The uncertainty in the critical temperatures from factors such as composition variations was estimated to be about  $\pm 25^\circ\text{C}$  or  $\pm 10$  km.

### **6.1.2 Seismogenic width constraints**

The results of the thermal models were compared to seismic, tsunami, and geodetic data which provided constraint to the widths of the seismogenic zone. The seismic data included main shock, aftershock, and intermediate magnitude thrust earthquakes and provided constraint on the coseismic rupture width and downdip rupture extent, while the tsunami data provided the updip rupture limit only. The geodetic data provided updip and downdip constraint for both the coseismic and interseismic deformation from 2-D elastic dislocation models constrained by precise levelling, tide gauge, and coseismic surface deformation. The pattern of deformation observed in the surface deformation data was assumed to be elastic: strain accumulating along the subduction thrust plane during the interseismic period will be released in a sudden, coseismic rupture. For Cascadia, interseismic deformation was used to constrain the 2-D dislocation models, for South Alaska and Chile, only coseismic deformation was used, and for Nankai, both interseismic and coseismic surface deformation data was used.

#### **Uncertainty analysis**

The 2-D dislocation models were found to be sensitive to the convergence rate and to the dip of the subducting plate, and, for the coseismic deformation, to the amount of slip along the thrust plane. The scatter of the levelling and tide gauge data inferred  $\pm 10$  km horizontal uncertainty, and the combined uncertainty in the width of the locked and transition zones given by the dislocation models was about  $\pm 20$  km.

## 6.2 CONCLUSION

A comparison of the thermal and dislocation model results are presented in Figure 6.1. The Juan de Fuca plate (6-7.5 Ma), Cascadia, created narrow locked and transition zones. The thermal model results estimated widths from fairly narrow around Vancouver Island (45+45 km), wider in conjunction with the more gentle beneath the Olympic Peninsula (85+85 km), and more narrow farther south into Oregon (55+55 km) (Table 6.1). This compares well with the estimates from the 2-D dislocation model (Table 6.1). For both models, the landward limit of the locked zone is located offshore over the length of the margin. The landward limit of the transition zone lies within 20 km of the coast for most of the margin,

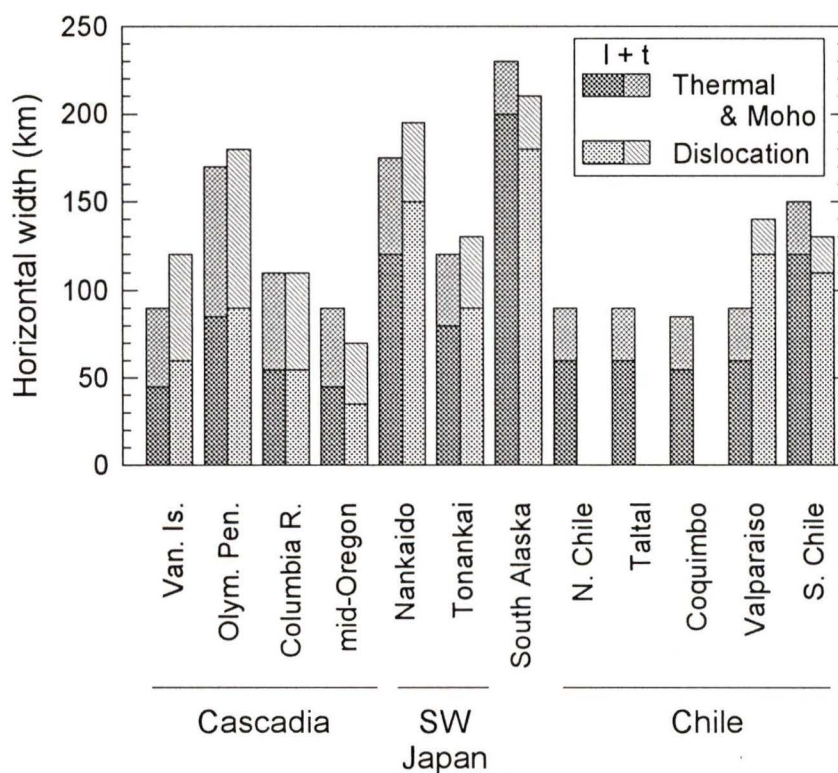


Figure 6.1. Histogram plot of the horizontal widths of the locked and transition zones from both the thermal and dislocation models. With the exception of the Valparaiso profile, Chile Margin, the agreement between the two models is very good. No dislocation models exist for North Chile, Taltal, and Coquimbo profiles as there was no interseismic nor coseismic deformation data. l+t: locked + transition zone.

| Margin       |               | 2-D Thermal model |                           | 2-D<br>dislocation<br>model<br>l+t (km) | Seismicity |                            |                           |
|--------------|---------------|-------------------|---------------------------|---|------------|----------------------------|---------------------------|
|              |               | l+t<br>(km)       | seaward<br>offset<br>(km) |   | Event      | Aftershock<br>distribution |                           |
|              |               |                   |                           |   |            | width<br>(km)              | seaward<br>offset<br>(km) |
| Cascadia     | Vancouver Is. | 45 + 45           | 0                         | 60 + 60                                 | --         | --                         | --                        |
|              | Olympic Pen.  | 85 + 85           | 0                         | 90 + 90                                 | --         | --                         | --                        |
|              | Columbia R.   | 55 + 55           | 0                         | 55 + 55                                 | --         | --                         | --                        |
|              | mid-Oregon    | 45 + 45           | 0                         | 35 + 35                                 | --         | --                         | --                        |
| South Japan  | Nankaido      | 120 + 55          | 40                        | 150 + 45                                | 1946       | 70                         | 50                        |
|              | Tonankai      | 80 + 40           | 40                        | 90 + 40                                 | 1944       | 80                         | 70                        |
| South Alaska |               | 200 +(30)         | 70                        | 180 + 30                                | 1964       | 180                        | 70                        |
| Chile        | North Chile   | 60 + (30)         | 50                        | --                                      | --         | --                         | --                        |
|              | Taltal        | 60 + (30)         | 50                        | --                                      | --         | --                         | --                        |
|              | Coquimbo      | 55 + (20)         | 50                        | --                                      | 1943       | ~70†                       | 40†                       |
|              | Valparaiso    | 60 + (20)         | 40                        | 120 + 20                                | 1971/85    | 60/80                      | 40/20                     |
|              | South Chile   | 120 + 30          | 50                        | 110 + 20                                | 1960       | ~150†                      | 0†                        |

Table 6.1. Estimated locked and transition zone widths (l+t) from the thermal and 2-D elastic dislocation models. The locked zone widths are compared to the aftershock seismicity distribution associated with great and megathrust events considered in this study. Those margins for which the thermal-Moho model was used to constrain the downdip limit of the locked zone have transition zone widths given in parenthesis. The seaward offset is the distance landward from the deformation front for the updip limit. †: denotes poorly constrained seaward and landward rupture limits for this earthquake.

except for the Olympic Peninsula, where it is about 70-80 km landward.

The subduction of Philippine Sea plate (15 Ma), Nankai (SW Japan), produced wider locked and transition zone widths for the Tonankai profile (80 + 40 km) than for the more northern Nankaido profile (120 + 55 km), but compares well with the estimates from the 2-D dislocation model (Fig. 6.1). The greater widths for Nankaido are due to a more gentle plate dip at 100 km landward of the deformation front. The Philippine Sea Plate is initially cooler than the Juan de Fuca Plate, and so reaches the 100-150°C stable-sliding to stick-slip transition temperature at a greater distance downdip, moving the seaward limit about 40 km

landward. The model width estimates match the aftershock and tsunami inversion rupture areas fairly well (Table 6.1).

For South Alaska, the subduction of the older, colder, gently dipping Pacific Plate (50 Ma) creates a wide locked zone (Fig. 6.1). The plate steepens landward and the 350°C downdip thermal limit occurs around a depth of 80 km. The base of the continental lithosphere may determine the downdip limit with serpentinization of forearc mantle olivine, initiating stable-sliding. Assuming an average forearc Moho depth of 40-45 km from seismic refraction data, the locked zone width for the South Alaska profile is 175 km, or about 245 km landward of the deformation front. A poorly constrained model transition zone straddles the Moho by 15 km updip and downdip. The locked and transition corresponds well with the 2-D dislocation results of 180+30 km (210 km landward of the deformation front) (Fig.6.1). The model width estimates match the aftershock and tsunami inversion rupture areas from the 1964 megathrust earthquake fairly well (Table 6.1).

For Chile, both the thermal and Moho downdip limits are required on account of the great variation in the subducting age (5-50 Ma, south to north). For the South Chile profile (5 Ma), the Nazca Plate is of similar age to the Juan de Fuca Plate for the Cascadia Margin but the much thinner sediment cover at the deformation front allows for greater plate cooling. The updip thermal limit is therefore 50 km landward of the deformation front. The widths are in good agreement with the 2-D dislocation model (Fig. 6.1). Northward, the Valparaiso, Coquimbo, Taltal, and North Chile profile locked zone widths are considered to be thermal updip and Moho downdip constrained. For the Valparaiso profile, these width estimates compare poorly with the 2-D dislocation model (120+20 km), a discrepancy that remains unresolved (Fig. 6.1). The width estimates from the thermal model for the South Chile profile compare well with tsunami inversion rupture area for the 1960 megathrust earthquake (Table 6.1). The 1971 and 1985 great thrust events produce aftershock rupture areas which also compare well with the thermal updip and Moho downdip model for the Valparaiso profile (Table 6.1).

**BIBLIOGRAPHY**

- Abe, K., Size of great earthquakes of 1837-1974 inferred from tsunami data, *Journal of Geophysical Research*, 84, 1561-1568, 1979.
- Abers, G.A., Relationship between shallow- and intermediate-depth seismicity in the eastern Aleutian subduction zone, *Geophysical Research Letters*, 19, 2019-2022, 1992.
- Adams, J., Paleoseismicity of the Cascadia subduction zone: Evidence from turbidites off the Oregon-Washington margin, *Tectonics*, 9, 569-583, 1990.
- Aguirre, L., The southern Andes, in *The Ocean Basins and Margins*, vol. 7A. The Pacific Ocean, edited by A. E. M. Nairn, F. G. Stehli, and S. Uyeda, pp. 265-376, Plenum Press, New York, 1985.
- Aida, I., Numerical experiments for the tsunamis generated off the coast of the Nankaido district, *Bulletin of Earthquake Research Institute, University of Tokyo*, 56, 715-730, 1981.
- Algermissen, S. T., W. A. Rinehart, R. W. Sherburne, and W. J. Dillinger, Preshocks and aftershocks of the Prince William Sound earthquake of March 28, 1964, 10-3, vol. II, Coast and Geodetic Survey Publication, 1969.
- Ambos, E. L., W. D. Mooney, and G. S. Fuis, Seismic refraction measurements within the Peninsular terrane, south central Alaska, *Journal of Geophysical Research* 100, 4079-4095, 1995.
- Ando, M., Source mechanism and tectonic significance of historical earthquakes along the Nankai Trough, *Tectonophysics*, 27, 119-140, 1975.
- Ando, M., A fault model of the 1946 Nankaido earthquake derived from tsunami data, *Physics of Earth and Planetary Interiors*, 28, 320-336, 1982.
- Apperson, K. D., and C. Frohlich, The relationship between Wadati-Benioff zone geometry and P,T,B axes of intermediate and deep focus earthquakes, *Journal of Geophysical Research* 92, 13821-13831, 1987.
- Araujo, M., and G. Suarez, Geometry and state of stress of the subducted Nazca plate beneath central Chile and Argentina: evidence from teleseismic data, *Geophysical Journal International*, 116, 283-303, 1994.
- Ashi, J., and Taira, A., Thermal structure of the Nankai accretionary prism as inferred

- from the distribution of gas hydrate BSRs, in *Thermal Evolution of the Tertiary Shimanto Belt, Southwest Japan: An example of ridge-trench interaction*, edited by M.B. Underwood, *Special Paper*, 273, 137-149, 1993.
- Atwater, B., A. Nelson, J. Clague, G. Carver, D. Yamaguchi, P. Bobrowski, J. Bourgeois, M. Darienzo, W. Grant, E. Hemphill-Haley, H. Kelsey, G. Jacoby, S. Nishenko, S. Palmer, C. Peterson, and M. Reinhart, Summary of coastal geologic evidence for past great earthquakes at the Cascadia subduction zone, *Earthquake Spectra*, 11, 1-18, 1995.
- Atwater, B.F., and D.K. Yamaguchi, Sudden, probable coseismic submergence of Holocene trees and grass in coastal Washington State, *Geology*, 19, 706-709, 1991.
- Atwater, B. F., Evidence for great Holocene earthquakes along the outer coast of Washington State, *Science*, 236, 942-944, 1987.
- Barazangi, M., and B. L. Isacks, Spatial distribution of earthquakes and subduction of the Nazca Plate beneath South America, *Geology*, 4, 686-692, 1976.
- Barker, F., G.L. Farmer, R.A. Ayuso, G. Plafker, and J.S. Lull, The 50 Ma granodiorite of the eastern Gulf of Alaska: melting in an accretionary prism in the forearc, *Journal of Geophysical Research*, 97, 6757-6778, 1992.
- Barrientos, S. E., and S. N. Ward, The 1960 Chile earthquake: inversion for slip distribution from surface deformation, *Geophysical Journal International*, 103, 589-598, 1990.
- Barrientos, S. E., G. Plafker, and E. Lorca, Postseismic coastal uplift in southern Chile, *Geophysical Research Letters*, 19, 701-704, 1992.
- Barrientos, S. E., Dual seismogenic behaviour: The 1985 Central Chile earthquake, *Geophysical Research Letters*, 22, 3541-3544, 1995.
- Barrientos, S. E., Slip distribution of the 1985 Central Chile earthquake, *Tectonophysics*, 145, 225-241, 1988.
- Bartsch-Winkler, S. and H.R. Schmoll, Utility of radio carbon-dated stratigraphy in determining late Holocene earthquake recurrence intervals, upper Cook Inlet, Alaska, *Geological Society of America Bulletin*, 104, 684-694, 1992.
- Beaudoin, B. C., G. S. Fuis, W. J. Lutter, W. D. Mooney, and T. E. Moore, Crustal velocity structure of the northern Yukon-Tanana upland, central Alaska: Results from TACT refraction/wide-angle reflection data, *Geological Society of America Bulletin*,

106, 981-1001, 1994.

- Beck, M.E., Jr., Analysis of Late Jurassic-Recent paleomagnetic data from active plate margins of South America, *Journal of South America Earth Science*, 1, 39-52, 1988.
- Behrmann, J.H., S.D. Lewis, R.J. Musgrave, et al., *Proceeding of the Ocean Drilling Program, Initial Reports, 141*: College Station, TX (Ocean Drilling Program), 1992.
- Benioff, H., F. Press, and S. Smith, Excitation of the free oscillations of the earth by earthquakes, *Journal of Geophysical Research* 66, 605-619, 1961.
- Berger, W. H., Deep-sea sedimentation, in *The geology of continental margins*, vol. 10, edited by C. A. Burk, and C. L. Drake, pp. 213-241, Springer-Verlag, New York, 1974.
- Bevis, M., and L. Isacks, Hypocentral trend surface analysis: probing the geometry of Benioff zones, *Journal of Geophysical Research* 89, 6153-6170, 1984.
- Blackwell, D.D., Heatflow analysis of the Cascadia subduction zone (How wide is the locked zone?), paper presented at Workshop on Oregon earthquake source zones, Oregon State University, Corvallis, 1991.
- Blackwell, D. D., J. L. Steele, and S. Kelley, Heat flow in the state of Washington and thermal conditions in the Cascade range, *Journal of Geophysical Research*, 95, 19495-19516, 1990.
- Blackwell, D. D., J. L. Steele, L. S. Carter, D. Smith, E. R. Decker, P. Morgan, W. R. Gosnold, M. Reiter, and J. Witcher, *Geophysics of North America*, CD-ROM data source, 1989.
- Blanpied, M. L., D. A. Lockner, and J. D. Byerlee, Fault stability inferred from granite sliding experiments at hydrothermal conditions, *Geophysical Research Letters*, 18, 609-612, 1991.
- Bol, A.J., Overprint magnetization in the support of northward displacement of the Chugach-Prince William Terrane, Alaska, *Journal of Geophysical Research*, 98, 22389-22400, 1993.
- Brocher, T. M., G. S. Fuis, M. A. Fisher, G. Plafker, J. J. Taber, and N. I. Christensen, Mapping the megathrust beneath the northern Gulf of Alaska using wide-angle seismic data, *Journal of Geophysical Research*, 99, 11663-11685, 1994.
- Brown, L., R. Reilinger, S. R. Holdahl, and E. I. Balazs, Postseismic crustal uplift near

- Anchorage, Alaska, *Journal of Geophysical Research*, 82, 3369-3378, 1977.
- Bruns, T. R., and W. C. Schwab, Structure and Seismic stratigraphy of the Yakataga segment of the continental margin, Northern Gulf of Alaska. United States Geological Survey. Department of the Interior. Map MF-1424. Scale 1:250 000, 1983.
- Burton, G., and W. Person, Earthquakes, *EOS Transcripts, AGU*, 66, 437, 1985.
- Byerlee, J. D., Friction of rocks, *Pageoph*, 116, 615-626, 1978.
- Byrne, D. E., D. M. Davis, and L. R. Sykes, Loci and maximum size of thrust earthquakes and the mechanics of the shallow region of subduction zones, *Tectonics*, 7, 833-857, 1988.
- Cahill, T., and B. L. Isacks, Seismicity and shape of the subducted Nazca Plate, *Journal of Geophysical Research*, 97, 17503-17529, 1992.
- Cande, S. C., R. B. Leslie, J. C. Parra, and M. Hobart, Interaction between the Chile ridge and the Chile trench: geophysical and geothermal evidence, *Journal of Geophysical Research*, 92, 495-520, 1987.
- Carlson, P.R., B.F. Molnia, S.C. Kittleson, and J.C. Jr. Hampson, Map distribution of bottom sediments on the continental shelf, northern Gulf of Alaska, *U.S. Geological Survey Miscellaneous Field Studies Map, MF-876*, 2 sheets, 1977.
- Cassidy, J., Review: Receiver function analysis studies in the southern Canadian Cordillera, *Canadian Journal of Earth Science*, 32, 1514-1519, 1995.
- Chelton, D. B., and D. B. Enfield, Ocean signals in tide gauge records, *Journal of Geophysical Research*, 91, 9081-9098, 1986.
- Chen, W., and P. Molnar, Focal depths of intracontinental and interplate earthquakes and its implications for the thermal and mechanical properties of the lithosphere, *Journal of Geophysical Research*, 88, 4183-4214, 1983.
- Choy, G. L., and J. W. Dewey, Rupture process of an extended earthquake sequence: teleseismic analysis of the Chilean earthquake of March 3, 1985, *Journal of Geophysical Research*, 93, 1103-1118, 1988.
- Christensen, D. H., and S. L. Beck, The rupture process and tectonic implications of the great 1964 Prince William Sound earthquake, *Pageoph*, 142, 29-53, 1994.
- Cifuentes, I. L., The 1960 Chilean Earthquakes, *Journal of Geophysical Research*, 94,

- 665-680, 1989.
- Cifuentes, I. L., and P. G. Silver, Low-frequency source characteristics of the great 1960 Chilean earthquake, *Journal of Geophysical Research*, *94*, 643-663, 1989.
- Clague, J. J., and P. T. Bobrowski, Evidence for a large earthquake and tsunami 100-400 years ago on Western Vancouver Island, British Columbia, *Quaternary Research*, *41*, 176-184, 1994.
- Clague, J. J., J. R. Harper, R. J. Hebda, and D. E. Howes, Late Quaternary sea levels and crustal movements, coastal British Columbia, *Canadian Journal of Earth Science*, *19*, 597-618, 1982.
- Clowes, R.M., C.J. Yorath, and R.D. Hyndman, Reflection mapping across the convergent margin of western Canada, *Geophysical Journal of Royal Astronomical Society*, *89*, 79-84, 1987.
- Cohen, S., S. Holdahl, D. Caprette, S. Hilla, R. Safford, and D. Schultz, Uplift of the Kenai Peninsula, Alaska, since the 1964 Prince William Sound earthquake, *Journal of Geophysical Research*, *100*, 2031-2038, 1995.
- Combellick, R.A., Paleoseismicity of the Cook Inlet region: evidence from peat stratigraphy in Turnagain and Knik arms, Alaska, *Alaska Division of Geological and Geophysical Surveys, Professional Report 112*, 1991.
- Comte, D., A. Eisenberg, E. Lorca, M. Pardo, L. Ponce, R. Saragoni, S. K. Singh, and G. Suarez, The 1985 Central Chile earthquake: A repeat of previous great earthquakes in the region?, *Science*, *233*, 449-453, 1986.
- Creager, J. S., D. W. Scholl, et al., *Initial Reports of the Deep Sea Drilling Project, vol. 19*, pp. 17-168, U.S. Government Printing Office, Washington, 1973.
- Crosson, R. S., and T. J. Owens, Slab geometry of the Cascadia subduction zone beneath Washington from earthquake hypocentres and teleseismic converted waves, *Geophysical Research Letters*, *14*, 824-827, 1987.
- Darlenzo, M. E., and C. D. Peterson, Episodic tectonic subsidence of Late Holocene salt marshes, northern Oregon, central Cascadia margin, *Tectonics*, *9*, 1-22, 1990.
- Davies, J. N., and L. House, Aleutian subduction zone seismicity, volcano-trench separation, and their relation to great thrust-type earthquakes, *Journal of Geophysical Research*, *84*, 4583-4591, 1979.

- Davis, E. E., and R. D. Hyndman, Accretion and recent deformation of sediments along the northern Cascadia subduction zone, *Geological Society of America Bulletin*, 101, 1465-1480, 1989.
- Davis, E. E., R. D. Hyndman, and H. Villinger, Rates of fluid expulsion across the northern Cascadia accretionary prism: constraints from new heat flow and multichannel seismic reflection data, *Journal of Geophysical Research*, 95, 8869-8889, 1990.
- Davis, E. E., and R. P. Riddihough, The Winona basin: structure and tectonics, *Canadian Journal of Earth Science*, 19, 767-788, 1982.
- DeMets, C., R. G. Gordon, D. F. Argus, and S. Stein, Current plate motions, *Geophysical Journal International*, 101, 425-478, 1990.
- Douglas, B. C., Global sea level rise, *Journal of Geophysical Research*, 96, 6981-6992, 1991.
- Dragert, H., and R.D. Hyndman, Continuous GPS monitoring of strain in the northern Cascadia subduction zone, *Geophysical Research Letters*, 22, 755-758, 1995.
- Dragert, H., R. D. Hyndman, G. C. Rogers, and K. Wang, Current deformation and the width of the seismogenic zone of the northern Cascadia subduction thrust, *Journal of Geophysical Research*, 99, 653-668, 1994.
- Dragert, H., and M. Liskowski, Crustal deformation measurements on Vancouver Island, British Columbia: 1976 to 1988, in *Global and Regional Geodynamics*, P. Vyskocil, C. Reigber, and P.A. Cross, editors, 241-250, Springer-Verlag, New York, 1990.
- Dumitru, T. A., Effects of subduction parameters on geothermal gradients in forearcs, with an application to Franciscan subduction in California, *Journal of Geophysical Research*, 96, 621-641, 1991.
- Dziewonski, A. M., and J. H. Woodhouse, An experiment in systematic study of global seismicity: centroid moment tensor solutions for 201 moderate and large earthquakes of 1981, *Journal of Geophysical Research*, 88, 3247-3271, 1983.
- Eisenberg, A., R. Husid, and J. E. Luco, A preliminary report: The July 8, 1971 Chilean earthquake, *Bulletin of the Seismological Society of America*, 62, 423-430, 1972.
- Engerbretson, D.C., A. Cox, and R.G. Gordon, Relative motions between oceanic and continental plates in the Pacific Basin, *Geological Society of America, Special Paper* 206, 1985.

- Fisher, M. A., and R. von Huene, Structure of the Upper Cenozoic strata beneath Kodiak Shelf, Alaska, *American Association of Petrology Geological Bulletin*, 64, 1014-1033, 1980.
- Forsythe, R., The late Paleozoic to early Mesozoic evolution of southern South America: a plate tectonic interpretation, *Journal of Geological Society of London*, 139, 671-682, 1982.
- Fryer, P., A. Fuenzalida, M. Pardo, A. Cisternas, L. Dorbath, C. Dorbath, D. Comte, and E. Kausel, On the geometry of the Nazca Plate subducted under central Chile (32-34.5°S) as inferred from microseismic data, *Tectonophysics*, 205, 1-11, 1992.
- Fryer, P., Evolution of the Mariana convergent plate margin system, *Review Geophysics*, 34, 89-125, 1996.
- Fuenzalida, A., M. Pardo, A. Cisternas, L. Dorbath, C. Dorbath, D. Comte, and E. Kausel, On the geometry of the Nazca Plate subducted under central Chile (32-34.5°S) as inferred from microseismic data, *Tectonophysics*, 205, 1-11, 1992.
- Fuis, G. S., and G. Plafker, Evolution of deep structure along the trans-Alaska crustal transect, Chugach Mountains and Copper River basin, southern Alaska, *Journal of Geophysical Research*, 96, 4229-4253, 1991.
- Fuis, G. S., E. L. Ambos, W. D. Mooney, N. I. Christensen, and E. Geist, Crustal structure of accreted terranes in Southern Alaska, Chugach Mountains and Copper River Basin, from seismic refraction results, *Journal of Geophysical Research*, 96, 4187-4227, 1991.
- Fyfe, W.S., N.J. Price, A.B. Thompson, Fluids in deep continental crust, *Elsevier*, Amsterdam, 383 pp., 1978.
- Gabrielse, H., J. W. H. Monger, J. O. Wheeler, and C. J. Yorath, Tectonic Framework: Morphogeological belts, tectonic assemblages, and terranes, in *Geology of the Cordilleran Orogen in Canada*, Part A ed., vol. G-2, edited by H. Gabrielse, and C. J. Yorath, pp. 15-28, Geological Survey of Canada, Geology of Canada,, 1991.
- Goodwin, E. B., G. S. Fuis, W. J. Nokleberg, and E. L. Ambos, The crustal structure of the Wrangellia Terrane along the East Glen Highway, Eastern-Southern Alaska, *Journal of Geophysical Research*, 94, 16037-16057, 1989.
- Govers, R., K.P. Furlong, and K.M.M. Rohr, The Explorer pseudo-plate: a case study of the dynamics of a subduction-spreading-transform triple junction, *in preparation*, 1996.

- Hatori, T., Tsunami magnitude and source area of the Aleutian-Alaska tsunamis, *Bulletin of Earthquake Research Institute*, 56, 97-110, 1981.
- Hatori, T., Vertical displacement in a tsunami source area and the topography of the sea bottom, *Earthquake Research Institute Bulletin*, 44, 1449-1464, 1966.
- Hayes, D. E., and M. Ewing, Pacific Plate boundary structure, in *The Sea*, edited by A. Maxwell, pp. 29-72, Wiley, New York, 1970.
- Heaton, T.H., and H. Kanamori, Seismic potential associated with subduction in the northwestern United States, *Bulletin of Seismological Society of America*, 74, 933-944, 1984.
- Hibbard, J. P., and D. E. Kargi, Structural and magmatic responses to spreading ridge subduction: An example from southwest Japan, *Tectonics*, 9, 207-230, 1990.
- Hill, I.A., A. Taira, J.V. Firth, et al., *Proceedings of the Ocean Drilling Program, Scientific Results, 131*: College Station, TX (Ocean Drilling Program), 1993.
- Hirahara, K., Three dimensional seismic structure beneath southwest Japan: The subducting Philippine plate, *Tectonophysics*, 79, 1-44, 1981.
- Holdahl, S.R., F. Faucher, and H. Dragert, Contemporary vertical crustal motion in the Pacific Northwest, in *Slow Deformation and Transmission of Stress in the Earth, Geophysics Monogram Service*, edited by S.C. Cohen and P. Vanicek, pp. 17-29, AGU, Washington, D.C., 1989.
- Holdahl, S. R., and J. Sauber, Coseismic slip in the 1964 Prince William Sound earthquake: a new geodetic inversion, *Pageoph*, 142, 56-82, 1994.
- Hower, J., W. V. Eslinger, M. Hower, and E. A. Perry, Mechanism of burial metamorphism of argillaceous sediments, *Geological Society of America Bulletin*, 87, 725-737, 1976.
- Hutchison, I., The effects of sedimentation and compaction on oceanic heat flow, *Geophysical Journal of the Royal Astronomical Society*, 82, 439-459, 1985.
- Hyndman, R. D., and E. E. Davis, A mechanism for the formation of methane hydrate and seafloor bottom-simulating reflectors by vertical fluid expulsion, *Journal of Geophysical Research*, 97, 7025-7041, 1992.
- Hyndman, R. D., C. J. Yorath, R. M. Clowes, and E. E. Davis, The northern Cascadia subduction zone at Vancouver Island: seismic structure and tectonic history, *Canadian*

- Journal of Earth Science*, 27, 313-329, 1990.
- Hyndman, R. D., G. C. Rogers, and H. Dragert, Thermal, pore pressure and vertical deformation limits on the zone of major thrust earthquake failure beneath the Vancouver Island subduction zone (abstract), *Seismological Research Letters*, 60, 2, 1989.
- Hyndman, R. D., Dipping seismic reflectors, electrically conductive zones, and trapped water in the crust over a subducting plate, *Journal of Geophysical Research*, 93, 13391-13405, 1988.
- Hyndman, R.D., and K. Wang, The rupture zone of Cascadia great earthquakes from current deformation and the thermal regime, *Journal of Geophysical Research*, 100, 22133-22154, 1995.
- Hyndman, R. D., K. Wang, and M. Yamano, Thermal constraints on the seismogenic portion of the southwestern Japan subduction thrust, *Journal of Geophysical Research*, 100, 15373-15392, 1995.
- Hyndman, R. D., The LITHOPROBE corridor across the Vancouver Island continental margin: the structural and tectonic consequences of subduction, *Canadian Journal of Earth Science*, 32, 1777-1802, 1995.
- Hyndman, R. D., and K. Wang, Thermal constraints on the zone of major thrust earthquake failure: the Cascadia subduction zone, *Journal of Geophysical Research*, 98, 2039-2060, 1993.
- Hyndman, R. D., K. Wang, T. Yuan, and G.D. Spence, Tectonic sediment thickening, fluid expulsion, and the thermal regime of subduction zone accretionary prisms: The Cascadia Margin off Vancouver Island, *Journal of Geophysical Research*, 98, 21865-21876, 1993.
- Hyndman, R., and K. Wang, The rupture zone of Cascadia great earthquakes from current deformation and the thermal regime, *Journal of Geophysical Research*, 100, 22133-22154, 1995.
- Hyndman, R. D., K. Wang, and M. Yamano, Thermal constraints on the seismogenic portion of the southwestern Japan subduction thrust, *Journal of Geophysical Research*, 100, 15373-15392, 1995.
- Hyndman, R. D., M. Yamano, & D.A. Oleskevich, The seismogenic zone of subduction thrust faults, submitted to *Island Arc*, 1996.

- Irving, E., Whence British Columbia?, *Nature*, 314, 673-674, 1985.
- Irwin, J.J., W.D. Sharp, R.R. Spangler, and R.E. Drake, Some paleomagnetic constraints on the tectonic evolution of the Coastal cordillera of Central Chile, *Journal of Geophysical Research*, 92, 3606-3614, 1987.
- Ito, K., Regional variations of the cutoff depth of seismicity in the crust and their relation to heat flow and large inland earthquakes, *Journal of the Physical Earth*, 38, 5223-5250, 1990.
- Jacoby, G. C., P. L. Williams, and B. M. Buckley, Tree ring correlation between prehistoric landslides and abrupt tectonic events in Seattle, Washington, *Science*, 258, 1621-1623, 1992.
- James, T. S., L. S. Hollister, and W. J. Morgan, Thermal modelling of the Chugach metamorphic complex, *Journal of Geophysical Research*, 94, 4411-4423, 1989.
- James, T., Potential effects of post-glacial rebound on crustal motion in Cascadia, *in preparation*, 1996.
- Jennings, S, and G.R. Thompson, Diagenesis of Plio-Pleistocene sediments of the Colorado River delta, southern California, *Journal of Sediment Petrology*, 56, 89-98, 1986.
- Johnson, J. M., K. Satake, S. R. Holdahl, and J. Sauber, The 1964 Prince William Sound earthquake: Joint inversion of tsunami and geodetic data, *Journal of Geophysical Research*, 101, 523-532, 1996.
- Johnson, J. M., and K. Satake, Slip distribution of the 1964 Alaska earthquake from inversion of tsunami waveforms, *EOS Transcript, AGU*, 43, 95, 1993.
- Johnson, L., and D. Monahan, General Bathymetric Charts of the Oceans (GEBCO). Canadian Hydrographic Service. H.S.H. Prince Albert I. Map 5-03. Scale 1:10000000, 1984.
- Jones, D.L., N.J. Siberling, P.J. Coney, and G. Plafker, Lithotectonic terrane map of Alaska, scale 1:2500000, in *Lithotectonic Terrane Maps of the North American Cordillera*, edited by N.J. Siberling and D.L. Jones, *U.S. Geological Survey Open File Rep.*, 84-523, A1-A12, 1984.
- Jones, D.L., N.J. Siberling, H.C. Berg, and G. Plafker, Tectonostratigraphic terrane map of Alaska, *U.S. Geological Survey Open File Report*, 81-792, 20 pp., 1981.

- Kadinski-Cade, K. A., Seismotectonics of the Chile Margin and the 1977 Cauçete earthquake of western Argentina, *Ph.D. Dissertation*, Cornell University, Ithaca, 1985.
- Kanamori, H., Tectonic implications of the 1944 Tonankai and the 1946 Nankaido earthquakes, *Physics of Earth and Planetary Interiors*, 5, 129-139, 1972.
- Kanamori, H., The energy released in great earthquakes, *Journal of Geophysical Research*, 82, 2981-2987, 1977.
- Kanamori, H., and J. Cipar, Focal process of the great Chilean earthquake, May 22, 1960, *Physics of Earth and Planetary Interiors*, 9, 128-136, 1974.
- Kanaya, H., and S. Ishirara, Uranium, thorium and potassium contents of Japanese granitic rocks: a summary up to 1972, in *The Natural Radiation Environment II*, edited by J.A.S. Adams, W.M. Lowder, and T.F. Gesell, pp. 517-533, U.S. Energy Research and Development Administration, Washington, D.C., 1975.
- Kelleher, J. A., Rupture zones of large South American earthquakes and some predictions, *Journal of Geophysical Research*, 77, 2087-2103, 1972.
- Korgen, B. J., G. Bodvarsson, and R. S. Mesecar, Heat flow through the floor of the Cascadia Basin, *Journal of Geophysical Research*, 76, 4758-4774, 1971.
- Kulm, L. D., R. von Huene, et al., *Initial Reports of the Deep Sea Drilling Project*, in, vol. 18, pp. 287-415, U.S. Government Printing Office, Washington, 1971.
- Lahr, J. C., and G. Plafker, Holocene Pacific-North American plate interaction in southern Alaska: implications for the Yakataga seismic gap, *Geology*, 8, 483-486, 1980.
- Langseth, M. G., and M. A. Hobart, A marine geothermal study over deformed sediments of the subduction complex off Oregon and Washington (abstract), *EOS Transcript, AGU*, 65, 1089, 1984.
- Lewis, T. J., W. H. Bentkowski, E. E. Davis, R. D. Hyndman, J. G. Souther, and J. A. Wright, Subduction of the Juan de Fuca plate: thermal consequences, *Journal of Geophysical Research*, 93, 15207-15225, 1988.
- Lewis, T. J., and W. H. Bentkowski, Potassium, uranium, and thorium concentrations of crustal rocks: a data file, *Geological Survey of Canada, Open File Rep.*, 1744, 1988.
- Lewis, T. J., Heat flux in the Canadian Cordillera, in *Neotectonics of North America*, vol. Decade of North American Geology Series, edited by D. B. Slemmons, E. R. Engdahl,

- D. D. Blackwell, and D. Schwartz, Geological Society of America, Boulder, Colorado, 1990.
- Lewis, S.D., J.H. Behrmann, R.J. Musgrave, and S.C. Cande (Eds.), *Proceedings of the Ocean Drilling Program, Scientific Results*, 141: College Station, TX (Ocean Drilling Program), 1995.
- Lewis, T. J., H. Bennetts, V.S. Allen, and F. Chan, Uranium, Thorium and Potassium concentrations and heat generated in samples of crustal rocks: a data file, *Geological Survey of Canada Open File Report*, 15, 1984.
- Lewis, T. J., W. H. Bentkowski, and R. D. Hyndman, Crustal temperatures near the LITHOPROBE Southern Canadian Cordillera transect, *Canadian Journal of Earth Science*, 29, 1197-1214, 1991.
- Li, X., Y. Furukawa, T. Nagao, S. Uyeda, and H. Suzuki, Heat flow in central Japan and its relations to geological and geophysical features, *Bulletin of Earthquake Research Institute*, 64, 1-36, 1989.
- Lomnitz, C., and A. Hax, Clustering in aftershock sequences, in *The Earth beneath the continents*, Steinhart, J.S. and Smith, T.J., editors, American Geophysical Union, 502-508, 1966.
- MacKay, M.E., G.F. Moore, G.R. Cochrane, J.C. Moore, and L.D. Kulm, Landward vergence and oblique structural trends in the Oregon margin accretionary prism: implications and effect on fluid flow, *Earth and Planetary Science Letters*, 109, 477-491, 1992.
- Malgrange, M., A. Deschamps, and R. Madarianga, Thrust and extensional faulting under the Chilean coast: 1965, 1971 Aconcagua earthquakes, *Geophysical Journal of Astronomical Society*, 66, 313-331, 1981.
- Mann, D.H., and A.L. Crowell, A large earthquake occurring 700-800 years ago in Ailik Bay, southern coastal Alaska, *Canadian Journal of Earth Science*, 33, 117-226, 1996.
- Massey, N.W.D., The Mechosin Igneous Complex, southern Vancouver Island; ophiolite stratigraphy developed in an emergent island setting, *Geology*, 14, 602-605, 1986.
- Matumoto, T., and R. A. Page, Micro aftershocks following the Alaska earthquake of March 28, 1964: Determination of hypocentres and crustal velocities in the Kenai Peninsula-Prince William Sound area, in *The Prince William Sound, Alaska, earthquake of 1964 and aftershocks*, edited by L. Leipold, pp. 157-173, U.S. Coast and Geodetic Survey, U.S. Government Printing Office, Washington, D.C., 1969.

- McCann, W. R., S. P. Nishenko, L. R. Sykes, and J. Krause, Seismic gaps and plate tectonics: Seismic potential for major boundaries, *Pageoph*, 117, 1082-1147, 1979.
- Mendoza, C., S. Hartzell, and T. Monfret, Wide-band analysis of the 3 March 1985 Central Chile earthquake: Overall source process and rupture history, *Bulletin of Seismological Society of America*, 84, 269-283, 1994.
- Minster, J. B., and T. H. Jordan, Present-day plate motions, *Journal of Geophysical Research*, 83, 5331-5334, 1978.
- Mitchell, C. E., P. Vincent, R. J. Weldon II, and M. A. Richards, Present-day vertical deformation of the Cascadia Margin, Pacific Northwest, United States, *Journal of Geophysical Research*, 99, 12257-12277, 1994.
- Miyashita, K., and M. Matsu'ura, Inversion analysis of static displacement data associated with Alaska earthquake of 1964, *Physics of Earth and Planetary Interiors*, 26, 333-349, 1978.
- Mizoue, M., M. Nakamura, N. Seto, and Y. Ishiketa, Three layered distribution of microearthquakes in relation to focal mechanism variation in the Kii Peninsula, southwest Japan, *Bulletin of Earthquake Research Institute, University of Tokyo*, 58, 287-310, 1983.
- Monger, J. W. H., and H. C. Berg, Lithotectonic terrane map of western British Columbia and southeastern Alaska, *U.S. Geological Survey Open File Report* 84-523, 1984.
- Mooney, W. D., and C. S. Weaver, Regional crustal structure and tectonics of the Pacific coastal states; California, Oregon, and Washington, in *Geophysical framework of the continental United States*, vol. Geological Society of America Memoir 172, edited by L. C. Pakiser, and W. D. Mooney, pp. 129-161, Geological Society of America, Boulder, Colorado, 1989.
- Moore, G. F., T. H. Shipley, P. L. Stoffa, D. E. Karig, A. Taira, S. Kuramoto, H. Tokuyama, and K. Suyehiro, Structure of the Nankai Trough accretionary zone from multichannel seismic reflection data, *Journal of Geophysical Research*, 95, 8753-8765, 1990.
- Moore, J. C., J. Diebold, M. A. Fisher, T. Brocher, M. Talwani, J. Ewing, R. von Huene, C. Rowe, D. Stone, C. Stephens, and D. Sawyer, EDGE deep seismic reflection transect of the eastern Aleutian arc-trench layered lower crust reveals underplating and continental growth, *Geology*, 19, 420-424, 1991.
- Moore, G.W., Growth of the Andes by rejuvenated subduction, *International Geological*

- Review*, 37, 437-447, 1995.
- Moore, D.E., D.A. Lockner, M. Shengli, R. Summers, and J.D. Byerlee, Strengths of serpentinite gouges to 200°C (abstract), *EOS, Transactions of the American Geophysical Union*, 76, 632, 1995.
- Nakamura, S., An analysis of the 1985 Chilean tsunami, *Marine Geodesy*, 15, 277-281, 1992.
- Nelson, A.R., A 7500-yr record of Cascadia tsunamis in Southern coastal Oregon (abstract), *Geological Society of America*, Spring 1996.
- Nelson, A. R., and K. Kashima, Diatom zonation in southern Oregon tidal marshes relative to vascular plants, foraminifera, and sea level, *Journal of Coastal Research*, 9, 673-697, 1993.
- Nishenko, S. P., Seismic potential for large and great interplate earthquakes along the Chilean and southern Peruvian margins of South America: A quantitative reappraisal, *Journal of Geophysical Research*, 90, 3589-3615, 1985.
- Nishenko, S.P., and K.H. Jacob, Seismic potential of the Queen Charlotte-Alaska-Aleutian seismic zone, *Journal of Geophysical Research*, 95, 2511-2532, 1990.
- Norabuena, E. O., J. A. Snoke, and D. E. James, Structure of the subducting Nazca Plate beneath Peru, *Journal of Geophysical Research*, 99, 9215-9226, 1994.
- Okino, I., Y. Shimakaya, and S. Nagaoka, Evolution of the Shikoku basin, *Journal of Geomagnetism and Geoelectricity*, 46, 463-479, 1994.
- Page, R. A., C. D. Stephens, and J. C. Lahr, Seismicity of the Wrangell and Aleutian Wadati-Benioff zones and the North American plate along the trans-Alaska crustal transect, Chugach Mountains and Copper River basin, southern Alaska, *Journal of Geophysical Research*, 94, 16059-16082, 1989.
- Pacheco, J., L.R. Sykes, and C.H. Scholz, Nature of seismic coupling along simple plate boundaries of the subduction type, *Journal of Geophysical Research*, 98, 14133-14159, 1993.
- Pararas-Carayannis, G., A study of the source mechanism of the Alaska earthquake and tsunami of March 27, 1964, *Pacific Science*, 21, 301-310, 1976.
- Peltier, W.R., and X. Jiang, Glacial isostatic adjustment and Earth rotation: Refined constraints on the viscosity of the deepest mantle, *Journal of Geophysical Research*,

- 101, 3269-3290, 1996.
- Plafker, G., and J. C. Savage, Mechanism of the Chilean earthquakes of May 21 and 22, 1960, *Geological Society of America Bulletin*, 81, 1001-1030, 1970.
- Plafker, G., Alaskan earthquake of 1964 and Chilean earthquake of 1960: Implications for arc tectonics, *Journal of Geophysical Research*, 77, 901-925, 1972.
- Plafker, G., J. C. Moore, and G. R. Winkler, Geology of the southern Alaska margin, in *The Cordilleran Orogen: Alaska*, The Geology of North America ed., vol. G-1, edited by G. Plafker, H. C. Berg, and D. L. Jones, *Geological Society of America*, Boulder, Colorado, 1994.
- Plafker, G., W. J. Nokleberg, and J. S. Lull, Bedrock geology and tectonic evolution of the Wrangellia, Peninsular, and Chugach terranes along the Trans-Alaska Crustal Transect in the Chugach Mountains and southern Copper River basin, *Journal of Geophysical Research*, 94, 4255-4295, 1989.
- Plafker, G., and G. Claypool, Petroleum source potential of rocks dredged from the continental slope in the eastern Gulf of Alaska, *U.S. Geological Survey Open File Report*, 79-295, 1979.
- Plafker, G., Tectonics of the March 27, 1964 Alaska earthquake, *U.S. Geological Survey Professional Paper 543-I*, 1969.
- Plafker, G., Tectonics, in *The great Alaska earthquake of 1964*, pp. 47-122, National Academy of Sciences, Washington, D.C., 1971.
- Plafker, G., Lajoie, K.R., and M. Rubin, Determining the recurrence intervals of great subduction earthquakes in southern Alaska by radiocarbon dating, in *Radiocarbon dating after four decades*, edited by R.E. Taylor, A. Long, and R.S. Kra, Springer-Verlag, New York, pp. 436-452, 1992.
- Plumley, P.W., R.S. Coe, and T. Byrne, Paleomagnetism of the Paleocene Ghost Rocks Formation, Prince William terrane, Alaska, *Tectonics*, 2, 295-314, 1983.
- Ponko, S. C., and S. M. Peacock, Thermal modelling of the southern Alaska subduction zone: insight into the petrology of the subducting slab and overlying mantle wedge, *Journal of Geophysical Research*, 100, 22117-22128, 1995.
- Press, F., A. Ben-Menahem, and M. N. Toksoz, Experimental determination of earthquake fault length and rupture velocity, *Journal of Geophysical Research*, 66, 3471-3485, 1961.

- Protti, M., F. Gundel, and K. McNally, The geometry of the Wadati-Benioff zone under southern Central America and its tectonic significance: results from a high-resolution local seismographic network, *Physics of Earth and Planetary Interiors*, 84, 271-287, 1994.
- Ranken, B., R. K. Cardwell, and D. Karig, Kinematics of the Philippine Sea plate, *Tectonics*, 3, 555-575, 1984.
- Rayleigh, C.B., and M.S. Patterson, Experimental deformation of serpentinite and its tectonic implications, *Journal of Geophysical Research*, 70, 3965-3985, 1968.
- Rea, D. K., I. A. Basov, T. R. Janecek, A. Palmer-Julson, et al., *Proceedings of the Ocean Drilling Program, Initial Reports, vol. 145*, pp. Sites 881-887, College Station, Texas, 1993.
- Reagor, G., S. Goter, D. Herzog, S.A. Sipkin, J. Taggart, et al., Global hypocentre data base CD-ROM and EPIC retrieval software, v. 3.0, *National Earthquake Information Centre (NEIC)*, U.S. Geological Survey, 1994.
- Reed, B. L., and M. A. Lanphere, Alaska-Aleutian range batholith; Geochronology, chemistry, and relation to circum-Pacific plutonism, *Geological Society of America Bulletin*, 84, 2583-2610, 1973.
- Reed, B. L., A. T. Miesch, and M. A. Lanphere, Plutonic rocks of Jurassic age in the Alaska-Aleutian Range batholith: Chemical variations and polarity, *Geological Society of America Bulletin*, 94, 1232-1240, 1983.
- Reilinger, R., and J. Adams, Geodetic evidence for active landward tilting of the Oregon and Washington Coastal Ranges, *Geophysical Research Letters*, 9, 401-403, 1982.
- Reimnitz, E., Effects in the Copper River delta, in *The Great Alaska earthquake of 1964: oceanography and coastal engineering*, Committee on the Alaska Earthquake, National Research council, National Academy of Sciences, Washington, D.C., pp. 290-302, 1972.
- Reinen, L.A., J.D. Weeks, and T.E. Tullis, The frictional behaviour of serpentinite: Implications for aseismic creep on shallow crustal faults, *Geophysical Research Letters*, 18, 1921-1924, 1991.
- Riddihough, R. P., and R.D. Hyndman, Canada's active western margin -the case for subduction, *Geoscience Canada*, 3, 269-278, 1976.
- Riddihough, R. P., Recent movements of the Juan de Fuca plate system, *Journal of*

- Geophysical Research*, 89, 6980-6994, 1984.
- Riddihough, R. R., and R. D. Hyndman, Modern plate tectonic regime of the continental margin of western Canada, in *Geology of the Cordilleran Orogen in Canada*, vol. G-2, edited by H. Gabrielse, and C. J. Yorath, pp. 435-455, Geological Survey of Canada, Geology of Canada, 1991.
- Riddihough, R. P., Magnetic anomalies. Department of Energy, Mines, and Resources, Canada. Open File Report 85-20. Map JFP11, 1985.
- Roeske, S. M., L. W. Snee, and T. L. Pavlis, Strike-slip and accretion events along the southern Alaska plate margin in the Cretaceous and early Tertiary, *Geological Society of America Abstract Program*, 23, 428-429, 1991.
- Rogers, G.C., An overview of contemporary tectonics in the Pacific Northwest (abstract), Geological Association of Canada Annual Meeting, A-90, 1995.
- Rogers, G. C., An assessment of the megathrust earthquake potential of the Cascadia subduction zone, *Canadian Journal of Earth Science*, 25, 844-852, 1988.
- Rogers, G. C., Some comments on the seismicity of the northern Puget Sound - southern Vancouver Island region, in Earthquake hazards of the Puget Sound region, U.S. *Geological Survey Open File Report*, vol. 83-19, pp. 19-39, 1983.
- Rogers, G. C., C. Spindler, and R. D. Hyndman, Seismicity along the Vancouver Island LITHOPROBE corridor. paper presented at the LITHOPROBE Southern Cordillera symposium, University of Calgary, Alberta, 1990.
- Ruff, L. J., and B. W. Tichelaar, What controls the seismogenic plate interface in subduction zones?, in preparation, 1995.
- Ruff, L. J., and H. Kanamori, Seismic coupling and uncoupling at subduction zones, *Tectonophysics*, 99, 99-117, 1983.
- Ruina, A. L., Slip instability and state variable friction laws, *Journal of Geophysical Research*, 88, 10359-10370, 1983.
- Rundle, B. F., Viscoelastic crustal deformation by finite quasi-static sources, *Journal of Geophysical Research*, 83, 5937-5945, 1978.
- Satake, K., K. Shimazaki, Y. Tsuji, and K. Ueda, Time and size of a giant earthquake in Cascadia inferred from Japanese tsunami records of January 1700, *Nature*, 379, 246-249, 1996.

- Satake, K., K. Shimazaki, and Y. Tsuji, A possible Cascadia earthquake of January 26, 1700 as inferred from tsunami records in Japan (abstract), *Geological Association of Canada / Mineral Association of Canada Spring meeting*, Victoria, 1995.
- Sato, T., and M. Matsu'ura, Cyclic crustal movement, steady uplift of marine terraces, and evolution of the island arc-trench system in southwest Japan, *Geophysical Research International*, 111, 617-629, 1992.
- Savage, J. C., A dislocation model of strain accumulation and release at a subduction zone, *Journal of Geophysical Research*, 88, 4984-4996, 1983.
- Savage, J. C., and W. Thatcher, Interseismic deformation at the Nankai Trough, Japan, subduction zone, *Journal of Geophysical Research*, 97, 11117-11135, 1992.
- Savage, J.C., M. Liskowski, and W.H. Prescott, Strain accumulation in western Washington, *Journal of Geophysical Research*, 96, 14493-14507, 1991.
- Savage, J.C., and G. Plafker, Tide gauge measurements of uplift along the south coast of Alaska, *Journal of Geophysical Research*, 96, 4325-4335, 1991.
- Schmitz, M., A balanced model of the southern Central Andes, *Tectonics*, 13, 484-492, 1994.
- Scholtz, C. H., Mechanics of faulting, *Annual Review Earth and Planetary Science*, 17, 309-334, 1988.
- Scholtz, C. H., *The Mechanics of Earthquakes and Faulting*, Cambridge University Press, New York, 1990.
- Schwarz, G., G. Chong, D. Kruger, E. Martinez, W. Massow, V. Rath, and J. Viramonte, Crustal high conductivity in the southern Central Andes and their tectonic implications, in *Tectonics of the Southern Central Andes*, edited by K. J. Reutter et al., pp. 49-68, Springer-Verlag, New York, 1994.
- Schweller, W. J., L. D. Kulm, and R. A. Prince, Tectonics, structure, and sedimentary framework of the Peru-Chile Trench, in *Nazca Plate: Crustal formation and Andean convergence*, Memoir ed., vol. 154, edited by L. D. Kulm, J. Dymond, E. J. Dasch, D. M. Hussong, and R. Roderick, p. 824, *Geological Society of America*, Washington, 1981.
- Seno, T., S. Stein, and A. E. Gripp, A model for the motion of the Philippine Sea Plate consistent with NUVEL-1 and geological data, *Journal of Geophysical Research*, 98, 17941-17948, 1993.

- Sheffels, B. M., Lower bound on the amount of crustal shortening in the central Bolivian Andes, *Geology*, 18, 812-815, 1990.
- Shi, Y., C.-Y. Wang, M. G. Langseth, M. Hobart, and R. von Huene, Heat flow and the thermal structure of the Washington-Oregon accretionary prism - A study of the lower slope, *Geophysical Research Letters*, 15, 1113-1116, 1988.
- Singh, S. K., and F. Mortera, Source time functions of large Mexican subduction earthquakes, morphology of the Benioff zone, age of the plate, and their tectonic implications, *Journal of Geophysical Research*, 96, 21487-21502, 1991.
- Skinner, B. J., and S. C. Porter (eds.), *Physical Geology*, 1st ed., John Wiley & Sons, New York, 1987.
- Snavely, P. D., Peripheral rocks -- Tertiary geology of the northwestern part of the Olympic Peninsula, Washington, in *Tertiary Olympic terrane, southwest Vancouver Island and northwest Washington*, edited by J. E. Muller, P. D. Snavely, and R. W. Tabor, Geological Association of Canada, Guidebook, 1983.
- Spence, G. D., R. D. Hyndman, E. E. Davis, and C. J. Yorath, Seismic structure of the northern Cascadia accretionary prism: Evidence from new multichannel seismic reflection data, in *Continental Lithosphere: Deep reflections*, Geodynamics ed., vol. 22, pp. 257-263, American Geophysical Union, Washington, D.C., 1991a.
- Spence, G. D., R. D. Hyndman, S. G. Langton, E. E. Davis, and C. J. Yorath, Multichannel seismic reflection profiles across the Vancouver Island continental shelf and slope, *Geological Survey of Canada Open File Report*, 2391, 1991b.
- Spence, G.D., R. M. Clowes, and R.M. Ellis, Seismic structure across the active subduction zone of western Canada, *Journal of Geophysical Research*, 90, 6754-6772, 1985.
- Stauder, W., Mechanisms and spatial distribution of Chilean earthquakes with relation to subduction of the oceanic plate, *Journal of Geophysical Research*, 78, 5033-5061, 1973.
- Stephens, C.D., R.A. Page, and J. C. Lahr, Reflected and mode-converted seismic waves within the shallow Aleutian subduction zone, southern Kenai Peninsula, Alaska, *Journal of Geophysical Research*, 95, 6883-6897, 1990.
- Stesky, R., Mechanisms of high temperature frictional sliding in Westerly granite, *Canadian Journal of Earth Science*, 15, 361-375, 1978.

- Stesky, R. The mechanical behaviour of faulted rock at high temperature and pressure, Ph. D. Thesis, *Massachusetts Institute of Technology*, Cambridge, 1975.
- Sykes, L.R., and R.C. Quittmeyer, Repeat times of great earthquakes along simple plate boundaries, in *Earthquake Prediction: An international review*, Maurice Ewing Services, D.W. Simpson and P.G. Richards, editors, 217-247, American Geophysical Union, Washington, D.C., 1981.
- Sykes, L. R., Aftershock zones of great earthquakes, seismicity gaps, and earthquake prediction for Alaska and the Aleutians, *Journal of Geophysical Research*, 76, 8021-8041, 1971.
- Taira, A., Byrne, T., and J. Ashi, *Photographic Atlas of an Accretionary Prism: Geological structures of the Shimanto Belt, Japan*, University of Tokyo Press, Tokyo, 1992.
- Taira, A., I. Hill, J. V. Firth, et al., *Proceedings of the Ocean Drilling Program, Initial Reports, 131-132*, College Station, TX (Ocean Drilling Program), 1991.
- Taira, A., The Shimanto Belt in Shikoku - Evolution of Cretaceous to Miocene accretionary prism, *Modern Geology*, 12, 5-46, 1988.
- Thatcher, W., and J. B. Rundle, A viscoelastic coupling model for the cyclic deformation due to periodically repeated earthquakes at subduction zones, *Journal of Geophysical Research*, 89, 7631-7640, 1984.
- Thatcher, W., The earthquake deformation cycle at the Nankai Trough, southwest Japan, *Journal of Geophysical Research*, 89, 3087-3101, 1984.
- Thornburg, T. M., L. D. Kulm, and D. M. Hussong, Submarine-fan development in the southern Chile Trench: A dynamic interplay of tectonics and sedimentation, *Geological Society of America Bulletin*, 102, 1658-1680, 1990.
- Thornburg, T. M., and L. D. Kulm, Sedimentation in the Chile Trench: Depositional morphologies, lithofacies, and stratigraphy, *Geological Society of America Bulletin*, 98, 33-52, 1987a.
- Thornburg, T. M., and L. D. Kulm, Sedimentation in the Chile Trench: Petro facies and provenance, *Journal of Sediment Petrology*, 57, 55-74, 1987b.
- Tichelaar, B. W., and L. J. Ruff, Seismic coupling along the Chilean subduction zone, *Journal of Geophysical Research*, 96, 11997-12022, 1991.

- Tichelaar, B. W., and L. J. Ruff, Depth of seismic coupling along subduction zones, *Journal of Geophysical Research*, 98, 2017-2037, 1993.
- Trehu, A. M., I. Asudeh, T. M. Brocher, J. H. Luetgert, W. D. Mooney, J. L. Nabelek, and Y. Nakamura, Crustal architecture of the Cascadia forearc, *Science*, 266, 237-242, 1994.
- Trehu, A. M., and Y. Nakamura, *U.S. Geological Survey Open-File Rep.*, 93-317, 1993.
- Tse, S. T., and J. R. Rice, Crustal earthquake instability in relation to the depth variation of frictional slip properties, *Journal of Geophysical Research*, 91, 9452-9472, 1986.
- Turcotte, D. L., and G. Schubert, Heat Transfer, in *Geodynamics - Applications of continuum physics to geological problems*, 1st ed., pp. 134-144, John Wiley & Sons, Inc., New York, 1982.
- Turner, R.F., Geological and operational summary, Kodiak Shelf stratigraphic test wells, western Gulf of Alaska, *Minerals Management Service, Outer Continental Shelf Report MMS 87-0109*, 341 pp, 1987.
- Uyeda, S., and T. Watanabe, Terrestrial heat flow in Western South America, *Tectonophysics*, 83, 63-70, 1982.
- van den Beukel, J., and R. Wortel, Temperatures and shear stresses in the upper part of a subduction zone, *Geophysical Research Letters*, 14, 1057-1060, 1987.
- van Andel, T. H., G. Heath, and T. C. Moore, Cenozoic history and paleoceanography of the central equatorial Pacific Ocean, *Geological Society of America Memoir*, 143, 134, 1975.
- Vanicek, P., R. O. Castle, and E. I. Balazs, Geodetic levelling and its applications, *Review Geophysics*, 18, 505-524, 1980.
- Vergara, M., B. Levi, J. O. Nystrom, and A. Cancino, Jurassic and Early Cretaceous island arc volcanism, extension, and subsidence in the Coast Range of central Chile, *Geological Society of America Bulletin*, 107, 1427-1440, 1995.
- Vergara, M., and F. Munizaga, Age and evolution of the Upper Cenozoic andesitic volcanism in Central-south Chile, *Geological Society of America Bulletin*, 85, 603-606, 1974.
- Vergara, M., Note on the paleovolcanism in the Andean geosyncline from the central part of Chile. Proceedings, 24th International Geological Congress, Canada, 1972.

- von Huene, R., J. Corvalan, J. Korstgard, and Scientific party, Cruise Report SO101-Condor, GEOMAR, *Initial Findings*, 1995.
- von Huene, R., M. A. Fisher, and T. R. Bruns, Geology and evolution of the Kodiak Margin, Gulf of Alaska, in *Geology and resource potential o the continental margin of western North America and adjacent ocean basins -- Beaufort Sea to Baja California*, vol. 6, edited by D. W. Scholl, A. Grantz, and J. G. Vedder, pp. 191-212, Circum-Pacific Council for the Energy and Mineral Resources, Earth Sciences Series, Houston, Texas, 1987.
- Vrolijk, P., On the mechanical role of smectite in subduction zones, *Geology*, 18, 703-707, 1990.
- Wang, K., T. Mulder, G. C. Rogers, and R. D. Hyndman, Case for very low coupling stress on the Cascadia subduction fault, *Journal of Geophysical Research*, 100, 12907-12918, 1995a.
- Wang, K., Hyndman, R.D., and M. Yamano, Thermal regime of the Southwest Japan subduction zone: effects of age history of the subducting plate, *Tectonophysics*, 248, 53-69, 1995b.
- Wang, K., Coupling of tectonic loading and earthquake fault slips at subduction zones, *PAGEOPH*, 145, 437-559, 1995.
- Wang, K., Kinematic models of dewatering accretionary prisms, *Journal of Geophysical Research*, 99, 4429-4438, 1994.
- Wang, K., H. Dragert, and H.J. Melosh, Finite element study of uplift and strain across Vancouver Island, *Canadian Journal of Earth Science*, 31, 1510-1522, 1994.
- Wang, K., R. D. Hyndman, and E. E. Davis, Thermal effects of sediment thickening and fluid expulsion in accretionary prisms: Model parameter and analysis, *Journal of Geophysical Research*, 98, 9975-9984, 1993.
- Wang, K., and E. E. Davis, Thermal effects of marine sedimentation in hydrothermally active areas, *Geophysical Journal International*, 110, 70-78, 1992.
- Westbrook, G. K., B. Carson, R. J. Musgrave, et al., *Proceedings of the Ocean Drilling Program, Initial Reports*, vol. 146, College Station, TX (Ocean Drilling Program), 1994.
- Wigger, P. J., M. Schmitz, M. Aranedo, G. Asch, S. Baldzuhn, P. Giese, W. D. Heinsohn, E. Martinez, E. Ricaldi, P. Rower, and J. Viramonte, Variation in the crustal structure

- of the Southern Central Andes deduced from seismic refraction investigations, in *Tectonics of the Southern Central Andes*, 1st ed., edited by K. J. Reutter, E. Scheuber, and P. J. Wigger, pp. 23-48, Springer-Verlag, Berlin, 1994.
- Wortel, M. J. R., and S. A. P. L. Cloetingh, Accretion and lateral variations in tectonic structure along the Peru-Chile trench, *Tectonophysics*, 112, 443-462, 1985.
- Wyss, M., Estimating maximum expectable magnitude of earthquakes from fault dimensions, *Geology*, 7, 336-340, 1979.
- Yamano, M., Recent heat flow studies in and around Japan, in *Terrestrial heat flow and Geothermal energy in Asia*, edited by M.L. Gupta and M. Yamano, pp. 173-201, Oxford and IBH Publishing Co., New Delhi, 1995.
- Yamano, M., J. P. Foucher, M. Kinoshita, A. Fisher, and R. D. Hyndman, Heat flow and fluid regime in the western Nankai accretionary prism, *Earth and Planetary Science Letters*, 109, 451-462, 1992.
- Yamano, M., S. Honda, and S. Uyeda, Nankai Trough: A hot trench?, *Marine Geophysical Research*, 6, 187-203, 1984.
- Yeats, R. S., S. R. Hart, et al., *Initial Reports of the Deep Sea Drilling Project*, vol. 34, pp. 17-120, U.S. Government Printing Office, Washington, 1976.
- Yorath, C. J., Petroleum geology of the Canadian Pacific continental margin, in *Geology and resource potential of the continental margins of western North America and adjacent basins - Beaufort Sea to Baja California*, Circum Pacific Council for Energy and Mineral Resources, Earth Sciences Series ed., vol. 6, edited by D. W. Scholl, A. Grantz, and J. Vedder, pp. 283-304, United States Geological Survey, Menlo Park, California, 1987.
- Zhao, D., D. Christensen, and H. Pulpan, Tomographic imaging of the Alaska subduction zone, *Journal of Geophysical Research*, 100, 6487-6504, 1995.

## VITA

**SURNAME:** Oleskevich

**GIVEN NAMES:** Daniel Alexander

**PLACE OF BIRTH:** Montreal, Québec, Canada

### EDUCATIONAL INSTITUTIONS ATTENDED:

|  |           |
|--|-----------|
| University of Victoria, Victoria, British Columbia | 1994-1996 |
| University of Waterloo, Waterloo, Ontario          | 1988-1993 |
| John Abbott College, Montreal, Québec              | 1986-1988 |

### DEGREES AWARDED:

|  |      |
|--|------|
| B.Sc. (Honours) Applied Physics - co-operative | 1993 |
| Diploma of Collegial Studies (Honours)         | 1988 |

### HONOURS AND AWARDS:

- University of Victoria Graduate Teachers Fellowship 1994-1996
- Birks Bronze Medal for High Academic Achievement and School Life contribution, Montreal 1986
- Montreal Board of Trade Outstanding Student Award 1986  
Science & Mathematics, Montreal
- Outstanding Academic Achievement scholarship 1986  
Montreal

### PUBLICATIONS

- Hyndman, R.D., M. Yamano & D.A. Oleskevich, Thermal composition controls on the seismogenic zone of subduction thrust faults, *Island Arc*, in press.
- Hyndman, R.D., K. Wang, H. Dragert, G.C. Rogers, & D.A. Oleskevich, Cascadia megathrust earthquake potential: constraints from current deformation measurements and from the thermal regime, *GAC/MAC Abstract*, 20, A-48, 1995.
- Oleskevich, D.A., R.D. Hyndman, & K. Wang, Thermal constraints to Great Earthquake Rupture Zones, *CGU Abstract*, 171, 1996.
- Oleskevich, D.A., R.D. Hyndman, & K. Wang, Thermal constraints of great earthquakes of selected eastern Pacific subduction zones, *EOS supplement*, 76, 415, 1995.
- Oleskevich, D.A., R.D. Hyndman, & K. Wang, Comparison of selected profiles along the Cascadia Margin through thermal constraint modelling, *CGU Abstract*, 79, 1995.
- Oleskevich, D.A., R.D. Hyndman, & K. Wang, Thermal constraint modelling along the Cascadia subduction zone, *GAC/PAC Abstract*, 20, A-77, 1995.
- Oleskevich, D.A., R.D. Hyndman, & K. Wang, Thermal models for the Oregon Cascadia Margin and the width of the locked zone subject to megathrust earthquakes, *EOS supplement*, 75, 621, 1994.

## PARTIAL COPYRIGHT LICENSE

I hereby grant the right or lend my thesis to users of the University of Victoria Library, and to make single copies only for such users or in response to a request from the Library of any other university, or similar institution, on its behalf or for one of its users. I further agree that permission for extensive copying of this thesis for scholarly purposes may be granted by me or a member of the University designated by me. It is understood that copying or publication of this thesis for financial gain shall not be allowed without my written permission.

Title of Thesis:

Thermal Constraints on Great Thrust Earthquake Rupture Zones

Author

A thick black horizontal bar redacting the author's name.

Daniel Alexander Oleskevich  
September 18, 1996.